Application and development of advanced Lorentz microscopy techniques for the study of magnetic nanostructures

Robert J. Beacham MPhys

Presented as a thesis for the degree of Ph.D. at the School of Physics and Astronomy, University of Glasgow August 2013

Abstract

Understanding the magnetic structure and behaviour of domain walls has attracted recent attention in both academia and industry as it is of fundamental importance for the development of magnetic storage media. At the University of Glasgow we specialise in direct magnetic imaging through Lorentz electron microscopy. This PhD project presents an investigation into the development of magnetic imaging methods in the TEM and their application in imaging narrow domain walls in multilayer magnetic structures.

Lorentz microscopy techniques are limited in quantitative magnetic imaging as this generally requires using scanning imaging modes which limits the capability of imaging dynamic processes. The first imaging method developed in this study is a phase gradient technique with the aim of producing quantitative magnetic contrast proportional to the magnetic induction of the sample whilst maintaining a live imaging mode. This method uses a specifically engineered, semi-electron-transparent graded wedge aperture to controllably perturb intensity in the back focal plane. The results of this study found that this method could produce magnetic contrast proportional to the sample induction, however the required gradient of the wedge aperture made this contrast close to the noise level with large associated errors.

In the second part of this study we investigated the development of a technique aimed at gaining sub-microsecond temporal resolution within TEMs based on streak imaging. We are using ramped pulsed magnetic fields, applied across nanowire samples to both induce magnetic behaviour and deflect the electron beam across the detector with respect to time. We are coupling this with a novel pixelated detector on the TEM in the form of a Medipix/Timepix chip capable of microsecond exposure times without adding noise. Running this detector in integral mode and allowing for practical limitations such as experiment time and aperture stability, the resultant streak images were taken in Fresnel, Foucault and low angle diffraction imaging modes. We found that while this method is theoretically viable, the limiting factor was the contrast of the magnetic signal in the streak and therefore the total image counts.

Domain walls (DWs) in synthetic antiferromagnetically (SAF) coupled films patterned as nanowires offer exciting possibilities; the domain walls in these multilayers have narrower widths and reduced magnetostatic energy compared to those in single layer nanowires. In this study Co90Fe10/Ru/Co90Fe10 films were used to investigate the existence and structure of these walls. Nanowires were fabricated in these films and the DW structure was studied with respect to both wire width and varying magnetic layer thickness. It was found that while the DW structure does not appear to vary with the range of wire widths used, it changed significantly with varying thickness. The narrow DWs were observed to form only in samples with an unbalanced ratio of 1.25 : 1 or below; 1.75 : 1 and 2 : 1 samples were both observed to form transverse domain walls.

Acknowledgements

First and foremost, I would like to express my sincere gratitude to my supervisors Dr. Stephen McVitie and Dr. Damien McGrouther, their excellent guidance, support and encouragement have been invaluable throughout the last four years. Both Dr McVitie and Dr McGrouther have aided me with both the theoretical and experimental work throughout this study.

I would also like to thank Dr Sam McFadzean, Colin How, Billy Smith and Brian Miller for their tireless work in maintaining all the equipment in the MCMP group, particularly the CM20 microscope as well as their continuous instruction and endless patience.

Special thanks go to the full collaboration of Christopher Marrows, Serban Lepadatu, Gavin Burnell, Thomas Moore, Ales Hrabec, Damien McGrouther, Maria Jose Benitez Romero and Stephen McVitie who were all involved in the deposition, fabrication and investigation of the SAF materials in this study. The biannual collaborative meetings also provided essential guidance and perspective on the magnetic imaging of these samples.

I would also like to thank all members of the Materials and Condensed Matter Physics past and present who have made my time at the University of Glasgow thoroughly enjoyable.

Finally I would like to thank my parents Malcolm and Lucy Beacham and my two brothers Mike and Tom for their support and guidance throughout my PhD. My gratitude also goes to all of my friends both within and outside the department for their support particularly during the final months of writing.

Thank you to every single one of you.

Declaration

This thesis is a record of the work carried out by myself in the Materials and Condensed Matter Physics Group of the Department of Physics and Astronomy at the University of Glasgow during the period 2009 - 2013. The work described herein is my own with the exception of the fabrication of the permalloy nanowires in chapter 4, which was carried out at the University of Glasgow before my arrival. The milling of the circular aperture samples, also in chapter 4, was performed by Brian Miller at the University of Glasgow. The plasma deposition of the permalloy continuous films in chapter 5 was performed by Dr Damien McGrouther. The work outlined in chapter 6 was a collaborative work between the MCMP group at the University of Glasgow and the University of Leeds; the multilayer deposition and the EBL and Argon milling sample fabrication was performed by Dr Serban Lepadatu in Leeds along with the major hysteresis loops of the sample. The 3D OOMMF simulation scripts used in chapter 6 and the cross sectional images of the samples were done by Dr Maria J Benitez.

Some of the works in this thesis have been published at following conferences:

"Medipix2/Timepix detector for time resolved Transmission Electron Microscopy" R. Beacham, A. Mac Raighne, D. Maneuski, V. O'Shea, S. McVitie and D. McGrouther 2011 JINST 6 C12052

This thesis has not previously been submitted for a higher degree.

Contents

List of Figures

Chapter 1

Ferromagnetism and Antiferromagnetism in Thin Films

1.1 Introduction

The advancement over recent decades of both lithography and observation techniques, as well as the increasing demand for high density magnetic recording devices, has led to research into the understanding of magnetic behaviour on the nanoscale. The work presented in this thesis investigates and develops the magnetic imaging techniques used in Lorentz transmission electron microscopy for characterisation of magnetic nanostructures, as well as researching the varying magnetic structures present in coupled multilayer systems and the potential impact and application of these methods and structures. The net properties and behaviour of magnetic nanostructures both in stable and dynamic states are defined by the internal magnetic properties and the geometry of the nanostructures. These properties along with their origins and effect on the net magnetic structure and behaviour will be discussed in this chapter. The different types of magnetism and the associated energies that define magnetic structure will be discussed in sections 1.2 and 1.3. In parts 1.4 and 1.5, magnetic hysteresis and domain walls are introduced along with how these walls can be moved under the application of both external magnetic fields and currents. Finally the methods used for the simulation of magnetic structures will be

discussed along with their application and use in this study.

1.2 Thin Film Magnetism

All magnetism in solid materials is created through the vector sum of individual atomic moments; these are created by the orbiting electrons around atoms in a similar way to the magnetic field created by a current carrying coil of wire. The vector sum of each of these atomic magnetic moments generates the net moment of a material; the relative orientation and interaction between different moments in a material is the source of the varying types of magnetism. In diamagnetic materials the outer electrons in the atom are paired with identical orbits but opposite spins producing no net magntic moment in the absence of an external field. Paramagnetism is where each atom has a magnetic moment due to an imbalance in the electron spins caused by unpaired electrons or partially filled orbitals; however these magnetic moments are independent of each other and therefore are randomly oriented in field free space. In the absence of an external field these moments will again sum to a zero net magnetisation. Ferromagnetism has atomic magnetic moments similar to those in paramagnets but the neighbouring moments strongly intact, through the exchange interaction, creating net magnetic order and therefore a spontaneous net moment in the absence of an external field. The magnetisation of a sample is a measure of the total magnetic moment per unit volume. This magnetic ordering is dependent on both the external field and the temperature; as the temperature is increased the thermal energy of the atomic moments are also increased until the thermal energy overcomes the moment interaction. At this point, known as the Curie temperature, the thermal energy is sufficient to randomly orient the moments and it reverts to paramagnetic behaviour. As well as aligning the neighbouring atomic moments parallel in ferromagnetism, the exchange interaction is also capable of aligning them antiparallel, this is known as antiferromagnetism; this antiparallel alignment means that while these are structured magnetic materials with interacting neighbouring moments, their net moment is still zero. The magnetic materials used

in this study are exclusively ferromagnetic and the following sections will discuss the magnetic energies associated with this.

1.3 Magnetic Energy

The magnetic structure in ferromagnetism is defined by five magnetic energy terms; minimising the sum of these energies in both global and local minima explains the formation of magnetic domains, and the behaviour of these domains under applied magnetic fields. In the following sections, these energies will be discussed along with their influence of the final magnetic structure.

1.3.1 Exchange Energy

The first of these energies is the exchange energy, this has two main components: the direct exchange, usually simply referred to as exchange, between spins of neighbouring atoms and the indirect exchange carried by the conduction electrons in metals. The sources and influence on the total magnetic structure of both of these interactions will be discussed in this section.

Exchange

The exchange interaction is a quantum mechanical phenomenon between adjacent atomic spins, and describes the tendency for these spins to align either parallel or antiparallel leading to ferromagnetism and antiferromagnetism respectively. This interaction was first described by Weiss in 1907. He postulated a molecular field associated with the magnetisation, equation 1.1 shows this relationship where H_m is the molecular field, M is the magnetisation and ω is the Weiss constant [1, 2]. This equation postulates that this field is parallel to the magnetisation at all times and is proportional to it. This field is not real, it is a postulate of the exchange phenomenon which mimics the observed reaction between magnetic moments.

$$\mathbf{H_m} = \omega \mathbf{M} \tag{1.1}$$

The exchange phenomenon was later more fully explained by postulating it as an overlap interaction between atomic spins. This model uses the Heisenberg exchange Hamiltonian to calculate the exchange energy between two interacting spins, shown in equation 1.2. In this equation, the exchange integral, J_{ij}, is dependent on the exchange stiffness, A, this is a material parameter defined as the strength of the exchange interaction between adjacent magnetic moments and is measured in J/m.

$$E_{ex} = -\sum_{i<j} 2J_{ij}\mathbf{S}_i \cdot \mathbf{S}_j \tag{1.2}$$

Where E_{ex} is the exchange energy, and $\mathbf{S}_i$ and $\mathbf{S}_j$ are the spin vectors of the interacting atoms. This interaction is effectively an overlap interaction between the wavefunctions of the neighbouring electrons, and leads to the property that it falls dramatically with distance; because of this we can assume that it is only effective for nearest neighbour atoms and the energy becomes:

$$E_{ex} = -2JS^2 \sum_{ij} cos\theta_{ij} \tag{1.3}$$

where S is the magnitude of the spin, θ_{ij} is the angle between the neighbouring spins and J is the exchange integral. If J is positive then the energy is minimised when $\theta_{ij} = 0$, meaning that neighbouring atomic spins are parallel, and the material becomes ferromagnetic, shown in figure 1.1a. Conversely if J is negative then the energy is minimised when the neighbouring spins are antiparallel forming an antiferromagnet.

The exchange interaction is localised on the atomic scale, but can also be characterised by the exchange length; this distance is considered to be the length scale where the exchange interaction dominates all other magnetic energy terms meaning that no change in the magnetisation direction is expected. This parameter is material dependent, related to both the saturation magnetisation and the exchange stiffness, in Permalloy this is $\sim 4nm$. To put this into perspective, a 180° DW in a continuous permalloy film in typically $\sim 100nm$ wide.

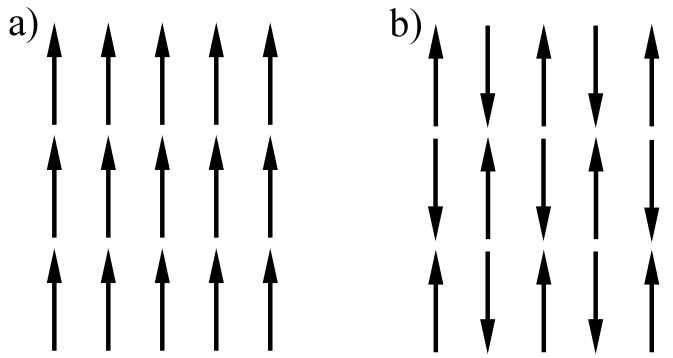

Figure 1.1: (a)Schematic of magnetic orientation in ferromagnetic and (b) antiferromagnetic structures.

Indirect Exchange

The indirect exchange interaction, also known as the Ruderman-Kittel-Kasuya-Yosida (RKKY) interaction, is a coupling between two magnetic elements via the conduction electrons within a metallic spacer. Vonsovskii [3] and Zener [4] first introduced this interaction through the 3d conduction electrons in transition metals, these electrons are polarised by direct exchange with the bound electron spins of a magnetic material, this induced magnetisation within the electron cloud indirectly links magnetic elements. This effect spatially oscillates with distance from the initial interaction between parallel and antiparallel alignments of spins [5, 6, 7, 8, 9].

This interaction is characterised by a coupling constant J, measured in J/m^2 and has typical values ranging from 0.5 to $5Jm^{-1}$ [10]. This magnitude of the coupling and the oscillation frequency is material dependent and its application in this study will be discussed further in section 1.6.

1.3.2 Magnetostatic Energy

The magnetic moments within a ferromagnet gives rise to the magnetostatic energy. These moments are dipolar and therefore generate a magnetic field opposing the magnetisation; this field can be internal, known as demagnetising field, or external, stray field, to the solid and are collectively known as magnetostatic. These dipoles also cause magnetic charge to build up at the surfaces of the structure and at any

point where the magnetisation is divergent. Figure 1.2 shows a schematic diagram of an arbitrary magnetic shape where the magnetostatic field at point P, defined by the position vector **r**, originates from the charges at the sample surface and within the volume. This is defined mathematically in equation 1.4. The field outside the sample is known as the stray field, while inside the sample the field is the demagnetising field.

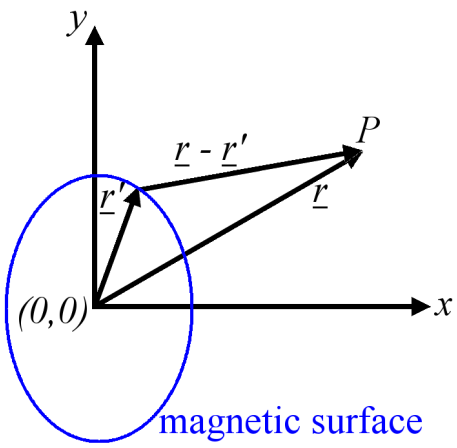

Figure 1.2: Magnetic field at point P, as defined by vectors r' and r, associated with surface and volume integrals shown in equation 1.4.

$$\mathbf{H_m} = \frac{1}{4\pi}\left(\int_V \frac{-\nabla\cdot\mathbf{M}}{(\mathbf{r}-\mathbf{r}')^2}dV' + \int_S \frac{\mathbf{M}.\mathbf{n}}{(\mathbf{r}-\mathbf{r}')^2}dS'\right) \tag{1.4}$$

Where $\mathbf{H_m}$ is the magnetostatic field, $\mathbf{r}$ and $\mathbf{r}'$ are position vectors defined in figure 1.2 and $\mathbf{n}$ is the outward pointing unit vector. The energy that this produces, E_d, as shown in equation 1.5, is minimised by minimising $\mathbf{H_m}$ shown in equation 1.4; the first term in this equation is minimised by reducing the divergence of the magnetisation within the structure while the second is minimised by forcing the magnetisation to lie parallel to the edges at the surface of the structure. This is most commonly done with the formation of magnetic domains, explained later in this chapter.

$$E_d = -\frac{\mu_0}{2}\int_V \mathbf{M}\cdot\mathbf{H_m}dV \tag{1.5}$$

Shape Anisotropy

The shape anisotropy, as the name suggests, creates a preferred direction of magnetisation through the control of the shape of the sample. This phenomenon is a magnetostatic energy as it is related to charge build up at the sample edges. If the magnetisation is perpendicular to the edge of the structure, charges build up at the edges and generate both demagnetising and stray fields. Figure 1.3 shows a schematic diagram of a 2-dimensional elliptical magnetic structure, magnetised along the long and short axes in 1.3*a* and *b* respectively. The strength of the demagnetising field is dependent on the distance between the opposing charges. When the magnetisation lies along the long axis of a sample these charges are further apart than if it falls along the short axis, meaning that the demagnetising field is reduced, minimising the anisotropy energy and creating a preferred magnetisation direction.

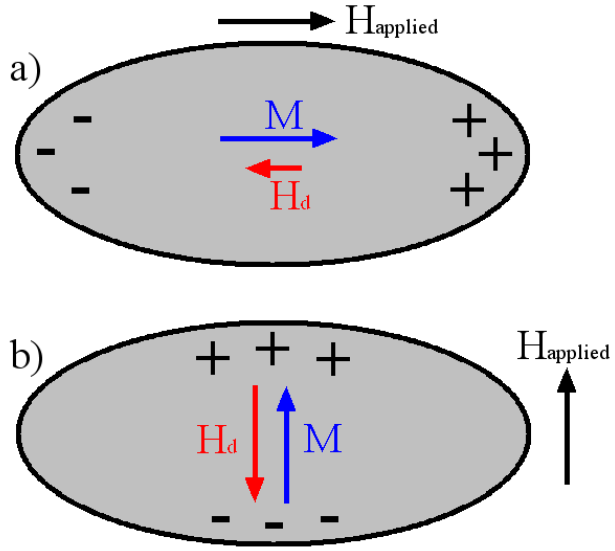

Figure 1.3: Schematic diagram of 2-dimentional ellipsoidal magnetic structure magnetised along the (a) long and (b) short axes, showing the effect of sample shape on the demagnetising field (red arrows). The size of the arrows represent the magnitude of the field.

1.3.3 Anisotropy Energy

Throughout the discussions of the exchange and the magnetostatic energies, the magnetic interactions have been assumed to be isotropic, meaning that the direction of magnetisation within the structure has not affected the internal energies; this is not always the case. Magnetic anisotropy describes the directional dependence of the magnetisation with respect to both the crystal lattice and the total shape of the nanostructure. The most common type of this is magnetocrytalline anisotropy, this where the magnetisation has a preferred direction within the crystal lattice. This preferred direction, known as the easy axis, is due to the asymmetrical atomic orbitals coupling to the crystal structure; in the absence of a magnetic field the magnetisation will tend to lie along the easy axis. The second type of anisotropy discussed in this section is shape anisotropy, where the external size and shape of the sample effects the magnetic structure [11, 12, 13].

Magnetocrystalline Anisotropy

The simplest form of magnetocrysalline anisotropy is uniaxial anisotropy, this is where magnetic anisotropy is a function of only one directional parameter [13]. This is most common in hexagonal crystal lattices as these are typically asymmetrical in one direction. In most hexagonal crystals, the easy axis lies along the c-axis of the lattice. In cubic structures, the symmetry leads to the magnetocrystalline anisotropy being less clearly directed. The energy associated with the magnetocrystalline anisotropy in a cubic structure is shown in equation 1.6.

$$E_\alpha = K_1(\alpha_1^2\alpha_2^2 + \alpha_2^2\alpha_3^2 + \alpha_3^2\alpha_1^2) + K_2(\alpha_1^2\alpha_2^2\alpha_3^2) + \cdots \tag{1.6}$$

Where E_α is the anisotropy term, K_1 and K_2 are constants and α_1, α_2 and α_3 are cosines of the angles the magnetisation direction makes with the edges of the cubic lattice [1]. The higher order terms of this equation are generally neglected as thermal excitation is of a comparable level, and the K_1 term is dominant compared to the higher order constants. K is measured in Jm^{-3} and has typical values of $K_1 = 45 \times 10^{-4} Jm^{-3}$ and $4.8 \times 10^{-4} Jm^{-3}$ for cobalt and iron respectively [14].

Permanent magnets are characterised by high magnetocrystalline anisotropy as this keeps the magnetisation in a single direction. Conversely soft magnetic materials have low anisotropy allowing the magnetisation to rotate freely within the lattice. In polycrystalline materials, such as permalloy, there is still an easy axis within each crystal, however as each crystal is randomly orientated there is no overall preferred direction. The magnetisation direction in such a material fluctuates with the changing crystal orientation, this is known as magnetic ripple [15].

1.3.4 Zeeman Energy

The Zeeman energy is associated with the interaction between the internal magnetisation of the sample and an externally applied magnetic field. The resultant energy is shown in equation 1.7 where μ_0 is the permittivity of free space, $\mathbf{H}$ is the applied magnetic field and $\mathbf{M}$ is the magnetisation of the sample [12]. This shows that the Zeeman energy is minimised if the magnetisation is parallel to the applied field, and is proportional to both the magnitude of that applied field and the total magnetisation integrated over the sample volume. This means that in the presence of a field the magnetisation of a sample will tend to point parallel to it, and depending on the material, a high enough field can make the Zeeman energy dominate all other energy terms.

$$E_Z = -\mu_0 \int \mathbf{M} \cdot \mathbf{H} dV \tag{1.7}$$

1.3.5 Magnetostriction Energy

Changing the magnetisation in a sample rotates the atomic orbitals. These orbitals are asymmetrical, therefore in a crystal lattice, when the magnetisation rotates it changes the physical dimensions of the lattice. The resultant strain is known as the magnetostriction [16]. This can occur spontaneously or be induced by external fields. The magnetostriction, λ, is defined as the fractional change in the sample size, shown in equation 1.8 where l is the length of the sample. When λ is in the

same direction as the applied field, this is known as the saturation magnetisation.

$$\lambda = \frac{dl}{l} \tag{1.8}$$

$$E_\lambda = \int \left(\frac{3}{2} \lambda_S \sigma sin^2 \alpha \right) dV \tag{1.9}$$

Any deviation from this comes with a cost in energy, E_λ, shown in equation 1.9 where α is the angle between the magnetisation and the stress, σ is the tension in the system and λ_S is the saturation magnetostriction [17]. The materials used in this study, including permalloy, have insignificant magnetostriction, therefore this energy term is largely neglected and the sample dimensions are considered constant.

1.3.6 Total Energy

The total magnetic structure of a sample is defined by minimising the total energy, E_{total}, formed of these five terms, as shown in equation 1.10. The determining factors of these energies are the atomic moment, exchange constant, anisotropy, sample shape and the applied field. How this total energy is minimised depends on which magnetic energy dominates the equation.

$$E_{total} = E_{ex} + E_m + E_\alpha + E_Z + E_\lambda \tag{1.10}$$

Figure 1.4 shows schematic diagrams of a rectangular ferromagnetic sample with three different magnetic structures. Figure 1.4a displays a single domain state, in this structure all the atomic moments are aligned parallel. This minimises the exchange energy as there is no rotation between neighbouring spins, however there is significant demagnetising (shown in red) and stray fields (shown in blue) due to the charge build up at the edges; this structure is only likely to form under a high applied field or if the sample has large uniaxial anisotropy and is typical in permanent magnets. Figure 1.4b then shows a multi-domain state; here the surface charge, and therefore

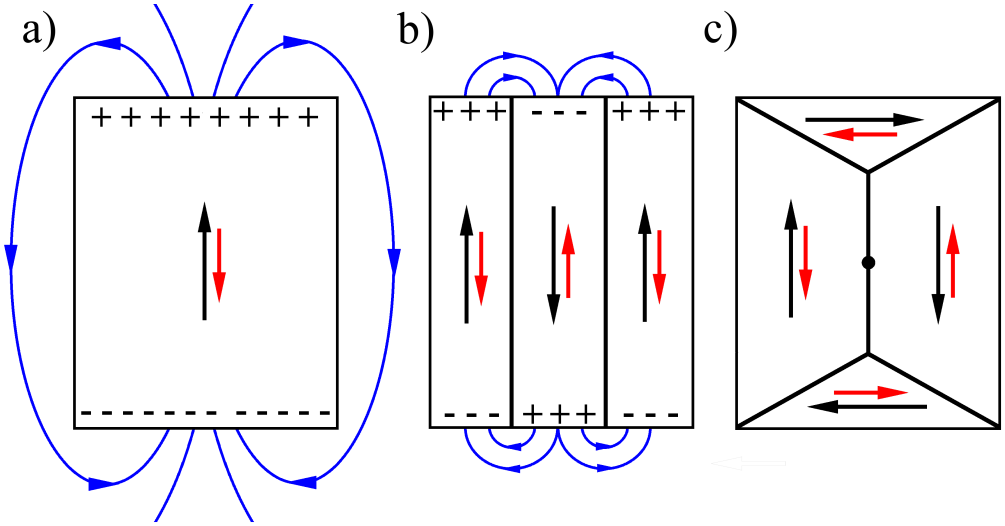

Figure 1.4: Schematic diagram of possible magnetic orientations in single layer ferromagnetic sample, showing (a) single domain (b) multi-domain and (c) flux closure states. Black and red arrows show magnetisation and demagnetising field respectively.

the magnetostatic energy, is reduced at the cost of exchange energy at the domain boundaries. This state is unlikely to form under an applied field as the domains oppose each other, however it may still form in a uniaxially anisotropic sample. In the absence of both magnetocrystalline anisotropy and external fields the structure will most likely form a flux closure state, as shown in figure 1.4*c*. In this configuration the magnetostatic energy is minimised as there is very little surface charge. This configuration does have high exchange energy at the domain boundaries but is still typically the lowest energy state in most soft ferromagnets.

1.4 Hysteresis

Hysteresis is where the magnetisation is not a single valued function of the applied field [18]. This phenomenon is most commonly observed in ferromagnetic materials; paramagnets don't show hysteresis as their atomic moments are independent. Within ferromagnetism this means that the magnetisation within the sample is dependent on the path taken to get there. The path of the magnetisation, as the applied field varies between high positive to high negative fields may be observed as a hysteresis

loop; example loops of both hard and soft ferromagnets are shown schematically in figure 1.5.

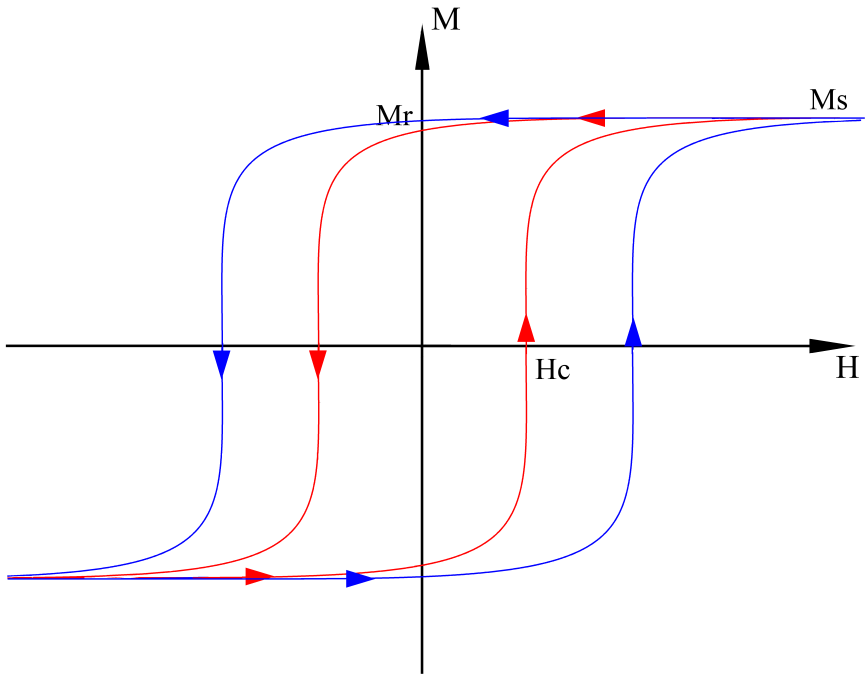

Figure 1.5: Example hysteresis loops of both soft (red) and hard (blue) magnetic materials.

At high applied fields, the maximum sample magnetisation is known as the saturation magnetisation, M_s; where all the atomic magnetic moments within a sample are aligned parallel to the applied field direction, creating a maximum total net moment. From this point of saturation, as the applied field is reduced, the magnetisation reduces as the Zeeman energy and therefore the magnetic structure changes. When the applied field reaches zero, the magnetisation is known as the remanence magnetisation, M_r; the value of this is material and axis dependent with low values typically associated with soft magnetic materials. The field required to reduce the total magnetisation to zero is known as the coercivity, H_c. From here, the magnetisation increases with the field until it reaches saturation in the opposite direction. The reverse of this, going from high negative to high positive fields shows that the behaviour is symmetrical, resulting in multiple possible magnetisation values for each

applied field [1].

There are two main types of ferromagnetic materials, hard and soft materials. Figure 1.5 shows example hysteresis loops from both types of sample, shown in red and blue respectively. Soft magnetic materials are categorised by low coercivity and a small hysteresis area. Hard materials are opposite to this leading to larger overall loops [18, 16]. For example a hard material such as $NdFeB$ has a coercivity in excess of $1 \times 10^4 Oe$ whilst Permalloy, a relatively soft material, has a value of $<10Oe$. In this work hysteresis loops will be used to identify the basic characteristics of both single and multiple layer continuous thin films; this information is essential to better understand the magnetic behaviour of fabricated nanostructures.

1.5 Magnetic Domains and Domain walls

As discussed in the previous section, magnetic domains form in ferromagnets as it minimises the total energy within the sample [16]. Multiple domains only form if the saving in total energy is greater than the energy cost associated the existence of domain walls separating them. Within these walls the magnetisation rotates coherently from one domain to the other typically resulting in antiparallel magnetisation on either side of the wall. Walls in continuous ferromagnetic films typically vary from 1 to $100nm$ in width.

1.5.1 Domain walls in continuous films

The structure of a domain wall is a balance between magnetic energies, particularly the magnetostatic, exchange and anisotropy energies, and is generally defined by the sample size. In a bulk material, if the domain wall is separating two domains of antiparallel magnetisation (180°) then a Bloch wall is formed. This type of wall, seen in figure 1.6a, is where the magnetic moments within the wall rotate about an axis perpendicular to the wall axis. This causes charges to build on the surface of the sample at the centre of the wall, creating stray and demagnetising fields and

increasing the magnetostatic energy. Once the thickness of a sample approaches a critical value, typically $\sim 30nm$ [13], the rise in magnetostatic energy from the proximity of the surface charges makes Bloch walls energetically unfavourable and Néel walls form. These walls, seen in figure 1.6b, are characterised by the magnetisation within the wall rotating in plane with the sample effectively creating a one dimensional wall. This reduces the magnetostatic energy of the wall at the surfaces at the expense of producing demagnetising fields within the volume; however as the wall width is larger than the film thickness, the magnetostatic energy is still reduced [16]. according to the Néel model, the total energy of a Néel wall is dependent on the angle between the two separated domains, with a 90° wall having just 12% of the energy of a 180° wall [17]. This saving in energy with forming lower angled walls can result in more complex walls forming. Figure 1.6c shows a cross-tie wall, these are two dimensional walls and are an intermediate stage between Bloch and Néel walls. This type of wall is much wider than either of the others however the saving in energy from forming multiple 90° walls allows this structure to exist [17, 1, 16].

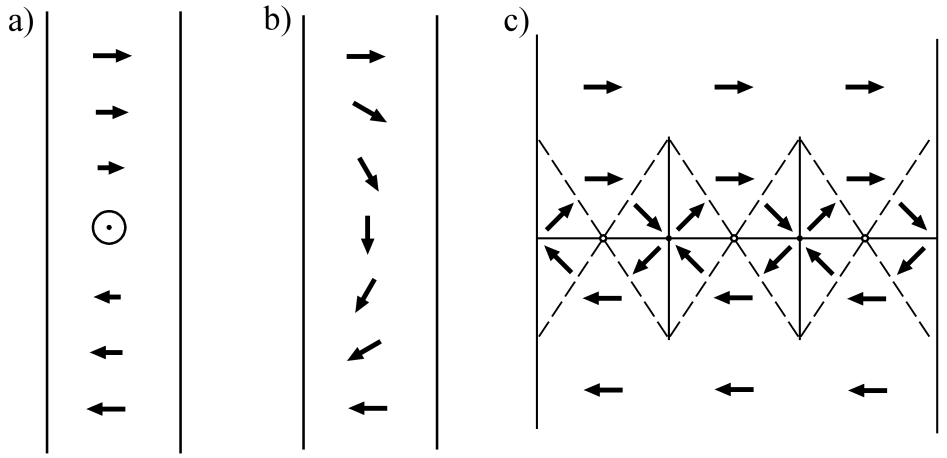

Figure 1.6: Plan view diagram of (a) Bloch walls in bulk samples, (b) Néel walls in thin films and (c) cross-tie wall in intermediate stage.

1.5.2 Domain Walls in Nanowires

Néel walls form when the sample is restricted in thickness. In a nanowire, where the sample is restricted in width as well, the domain walls form into more complex magnetic structures in a similar manner to the cross-tie walls in continuous films. In soft magnetic nanowires, the two dimensional size constraints lead to an increase in shape anisotropy causing the magnetisation to align parallel to the edges of the wire. This alignment of the magnetisation forces any DWs in the nanowire to be either head-to-head or tail-to-tail walls; these walls have higher energy that their 180° counterparts. The charge associated with these walls causes the magnetic structure to be more complex than the simple coherent rotation of magnetic moments seen in continuous films. There are three main types of these head-to-head (or tail-to-tail) walls, transverse, asymmetric transverse and vortex, as shown in figure 1.7.

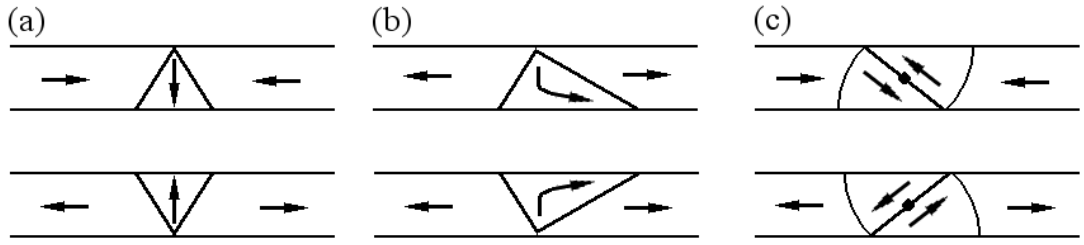

Figure 1.7: Schematic diagram of (a) transverse, (b) asymmetric transverse and (c) vortex domain walls.

Vortex domain walls (VDWs), shown schematically in figure 1.7*c*, are characterised by the magnetisation rotating about a central vortex within a Néel wall, this wall is positioned at an angle to the wire with two further rotations on either side ending in moments parallel to the wire edges.

In a transverse domain wall (TDW) the magnetisation rotates through what are effectively, two symmetrical 90° walls forming a 'V', with an area of magnetisation perpendicular to the wire in its centre, shown in 1.7*a*. The intermediate between these two types is an asymmetric transverse wall, shown in 1.7*b*, this is the same

as TDW but there is a small rotation in the central region giving a component parallel to the wire edge. Which of these walls forms is dependent on their relative energies. The phase diagram of when these walls form in nanowires with respect to wire thickness and width was created in 2005 by Nakatani et.al, shown in figure 1.8 [19]. It can be seen that vortex walls form in larger, thicker wires whilst transverse walls require either very narrow or very thin wires. It is worth noting at this stage that the width of the wall itself varies from with wire width and wire thickness from $\sim 15nm$ in sub-$50nm$ wide wires to $\sim 350nm$ in $450nm$ wider wires [19].

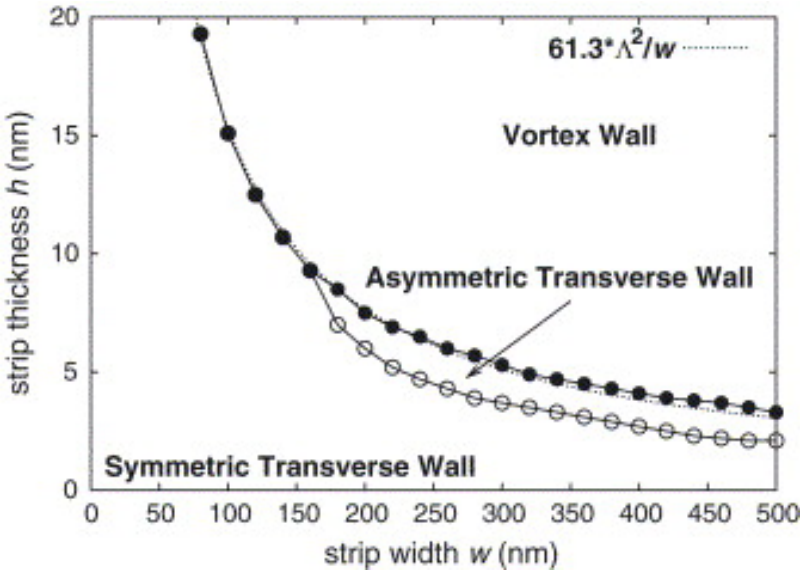

Figure 1.8: Phase diagram of domain wall types in nanowires with varying width and thickness [19].

1.5.3 Domain Wall Motion

Magnetic domains and domain wall dynamics are of crucial importance in technologies such as magnetic logic devices, magnetic storage media and spintronic applications. This and the recent development of lithography techniques to fabricate high quality nanostructures has led to increased interest in the physics behind domain wall mobility in nanostructures over the last decade [20, 21]. There are two main ways of moving domain walls in nanowires: applied magnetic fields and applied electric currents.

Domain wall motion under applied magnetic fields

As stated previously, the main energies involved in determining the magnetic domain structure within nanowires are the exchange and the magnetostatic energies of the nanostructure. When an external magnetic field is applied, the Zeeman energy is changed and begins to influence the magnetic structure [1].

The Zeeman energy, defined by equation 1.7, is proportional to $\int \mathbf{M} \cdot \mathbf{H} dV$. This means that this energy is minimised when the magnetisation of the sample is parallel to the applied field. Therefore, if the field is applied parallel to the wire axis, then it is also perpendicular to the magnetic moments in the centre of the wall, producing a torque, $\mathbf{M} \times \mathbf{B}$. This torque rotates these moments, moving the domain wall, increasing the size of the domain parallel to the field and decreasing the antiparallel domain [1, 22]. Before this occurs, the torque must reach a threshold to overcome any pinning potentials in the sample. Equation 1.11, shows how the velocity of a wall, ν, varies with the applied field once above the threshold field [16, 23].

$$\nu = \mu(H - H_t) \tag{1.11}$$

Where ν is the domain wall velocity, H is the applied field and H_t is the threshold field. μ is the domain wall mobility, defined as the rate of change of velocity with applied field. This is a defining parameter of the DW motion and is dependent on the sample dimensions as well as the exchange stiffness (A), the saturation magnetisation (M_s), and the sample anisotropy. Domain wall mobilities as high as $\sim 30 - 40 ms^{-1} Oe^{-1}$ have been measured in continuous permalloy films [24]. Equation 1.11 predicts the velocity increasing linearly with the applied field; this is true up to the "Walker limit" [25]. When the field is increased beyond this, vortices and anti-vortices are nucleated within the wall which transit the wall before being annihilated; the presence of these vortices reduces the torque, slowing the DW movement. Their transit produces an oscillatory velocity with respect to field [26, 27, 28].

Domain wall motion under applied electric currents

In this technique, domain walls are moved by the application of spin polarised currents. When this is applied, the interaction between the spins on the conduction electrons and the exchange field creates a torque on the domain wall. This torque, similar to that in the applied field case rotates the spins within the wall, moving the wall through the wire. Moving domains with applied currents have been used extensively in permalloy ($Ni_{81}Fe_{19}$) nanowires; this material is suitable for this process due to its low magnetic anisotropy and high Curie temperature [29, 30, 31, 32]. One of the main properties of current driven DW motion is that all the DWs in a single wire move in the same direction; this is not the case in the field driven case.

Domain wall velocities in permalloy nanowires vary but can reach up to $110ms^{-1}$, with a required current density of $\sim 1 \times 10^{12} Am^{-2}$. However, when high current densities are used the wire heats up via Joule heating and can melt or deform. One of the main advantages of this technique is that the wall can be moved in much shorter timescales than with applied fields [33]; this high speed movement allows current based magnetic media, such as race track memory to be viable against more proven technologies.

1.6 Synthetic Antiferromagnetism

Synthetic antiferromagnets (SAFs) are three layer systems consisting of two ferromagnetic layers separated by a thin layer of a non-magnetic transition metal. The transition metal acts as a conductor for the Ruderman-Kittel-Kasuya-Yosida (RKKY) interaction. This interaction, also known as indirect exchange, is a three stage process involving all three layers of the SAF. First the magnetic moments within one of the ferromagnetic layers directly interact, through the exchange interaction, with the conduction electrons in the spacer layer. The conduction electron cloud in the spacer layer interacts with the second ferromagnetic layer. Once again the direct exchange interaction aligns the moments of the layer with the conduction electrons; through this process, the two ferromagnetic layers are indirectly coupled.

The spin polarisation of the coupling between the conduction electrons and the ferromagnetic layers, decays oscillatorially with distance. This means that the relative alignments of the two layers oscillate between ferromagnetic and antiferromagnetic with the thickness of the spacer layer. An example of this oscillation is shown in figure 1.9 [34]. When the thickness of this spacer layer is tuned so that the ferromagnetic layers are antiferromagnetically coupled and the layers are of equal thickness, the structure is known as a Synthetic Antiferromagnet (SAF). The coupling between the layers of a SAF results in a dramatic reduction in the magnetostatic energy as they are always in a flux closed state [35]. These devices have also received considerable attention due to their potential application in spin valve devices, MRAM, and both reading and writing heads in magnetic recording media [36, 37, 38].

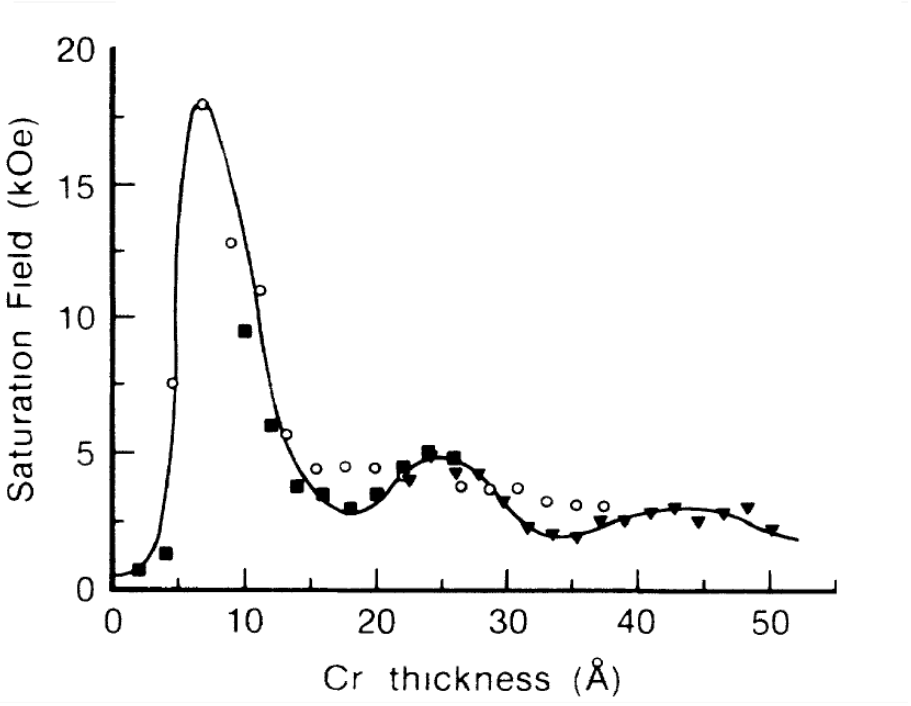

Figure 1.9: RKKY oscillation for a Chromium spacer of varying thickness between two layers of Iron [34]. Peaks and troughs represent AFM and FM coupling respectively.

The final part of this study will investigate the structure and behaviour of domain walls in SAF materials, looking at both continuous films and nanostructures. These structures lower the magnetostatic energy, allowing narrow domain walls to form

[39]. These walls are postulated to have the same width as 180° DWs in continuous films, i.e. $\sim 100nm$. They should also be independent of wire width and be able to be moved by currents up to two orders of magnitude lower than current, single layer nanowires. If proven, these properties are ideal for the advancement of technologies such as race track memory as it will increase the potential aerial density [40]. These walls and the foundation for their postulated structure and behaviour will be further discussed in chapter 6.

1.7 Magnetic simulations

Micromagnetic simulations are a highly useful tool used for predicting magnetic structures and behaviour. In this study, these simulations were done using Object Oriented Micromagnetic Framework (OOMMF) [41]. This framework utilises the Landau-Lifshitz-Gilbert equation, shown in equation 1.12, to simulate the magnetic structure of user defined samples. In this equation $\mathbf{H}_{eff}$ is an effective field defined by equation 1.13 and includes the total magnetic energy defined previously.

$$\frac{d\mathbf{M}}{dt} = -\gamma \mathbf{M} \times \mathbf{H}_{eff} - \frac{\gamma \alpha}{M_s^2} \mathbf{M} \times (\mathbf{M} \times \mathbf{H}_{eff}) \tag{1.12}$$

$$\mathbf{H}_{eff} = -\frac{1}{\mu_0} \frac{dE_{tot}}{d\mathbf{M}} \tag{1.13}$$

Where $\mathbf{M}$ and M_s are the magnetisation and the saturation magnetisation respectively, t is the time, γ is the gyromagnetic ratio and α is the damping coefficient [42, 41], μ_0 is the permeability of free space, $\mathbf{H}_{eff}$ is the effective field and E_{tot} is the total magnetic energy including the crystalline anisotropy, exchange, magnetostatic and Zeeman energies. The torque, $\frac{d\mathbf{M}}{dt}$ is minimised when the effective field is parallel to the magnetisation. We know that $\mathbf{M}$ arises due to angular momentum considerations meaning that as the magnetisation moves, it precesses about $\mathbf{H}_{eff}$. The first term of the LLG equation defines the precession of the magnetisation around the effective field. If only this term is taken into account, this procession is conical

as illustrated in figure 1.10a. The second term in the LLG equation defines the magnetic damping of the system, causing the magnetisation to spiral towards the effective field, shown in 1.10b, reducing $\frac{d\mathbf{M}}{dt}$.

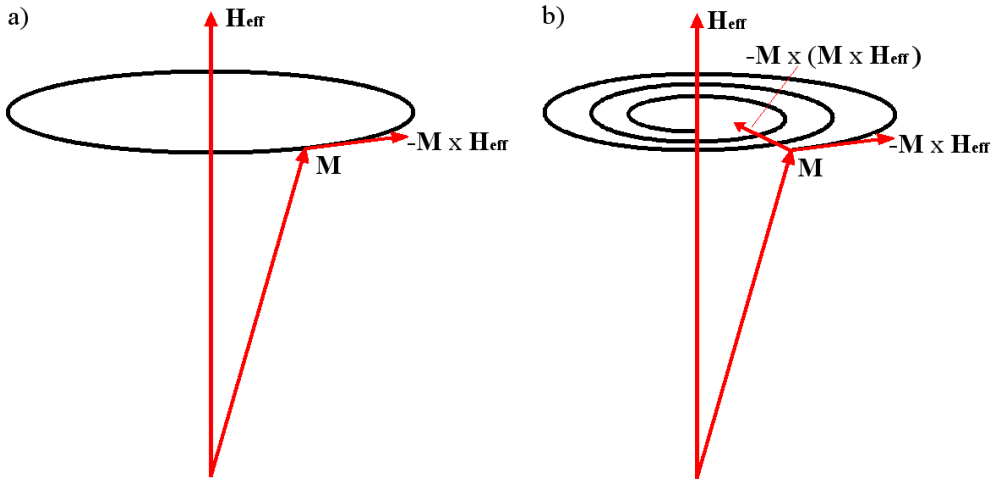

Figure 1.10: Magnetisation procession around the effective field both with (a) and without (b) damping

Ideally, simulations would calculate the orientation of every atomic moment in the structure. However, this is unrealistic due to constraints on computing power and time. For this reason OOMMF simulates complete structures by breaking them into discrete 3D cells, the dimensions of which are user defined. Each cell has a constant magnitude of magnetisation and is typically chosen to have a size comparable to the exchange length in order to maximise the cell size without compromising the magnetic simulation. All simulations in this study use a cell size of $5nm$ as this is the approximate exchange length for Permalloy. A simulation is normally broken into steps where each step is defined by a fixed value of a variable, typically an applied field or current. Each step of the simulation is allowed to relax and $\frac{d\mathbf{M}}{dt}$ reduce until equilibrium is reached, usually defined as $\frac{d\mathbf{M}}{dt}<1\times10^{-5}$. The structure is then saved and the variable is changed before the next step begins. This software has been used extensively in this study to model both two and three dimensional magnetic structures. The simulated structures have subsequently been used to generate predicted image intensities within TEMs.

This system does have limitations however it is very useful at predicting both magnetic structures and TEM images of these structures. Simulated structures will typically have perfect and sharp edges as well as uniform thickness; this will not be the case experimentally. Real structures will have defects both within the main material and at the fabricated edges of nanostructures; these defects will affect the magnetic structure and behaviour of a sample and must be considered when comparing experimental and predicted results. OOMMF also runs simulations at a temperature of 0K; this neglects any noise or behaviour caused by thermal effects. This may produce inconsistencies between prediction and experiment particularly with regards to domain wall motion and mobility, however they still prove to be highly useful and will be utilised throughout this study.

In this thesis the development of two possible magnetic imaging methods designed to improve current limitations within the TEM will be investigated. It will also discuss how SAF materials may be utilised to generate new types of domain walls in nanowires and the possible application of these into improving current magnetic storage media. The following chapters will discuss the fabrication of magnetic nanostructures and the characterisation techniques used in this study, before the results gained over the three projects are discussed in chapters 4, 5 and 6 respectively.

Bibliography

[1] Jakubovics J.P. *Magnetism and magnetic materials.* Cambridge University Press, 1994.

[2] Weiss P. *J. De. Phys.*, 6(661), 1907.

[3] Vonovskii S.V. and Turov E.A. *JETP*, 24(4):419–428, 1953.

[4] Zener C. Interaction between the d shells in the transition metals. *Phys. Rev.*, 81:440–444, Feb 1951.

[5] Ruderman M.A. and Kittel C. Indirect exchange coupling of nuclear magnetic moments by conduction electrons. *Phys. Rev.*, 96(1):99 –102, October 1954.

[6] Yosida K. Magnetic properties of Cu-Mn alloys. *Physical Review*, 106(5):893–898, 1957.

[7] Kasuya T. A Theory of Metallic Ferromagnetism and Antiferromagnetism on Zeners Model. *Progress of Theoretical Physics*, 16(1):45–57, 1956.

[8] Kittel C. *Introduction to Solid State Physics.* John Wiley and Sons, 1976.

[9] Parkin S.S.P. More N. and Roche K.P. Oscillations in Exchange Coupling and Magnetoresistance in Metallic Superlattice Structures - CO/RU, CO/CR, and FE/CR. *Physical Review Letters*, 64(19):2304–2307, MAY 7 1990.

[10] Wintz S. et.al. Direct observation of antiferromagnetically oriented spin vortex states in magnetic multilayer elements. *Appl. Phys. Lett.*, 99(14), OCT 3 2011.

[11] Cowburn R.P. Property variation with shape in magnetic nanoelements. *Journal of Physics D - Applied Physics*, 33(1):R1–R16, JAN 7 2000.

[12] Coey J.M.D. *Magnetism and magnetic materials.* Cambridge University Press, 2010.

[13] Aharoni A. *Inroduction to the Theory of Ferromagnetism.* Oxford University Press, 1996.

[14] Cullity B.D. Graham C.D. *Introduction to Magnetic Materials.* John Wiley and Sons, 2011.

[15] Fuller H.W. and Hale M.E. Determination of Magnetisation Distribution in Thin Films Using Electron Microscopy. *Journal of Applied Physics*, 31(2):238–248, 1960.

[16] Jiles D. *Magnetism and magnetic materials.* Taylor and Francis, 2nd edition, 1998.

[17] Hubert A. and Schaefer R. *Magnetic Domains: the analysis of magnetic microstructures.* Springer, 1988.

[18] Robinson F.N.H. *Macroscopic Electromagnetism*. Pergamon Press, 1st edition, 1973.

[19] Nakatani Y. Thiaville A. and Miltat J. Head-to-head domain walls in soft nano-strips: a refined phase diagram. *J. Magn. Magn. Mater.*, 290(Part 1, SI):750–753, APR 2005.

[20] Ono T. Miyajima H. Shigeto K. Mibu K. Hosoito N. Shinjo T. Propagation of a magnetic domain wall in a submicrometer magnetic wire. *Science*, 284:468–470, 1999.

[21] Allwood D.A. Xiong G. Faulkner C.C. Atkinson D. Petit D. and Cowburn R.P. Magnetic domain-wall logic. *Science*, 309(5741):1688–1692, SEP 9 2005.

[22] Mougin A., Cormier M., Adam J. P., Metaxas P. J., and Ferre J. Domain wall mobility, stability and Walker breakdown in magnetic nanowires. *EPL*, 78(5), 2007.

[23] Hatfield W.B. Domain wall Velocities in Permalloy Films. *J. Appl. Phys.*, 37(4):1934–&, 1966.

[24] Konishi S. Yamada S. and Kusuda T. Domain-wall velocity, mobility and mean free path in permalloy films. *IEEE Trans. Magn.*, MAG7(3):722–&, 1971.

[25] Yang J. Nistor C. Beach G.S.D. and Erskine J.L. Magnetic domain-wall velocity oscillations in permalloy nanowires. *Phys. Rev. B*, 77(1), JAN 2008.

[26] Porter D.G. and Donahue M.J. Velocity of transverse domain wall motion along thin, narrow strips. *J. Appl. Phys.*, 95(11, Part 2):6729–6731, 2004.

[27] Martinez E. Lopez-Diaz L. Alejos O. Torres L. Thermally activated domain wall depinning in thin strips with high perpendicular magnetocrystalline anisotropy. *J. Appl. Phys.*, 79, 2009.

[28] Martinez E., Lopez-Diaz L., Alejos O., Torres L., and Carpentieri M. Domain-wall dynamics driven by short pulses along thin ferromagnetic strips: Micromagnetic simulations and analytical description. *Phys. Rev. B*, 79(9), MAR 2009.

[29] Luc T. Masamitsu H. Xin J. Rai M. Rettner C. and Parkin S.S.P. Oscillatory dependence of current-driven magnetic domain wall motion on current pulse length. *Nature*, 443(7108):197–200, SEP 14 2006.

[30] Masamitsu H. Thomas L. Charles R. Rai M. Yaroslaw B. and S.S.P. Parkin. Current driven domain wall velocities exceeding the spin angular momentum transfer rate in permalloy nanowires. *Phys. Rev. Lett.*, 98(3), JAN 19 2007.

[31] Yamaguchi A. Ono T. Nasu S. Miyake K. Mibu K. and Shinjo T. Real-space observation of current-driven domain wall motion in submicron magnetic wires. *Phys. Rev. Lett.*, 92(7), FEB 20 2004.

[32] Klaui M. Vaz C.A.F. Bland J.A.C. Wernsdorfer W. Faini G. Cambril E. Heyderman L.J. Nolting F. and Rudiger U. Controlled and reproducible domain wall displacement by current pulses injected into ferromagnetic ring structures. *Phys. Rev. Lett.*, 94(10), MAR 18 2005.

[33] Thomas L. Hayashi M. Jiang X. Moriya R. Rettner C. Parkin S.S.P. Oscillatory dependence of current-driven magnetic domain wall motion on current pulse length. *Nature*, 443(7108):197–200, SEP 14 2006.

[34] Parkin S.S.P. More N. and Roche K.P. Oscillations in Exchange Coupling and Magnetoresistance in Metallic Superlattice Structures - Co/Ru, Co/Cr and Fe/Cr. *Phys. Rev. Lett.*, 64(19):2304–2307, MAY 7 1990.

[35] Inomata K. Nozaki T. Tezuka N. and Sugimoto S. Magnetic switching field and giant magnetoresistance effect of multilayers with synthetic antiferromagnet free layers. *Appl. Phys. Lett.*, 81(2):310–312, JUL 2002.

[36] Zhen L. Skomski R. Liou S-H. Michalski S. Chipara M. Kirby R.D. Magnetization precession and domain-wall structure in cobalt-ruthenium-cobalt trilayers. *J. Appl. Phys.*, 109(7), APR 2011.

[37] Pham H. Cimpoesu D. Plamada A-V. Stancu A. Spinu L. Dynamic critical curve of a synthetic antiferromagnet. *Appl. Phys. Lett.*, 95(22), NOV 30 2009.

[38] Fukuma Y. Fujiwara H. and Visscher P. B. Toggle switching of weakly coupled synthetic antiferromagnet for high-density magnetoresistive random access memory. *J. Appl. Phys.*, 103(7), APR 2008.

[39] *Lepadatu S. private communication.*

[40] *US patent 8089797 - Nanowire racetrack memory.*

[41] Donahue M.J. and Porter D.G. Oommf user's guide, 1999.

[42] Gilbert T.L. A phenomenological theory of damping in ferromagnetic materials. *IEEE Trans. Magn.*, 40(6):3443–3449, NOV 2004.

Chapter 2

Sample Fabrication

2.1 Introduction

Recent developments in both deposition and lithography techniques have meant that fabricating nanoscale devices is now possible. This has led to a high demand for research into magnetic nanostructures for applications such as generating smaller, higher density magnetic storage devices. The magnetic samples fabricated in this study were both continuous film and nanostructures in both single and multilayers. Various peripheral depositions have also been required such as charge dissipation layers. In this chapter, the sputtering and milling techniques used to fabricate samples in this study will be discussed. The substrates used in this study will be first considered in section2.2; this will describe both solid substrates and membrane samples used in the TEM. The various methods of sample deposition, namely thermal evaporation and plasma sputtering, will then be considered along with their relative advantages and their specific use in this study. Sections 2.4 and 2.5 will then consider focused ion beam lithography and electron beam lithography respectively as methods of fabricating nanostructures in thin films. Finally argon milling will be discussed. This was performed at the University of Leeds as part of the project discussed in the final results chapter.

2.2 Solid and Membrane Substrates

In this study, two types of sample substrates were used. The first of these is a solid sample substrate; these are simple blocks of silicon with an upper surface oriented to the (111) plane. This crystal surface provides a smooth, stable environment for the deposited film. In this study these substrates are used to hold synthetic antiferromagnetic multilayer structures for capturing hysteresis loops as well as magnetoresistance measurements. This will be further discussed in chapter 6.

The majority of the samples fabricated and investigated in this study use the second type of sample substrate, this is a membrane sample used in TEM. Unlike solid substrates, TEM samples have to be electron transparent and therefore very thin. The substrates used in this study consist of $100 \times 100\mu m$, $35nm$ thick membranes of Si_3N_4 spanning a gap in a silicon base, as shown in figure 2.1 [1].

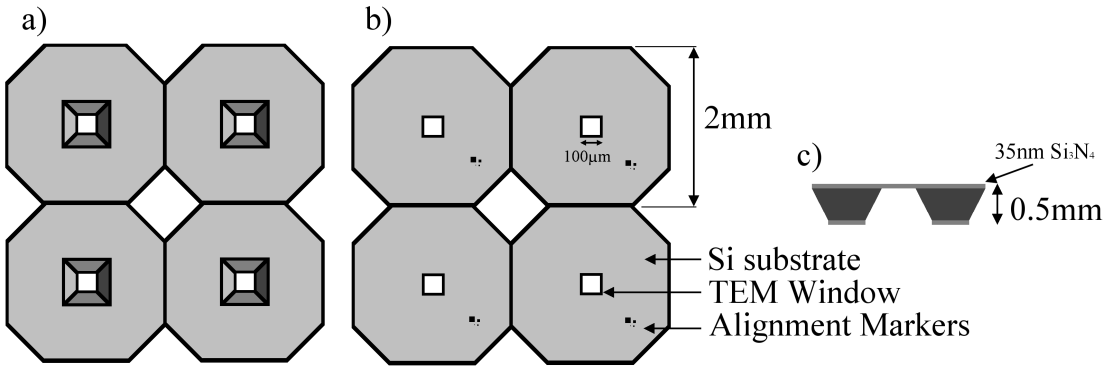

Figure 2.1: Diagram of a 2x2 block of membrane samples used in TEMs from (a) bottom, (b) top and (c) cross sectional view. Showing position of alignment markers with respect to the membrane, not to scale.

These substrates are made by Kelvin Nanotechnology Ltd. (KNT). Before sputtering they are initially cleaned in acetone, isopropanol IPA and finally methanol, before being baked to remove any residual solvent. The alignment markers shown in figure 2.1 are consistently positioned with respect to the membranes, to help with the alignment procedure during the lithography processes described in sections 2.5 and 2.6.

These membranes are well established as TEM substrates. They provide a stable platform for the deposition of samples whilst minimising the interaction between the electron beam and the substrate. These samples have been used at all stages of this study as most of the work done has been within the TEM. However these samples have their difficulties, one of the major problems is their lack of conductivity. Si_3N_4 is an electrical insulator, therefore if the structure being images is an isolated metal it will not be able to discharge. This build-up of charge means that when the electron beam hits the sample the beam will be deflected, reducing the capability of the imaging. This is solved by depositing a $5 - 10nm$ continuous film of either carbon or aluminium onto the back of the membrane to dissipate the charge from the areas of interest.

2.3 Sample Deposition

In this study, two main materials were required for deposition; the first is thin film permalloy of thickness $\sim$20 to 30nm, the second is multilayers of cobalt-iron ($Co_{90}Fe_{10}$)and ruthenium (Ru), reaching minimum thicknesses of 7Å. As well as these main sample materials, carbon and aluminium were both used as charge dissipative layers. In this section, the methods used to deposit these materials will be discussed along with their advantages and disadvantages in relation to their specific use in this study.

2.3.1 Thermal Evaporation

Thermal evaporation uses a ceramic boat to heat the seed material to the point of vaporisation. The vaporised material condenses onto the target substrate, forming a thin film. To minimise the risk of contamination, the evaporation is performed under vacuums of $\sim 5 \times 10^{-6} mbar$.

Figure 2.2 shows a schematic diagram of the thermal evaporator used at the University of Glasgow. This consists of a glass vacuum chamber pumped by a diffusion

pump and backed by a turbo pump. Together with a bakeout system, used for 8 hours at $70-100°C$, the minimum pressure can reach $\sim 2 \times 10^{-7} mbar$, although this increases to between 3 and $5 \times 10^{-6} mbar$ during evaporation. This vacuum is aided by copper condenser coils in the chamber which are cooled by liquid nitrogen prior to evaporation.

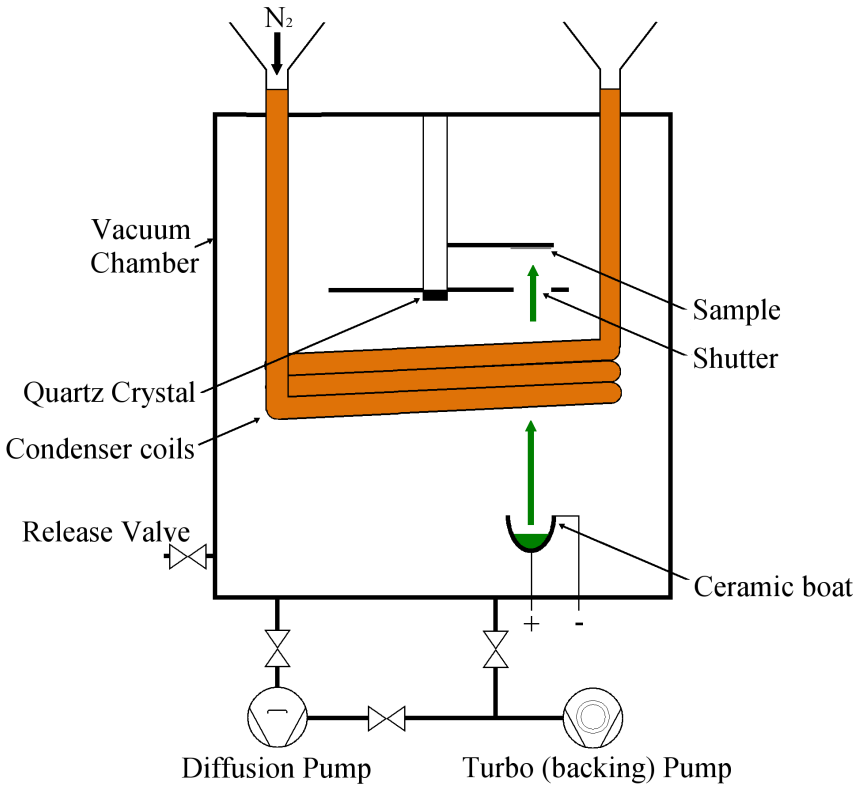

Figure 2.2: Schematic diagram of thermal evaporation chamber showng the relative positions of the ceramic bowl, thickness crystal and sample.

A high current is passed through the ceramic boat, which is resistively heated to the point of evaporation [2, 3]. Permalloy requires a temperature of $\sim 1730°$ to evaporate [4], this typically requires $\sim 25-30A$ through the boat. The quartz crystal, shown schematically in figure 2.2, is used to monitor the thickness of the material being deposited. The crystal is mechanically oscillated at a known resonant frequency; as the material builds up on the crystal, at the same rate as on the sample, the resonant frequency changes; this is known as quartz crystal microbalancing. This change is used to measure the thickness of the deposited material. This measurement

is calibrated for each material, as it is density dependent, and is monitored in real time. Once calibrated, the instrument can deposit thin films to an accuracy of $\sim 2nm$ [5].

In this study thermal evaporation was used for depositing aluminium and carbon as charge dissipative layers on the Permalloy and SAF samples respectively. This technique was ideal for this purpose as these layers are approximately $5nm$ thick and its relative inaccuracy in thickness, compared to plasma sputtering or pulsed laser deposition, is not vital. These layers were typically put on the back of the membranes to minimise any influence this layer may have on the sample behaviour.

2.3.2 Plasma Sputtering

Plasma sputtering is a widely used technique for depositing polycrystalline thin films. This system contains an anode and a cathode inside the vacuum chamber, typically held at a base pressure of $7 \times 10^{-5} mbar$. The material meant for evaporation (target) is attached to the cathode, whist the substrate is on the anode. A low pressure of inert gas (argon) is then pumped into the chamber, raising the pressure to between 1×10^{-3} and $4 \times 10^{-3} mbar$.

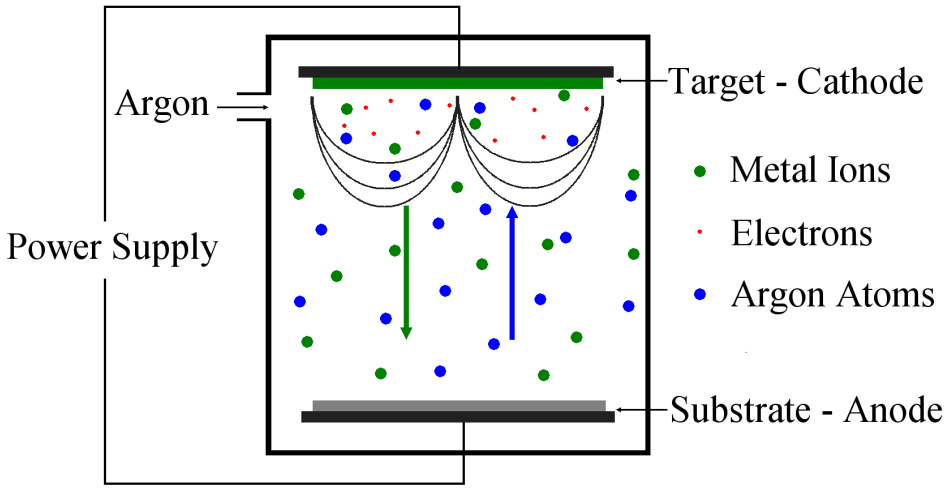

Figure 2.3: Schematic diagram of plasma sputtering.

Electrons from the cathode ionise the gas forming a localised plasma. The argon ions are then accelerated toward the target material dislodging atoms from the material surface. The displaced target atoms in turn get deposited on all the surfaces in the chamber, including the substrate [3]. This is shown schematically is figure 2.3. The thickness of this sputtering has been previously calibrated with respect to both argon pressure and exposure time. The main advantage of this technique is that it doesn't require material heating allowing it to be suitable for sputtering materials with high melting points. The system used in this study is a homebuilt sputterer at the University of Leeds and is capable of depositing films to single angstrom accuracy [6].

In this study plasma sputtering has been used at the University of Leeds for depositing the thin film multilayer structures of $Co_{90}Fe_{10}$ and Ru for the synthetic antiferromagnets used in chapter 6. Also on the same samples plasma sputtering was used to deposit the aluminium and titanium hard mask layers used in the fabrication, further explained in section 2.6. These layers were both deposited at rates of approximately $0.6 Å s^{-1}$ with layer thicknesses ranging between $0.7nm$ and $20nm$ and assumed to have an accuracy of ± 1Å. This technique was also used in chapters 4 and 5 of this thesis to deposit thin film Permalloy for nanostructure fabrication and use in the development of the imaging techniques in chapters 4 and 5.

2.4 Focussed Ion Beam Lithography

The Focussed Ion Beam (FIB) instrument consists of a column similar to that used in scanning electron microscopy (SEM) but using an ion beam. This is designed to image and mill samples using a highly focussed ion beam as well as deposit material onto defined areas down to a minimum of $\sim 20nm$ [7]. In this study an FEI Nova 200 Dualbeam instrument is utilised. This system has two columns, a standard SEM, and a FIB column. Like most research systems, the FEI Nova 200 uses a liquid metal ion source (LMIS). These use a variety of materials; however gallium is most common due to its low melting point, low vapour pressure and low volatility

[8, 9, 10]. The gallium is stored in a reservoir above a tungsten needle, during operation the reservoir is heated and liquid gallium flows to the end of the needle, where it is extracted by field emission. The liquid at the end of the needle forms a tip of approximately $5nm$ radius [8]. The Nova 200 typically uses a beam energy of $30keV$ with beam currents ranging from $1.5pA$ to $20nA$ [11]. The condensed spot current spreads according to a normal distribution with its size being defined by the FWHM; this size scales proportionally with the beam current down to a minimum of $\sim 6nm$. It is worth noting that the tail of the beam outside the FWHM of the distribution still contributes to both the milling and irradiation of the sample and that it is this tail of low intensity that is most likely to either leave Ga implantation or to create unwanted damage to the sample. During fabrication, it is advised that the spot size be of the same order as the smallest feature being milled. At the University of Glasgow, this instrument is used extensively for the preparation of TEM samples and surface studies [12, 13, 14, 15].

The Ion Column

The ion column, shown schematically in figure 2.4, has two main lenses, the condenser lens, along with the variable aperture define the current and diameter of the beam, while the objective lens focusses it onto the sample. Below the apertures sits an octopole to correct any stigmation of the beam that may be induced by the other lenses; this is also used to scan the beam across the sample during irradiation. A set of beam blanking lenses are also present to quickly deflect the beam onto the side of the column, this may be used to avoid unnecessary irradiation of the sample or whilst the electron beam is being used [12].

Ion Milling

When the ion hits the sample, its kinetic energy is transferred to the solid [16]. This energy transfer causes several things, the Ga^+ ions reflect and backscatter, the atoms in the sample are sputtered and emitted, the sample is damaged, the sample heats up, and both electrons and electromagnetic radiation are emitted. If the sample atom gains more energy than the displacement energy, typically $\sim 20eV$,

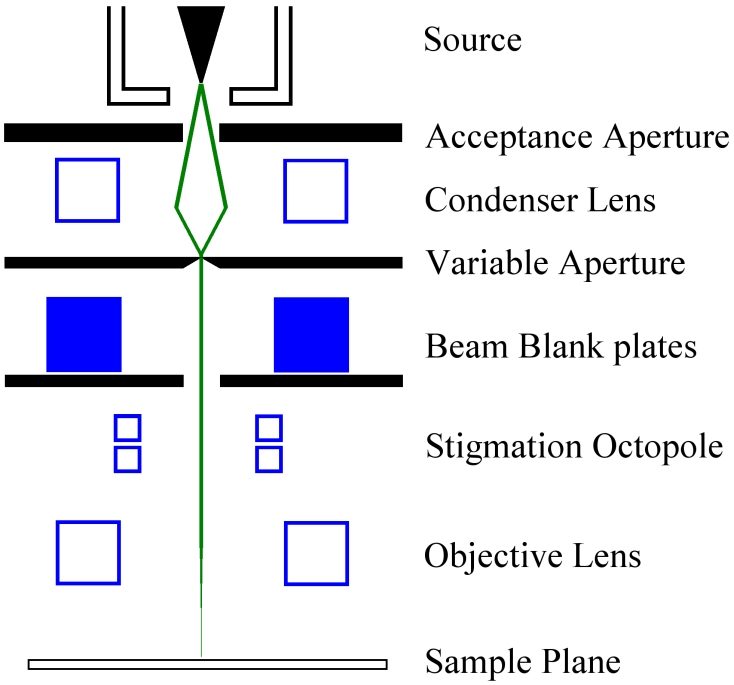

Figure 2.4: Schematic diagram of focussed ion beam column showing beam path and relative positions of apertures and lenses.

then the atom will be emitted from its initial position [8, 16]. This atom may go on to displace other atoms or simply be removed from the sample completely. As the ion beam is rastered across the sample, this displacement of atoms becomes a milled trench in the material. The Ga^+ ion, which now has a significantly reduced energy can be implanted into the sample. The implantation of the Ga^+ ions as well as the heating, damage and internal atomic displacement can affect the sample's crystallography, grain structure and magnetic characteristics [14, 15].

Ion Beam Imaging

As the ions enter the samples, some of the kinetic energy of the incident ions is transferred to the electrons in the sample which are then emitted. These electrons are known as ion induced secondary electrons and are used in the ion column for imaging the material similarly to in an SEM. Due to the size of the ions and the probe size from the column, this imaging has a lower resolution than SEMs of $\sim 6nm$ [11]. The other effect worth noting is that even scanning the sample with the ion beam for this purpose damages the sample and implants Ga^+ ions affecting both the

structural and the magnetic properties of the material [8].

Scanning Electron Beam Column

Scanning electron microscopy (SEM) is a surface technique which uses an electron probe to characterise samples in terms of their composition and topography. The column in the FEI Nova 200 Dualbeam instrument is a standard SEM column with a thermionic LaB_6 electron source, this is generally operated at $30keV$. The beam is condensed with magnetic lenses and has a maximum resolution of $1.1nm$ [17].

Once the electrons enter the sample they scatter both elastically and inelastically in the sample. The inelastically scattered electrons produce two main effects; the first is that the incident electrons interact with the specimen and eject electrons from the sample atoms. These secondary electrons typically have an energy of $< 5eV$, therefore to escape the sample they must be generated within the first few angstroms of the surface. This means that this signal is very effective at imaging the topography of the sample. The incident electrons can also excite the sample electrons into higher orbitals, when collapsing back into their ground state these release X-Rays with characteristic energies. These X-rays are used to gain compositional information about the sample. Finally, through multiple scattering events, the incident beam can also be elastically scattered back out of the sample, these are known as backscattered electrons; the probability of this scattering increases with atomic number and is therefore used for both Z-contrast and topographic imaging. In this study, as well as imaging the sample, the SEM within the dualbeam instrument is used for aligning the FIB column. This is needed because, as discussed previously, imaging with the ion beam damages the sample, therefore the electron and ion beams are aligned with each other away from the area of interest and the final milling position found using the SEM.

Electron Beam Deposition

The dual beam system is also capable of depositing layers of material onto areas of the sample as small as $20nm$ [7]. This involves injecting a gas precursor into the

volume just above the sample and allowing the electron beam to pass through it before hitting the sample. The most common precursor, and the only one used in this study, is $C_9H_{16}Pt$. This is injected through a needle positioned approximately $100\mu m$ above the surface of the sample. This needle allows for a very high gas flux close to the point of injection, whilst keeping the total chamber pressure low enough not to cause damage. As the electron beam is rastered across the sample, it passes through the high flux gas, depositing material onto the sample. In the case of $C_9H_{16}Pt$, platinum is deposited. This is often used to create protective layers on a material before milling. In this study this technique is used to deposit platinum onto TEM membrane substrates in order to fabricate structures with varying thickness and therefore varying electron transmission; these structures will be used in the TEM to modify the electron beam for the imaging technique developed in chapter 4.

2.5 Electron Beam Lithography

Electron beam lithography (EBL) has been used for the fabrication of nanostructures for over 50 years [18]. It has been demonstrated to be capable of fabricating nanowires below 10nm in width on membranes, and as narrow as 3nm on solid substrates [19, 20, 21]. Figure 2.5 shows a schematic diagram of the main stages of EBL.

The first step is to spin two resist layers of poly(methyl methacrylate) (PMMA), each with different densities, directly onto the substrate [22]. The EBL process then exposes the desired structure shape in the PMMA with an electron beam of current $\sim 50pA$. When the PMMA is exposed to the electron beam, the polymer chains break down and become soluble. To develop the pattern a mixture of 4-methyl-2-pentanone (MIPK) and isopropyl alcohol (IPA) at a ratio of 1:3 is used for 70 seconds before being washed in IPA leaving the desired negative. The sample metal is then deposited onto this negative pattern, filling the gaps in the resist. Finally the sample is bathed in acetone for 20 to 30 minutes to lift off the PMMA resist and leave only the desired metal. This lift off process is usually expedited by using an ultrasonic bath however this is unsuitable for this study as it is likely to damage the membrane

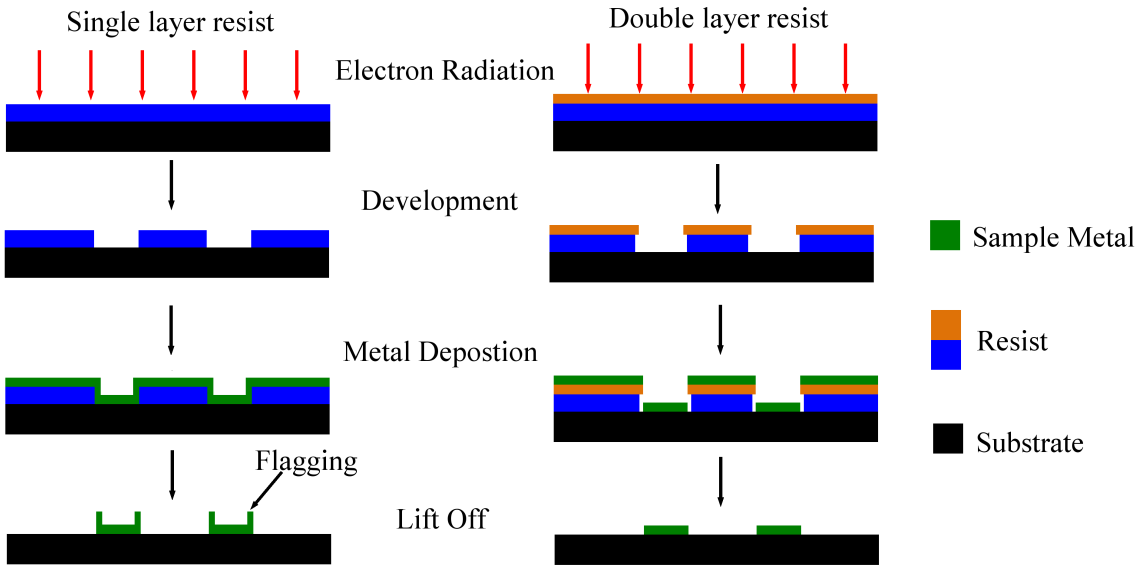

Figure 2.5: Schematic diagram of electron beam lithography process.

samples.

One of the main problems with this method is if the metal attaches to the sides of the resist before lift-off; when the resist is dissolved this metal is raised or folded over the rest of the sample, this is known as flagging and is shown in figure 2.5. This tendency is the reason for having two layers of resist; the lower layer of PMMA is more soluble than the upper so that after the initial development an overhang is created, as seen in figure 2.5. This reduces the probability of the metal attaching to the resist and therefore minimises flagging. However if the lower layer of resist is too thin or the metal is too thick then this can still occur.

In this study, this method was used to fabricate nanostructures in single layer Permalloy for the development of imaging processes in chapter 4, this technique was utilised in this case as it is well understood to have minimal effect on the magnetic structure and can be used to fabricate simple structures to a high degree of accuracy [15]. This was needed so that the development of these imaging techniques could be done on structures whose true magnetic behaviour was not in question.

2.6 Argon Milling

Argon milling is similar to focussed ion beam milling in that it utilises accelerated ions to displace atoms from the surface of the sample. The main difference between the two techniques is that focussed ion beam milling focusses the gallium ions onto the sample, avoiding the desired nanostructure; conversely, argon milling blankly illuminates a large area of the sample, with the required nanostructure being protected by a hard mask, typically an Al, Ti bilayer. This method is used extensively in combination with EBL to fabricate metallic or metal-oxide nanostructures, such as nanowires or magnetic tunnel junctions [23, 24, 25, 26, 27].

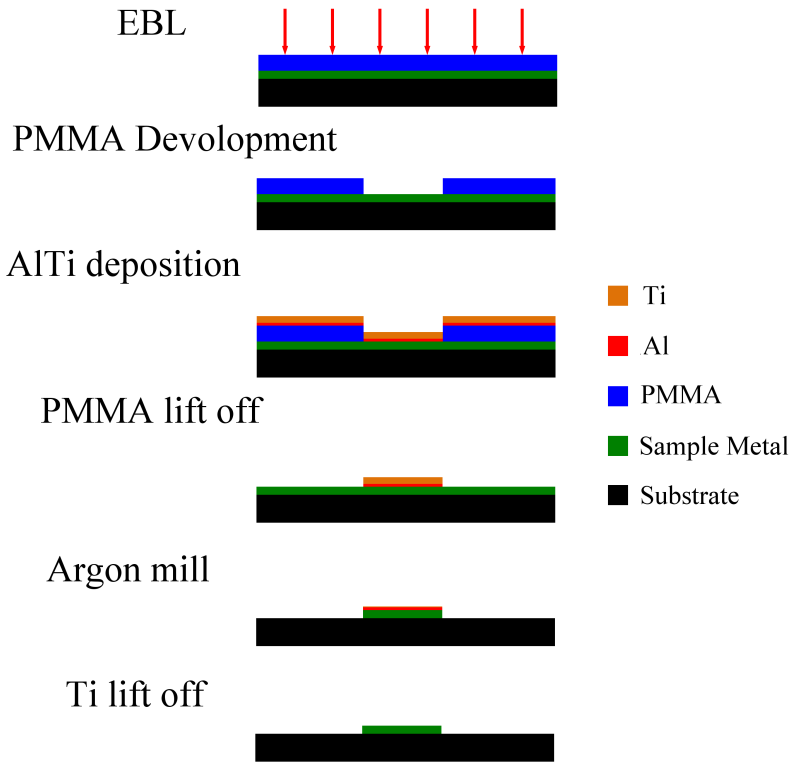

Figure 2.6: Schematic diagram of Argon ion milling technique.

Figure 2.6 shows a schematic of the full fabrication procedure. The sample material is deposited first as a continuous film and covered with a layer of PMMA. The electron irradiation and lift off processes are then carried out on the PMMA identically to in EBL. The now patterned sample is covered with an $Al - Ti$ hard mask bilayer;

this will protect the desired material from the eventual argon ion irradiation. The titanium top layer is resistant to argon milling making it an efficient mask for the nanostructure. The aluminium is then used to lift off the residual titanium after fabrication. Once the hard mask is deposited, the PMMA is lifted off leaving the continuous film sample material and a specified area of hard mask. The whole sample is then irradiated with argon ions with energies typically in the range 600 - 1000eV, these etch the sample material in any areas not protected by the hard mask. In this study this irradiation was done with an ion current of 0.2A for approximately 6 minutes, this was tuned so as to mill through all the sample material but not break the Si_3N_4 membrane. Finally the Aluminium is lifted off by bathing the sample in a Microposit MF-319 developer for approximately 15 minutes. This takes with it any residual Titanium and leaving only the desired pattern. Similarly to the EBL lift-off, we avoided the use of an ultrasonic bath at this stage to minimise the possibility of damage to the membrane [28, 26]. In this study, this technique has been used to fabricate the synthetic antiferromagnetic multilayer structures. The use of this technique and the reasons for its implementation over other fabrication methods will be discussed in chapter 6.

Bibliography

[1] Khamsehpour B. Wilkinson C. D. W. Chapman J. N. and Johnston A. B. High resolution patterning of thin magnetic films to produce ultrasmall magnetic elements. *J. Vac. Sci. Technol. B*, 14(3361), 1996.

[2] Eckertova L. *Physics of thin Films*. Plenum Press Publishing, 1986.

[3] Ohring M. *The Materials Sciecne of Thin Films*. Academic Press Ltd., 1991.

[4] Condas G. A. and Yarbrough R. B. Permalloy film deposition by flash evaporation. *Review of Scientific Instruments*, 42(8):1168 – 1171, April 1971.

[5] *McGrouther D. private communication.*

[6] *Lepadatu S. private communication.*

[7] FEI. *Nova 200 Platinum deposition technical note.*

[8] Volkert C.A. and Minor A.M. Focused ion beam microscopy and micromachining. *MRS Bulletin*, 32:389 – 399, MAY 2007.

[9] Prewett P.D. and Mair G.L.R. *Focussed Ion Beams From Liquid Metal Ion Sources*. John Wiley and Sons, 1987.

[10] Orloff J. High-resolution focused ion beams. *Rev. Sci. Instrum.*, 64(5):1105, Feb. 1993.

[11] *XT Novananolab User Manual 4022 262 52351.*

[12] Langford R. M. and Petford-Long A. K. Preparation of transmission electron microscopy cross-section specimens using focused ion beam milling. *J. Vac. Sci. Technol. A*, 19(5):2186 – 2193, Sept. 2001.

[13] Basith M.A. McVitie S. McGrouther D. Chapman J.N. Reproducible domain wall pinning by non-topographic features in a ferromagnetic nanowire. *Appl. Phys. Lett.*, 100, 2012.

[14] Basith M. A. McVitie S. McGrouther D. Chapman J. N. and Weaver J.M.R. Direct comparison of domain wall behavior in permalloy nanowires patterned by electron beam lithography and focused ion beam milling. *J. Appl. Phys.*, 110(8), OCT 15 2011.

[15] Basith M.A. *A TEM Investigation of Patterned Ferromagnetic Nanostructures by Lithographic Techniques*. PhD thesis, University of Glasgow, UK, 2011.

[16] Melngailis J. Focused ion beam technology and applications. *J. Vac. Sci. Technol. B*, 5:469 – 495, 1987.

[17] FEI. *Nova 200 Nanolab product data sheet.*

[18] Hahmann P. and Fortagne O. 50 years of electron beam lithography: Contributions from jena (germany). *Microelectronic Engineering*, 86(4-6):438–441, 2009.

[19] Maile B.E. Henschel W. Kurz H. Rienks B. Polman R. and Kaars P. Sub-10 nm linewidth and overlay performance achieved with a fine-tuned ebpg-5000 tfe electron beam lithography system. In *Microprocesses and Nanotechnology Conference, 2000 International*, pages 254 –255, jul 2000.

[20] Yamazaki K. and Namatsu H. 5-nm-order electron-beam lithography for nanodevice fabrication. *Jpn. J. Appl. Phys.*, 43:3767–3771, 2004.

[21] Beaumont S.P. Bower P.G. Tamahura T. and Wilkinson C.D.W. Sub-20nm-wide Metal Lines by Electron-Beam Exposure of Thin Poly(methyl methacrylate) Films and Liftoff. *Applied Physics Letters*, 38(6):436–439, 1981.

[22] Cumming D.R.S. Thoms S. Beaumont S.P. and Weaver J.M.R. Fabrication of 3 nm wires using 100 keV electron beam lithography and poly(methyl methacrylate) resist. *Applied Physics Letters*, 68(3):322–324, JAN 15 1996.

[23] Seemann K.M. Mokrousov Y. Aziz A. Miguel J. Kronast F. Kuch W. Blamire M. G. Hindmarch A.T. Hickey B.J. Souza I. and Marrows C.H. Spin-Orbit Strength Driven Crossover between Intrinsic and Extrinsic Mechanisms of the Anomalous Hall Effect in the Epitaxial L1(0)-Ordered Ferromagnets FePd and FePt. *Phys. Rev. Lett.*, 104(7), FEB 19 2010.

[24] Kitade Y. Komoriya H. and Maruyama T. Patterened media fabricated by lithography and argon-ion milling. *IEEE Trans. Magn.*, 40(4, Part 2):2516–2518, JUL 2004.

[25] Tanigawa H. Koyama T. Yamada G. Chiba D. Kasai S. Fukami S. Suzuki T. Ohshima N. Ishiwata N. Nakatani Y. and Ono T. Domain wall motion induced by electric current in a perpendicularly magnetized co/ni nano-wire. *Appl. Phys. Expr.*, 2(5), 2009.

[26] Hindmarch A.T. Parkes D.E. and Rushforth A.W. Fabrication of metallic magnetic nanostructures by argon ion milling using a reversed-polarity planar magnetron ion source. *Vacuum*, 86(10):1600–1604, APR 27 2012.

[27] Gallagher W.J. Parkin S.S.P. Lu Y. Bian X.P. Marley A. Roche K.P. Altman R.A. Rishton S.A. Jahnes C. Shaw T.M. Xiao G. Microstructured magnetic tunnel junctions. *J. Appl. Phys.*, 81(8, Part 2a):3741–3746, APR 1997.

[28] Melliar-Smith C.M. Ion etching for pattern delineation. *J. Vac. Sci. Technol.*, 13:1008, 1976 1976.

Chapter 3

Experimental Instrumentation

3.1 Introduction

After sample fabrication several instruments and techniques were used to characterise the magnetic behaviour of the samples. In this study the main characterisation technique is Lorentz TEM (LTEM). In this chapter, the TEM will be discussed in detail, as well as several other techniques that have been used to characterise the behaviour of the samples both in continuous films and in nanostructures. In sections 3.2 and 3.3 TEM and LTEM will be dicussed, including an overview of the modifications made to the Philips CM20 used at the University of Glasgow, and the various imaging modes it utilises. Finally the Medipix/Timepix chip and B-H Looper will be detailed in sections 3.4 and 3.5 respectively. All these techniques will be considered with respect to their individual uses, applications and relevence to this work.

3.2 The Transmission Electron Microscope

In 1925 Louis De Broglie published his theory of wave particle duality [1] and the idea that electrons are waves with very short wavelengths, calculated by equation 3.1:

$$\lambda = \frac{h}{\left(2m_0eV\left(1+\frac{eV}{2m_0c^2}\right)\right)} \tag{3.1}$$

Where p is momentum, h is Planck's constant $h = 6.626 \times 10^{-34}Js$, V is the acceleration voltage, e and m_0 are the charge and rest mass of the electron respectively and c is the speed of light. This theory led to the invention of the electron microscope by Ernst Ruska in 1931, with the aim of increasing resolution beyond the limits of optical microscopes [2, 3]. Using equation 3.1, the wavelength of the accelerated electrons can be calculated in a typical TEM of $200kV$ acceleration voltage to be $\lambda = 2.51pm$.

TEMs are typically held under vacuums of $\sim 10^{-6}mbar$; this ensures that the electrons move through the column unimpeded, this vacuum also protects the gun and internal components of the microscope, stopping them from becoming contaminated. They have three main sections, the upper column, the specimen region and the projector and image acquisition region, as shown in figure 3.1. The upper column contains the electron gun, generating the electrons and accelerating them at $200keV$ down the column, and the C1 and C2 lenses and apertures, which define and control the electron probe onto the sample. In the specimen region the sample sits in the centre of the objective lens, between the two pole pieces, see section 3.2.3. The objective lens is the primary imaging lens of the microscope further explained in figure 3.2.3. The lower region of the microscope projects the electrons onto the viewing screen and the camera, explained further in section 3.2.6. This region controls the imaging and diffraction modes being used and the final magnification of the image. The final resolution of the microscope is typically limited by aberrations within the magnetic lenses; the FEI Tecnai T20 TEM used in this study has a maximum resolution of $\sim$2Å. The following sections will explain the various parts of the column in more detail working from the electron gun downwards.

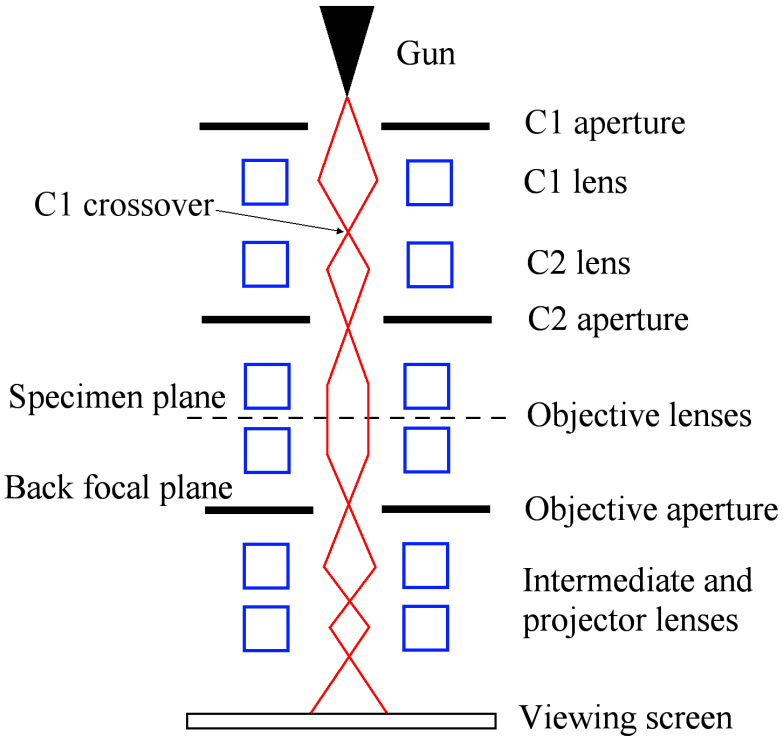

Figure 3.1: Schematic diagram of CTEM showing relative positions of lenses, apertures and the electron beam path.

3.2.1 Electron Gun

The electron gun is typically placed at the top of the electron column. There are two main types, thermionic and field emission. Traditional thermionic sources utilise Tungsten tips; these are heated until the energy of the electrons overcomes the work function of the material, and the electrons are emitted; the work function is the minimum amount of energy required to remove an electron from a solid. The current density of this emission is governed by the Richardson-Dushman Equation shown in equation 3.2.

$$J_s = AT^2 e^{\frac{-W}{kT}} \tag{3.2}$$

Where J_s is the current density of emission, T is the emission temperature, k is the Boltzmann constant, W is the work function of the material and A is the Richardson constant ($10 \times^6 Am^{-2}K^{-2}$) [4]. This equation shows that to increase

the current density of the emitted electron, the work function must be reduced. The Tecnai T20 that is used in this study utilises LaB_6 crystals on the filament to raise the melting point, this also reduces the work function to $2.4eV$ from $4.5eV$ in a Tungsten tip [5], thus reducing the temperature required to achieve the same current density. The LaB_6 filament in the T20 is heated to $\sim 1700K$ to produce a current density of $10^6 Am^{-2}$ [5].

Field emission guns (FEGs) apply a large electric field gradient across a tungsten tip with the tip itself forming the cathode. This causes the electrons to quantum mechanically tunnel out of the filament and towards the anode. FEGs are considered to be better than thermionic guns because they are sharper which allows for a more coherent beam of electrons both spatially and temporally [6]. This type of filament raises the brightness from $5 \times 10^{10} Am^{-2} Sr^{-1}$ in LaB_6 guns to $1 \times 10^{13} Am^{-2} Sr^{-1}$ at an operating temperature of 300K, where brightness is the electron current density per unit solid angle of the source [5]. Heat assisted FEGs use the field emission method but also moderately heat the tip, this acts to reduce the work function as well as keeping the tip free of contaminants. This combination is known as a Schottky field emission gun and is utilised in the Philips CM20 TEM used in this study. After emission, the electrons are accelerated through a series of anodes until they reach their operating energy of 200keV.

3.2.2 The Upper Column

All TEMs control the path of the electrons with magnetic lenses. These are made up of a core of iron, the polepiece, with a hole drilled in it, the bore. This is then surrounded with a coil of copper wire. When a DC current is passed through the coils, an axially symmetric magnetic field is created within the gap of the lens, as shown in figure 3.2 [7]. This field deflects the electrons through the Lorentz force and is used to focus the beam.

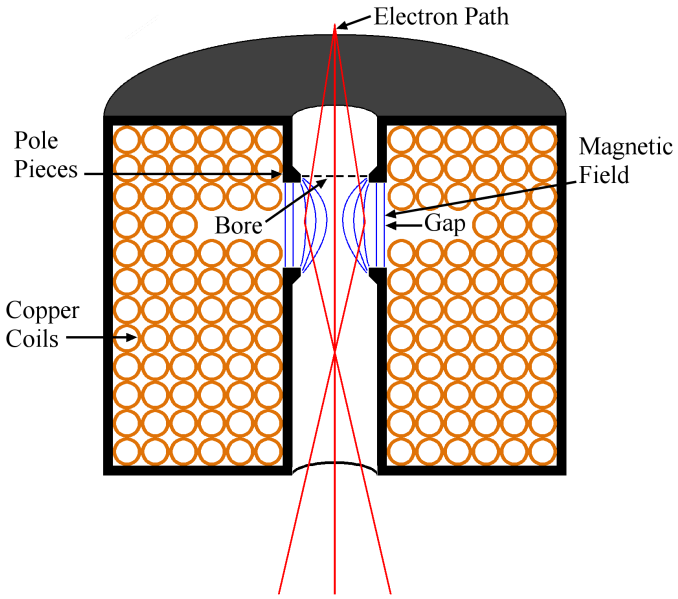

Figure 3.2: Schematic diagram of magnetic lens showing field lines and the electron path relative to the pole pieces.

Figure 3.1 shows a schematic diagram of a conventional transmission electron microscope (CTEM). Once the electrons have left the gun, they pass through the condenser system. There are two main lenses within the condenser system between the C1 and C2 apertures. The C1 lens forms a demagnified image of the source crossover, this demagnifies the gun crossover by approximately an order of magnitude [4]. This effectively acts as a source for the rest of the microscope. The C2 lens then controls the convergence angle of the beam hitting the sample; It can also be used to control the coherence of the electrons hitting the sample [8]. The most common two uses of this are parallel beam illumination where the coherence of the beam is maximised, and convergent beam illumination used for probing local areas on the sample. Finally the C2 aperture defines the maximum convergence angle of the beam, these typically range from $20\mu m$ to $200\mu m$ in diameter [5, 7].

3.2.3 Objective and Specimen Region

After passing the C2 aperture, the electrons enter the objective system. In a conventional TEM the two pole pieces of the objective lens surround the sample rod. This means that the sample sits in the centre of the lens field of $\sim 0.8T$. The rod is used to

mount the sample in the correct position as well as tilt, rotate or change the height of the sample. The sample is held at eucentric height, which is the central point between the upper and lower polepieces. Specific rods are also capable of applying magnetic fields or currents accross the sample.

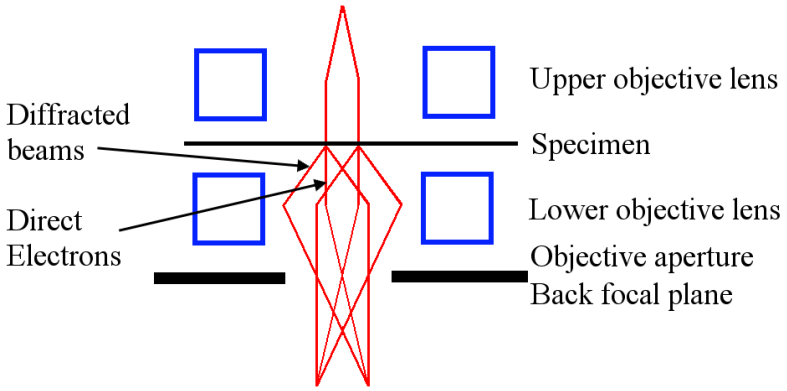

Figure 3.3: Schematic diagram of CTEM showing the beam path through the objective lens system and sample

The objective lens has a magnification of 50-100 times, and is the primary imaging lens of the microscope. The electrons pass through the upper pole piece and are incident on the specimen, which scatters the beam both elastically and inelestically. The lower objective pole piece then focusses the electron beam to form a diffraction pattern on the back focal plane, illustrated in figure 3.3, this is further discussed in section 3.2.4 [7].

3.2.4 Back Focal Plane

The diffraction pattern is formed on the back focal plane (BFP) of the objective lens. When the electrons pass the sample, the planes of atoms act as a diffraction grating and cause them to Bragg scatter. The interference of the electrons at the back focal plane forms the diffraction pattern. Figure 3.4 shows the beam path as the electrons are scattered from parallel atomic planes.

where h, k and l are the Miller indices which define the crystalline plane with respect to the unit cell. The Bragg equation below defines when constructive inter-

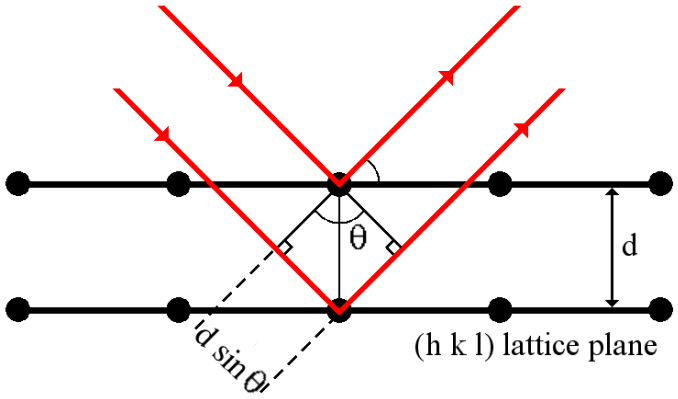

Figure 3.4: Schematic diagram showing beam path of Bragg scattered beam

ference occurs in the diffracted beams, this is when the difference in the beam path is equal to an integer multiple of the electron wavelength. This law is only applicable if $\lambda \lesssim 2d$ which is why this diffraction does not occur with visible light [9, 7].

$$n\lambda = 2dsin(\theta) \tag{3.3}$$

Where n is an integer, λ is the electron wavelength, d is the planar spacing and θ is the incident angle of the electrons. The main properties that can be readily determined by the diffraction pattern include crystallinity, crystallographic characteristics including lattice parameters and symmetry, grain morphology and sample orientation. Equation 3.3 leads to typical diffraction angles of up to $\sim 100mrad$.

The crystal structure can also be defined in terms of a reciprocal lattice, this defines the spatial frequencies of the crystal rather than the atomic positions. In this way every crystal has two lattices associated with it, one in real space and one in reciprocal space [9]. The diffraction pattern is an image of this reciprocal lattice, with the origin in the centre and units of spatial frequency (m^{-1}). The easiest way of thinking of this is that each visible point in the diffraction pattern represents a particular set of planes in the crystal, with a consistent spatial frequency [10]. These planes of atoms are defines by their Miller indices, as mentioned above. Figure 3.5 shows schematic examples three different lattice planes in a cubic structure defined by their Miller indices [7, 10].

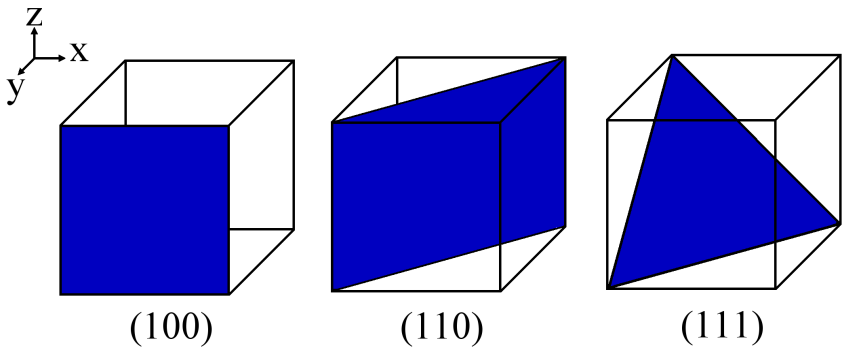

Figure 3.5: Example schematics of lattice planes in cubic structure.

Examples of how the crystal structure of the sample effects the diffraction pattern are seen in figure 3.6. All diffraction patterns contain a bright central spot of direct, unscattered electrons, as well as a distribution of scattered electrons at characteristic deflection angles. When the sample is polycrytaline, the crystals in the sample are all similar but at different orientations to the incident beam; this causes the diffraction spots to become rings, shown in 3.6*b*. For non-crystalline samples the distance between atoms is less narrowly defined, therefore these rings become more diffuse in the diffraction pattern as in 3.6*c*. The diffraction pattern can be seen on the imaging plane by adjusting the strength of the intermediate lenses, discussed in 3.2.6, to project the wavefunction of the back focal plane onto the viewing plane.

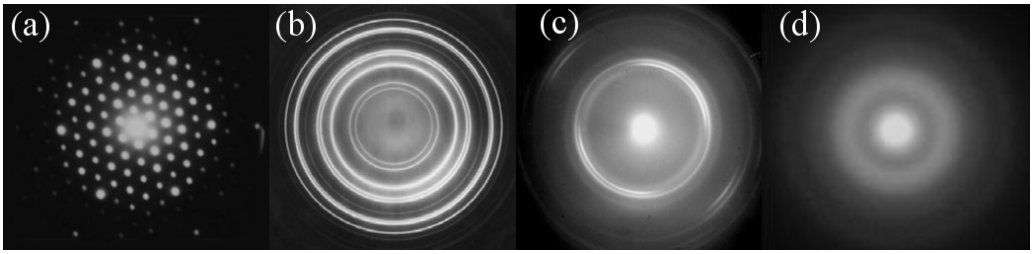

Figure 3.6: TEM diffraction patterns of (a) single crystal, (b) polycrystalline, (c) textured-polycrystalline and (d) amorphous samples [11].

3.2.5 Bright Field and Dark Field Imaging

There are two main types of contrast imaged in a TEM, diffraction contrast and phase contrast. In this study, phase contrast imaging was used to image magnetic structure,

which will be further discussed in section 3.3. Diffraction contrast is where intensity differences in the image are due to differences in diffraction from different parts of the sample [4]. To form diffraction contrast in the TEM, the objective aperture is used to select specific parts of the diffraction pattern to form the image, blocking unwanted diffracted beams. The two most common types of this are bright field and dark field. Bright field (BF) imaging is where only the central (undiffracted) beam is selected and the scattered electrons are blocked by the aperture, shown schematically in figure 3.7. The size of the aperture used can also be chosen to determine the limit of which beams contribute to the image [5, 4]. The contrast in BF images arises from the difference in electron scattering across the sample.

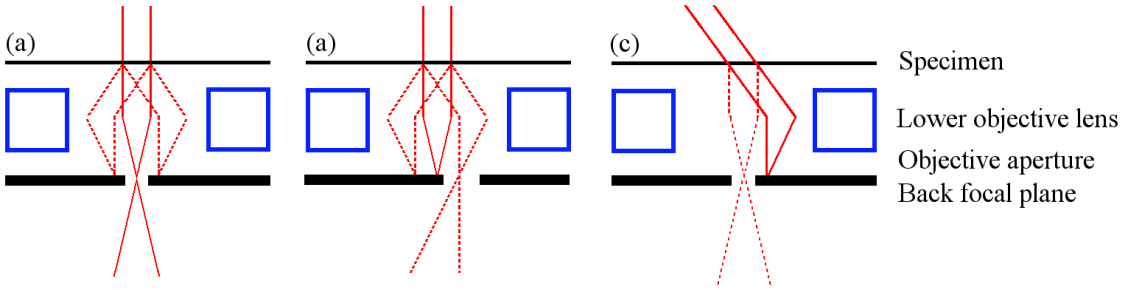

Figure 3.7: Schematic of beam path for (a) bright field (b) dark field imaging in shifted aperture and (c) tilted beam modes.

If only the scattered, or part of the scattered electrons are selected it is called dark field (DF) imaging. This technique is widely used for identifying areas of the sample of particular atomic mass or crystallographic orientation [12, 13, 14]. There are two possible methods of DF imaging. Either the aperture is shifted (fig.3.7b) or the beam is tilted to centre the diffracted beam on the back focal plane (fig. 3.7c). The latter is the most commonly used as the former utilises electrons from off axis trajectories which are more susceptible to lens aberrations and astigmatism [7]. The in focus imaging used in this study concentrated on BF imaging for the structural investigation of samples.

3.2.6 Lower Column and Image Acquisition

The lower column consists of the intermediate and projector lenses. This set of lenses is used to project the image onto the image plane and controls the magnification. The intermediate lens can also be varied to project either the diffraction pattern or the real space image onto the viewing screen [5]. This can be controlled and provides a variety of magnifications by altering the camera length of the microscope.

At the base of the column a phosphor screen is placed in the image plane for direct viewing by the operator. The most common detectors used for image acquisition in CTEMs are charge coupled devices (CCDs), these use a scintillator material to convert the electrons into light which is then channelled onto the CCD chip. This is connected to a PC for live imaging. The limitations of this camera and possible alternatives are discussed in section 3.4.

3.2.7 The FEI Tecnai T20

In this study the FEI Tecnai T20 CTEM was used used for non-magnetic imaging and sample characterisation. This microscope uses an LaB_6 thermionic source with an acceleration voltage of $200keV$. It utilises two detectors: an Olympus SIS Megaview III, for standard imaging and a Gatan Image Filter (GIF) used for higher resolution imaging and elemental mapping. This microscope has Lorentz lenses and is capable of operating in field free mode, discussed in section 3.3.1. However is predominantly used for BF and DF direct imaging.

3.3 Magnetic Imaging

The Philips CM20 FEG TEM/STEM is a specialist microscope used for magnetic imaging [15], and is used in this study for magnetic characterisation and manipulation. This microscope is also the basis for the magnetic imaging techniques developed in chapters 4 and 5. This section considers the CM20 and how it is designed for this type of imaging, and discusses the various techniques used in magnetic microscopy.

3.3.1 Field Free Mode

In a CTEM, the sample sits between the pole pieces of the objective lens, at this position the magnetic field of the sample can be in excess of 0.8T. This would significantly influence any magnetic structure or behaviour we are likely to see within a sample. For this reason, the CM20 is modified to allow for field free imaging. The microscope is equipped with two mini-lenses (Lorentz lenses) above and below the specimen. These become the imaging lenses when the objective lens is turned off allowing the sample to sit in field free space. As well as this, the lens gap has been increased to $\sim 20mm$ to allow room for the magnetic stage [15]. The resultant layout is shown schematically in figure 3.8.

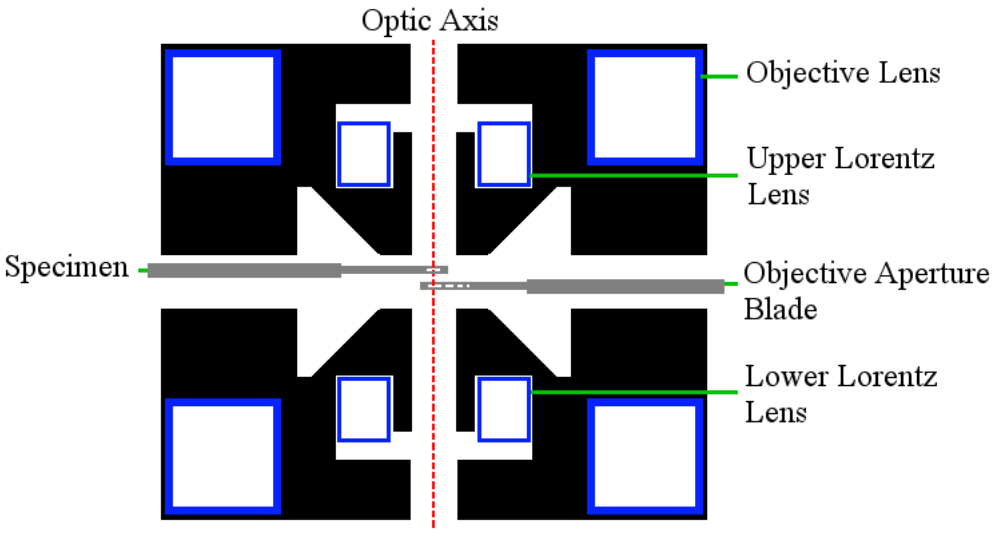

Figure 3.8: Schematic diagram of the Objective and Lorentz lenses

The result of the use of these lenses in this microscope is that the point resolution drops from $0.36nm$ with the objective lens on to $2.1nm$ using only the Lorentz lenses [15]. In addition to the advantage of field free imaging, the use of the Lorentz lenses leaves the objective lens available. A weak current can be passed through the objective lens, creating a controllable external field perpendicular to the sample plane. The sample can then be tilted to introduce an in plane component of the applied field. This setup allows in-situ magnetising experiments to be performed using a maximum perpendicular field of $\sim 0.8T$.

3.3.2 Lorentz Microscopy

Magnetic domains were first observed using a TEM by Hale et. al. in 1959. They did this in a CTEM by simply using the microscope out of focus and running the objective lens at zero milliamps creating field free space around the sample [16]. In the same paper they also postulated the use of the objective lens to make dynamic observations on reversing films. Since then the field of imaging magnetic structures in the TEM has gained the universal name of Lorentz microscopy. As mentioned in section 3.2.5 there are two main types of contrast, diffraction contrast and phase contrast, Lorentz microscopy uses the latter. This is where contrast arises through the interference of the electron waves passing through the sample [17]. In this section, the source of phase contrast will be discussed from classical, wave equation and quantum mechanical approaches.

Classical Approach

From a classical point of view all of Lorentz microscopy is based on one simple concept. As the electrons pass through a magnetic thin film, they are deflected by the Lorentz force due to the magnetic induction of sample. The Lorentz force is governed by equation 3.4. This shows that this force acts perpendicular to both the magnetic induction of the sample and the velocity of the incident electrons. An effect of this force is that magnetic domains of opposing polarities will deflect the electron beam in opposite directions. This difference in deflection is the basis of gaining magnetic contrast and is shown schematically in figure 3.9. Note in this diagram that the lower Lorentz lens is situated below the objective aperture. This is because the objective aperture is in the back focal plane of the objective lens, not the Lorentz lens. The result of this is that, when operating in field free mode, the beam must be slightly convergent on the sample to produce minimised central spots on the diffraction pattern. It is worth noting that within the microscopes used in this study this positioning is only true in the Philips CM20 and not the FEI Tecnai T20.

$$\mathbf{F_L} = -e\,[\mathbf{v} \times \mathbf{B}] \tag{3.4}$$

where F_L is the Lorentz force, e is the magnitude of the charge on an electron, $\mathbf{v}$ is the velocity of the incident electrons and $\mathbf{B}$ is the magnetic induction of the thin film.

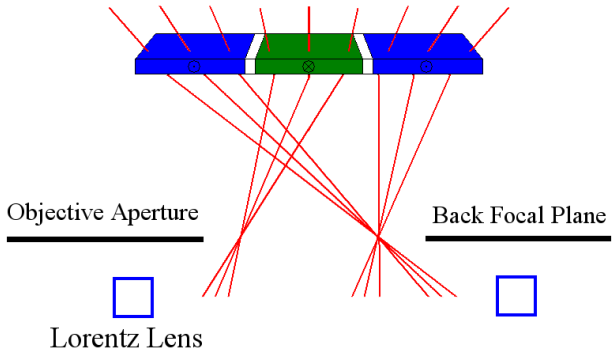

Figure 3.9: Schematic diagram of Lorentz deflection of electrons though a magnetic thin film in the CM20.

The resultant deflection angle (β) can be quantitatively calculated using equations 3.5 and 3.6 [18, 19].

$$\beta(x) = \frac{e\lambda}{h} \int_{-\infty}^{\infty} \mathbf{B}_{\perp}(x,y)dz \tag{3.5}$$

Here $\beta(x)$ is the angle of deflection, $B_{\perp}$ is the in plane component of the magnetic induction perpendicular to the deflection angle and λ and h are the wavelength of the electrons and Plank's constant respectively. For an area of uniform magnetisation, this can be integrated to:

$$\beta = \frac{e\lambda B_S t}{h} \tag{3.6}$$

where B_S is the saturation induction and t is the thickness of the thin film [18]. A $200kV$ microscope using electrons with wavelength $\lambda = 2.51pm$ passing through 20nm of permalloy ($B_S \approx 1T$) results in a deflection angle of $\beta = 1.2 \times 10^{-5} rad$ or $12\mu rad$. This is small when compared to Bragg scattering angles of up to $\sim$ 10s of $mrad$.

Wave equation approach

The wave equation approach, shown mathematically in equations $incident_w ave_e qn$ to $intensity_w ave_e qn_1$ is a method of calculating TEM phase contrast images by treating the electrons as waves and the magnetic sample as a phase object inducing a phase shift in the transmitted electrons. Lorentz microscopy exploits this phase shift allowing the magnetic structure, to be determined.

This approach calculates the wavefunction at the specimen, the back focal and the image planes, defined in figure 3.1, as the electrons pass down the microscope. The electrons incident on the sample at the specimen plane are described by a simple wave equation 3.7: While the sample then introduces a phase shift on the electrons producing a modified wavefunction for electrons exiting the sample, shown in equation 3.8.

$$\psi_i(r) = e^{ikz} \tag{3.7}$$

$$\psi_e(r) = A(x,y)e^{i[kz+\phi]} \tag{3.8}$$

where ψ_i and ψ_e are the wavefunctions incident and exiting the sample respectively, $A(x,y)$ is the amplitude function in terms of the spatial frequency axes, k is the wavenumber and ϕ is the total phase shift. The wave passing through the back focal plane of the microscope can be described by equation 3.9. This wavefunction is in reciprocal space, dependent on the spatial frequency axes k_x and k_y.

$$\Psi_{BFP}(k_x,k_y) = FT[\psi_e(r)] \times APF(k_x,k_y) \times e^{i\chi(K)} \tag{3.9}$$

Here FT is a the Fourier transform operator, $APF(k_x,k_y)$ is the aperture function and $\chi(K)$ is the transfer function, in terms of the spatial frequency, of the microscope. This can then be inverse Fourier transformed to calculate the wavefunction reaching the image plane, equation 3.10, and the modulus taken to give the image intensity, 3.11.

$$\Psi_{im}(x,y) = FT^{-1}\left[\Psi_{BFP}(k_x,k_y)\right] \tag{3.10}$$

$$I_{im}(x,y) = \Psi^*_{im}(x,y)\Psi_{im}(x,y) \tag{3.11}$$

Equation 3.11 is the result of wave optical calculations. However to fully understand Lorentz images, the phase of the electron wave must be considered along with the phase shift induced by a magnetic sample. Figure 3.10 shows two electron beam paths, P1 and P2, enclosing a magnetic sample. These beams will experience both a magnetic and electrostatic phase shift, ϕ_m and ϕ_e, induced by the magnetic vector potential, $\mathbf{A}$, and the mean inner potential, V, respectively. Equation 3.12 shows the relationship between the electrostatic phase shift, ϕ_e, and the electrostatic potential, V, where t is the sample thickness and E is the electron accelerating voltage.

$$\phi_e = \frac{\pi V t}{\lambda E} \tag{3.12}$$

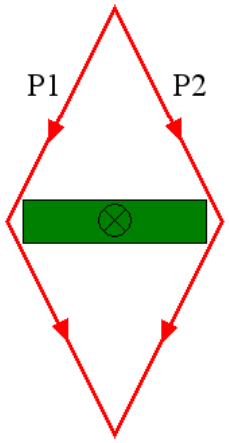

Figure 3.10: Schematic diagram showing two electron beam paths enclosing a magnetic specimen.

The magnetic phase shift induced by the interaction between the electron beam and the magnetic induction is quantified by the Aharonov-Bohm effect [20]. Equation 3.13 defines the magnetic phase change for the two beams illustrated in figure 3.10 [21].

$$\phi_m(r) = -\frac{e}{\hbar}\int_{-\infty}^{\infty}(\mathbf{A}.\hat{\mathbf{n}})\,dz \tag{3.13}$$

Where e is the magnitude of the charge on an electron, $\hbar$ is the reduced Planck's constant, $\hat{n}$ is the unit vector parallel to the electron beam. The magnetic vector potential, $\mathbf{A}$, can be written as a function of the magnetic induction [21].

$$\mathbf{A}(r) = \frac{1}{4\pi}\int\int\int\frac{\nabla\times\mathbf{B}(\mathbf{r}')}{|r-r'|}d^3r' \tag{3.14}$$

Where $\mathbf{B}$ is the magnetic induction. This integral is a convolution and can be expressed as in equation 3.15.

$$\mathbf{A}(r) = \frac{1}{4\pi r}\otimes\nabla\times\mathbf{B}(r) \tag{3.15}$$

Ignoring displacement and conduction currents this can be written in terms of the magnetisation, $\mathbf{M}(r)$, shown in equation 3.16, this is then substituted back into 3.13.

$$\mathbf{A}(r) = \frac{\mu_0}{4\pi r}\otimes\nabla\times\mathbf{M}(r) \tag{3.16}$$

$$\phi_m(r) = -\frac{e\mu_0}{4\pi\hbar r}\otimes\int_{-\infty}^{\infty}(\nabla\times\mathbf{M}(r))\cdot\hat{\mathbf{n}}dz \tag{3.17}$$

This integral can be calculated through the thickness of the material, defining the thin film to be the $x-y$ plane, resulting in 3.18. The total phase shift is the sum of the electrostatic and magnetic phase shifts.

$$\phi_m(r) = -\frac{e\mu_0 t}{4\pi\hbar r}\otimes[\nabla\times\mathbf{M}(r)]\cdot\hat{\mathbf{z}} \tag{3.18}$$

$$\phi(r) = \phi_e + \phi_m \tag{3.19}$$

Equation 3.18 shows the relationship between the magnetic phase shift and the magnetisation of the sample as the curl of the magnetisation. Figure 3.11 shows the

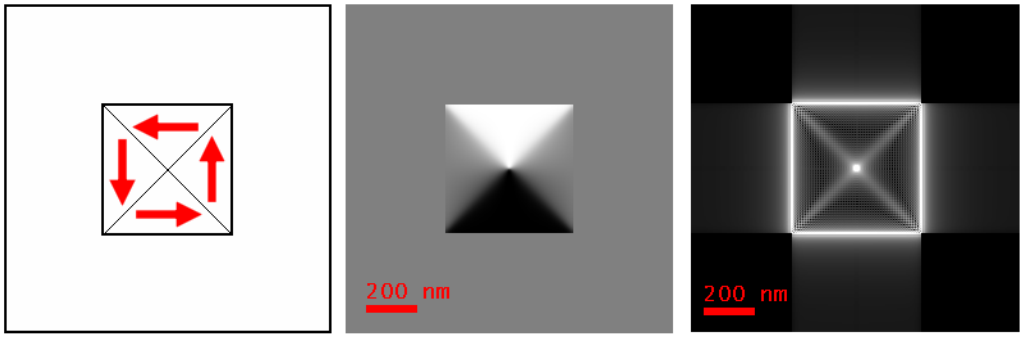

Figure 3.11: (a) Schematic diagram and simulated images of the (b) magnetisation and (c) curl of M ($\nabla \times \mathbf{M}(r)$) for a $500 \times 500nm$ square sample of $20nm$ thick permalloy.

relationship between M and $\nabla \times \mathbf{M}(r)$; 3.11$c$ shows the z-component of the curl which is dependent on the x-y plane of the magnetisation. The intensity of this image is representative of the phase shift in the wavefunction, as described in 3.18. The total phase change given in equation 3.19 can be used to quantitatively calculate contrast in Lorentz microscopy. In the following sections, a variety of Lorentz modes in the TEM will be discussed.

3.3.3 Fresnel Imaging

Fresnel imaging is the simplest method of Lorentz imaging, and the easiest to implement. It is predominantly used for in-situ imaging as well as recording real time videos of magnetic processes. Equation 3.6 shows that the deflection of the electrons is proportional to the integrated magnetic induction of the sample. This means that magnetic domains of opposing induction deflect the beam in opposite directions. Therefore two adjacent magnetic domains, with antiparallel induction, will cause the electrons to have either divergent or convergent deflection [18, 22]. This is illustrated in image 3.12.

This method produces magnetic contrast by simply defocussing the Lorentz lens. Doing this effectively moves the object plane for the lens by a set distance Δ. At defocus, the convergent or divergent beams lead to bright and dark fringes respectively at the domain wall positions. The intensity and width of these fringes is dependent

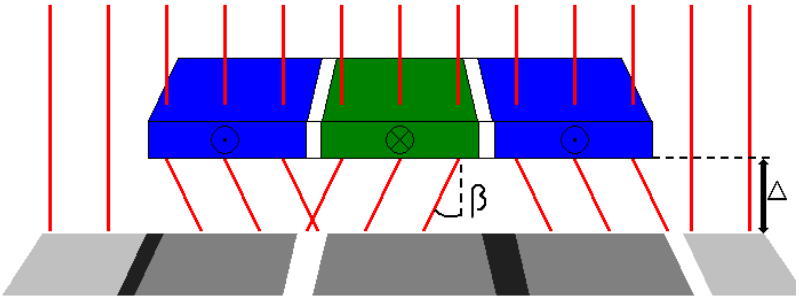

Figure 3.12: Schematic diagram of beam path and image intensity during Fresnel imaging.

on Δ, as a higher defocus will lead to a greater divergence or convergence of the beams.

While the DW positions will produce intensity fringes, the domains themselves have near constant intensity, only varied by the topographic contrast and the magnetic ripple. Magnetic ripple is characterised by small contrast fringes visibly similar to the ripples in water. This comes about from small changes in direction of the local magnetic induction. These changes oscillate around the mean direction of induction and can therefore be used to determine the net direction of the magnetic induction [17, 7]. As the defocus is increased, the contrast arising from the domain walls also increases, however, this comes at the cost of the resolution. Therefore when choosing a defocus value a compromise between the two must be reached.

Image 3.12 shows that outside the sample there is no magnetic deflection, therefore the deflected electrons from the sample interfere with the background electrons resulting in a bright and a dark fringes either side of the wire in the image. This edge contrast is shown in figure 3.13. This contrast can be used to identify the net direction of the magnetic induction within the sample. For example in figure 3.13 the dark edge changes side either side of the domain wall. This method is easily implemented and shows clear qualitative magnetic information. The contrast gained from this method is only linear with the integrated magnetic induction for low values of defocus however is mostly used in the non-linear regime as using it with low values of defocus produces very low contrast [23]. This means that it is generally a

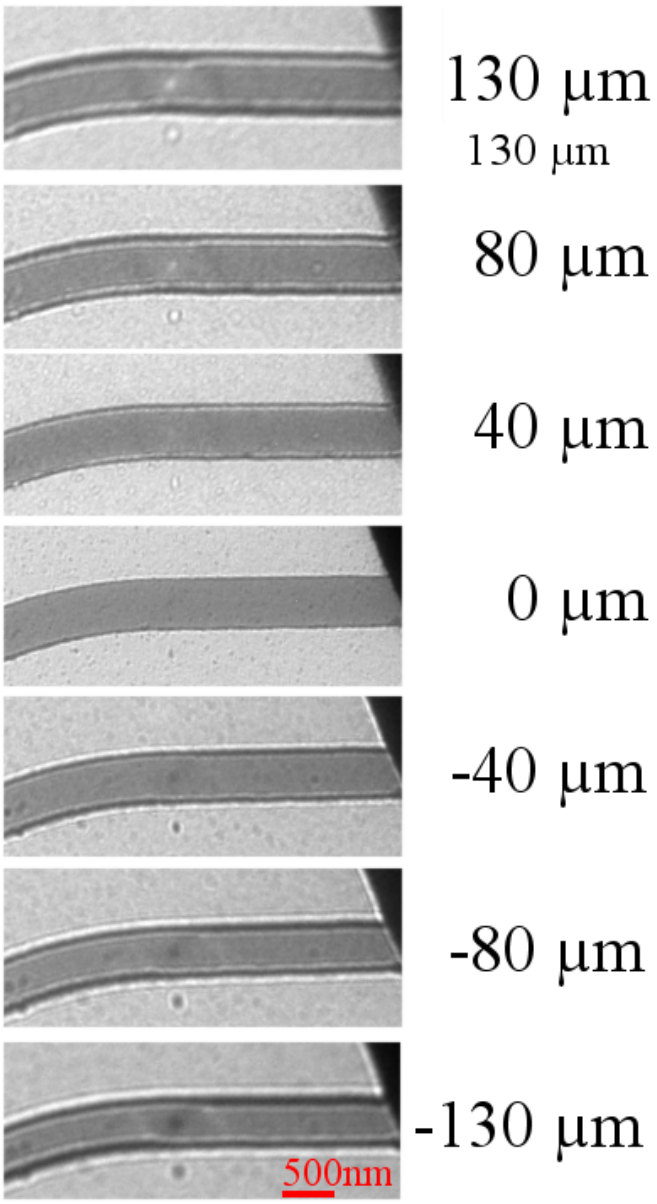

Figure 3.13: Series of Fresnel images of a vortex DW in a 20nm thick 500nm wide permalloy nanowire, showing variation in both DW and edge contrast as defocus is varied from 130 to $-130\mu m$.

non-quantitative technique with respect to the magnetic induction.

3.3.4 Foucault Imaging

Foucault imaging is another type of Lorentz microscopy, which uses the edge of the objective aperture to gain domain contrast in an in-focus image. Figure 3.9 shows how the magnetic deflection of the electrons leads to a splitting of the central diffraction spot on the back focal plane. In Foucault imaging, the edge of the objective aperture is used to block one these spots. The domain that produced that spot gets reduced in intensity significantly [22, 18]. This is shown schematically in figure 3.14.

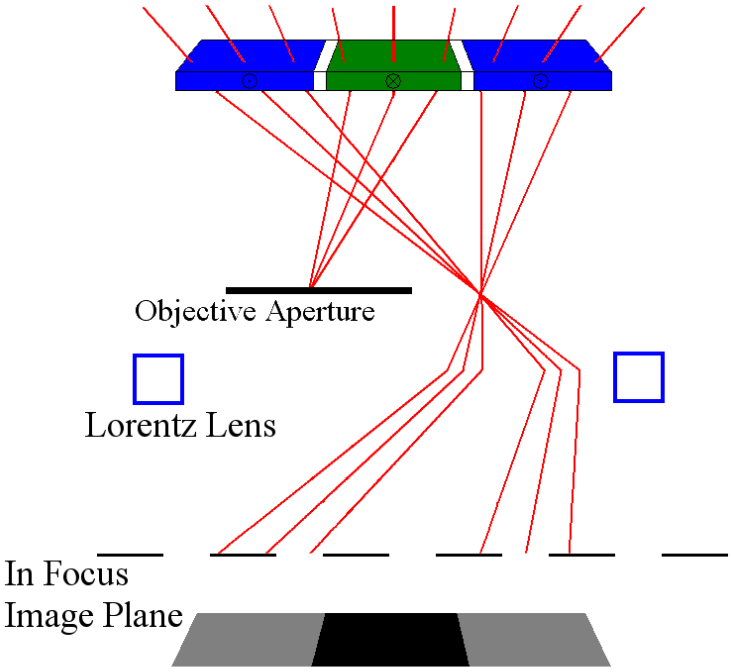

Figure 3.14: Schematic diagram of beam path through the sample and back focal planes during Foucault imaging, illustrating the use of non-parallel illumination to maximise the central spot separation in the back focal plane.

The position of the edge of the aperture determines the direction of sensitivity for the Foucault image. Figure 3.15 shows two such images of the same domain wall with orthgonal sensitivity. These two images show the magnetisation distribution throughout the sample, shown schematically in 3.15c. This method is highly dependent on both the exact position of the objective aperture, and the beam path. For

this method to work the size of the central diffraction spot must be minimised on the back focal plane, so that any splitting of this spot caused by a multiple domain sample may be maximised.

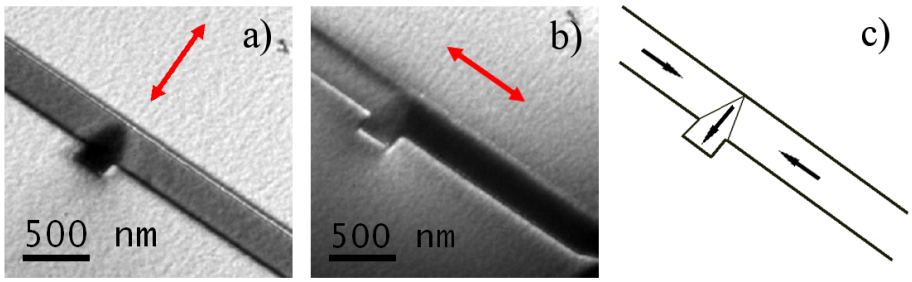

Figure 3.15: Examples of two foucault images of a transverse domain wall with orthogonal sensitivity, shown by arrows (a+b), and their associated schematic (c).

The final intensity of the domains is non-linear with magnetic induction so this is a purely qualitative technique and is highly sensitive to objective aperture drift. However, when aligned correctly, this technique produces high levels of domain contrast and is therefore very useful for magnetic imaging [17, 18, 24]. This method is harder to implement than Fresnel imaging but gives more information about the relative orientation of the magnetic induction of the domains.

3.4 Medipix/Timepix Acquisition

Current state-of-the-art TEM CCD detectors enable recording of high spatial resolution images. However they are limited in taking short exposures and low electron dose images. These limitations arise mainly because TEM CCD detectors do not directly collect electron intensity as the high electron kinetic energies would quickly lead to damage. Instead, images are indirectly recorded by detecting the light generated in a scintilator layer that is coupled to the CCD chip. This results in the electrons being scattered in the scintillator layer, inducing a noise in the image. Additionally, during the readout phase of the CCD, the electron beam must be deflected away from the detector to minimise undesired counts.

Direct radiation detectors have been used on TEM and STEM imaging and have shown significant benefits over conventional detectors [25, 26]. The layout and mounting of this detector at the base of the Philips CM20 is shown in figure 3.16. The simplest quantitative comparison between CCD and Medipix detectors is the detective quantum efficiency (DQE); this is a ratio between the square of the SNR into the detector to the SNR of the image. Effectively the DQE is a measure of any image noise induced by the detector itself. CCDs have DQE values up to ~0.5 whilst direct electron detectors such as the Medipix induce less noise and therefore have higher values.

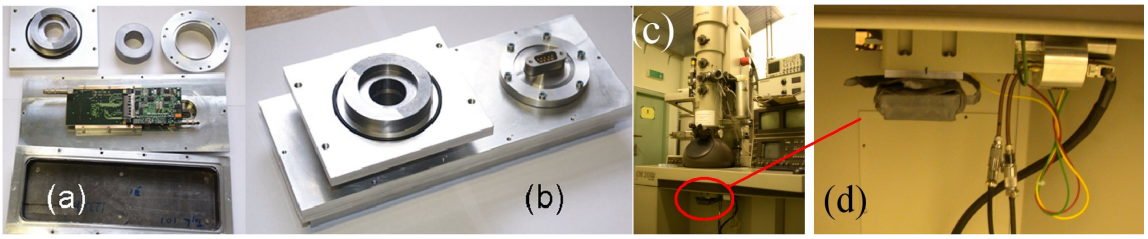

Figure 3.16: Photographs of the Medipix detector housing (a) with the components separated showing the CERN readout card and the IEAP USB.

The Timepix chip is controlled using the Pixelman software, a screenshot of which is shown in figure 3.17. This software is used for controlling the energy threshold limit for the electron detection and the acquisition time, as well as allowing for both hardware and software triggering of the acquisition [27].

Performance and detector comparison

The imaging performance of the Timepix detector was investigated at a variety of exposure times and compared to a conventional TEM CCD camera, Gatan model 794 Multiscan CCD, located directly above it.

Foucault images of a $300nm$ wide, $20nm$ thick permalloy wire containing a domain wall were aquired on both the Medipix and the CCD camera. Figures 3.18a-c show images obtained on the TEM CCD camera as the exposure time was reduced from $4ms$ to $1ms$, 3.18d shows the corresponding schematic. In fig. 3.18a, both the wire and the pinned domain wall are clearly visible. In figs. 3.18b and c, as the exposure

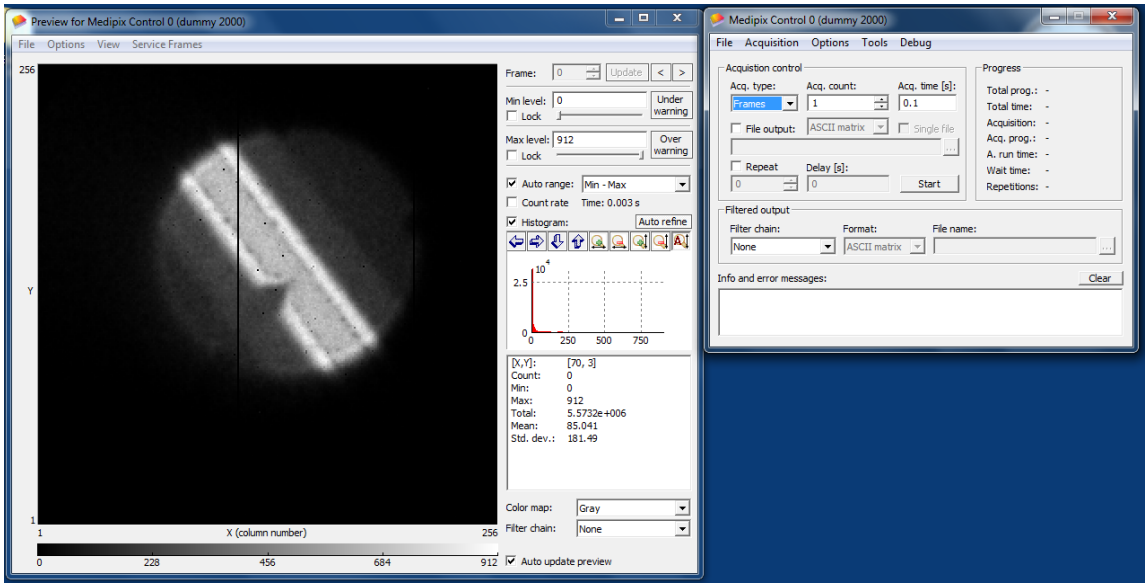

Figure 3.17: Screenshot of Pixelman software

time was reduced to $1ms$, the image became noisier and the presence of a ghost image was also observed. This latter effect is due to the image exposure time being comparable with the characteristic deflection time of the electron beam blanking (performed by electromagnetic coils in the projection system of the TEM). From this we can conclude that the shortest acceptable timescale that could be imaged using the TEM CCD camera was approximately $4ms$.

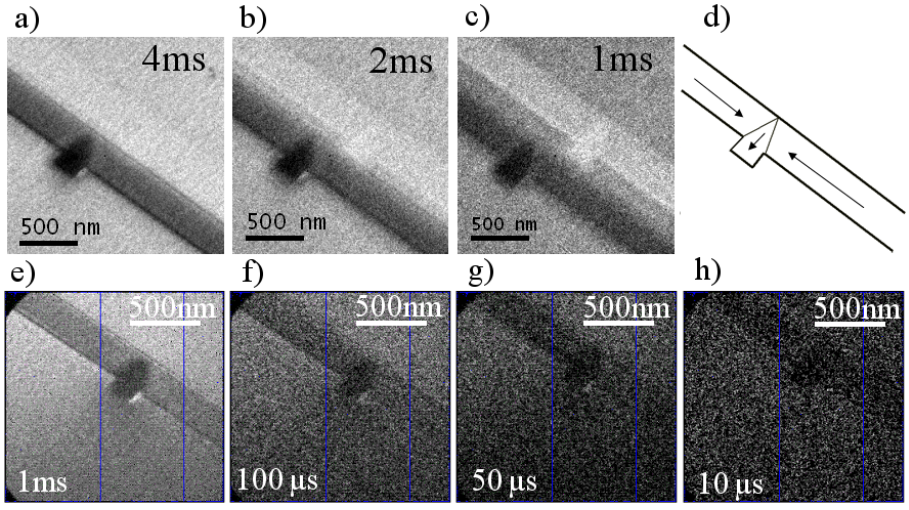

Figure 3.18: Images of low exposure timess from (a-c) the CCD with corresponding schematic (d) and (e-h) the Timepix detector

Figs 3.18$e-h$ show images of the same nanowire containing a trapped domain wall recorded on the Timepix detector at exposure times from $1ms$ down to $10\mu s$. In fig 3.18e, at 1ms exposure time, a clear image is obtained of the nanowire with a noise level that is visibly lower than in fig 3.18c. As the exposure time was reduced, the nanowire became less visible with the images becoming less intense and more dominated by noise. The source of noise in the Timepix images arises primarily because of the limited number of electrons striking each pixel during the exposure period. Statistically, $11\mu s$ is required to achieve an average intensity of 1 e- per pixel. The electron distribution in the beam is statistical in nature, obeying Poisson statistics meaning that the major source of noise for the shorter exposure times is statistical shot noise. A secondary and more minor source of noise is the charge sharing that can occur between pixels due to the high electron energies [26]. In the two shortest Medipix exposures, shown in 3.18$g-h$, the image of the wire and the domain wall can still just be discerned. This illustrates that the shortest acceptable timescale for single exposure imaging is limited to timescales of $100\mu s - 1ms$ by the available electron beam current.

An important benefit of Medipix2/Timepix type of detector is that the readout process does not add noise to the image as it does for TEM CCD cameras. This makes it possible to perform integral mode imaging where multiple short exposure images are acquired and summed together. Figure 3.19 shows a series of integral mode TEM bright field images of a $300nm$ wide notched nanowire where the exposure time for the individual exposures, ε, was reduced from $5ms$ to $500ns$ while maintaining constant total exposure time $= 0.01secs$. Thus, the number of frames, n, in each integral mode image was $n = 0.01/\varepsilon$.

From figure 3.19 it can be seen that the notched nanowire is observed clearly across the range of frame exposure times. However, for $\varepsilon = 500ns$ a slight blurring of the image was apparent. The total acquisition time for this image was between 20 and 25 minutes due to the large number of frames required, $n = 20000$, acquired at a rate of $13fps$. Thus, the blurring would be expected to arise from drifting of

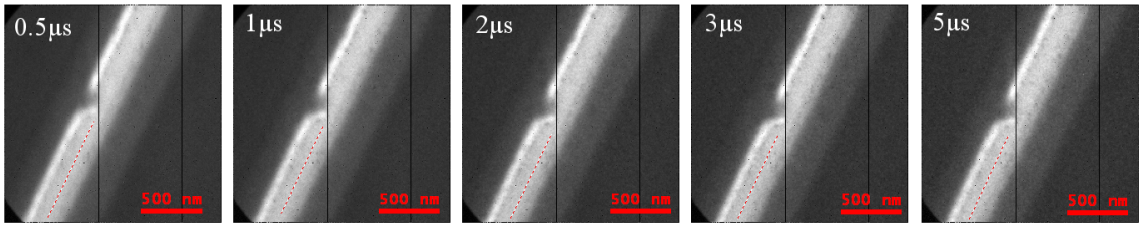

Figure 3.19: Series of integral images with varying single exposure times but constant total exposure of $0.01s$. The red lines show the region from which the intensity of linescans were obtained.

sample position during this time. Increasing the frame rate would reduce this effect. The Medipix detector were used in this study for high frame rate, low exposure time images to develop the high temporal resolution imaging technique further explained in chapter 5 [28].

3.5 SHB B-H Looper

The SHB 109a B-H looper is a magnetic measurement system designed to apply variable magnetic fields to samples of up to 6" in diameter and measure its effect. There are two sets of coils, one slightly larger than the other. The smaller of the coils can only hold a 3" wafer but can achieve fields of up to $200Oe$ compared to only $75Oe$ for the larger coils.

The main measurement of this system is an induction coil on the sample plane positioned at the back of the coils. This measures the magnetic flux within the sample and can be converted into magnetic induction (flux density) by multiplying by the sample's cross sectional area. In this study, this facility is used along with the varying magnetic field to produce hysteresis loops. The software attached to this equipment is also used to calculate measurements for saturation induction, coercivity and remanent magnetisation from the hysteresis loops. This equipment can also measure resistance, magnetostriction and permeability, although these capabilities have not been used in this study.

Bibliography

[1] De Broglie L. La nouvelle dynamique des quanta. *Ann. Phys. 3*, 3:22–128, 1925.

[2] Ruska E. The electron microscope and electron microscopy. *Rev. Mod. Phys.*, 59(3-l), July 1987.

[3] Richards D. Near-field microscopy:throwing light on the nanoworld. *Phil. Trans. R. Soc. Lond. A*, 361(1813):2843–2857, December 2003.

[4] Egerton R.F. *Physical Principles of Electron Microscopy - An Intoduction to TEM, SEM and AEM*. Springer, 2008.

[5] Williams D.B. and Carter C.B. *Transmission Electron Microscopy I - Basics*. Springer, 1996.

[6] Laura E. Reuss Michael J. Dykstra. *Biological Electron Microscopy: Theory, Techniques, and troubleshooting*. Springer, 2003.

[7] Reimer L. Kohl H. *Transmission Electron Microscopy - Physics of Image Formation*. Springer, 2008.

[8] Taatjes D.J. and Mossman B.T. *Cell Imaging Techniques: Methods and Protocols*. Humana Press, 2005.

[9] Kittel C. *Introduction to Solid State Physics*. John Wiley and Sons, 1976.

[10] Williams D.B. and Carter C.B. *Transmission Electron Microscopy I - Diffraction*. Springer, 1996.

[11] Brownlie C. *A TEM Investigation of Controlled Magnetic Behaviour in Thin Ferromagnetic Films*. PhD thesis, University of Glasgow, UK, 2007.

[12] Wu X. and Baribeau J-M. Composition and strain contrast of Si(1-x)Ge(x) (x=0.20) and Si(1-y)C(y) (y ¡= 0.015) epitaxial strained films on (100) Si in annular dark field images. *Journal of Applied Physics*, 105(4), FEB 15 2009.

[13] Tran D.T. Jones I.P. Preece J.A. Johnston R.L. and Van den Brom C.R. TEM characterization of chemically synthesized copper-gold nanoparticles. *Journal of Nanoparticle Research*, 13(9):4229–4237, SEP 2011.

[14] Okuda M. Ogawa N. Takeguchi M. Hashimoto A. Tagaya M. Chen S. Hanagata N. and Ikoma T. Minerals and Aligned Collagen Fibrils in Tilapia Fish Scales: Structural Analysis Using Dark-Field and Energy-Filtered Transmission Electron Microscopy and Electron Tomography. *Microscopy and Microanalysis*, 17(5):788–798, OCT 2011.

[15] Chapman J.N. Johnston A.B. Heyderman L.J. McVitie S. Nicholson W.A.P. and Bormans B. Coherent Magnetic Imaging By TEM. *IEEE Transactions on Magnetics*, 30(6, Part 1):4479–4484, NOV 1994.

[16] Hale M.E. Fuller H.W. and Rubinstein H. Magnetic Domain Observations By Electron Microscopy. *Journal of Applied Physics*, 30(5):789–791, 1959.

[17] Williams D.B. and Carter C.B. *Transmission Electron Microscopy III - Imaging*. Springer, 1996.

[18] Chapman J.N. The Investigation of Magnetic Domain-Structures in Thin Foils by Electron-Microscopy. *Journal of Physics D-Applied Physics*, 17(4):623–&, 1984.

[19] Hirsch P. et.al. *Electron Microanalysis of Thin Crystals*. Krieger Publishing Company, 1977.

[20] Aharonov Y. and Bohm D. Significance of Electromagnetic Potentials in the Quantum Theory . *PHYSICAL REVIEW*, 115(3):485–491, 1959.

[21] McVitie S. and White G.S. Imaging amperian currents by Lorentz microscopy. *Journal of physics D - Applied physics*, 37(2):280–288, JAN 21 2004.

[22] Chapman J.N. and Scheinfein M.R. Transmission electron microscopies of magnetic microstructures. *Journal of Magnetism and Magnetic Materials*, 200(13):729 – 740, 1999.

[23] McVitie S. and Cushley M. Quantitative fresnel lorentz microscopy and the transport of intensity equation. *Ultramicroscopy*, 106(45):423 – 431, 2006.

[24] Chapman J.N. Morrison G.R. Jakubivics J.P. Taylor R.A. Determination of domain wall structures in thin foils of soft magnetic alloy. *Electron Microscopy and Analysis, IOP Conf. Ser. No. 68*, page 197, 1984.

[25] McMullan G. et al. Electron imaging with medipix2 hybrid pixel detector. *Ultramicroscopy*, 107(401), 2007.

[26] Mac Raighne A. Fernandez G.V. Maneuski D. McGrouther D. and OShea V. Medipix2 as a highly flexible scanning/imaging detector for transmission electron microscopy. *J.Inst conference proceeding 12th iWoRID*, Jan 2011.

[27] Vykydal Z. Jakubek J. and Pospisil S. Usb interface for medipix2 pixel device enabling energy and position-sensitive detection of heavy charged particles. *Nucl. Instrum. Meth. A*, 563:112, 2006.

[28] Llopart X. Campbell M. Dinapoli R. Segundo D.S. and Pemigotti E. Medipix2: a 64-k pixel readout chip with 55 mm square elements working in single photon counting mode. *IEEE Trans. Nucl. Sci.*, 49:2279, 2002.

Chapter 4

Linear Phase Gradient Imaging

4.1 Introduction

Understanding the magnetic structure and behaviour within nanostructures is of fundamental importance for the development of magnetic based and spintronic devices. Imaging this behaviour both directly and indirectly is crucial for this understanding and techniques such as Kerr microscopy, electron holography and Lorentz microscopy have been used for identifying and characterising magnetic structure and behaviour. As described earlier, the University of Glasgow specialises in Lorentz microscopy within TEMs. The three main magnetic imaging methods within these instruments, Fresnel, Foucault and DPC, all have their limitations. Fresnel imaging is the easiest to implement, however due to it being out of focus the information with respect to both size and magnetisation is generally considered to be non-quantitative. Foucault solves this as it is an in-focus technique, however the manner by which it blocks part of the central diffraction spot means that the domain contrast is not proportional to the magnetisation and is therefore purely qualitative. DPC is capable of high resolution imaging and quantitative measurements of magnetic induction; the JEOL ARM200 recently installed at the University of Glasgow has reached a maximum resolution in DPC mode of 0.7Å[1]. Because of this DPC is widely considered to be the most capable technique. It is however a scanning technique and therefore unsuitable for viewing dynamic processes. The ideal method would be a high resolution, in

focus technique, capable of quantitatively and directly observing magnetic processes without resorting to scanning modes.

This study aims to explore the possibility of a new TEM based magnetic imaging technique. It aims to improve on current techniques by quantitatively imaging magnetic induction in thin film samples, whilst maintaining spatial resolution and not resorting to scanning modes. This is not meant as a replacement for DPC, but rather as a simpler way to gain quantitative magnetic information in in-situ TEM images.

This new technique involves replacing the simple circular objective aperture in a TEM with a specifically engineered, semi-electron-transparent graded aperture. This aperture is effectively a wedge with varying thickness. Equation 4.1 shows how the electron intensity, I, varies with the sample thickness, t, where I_0 is the incident intensity and λ is the mean free path for inelastic scattering in the sample [2].

$$I = I_0 e^{-(t/\lambda)} \tag{4.1}$$

The electron transmission (transparency) through the wedge will vary as the thickness does, giving a transmission gradient. When placed in the back focal plane of the microscope, this will perturb the diffraction pattern by reducing the intensity across the pattern in reciprocal space in accordance with equation 4.1. The electrons passing through a magnetic sample are deflected, resulting in a splitting of the central diffraction spot. The graded aperture modifies the complex disturbance in the back focal plane along the axis of the aperture gradient by generating an intensity difference between the split spots. This will lead to intensity contrast between the magnetic domains. Figure 4.1 shows a schematic diagram of this imaging method in a TEM.

This type of imaging by gaining phase gradient contrast through wedge or double wedge absorbers has been demonstrated previously in X-Ray Microscopy [3, 4].

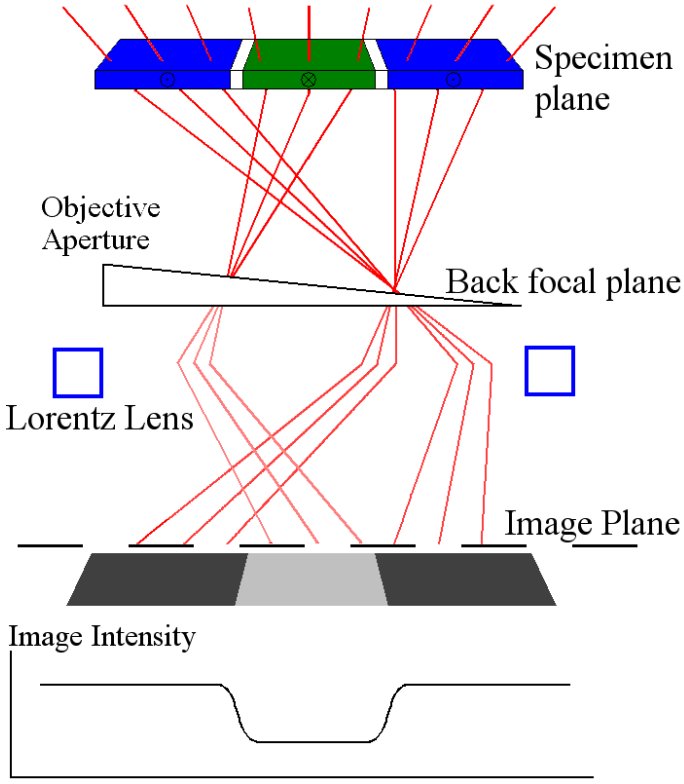

Figure 4.1: Schematic diagram of Phase Gradient Imaging within a TEM.

The difference between this and Foucault imaging is that the wedge apertures will be fabricated such that the electron transmission is linear with respect to position. This together with the fact that the magnitude of the spot splitting is linear with magnetic induction leads to the intensity difference in the image being proportional to the magnetic induction in the sample allowing the possibility that quantitative information may be extracted. The aim of this study is to develop this technique both in simulation and experimentally to quantitatively calculate the induction in magnetic samples. While this information will only be one-dimensional in the direction of the wedge gradient, it will be simpler to implement than current quantitative imaging techniques. Also while this technique may produce immediately visible magnetic contrast, there will be several steps of image manipulation before this becomes quantitative with respect to magnetic induction.

4.2 Theory of Phase Gradient Imaging

Before this technique can be experimentally implemented, it must be mathematically simulated to predict what levels of contrast can be expected. This technique was done using the mathematical wave equation approach introduced in chapter 3. This will allow the resultant images to be predicted as well as providing a method of extracting quantitative magnetic induction information from the final image, how this is done will be discussed in the following section. This mathematical theory will then be modelled using image formation in Digital Micrograph^{TM} (DM); as well as confirming the results from the theory, this model will allow us to visualise how the magnetic contrast may vary with the conditions of the aperture wedge. Both of these calculation methods will be used to explore the validity of this imaging method and identify any limiting factors within it. Further, they will provide the necessary proportions of the phase gradient aperture to maximise magnetic contrast. Once the simulations are understood this technique can be experimentally implemented by fabricating the wedge apertures using electron beam deposition and to image known magnetic structures on the Philips CM20.

Theoretical image calculation

As discussed in chapter 3, the wave equation approach to image calculation treats the electrons as waves and the magnetic sample as a phase object, inducing a phase shift in the transmitted electrons; it is this phase shift that is imaged in Lorentz microscopy. This method defines the waveform as it passes through the TEM with respect to the specimen, back focal and image planes. The initial wavefunction exiting the sample, $f(x)$ is a function of the intensity amplitude, A, sample thickness, z, and the induced total phase shift, ϕ, shown in equation 4.2; This total phase shift is the sum of the magnetic (ϕ_m) and electrostatic (ϕ_e) phase shifts shown in equations 4.3 and 4.4 respectively, where B_s is the saturation magnetic induction, t is the sample thickness and V is the electrostatic potential, $V = 21V$ in Permalloy [5]. Equation 4.3 is the differential form of magnetic phase equation 3.18 introduced in chapter 3 and is a simpler form of the phase equation and becomes relevant for use

in equation 4.14 at the end of this derivation.

$$f(x) = A(x)e^{i\phi} \tag{4.2}$$

$$\frac{d\phi_m}{dx} = \frac{-eB_s t}{\hbar} \propto B_s t \tag{4.3}$$

$$\phi_e = \frac{\pi V t}{\lambda E} \tag{4.4}$$

$$\phi = \phi_m + \phi_e \tag{4.5}$$

The wavefunction in 4.2 is Fourier transformed to give the wavefunction of the amplitude at the back focal plane, F(k), as displayed in figure 4.1.

$$FT[f(x)] = F(k) \tag{4.6}$$

This is then multiplied by the aperture function, defined as a linear transmission modification across k-space, resulting in equation 4.8 where $APF(k_x, k_y)$ is the aperture function defined in terms of the electron transmission across the aperture, m and c are the gradient and midpoint of the transmission gradient aperture with m measured in percentage of transmission per micrometre and $\Psi(k)$ is the wavefunction in a back focal plane after the aperture modification.

$$APF(k) = mk + c \tag{4.7}$$

$$\Psi(k) = F(k)(mk + c) = mkF(k) + cF(k) \tag{4.8}$$

Equation 4.9 is a standard Fourier transform showing how the transform of the differential of a function is related to the transform of the original function. This can be rearranged as below to give an expression for $kF(k)$.

$$\begin{aligned} FT\left[\frac{df(x)}{dx}\right] &= i2\pi kF(k) \\ kF(k) &= FT\left[\frac{1}{i2\pi}\frac{df(x)}{dx}\right] \end{aligned} \tag{4.9}$$

This is then substituted into 4.8 resulting in 4.10.

$$\Psi(k) = m\left[FT\left[\frac{1}{i2\pi}\frac{df(x)}{dx}\right]\right] + cF(k) \tag{4.10}$$

Equation 4.10 represents the wavefunction in the BFP directly below the graded aperture. This is then inverse Fourier transformed to give the wave equation in the image plane, $\Psi(x)$, shown in equation 4.11.

$$\Psi(x) = \frac{m}{i2\pi}\frac{d(f(x))}{dx} + cf(x) \tag{4.11}$$

$f(x)$ is then substituted from equation 4.2. The differential from 4.11 is expanded as shown in equation 4.12, producing the wave equation of the final image 4.13.

$$\begin{aligned} \left(\frac{df(x)}{dx}\right) = \left(\frac{d[Ae^{i\phi}]}{dx}\right) &= A\left(\frac{de^{i\phi}}{d\phi}\right)\left(\frac{d\phi}{dx}\right) + e^{i\phi}\left(\frac{dA}{dx}\right) \\ &= ie^{i\phi}A\left(\frac{d\phi}{dx}\right) + e^{i\phi}\left(\frac{dA}{dx}\right) \end{aligned} \tag{4.12}$$

$$\Psi(x) = \frac{mAe^{i\phi}}{2\pi}\left(\frac{d\phi}{dx}\right) - \frac{ime^{i\phi}}{2\pi}\left(\frac{dA}{dx}\right) + cAe^{i\phi} \tag{4.13}$$

The final image intensity, I_{im}, is calculated by multiplying Ψ by its complex conjugate. This gives the final equation, 4.14, which will be used to calculate image intensities from the transmission amplitude and the magnetic and electrostatic phase images of simulated samples.

$$I(x) = \Psi(x)^*\Psi(x) = A^2c^2 + \frac{mA^2c}{\pi}\left(\frac{d\phi}{dx}\right) + \frac{m^2A^2}{4\pi^2}\left(\frac{d\phi}{dx}\right)^2 + \frac{m^2}{4\pi^2}\left(\frac{dA}{dx}\right)^2 \tag{4.14}$$

Equation 4.14 is the final intensity equation, from which the integrated magnetic induction will be extracted. The first term is the in focus image in terms of the amplitude A and the central intensity transmission from the aperture, c; this term contains no phase information and is effectively the bright field image. The second term contains $\frac{d\phi}{dx}$, this is what we want as it can be used with 4.3 to quantitatively calculate the magnetic induction of the sample. This term is dependent upon both the gradient, m, and the central transmission, c, of the aperture. The third term of equation 4.14 is a squared term of phase gradient; this term means that to calculate the magnetic induction the image intensity equation will need to be solved quadratically. The final term is an amplitude gradient term; assuming a uniform sample thickness this term will only be non-zero at the sample edges and is expected to be dominated at these edges by the electrostatic phase contribution.

Equation 4.14 was used to simulate phase gradient images in Digital Micrograph^{TM} for a $600nm$ diameter circular sample of 5nm thick Permalloy, containing a magnetic vortex at the centre of the disk. The input conditions of magnetic phase, electrostatic phase and intensity amplitude of the wavefunction leaving the sample are shown in figure 4.2a, b and c respectively. The change in amplitude between outside and inside the sample shown in figure 4.2c was taken from previous experiments of $20nm$ thick permalloy.

This simulated sample was run through equation 4.14 using m and c values of $1.5\%\mu m^{-1}$ and 0.5 respectively, producing the images shown in figure 4.3. This shows the final intensity image, a, and the individual term images, $b-e$, representing the four terms in equation 4.14. Figure 4.3 also compares line profiles through the centre of each of these images and their relative magnitudes; the y-axis of this figure has the same scale for each profile but has been offset to display their relative differences more clearly. It can be seen that the final term of this expression has negligible magnitude when compared to the first three; this example has amplitude and phase inputs from experimentally typical values and therefore the final term will be disregarded for the remainder of this study. This means that the final expression for the image intensity

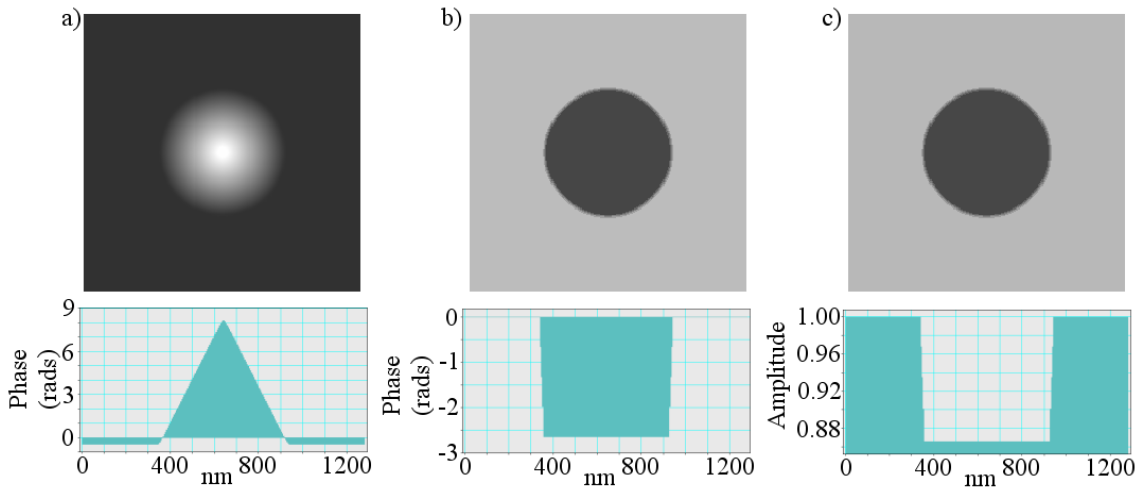

Figure 4.2: Wavefunction terms of initial magnetic state showing (a) magnetic phase, (b) electrostatic phase and (c) normalised amplitude. These are inputted into equation 4.14 to give the results shown in figure 4.3.

becomes 4.15.

$$I(x) = A^2c^2 + \frac{mA^2c}{\pi}\left(\frac{d\phi}{dx}\right) + \frac{m^2A^2}{4\pi^2}\left(\frac{d\phi}{dx}\right)^2 \tag{4.15}$$

Image simulation

As well as using the wave equation approach, this imaging technique is modelled using image formation in Digital Micrograph^{TM} (DM). As before the sample was first defined with a magnetic phase, an electrostatic phase and an amplitude image; these are substituted into equation 4.2 to give the wave equation leaving the sample at the sample plane. DM is used to Fourier transform this wave equation and multiply it by an aperture image representing the transmission of the aperture in the BFP, producing the wavefunction at the back focal plane, this is then inverse Fourier transformed and multiplied by its complex conjugate to form the final image intensity. This method is equivalent to the mathematical approach described above; the difference being that this uses image formation at each plane to model the TEM rather than the final calculated equation.

This method was used to simulate this imaging technique on a continuous sample of 20nm Permalloy with three magnetic domains separated by two 180° domain walls.

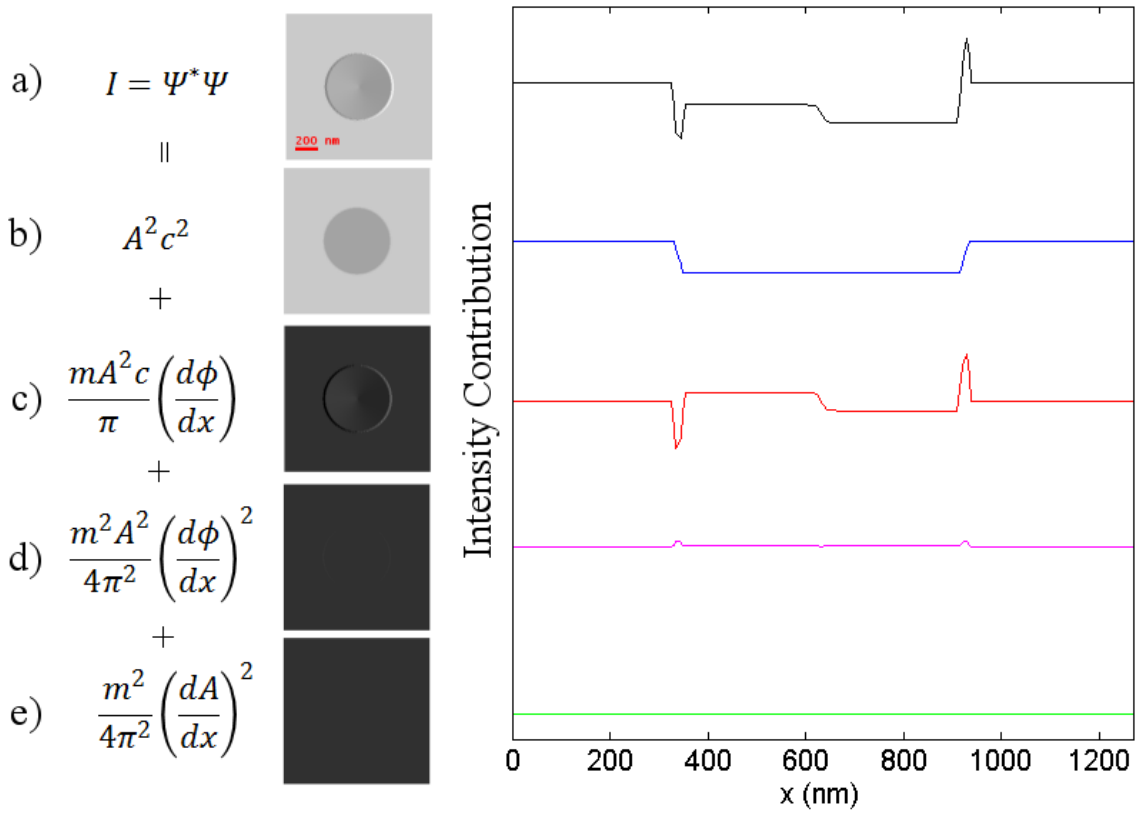

Figure 4.3: Comparison of images and intensity profiles of the final calculated intensity (a) and the four terms (b-e) from equation 4.14. Images are shown on the same grey scale. The y-axes of the graphs have been relatively displaced on the same scale to more clearly show the intensity differences between the equation terms.

Figure 4.4*a* shows a simulated sample magnetisation and line profile of this sample, 4.4*b* and *c* then show the magnetic phase, ϕ_m, of the sample and the transmission probability of the phase gradient aperture respectively. In this case the aperture varies from fully transparent to fully opaque over the full width of the diffraction pattern. In this sample both the electrostatic phase shift and the amplitude terms are considered to be constant.

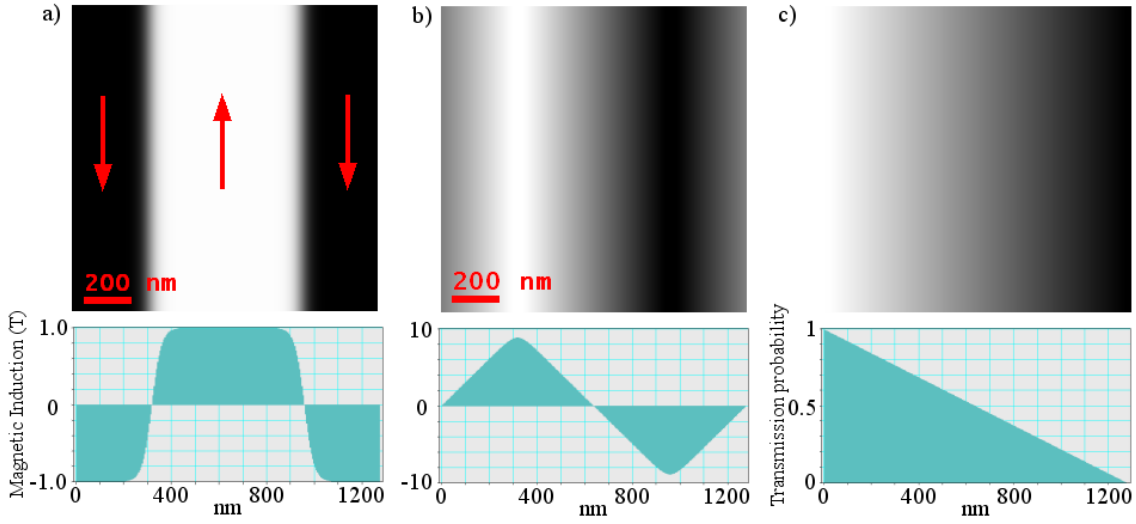

Figure 4.4: Initial state of the sample showing (a) the y-component of the magnetisation, (b) the magnetic phase of the sample and (c) the transmission probability over the diffraction pattern.

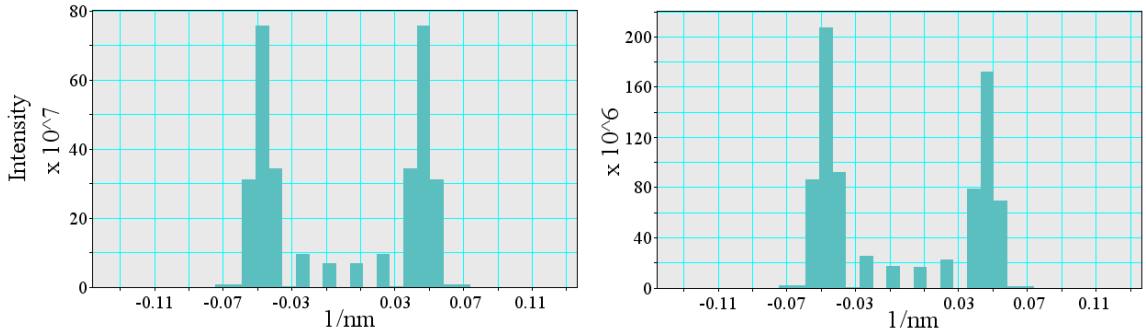

Figure 4.5: Diffraction pattern intensity before (a) and after (b) modification by the phase gradient aperture shown in 4.4*c*.

Figure 4.5 shows how the aperture illustrated above modifies the diffraction pattern. 4.5*a* shows the unmodified diffraction pattern generated by the Fourier trans-

form of initial wave equation and illustrates the intensity of the diffraction pattern just above the aperture. This is then multiplied by the transmission probability profile in 4.4*c*, producing the diffraction pattern intensity just after the aperture, the profile of which is shown in 4.5*b*. The modified diffraction pattern is then inverse Fourier transformed and multiplied by its complex conjugate, equations 4.16 and 4.17, generating the final simulated image intensity. The initial magnetisation and final image intensity of the continuous, three domain sample, are shown in figure 4.6*a* and *b* respectively. The intensity in 4.6*b* is reversed from the initial magnetisation state due to the negative gradient of the aperture. Where $\Psi(x)$ is the final image wavefunction and $I(x)$ is the image intensity.

$$\Psi(x) = FT^{-1}\left[FT\left[A(x)e^{i\phi}\right] \times APF(k)\right] \tag{4.16}$$

$$I(x) = \Psi(x)^{*}\Psi(x) \tag{4.17}$$

The simulations gained from this method indicated that this technique will produce a significant difference in intensity between magnetic domains, as shown in figure 4.6b, however these results will be verified using the wave equation approach to the simulations.

4.3 Simulation and aperture tuning

Before the phase gradient apertures could be manufactured, the images simulated with the methods described above had to be analysed. These simulations also allowed us to tune the variables of the wedge to maximise potential magnetic contrast. For this theoretical tuning we used the continuous, three domain sample of $20nm$ Permalloy introduced in the previous section. To design the wedge aperture, the diffraction pattern must be understood in real space in the TEM, i.e. the real space splitting of the central diffraction spot must be calibrated with respect to the objective aperture. A. Johnston demonstrated in 1995 that the separation between the split diffraction

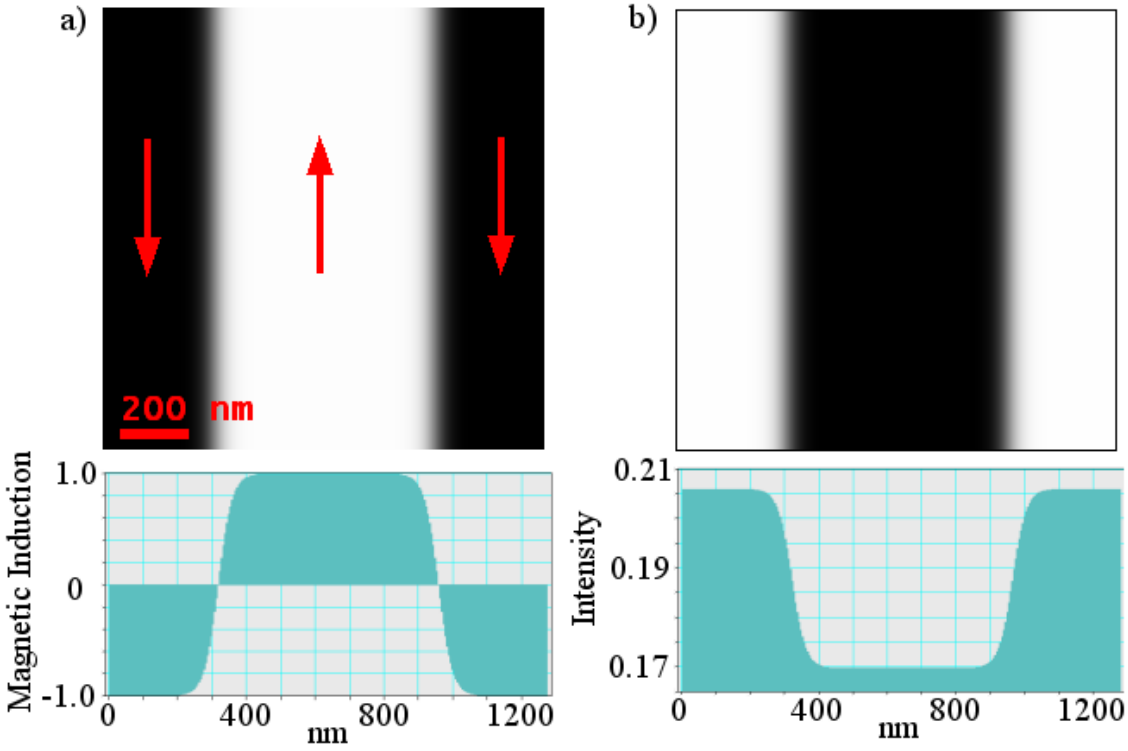

Figure 4.6: Comparison image between initial sample magnetisation (a) and final image intensity (b).

spots in the Philips CM20 is $3\mu m$ [6, 7, 8]. This was used to calibrate the necessary size of the wedge aperture in real space. This assumption was later discovered to be misinterpreted, was corrected and the experimental wedges reengineered to allow for this. This second attempt at the experiment used the lessons learned prior to the discovery of this mistake to improve this imaging technique further. This section and sections 4.4.1 and 4.4.2 outline work done using the assumption of a $3\mu m$ spot splitting before the correction and further work is outlined in section 4.4.3.

The contrast in the image was investigated with respect to the wedge variables to determine the visibility of the magnetic contrast (C). For this purpose contrast was defined as in equation 4.18 where I_{max}, I_{min} and I_{mean} are the maximum, minimum and mean intensity of the image respectively. For the purposes of this study a contrast level of $C > 0.1$ is defined for the contrast to be visible. This value was chosen to be sure of overcoming both image noise and any unwanted scattering from the aperture.

$$C = \frac{I_{max} - I_{min}}{I_{mean}} \tag{4.18}$$

Figure 4.7 shows the intensity profile of the diffraction pattern (blue) from the three domain sample superimposed onto a graph of transmission probability across the aperture (red); in this figure the x axis is shown in both real and reciprocal space. The phase aperture (red) is defined by two variables, the gradient measured in transmission percentage per micrometre, m, and the transmission probability through the centre of the diffraction pattern, c. Note that c is not necessarily the centre of the wedge as the aperture can be moved with respect to the diffraction pattern. This means that while the gradient is fixed after aperture fabrication, the midpoint value is dependent on aperture positioning in the back focal plane.

Given the definitions of C, m and c above, the image contrast was investigated with respect to both varying m and c. This research found that, as expected from equation 4.15, as m increases so does the contrast, this is expected as increasing m increases the difference in transmission between the two spots. It was also found that

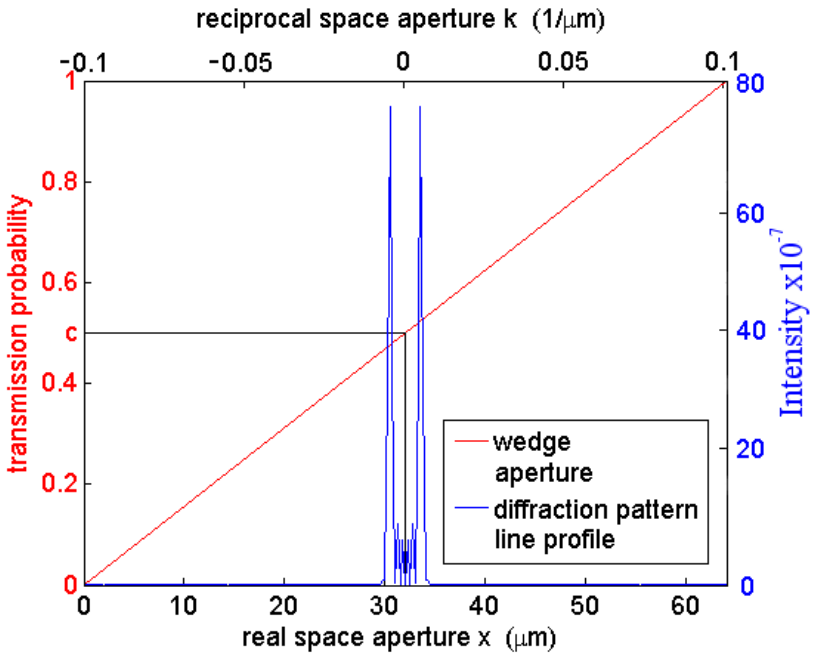

Figure 4.7: Intensity line profile of diffraction pattern with a to-scale phase aperture superimposed onto graph, shown in both reciprocal and real space dimensions.

the contrast increased as c was decreased, this is because increasing c increases the background term, A^2c^2, and therefore I_{mean}, faster than the magnetic intensity term thus reducing the magnetic contrast. Combining these two effects leads to figure 4.8 which shows lines of constant contrast with respect to m and c. The blue shaded region of figure 4.8 indicates where $C > 0.1$, and therefore theoretically visible. Assuming a gradient of $1.5\%\mu m^{-1}$, the diffraction pattern should be able to be placed anywhere on the graded aperture and still produce visible magnetic contrast. This correlates to the aperture varying from fully opaque to fully transparent over $66\mu m$ in real space.

As described earlier, the total phase shift is made up of the electrostatic and magnetic phase shifts, defined in equations 4.4 and 4.3. Equation 4.15 shows that the final image intensity is related to the phase gradient. Figure 4.9 compares the phase and phase gradients between magnetic and electrostatic phases for the $5nm$ thick Permalloy circle of $600nm$ diameter. This shows that in this case the electrostatic phase gradient is approximately five times larger than the magnetic phase. This

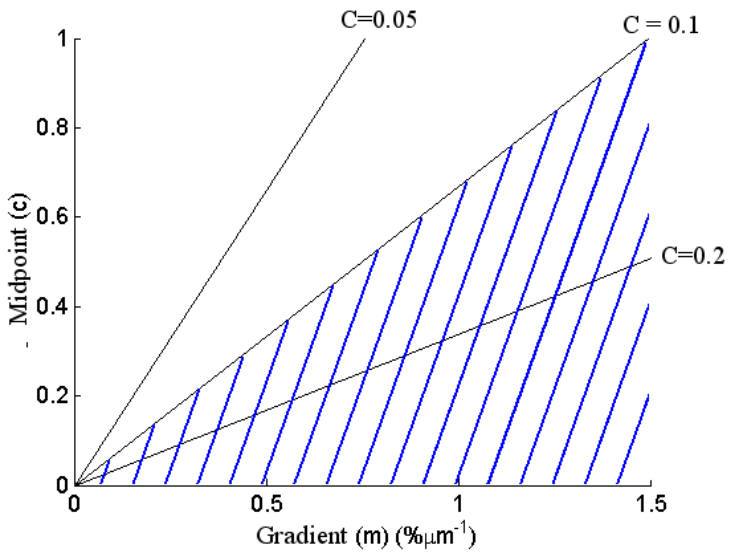

Figure 4.8: Graph lines of constant contrast with respect to c and m, the blue shaded region indicates the area of practical visibility as defined by $C > 0.1$.

means that the electrostatic contrast will be significantly more visible than the magnetic contrast, however this is only relevant at the sample edges meaning that it should be readily identifiable from the magnetic contrast.

So far in this chapter the graded aperture has been considered to only have an effect on the amplitude of the electron transmission. However as the electron beam passes through the aperture it is also Bragg scattered in exactly the same way as it would through a sample. This poses a problem for this imaging technique as it produces a source of electron scattering that is unwanted in this technique. For this reason, the Bragg scattering by the aperture must be minimised, this is done my tuning the deposition of the aperture to maximise the amorphousness of the material. This will be further discussed in the next section.

4.4 Experimental Phase Gradient Imaging

4.4.1 Wedge fabrication

The theoretical work has indicated that to be sure of gaining visible magnetic contrast the transmission gradient of the aperture needs to be above $1.5\%\mu m^{-1}$. To fabricate

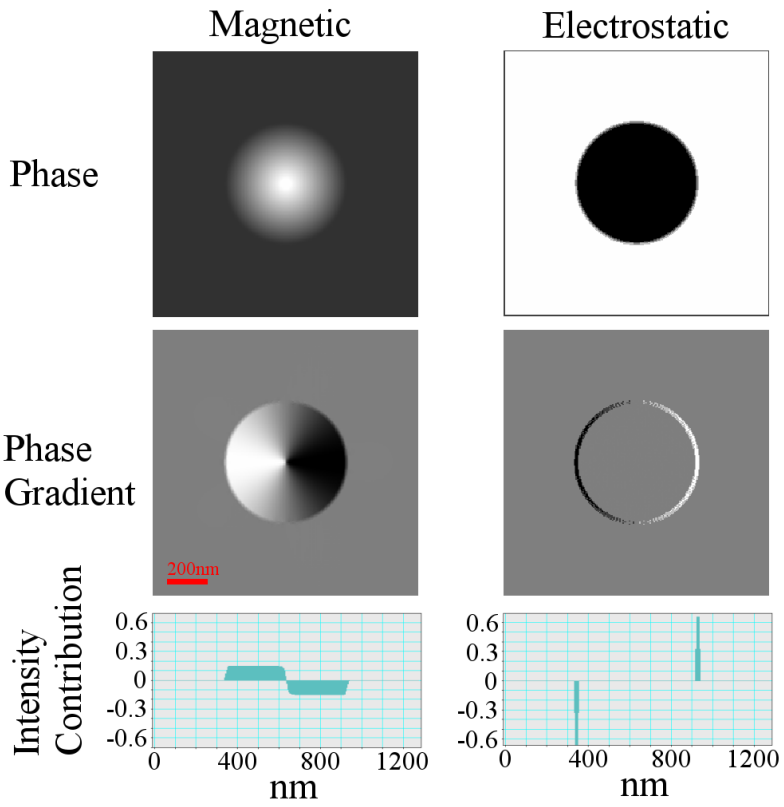

Figure 4.9: Images and profiles of the electrostatic and magnetic phases and phase gradients. Note the final image intensity is related to the phase gradient images through equation 4.15

the graded aperture, electron beam deposition was used in the Nova 200 dualbeam system [9]. However, before that could be done, the mounting of the aperture had to be considered. Figure 4.10a and b shows images of the objective aperture blade from the Philips CM20 microscope, showing that the blade contains circular slots designed to hold $2mm$ diameter disks, the apertures are then held on these disks. Our aperture will be fabricated on a Si_3N_4 TEM membrane substrate, described in chapter 2, these substrates are formed of $2mm$ square blocks of silicon and will not fit the aperture blade slots.

The circular slots mean the corners of the samples must be milled to form a $2mm$ circular sample whilst keeping the membrane at its centre unbroken. This was done by attaching the samples to a rod using soluble glue, allowing it to be more firmly held. A diamond saw was then used at low RPMs, and the sample rotated, milling the sample circular. This process was highly susceptible to the membrane breaking, however very few intact samples were required so this method was pursued. Figures 4.10c and d show images of these samples before and after milling. They also show a complete and a broken membrane on the square and circular samples respectively. These circular samples could now fit into the aperture rods and the fabrication process was able to proceed.

One of the main issues with this imaging technique was electron scattering from the aperture. This must be minimised by ensuring that the graded apertures be as amorphous as possible. The wedges will be fabricated from platinum using electron beam deposition (EBD) in the FEI Nova 200 Dualbeam instrument. This method of fabrication was chosen as it allows high degrees of control over the deposition area and can be programmed to deposit different depths at different locations, making it ideal for fabricating wedges. Previous studies have found that the platinum deposited with EBD contains small areas of crystalline platinum with crystals of up to a few nanometres [10, 11, 12]. The only controllable variable which is likely to affect the crystallinity of the deposition is the electron probe current. This current varies the speed of deposition and therefore the atomic layering. As an initial experiment,

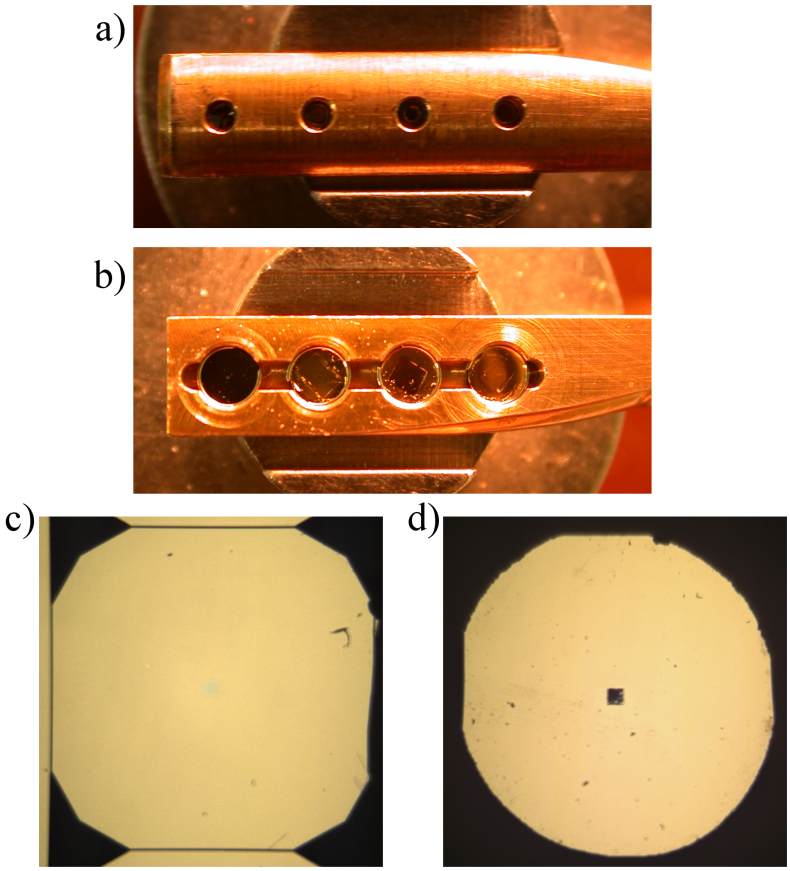

Figure 4.10: Photographs of the (a) bottom and (b) top of the objective aperture rod, showing 2mm diameter slots. As well as photographs of the Si_3N_4 membrane sample (c) before and (d) after milling.

EBD was used at a variety of currents to deposit $20nm$ of material. Diffraction patterns were taken of these samples to determine their levels of scattering. Figure 4.11 shows these patterns along with their in focus and line profile counterparts. The first scattering intensity peaks were used as a measure of the scattering from the aperture; these peaks (indicated by the red arrow) are at a spatial frequency of $4.15nm^{-1}$ from the centre of the pattern. These patterns show no further significant diffraction rings indicating that the sample is amorphous. The amorphous scattering ring indicated by the red arrow is a result of the average separation of the atoms within the amorphous structure. Minimising the intensity of this ring will minimise any potential problems that this scattering may induce. It can be seen that the sample 4.11c, deposited at $0.098nA$ has the lowest intensity ring of $\sim$600 counts compared to $\sim 620-650$ with deposition currents of $1.6nA$ and $0.4nA$. This difference is small but was still utilised and all subsequent wedges were deposited at $0.098nA$.

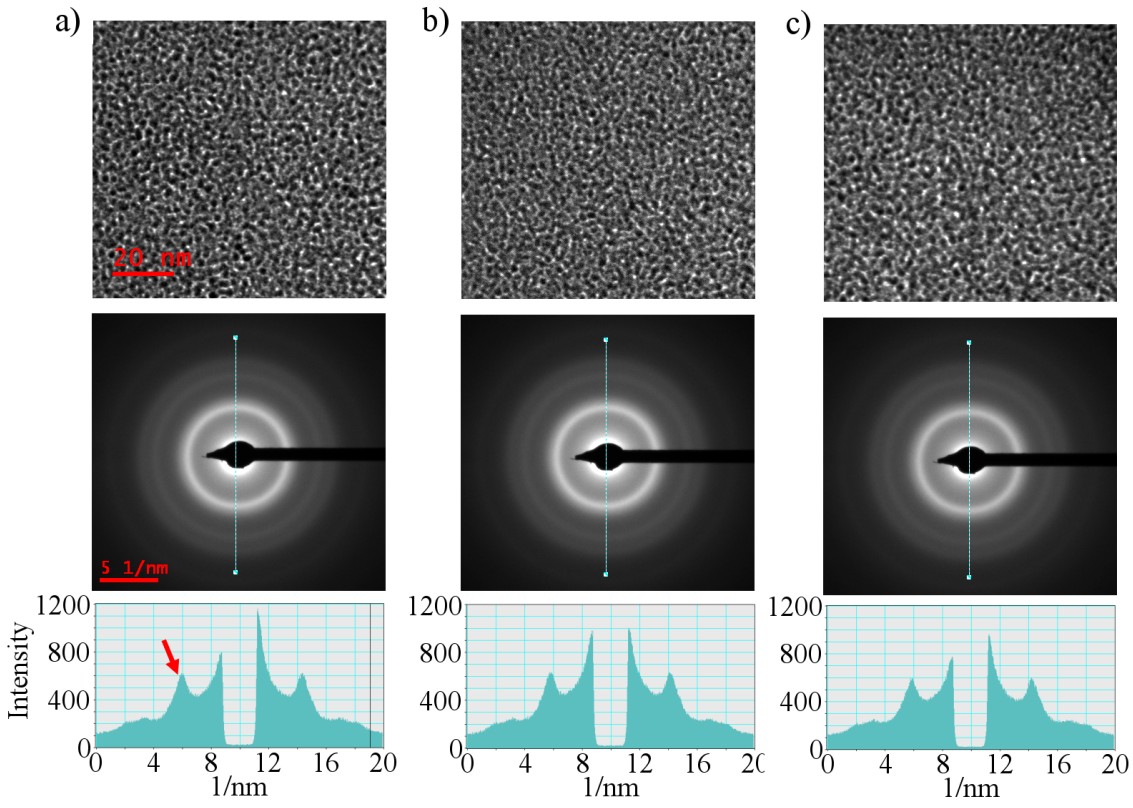

Figure 4.11: In focus images, diffraction patterns and accompanying line profiles of deposited platinum with electron currents of (a) 1.6nA (b) 0.4nA and (c) 0.098nA.

For the first set of wedges fabricated, a total wedge width of $\sim 10 \mu m$ was chosen. Assuming electron opacity at its maximum thickness this aperture has a transmission gradient of $\sim 10\% \mu m^{-1}$, this is well above the required levels to observe magnetic contrast. Each wedge was composed of 40 layers of Platinum, with each layer started $250nm$ offset from the previous. The maximum thickness, calibrated from previous depositions, was $200nm$, this was assumed to be sufficient for electron opacity [9, 13]. Initial TEM images of these wedges showed significant charging of the sample so thermal evaporation was used to deposit a continuous layer of $\sim 10nm$ aluminium to the back of the membrane to dissipate charge. Figure 4.12 shows SEM and TEM images of these wedges with their accompanying transmission profiles; note the transmission of the wedge is the square root of the TEM image intensity. The transmission gradient of 4.12b was measured to be $= 4.8\% \mu m^{-1}$, while the wedge is never fully opaque, this is still well above the required $= 1.5\% \mu m^{-1}$.

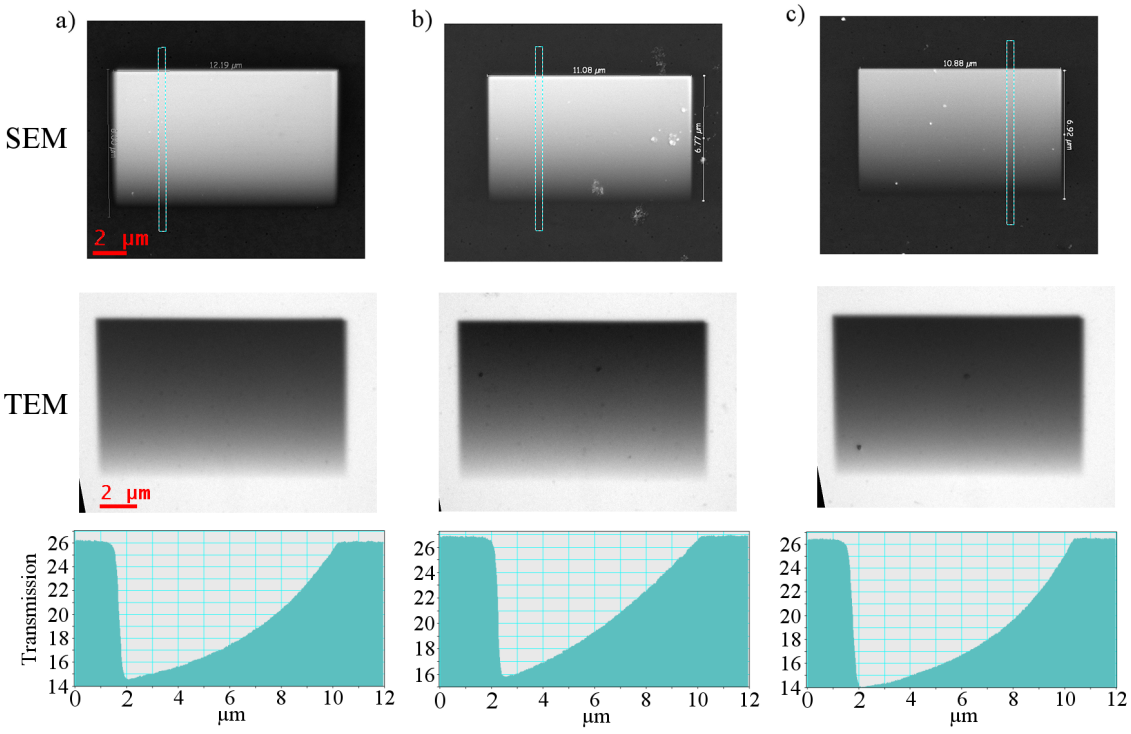

Figure 4.12: SEM and TEM images and normalised transmission profiles of 3 nominally identical phase gradient apertures. Showing the consistency of both the fabrication method and the aperture gradient.

4.4.2 Initial imaging - copper grid and magnetic samples

Before they were used experimentally, the transmission profiles of the wedges were put into the simulation script to predict the magnetic contrast levels. Figure 4.13 shows these results, where 4.13*a* is the standard three domain sample used previously, 4.13*b* is the fabricated wedge aperture transmission calibrated to the magnitude of the known spot splitting in real space and 4.13*c* is the resultant image intensity. This final image has a contrast level of $C = 0.8$, which is significantly higher than the visibility limit. These apertures were then loaded into the objective aperture rod of the CM20 and the imaging process was tested.

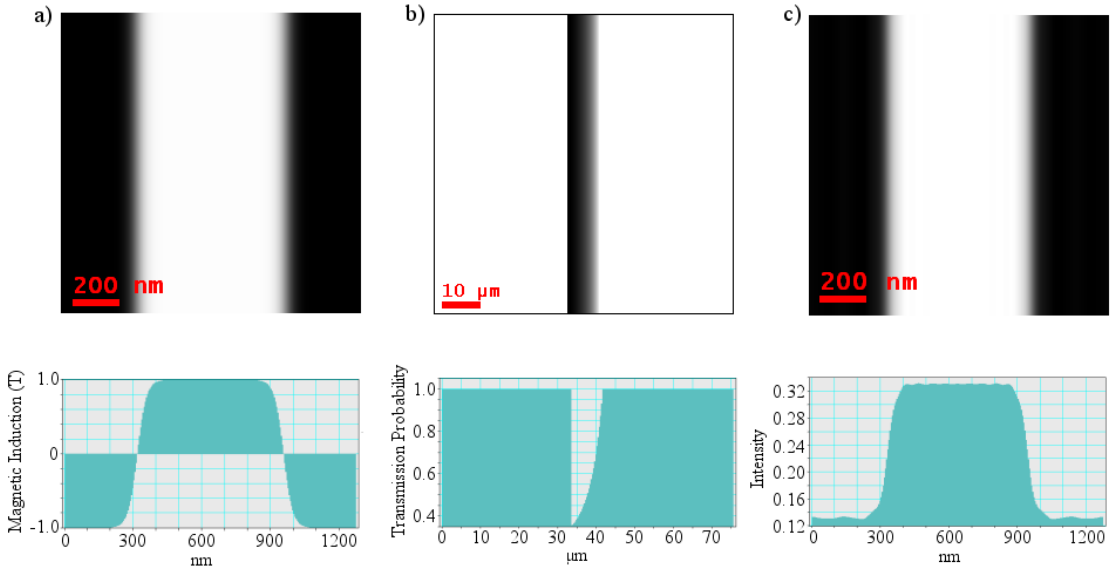

Figure 4.13: Theoretical image calculation from deposited apertures, showing (a) the initial induction, (b) the phase aperture calibrated to the size of the diffraction pattern in DM and (c) the final image intensity.

The first object imaged was a standard sample of 20-30nm thick holey-carbon-film; this is non-magnetic, but the edges of the holes will still produce gradients in the electrostatic phase. This was chosen initially because we know that the electrostatic phase gradient contrast is significantly higher than the magnetic phase gradient. The mean inner potential, V, of carbon is $\sim 9V$, slightly lower than the $21V$ in Permalloy; however this will still allow us to gauge how large the magnetic contrast will be in

reality. The results of this are shown in figure 4.14. This figure shows a bright field image, a, an image with the aperture in place, b, and an intensity line profile across one of the holes. In this example the central diffraction spot is placed approximately in the centre of the wedge. The phase gradient image and the accompanying line profile show electrostatic contrast in the form of bright and dark fringes at the top left and bottom right of the holes respectively, this correlates with the direction of the aperture gradient in the back focal plane. The magnitude of the intensity fringes either edge of the hole, 4100 and 2450 counts for the bright and dark fringes respectively and taking 3000 counts as the mean, correlate to contrast values of 0.36 and 0.18 respectively. Given these values, if the difference between the magnetic and electrostatic contrast is as large as predicted in 4.9, then the magnetic contrast should still be visible with these wedges.

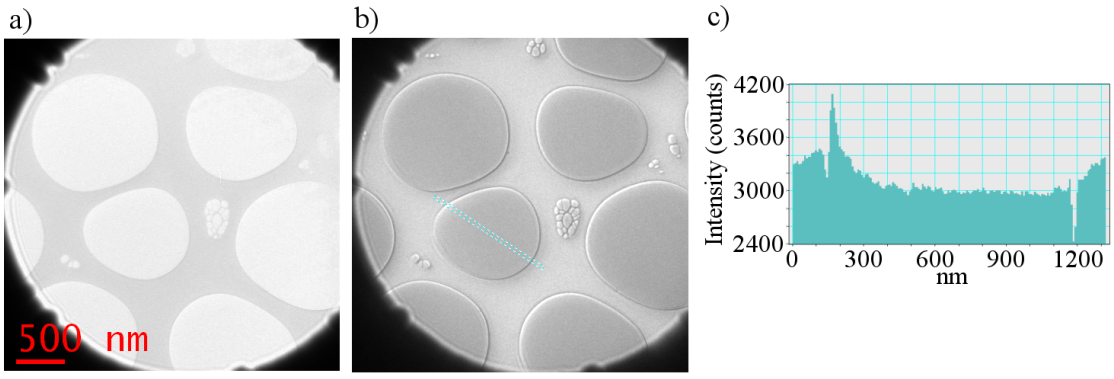

Figure 4.14: (a) In focus, (b) phase gradient images, and (c) intensity line profile of the phase gradient image for 20-30nm thick holey-carbon-film taken using the apertures shown in 4.12.

Figures 4.15 and 4.16 show the results of magnetic phase gradient imaging with these apertures. The sample consist of $1\mu m$ squares of $20nm$ Permalloy. Figure 4.15a shows a Fresnel image of the magnetic structure in a flux closed state with DWs forming a cross at its centre. 4.15b then shows an in-focus image with non-parallel illumination, this is effectively a bright field image of the sample with an out of focus image of the aperture superimposed onto it. This shows the direction of the transmission gradient with respect to the object with the image being darker on the

right hand side indicating a thicker portion of the wedge, as well as clearly displaying defects within the aperture which may affect the desired magnetic contrast. 4.15*c* then shows a phase gradient image. The lower of the two squares within this image shows one of the magnetic domains clearly, however this is due to the aperture defect, visible in the image indicated by the red arrow, blocking part of central diffraction spot. The upper of the two squares, away from any defects, shows no significant magnetic contrast. This is concerning as our simulations indicated that the contrast should be clearly visible.

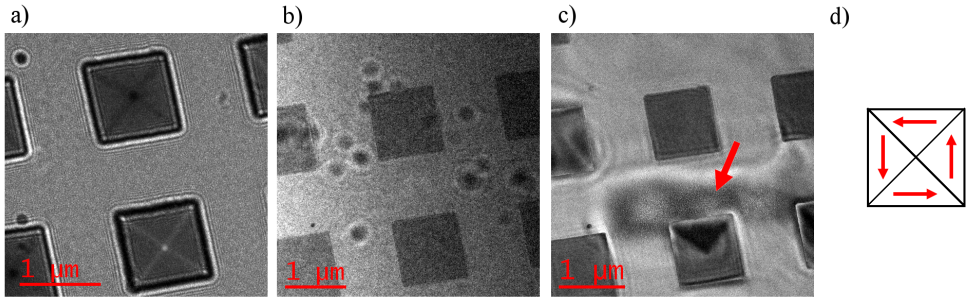

Figure 4.15: (a)Fresnel, (b) nonparallel illumination with a phase aperture and (c) phase gradient image of 20*nm* Permalloy squares, (d) schematic of magnetisation orientation in squares, showing the effect of aperture defects on the final magnetic contrast.

The experiment was repeated and figure 4.16 shows four images of the same object. Figures 4.16*a* and *b* are a standard in focus bright field image and a Foucault image with the sensitivity direction marked by the arrow respectively. This shows that the magnetic structure in this case is different to that of figure 4.15, formed of three domains but still displays flux closure. Whilst moving the central diffraction spot over the aperture in an attempt to observe magnetic contrast, figure 4.16*c* was seen, this appears to show visible magnetic contrast in a phase gradient image. However, when expanding the diffraction spot by going off parallel illumination, figure 4.16*d*, it was observed the central diffraction spots were separated over the edge of the aperture wedge. The means that one of spots is off the aperture entirely, while the other is on its edge. This condition is very similar to Foucault imaging with the difference being that the blocked part of the beam is passing through a semi-transparent objective

aperture. For this reason this was referred to as a pseudo-Foucault condition.

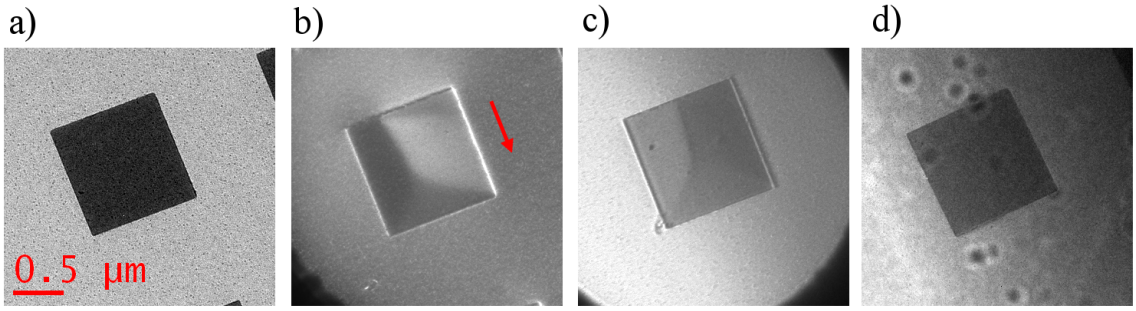

Figure 4.16: (a) In focus, (b) Foucault with sensitivity direction shown, (c) phase gradient image and (d) non-parallel illumination image, showing the magnetic contrast gained due to pseudo-Foucault conditions at the edge of the wedge.

In summary these phase gradient apertures gain no discernible magnetic contrast unless pseudo-Foucault conditions are reached with either the edges of the wedge or defects within the wedge itself. However figure 4.14 did appear to show visible electrostatic contrast of up to $C = 0.36$ in 20 to $30nm$ thick carbon. We previously calculated that for a $20nm$ thick permalloy sample, the electrostatic contrast will be approximately 5 times the magnetic contrast. If this holds true then the expected magnetic contrast from these aperture would be below the theoretical visibility limit of $C > 0.1$. This does not correlate with the initial calculations that these apertures, where gradients of $4.8\%\mu m^{-1}$ should be more than sufficient to produce visible magnetic contrast.

This led me to question the original assumption that the central diffraction spots are split by $3\mu m$ in real space. Figure 4.17 shows how this value will be proven, where L is the distance between the specimen and objective planes which in the CM20 is $\sim 3mm$, and D is the deflection distance in real space. We know that for a sample of $20nm$ thick Permalloy with a saturation induction of $1T$, $\beta = 1.21 \times 10^{-5} rads$. This results in a spot separation of $\sim 72nm$.

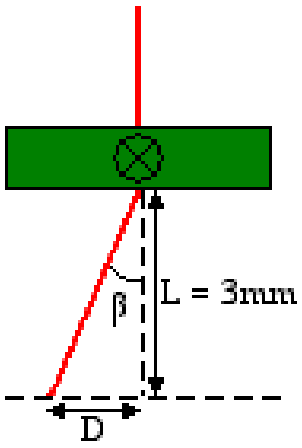

Figure 4.17: Schematic diagram of the proof of real space spot separation in the aperture plane.

4.4.3 Steeper wedges

The erroneous assumption of the $3\mu m$ spot spacing led to incorrectly calculating the aperture gradients required to observe magnetic contrast and the conclusion that steeper aperture wedges were necessary. For this reason new apertures were fabricated utilising the maximum EBD resolution of the FEI Dualbeam instrument, this is limited by the electron probe size and is approximately $20nm$ [13]. The aperture deposition was again set at 40 layers, and the current set at $0.098nA$ but the offset between steps was set at this resolution limit with a 50% overlap; this produced the wedge shown in figure 4.18*a*. Figure 4.18*b* and *c* are SEM, TEM and transmission profiles of two further apertures deposited with slightly larger offsets.

The transmission profiles shown in figure 4.18 illustrate that the transmission gradients are not constant; while this was not intentional it does provide very steep gradients close to the thin edge of the aperture. These apertures were inserted into the objective aperture rod and the subsequent phase gradient images are shown in figure 4.19.

This figure shows a series of images taken as the diffraction spot is scanned across the aperture at the points indicated on the transmission profile shown in figure 4.19*b*. Figure 4.19*c* and *f* are both pseudo-Foucault conditions at the thick and narrow edges

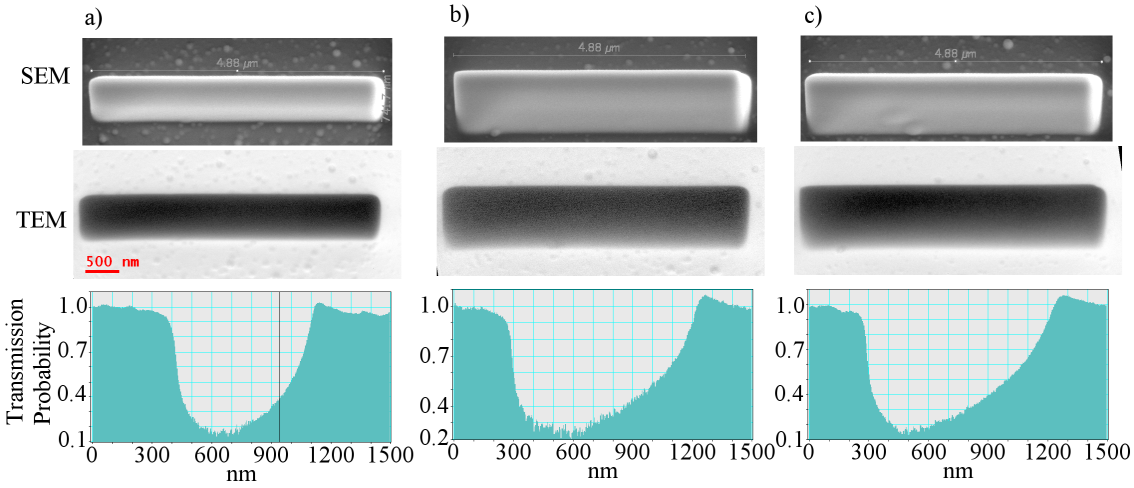

Figure 4.18: SEM, TEM and transmission profiles of narrow apertures.

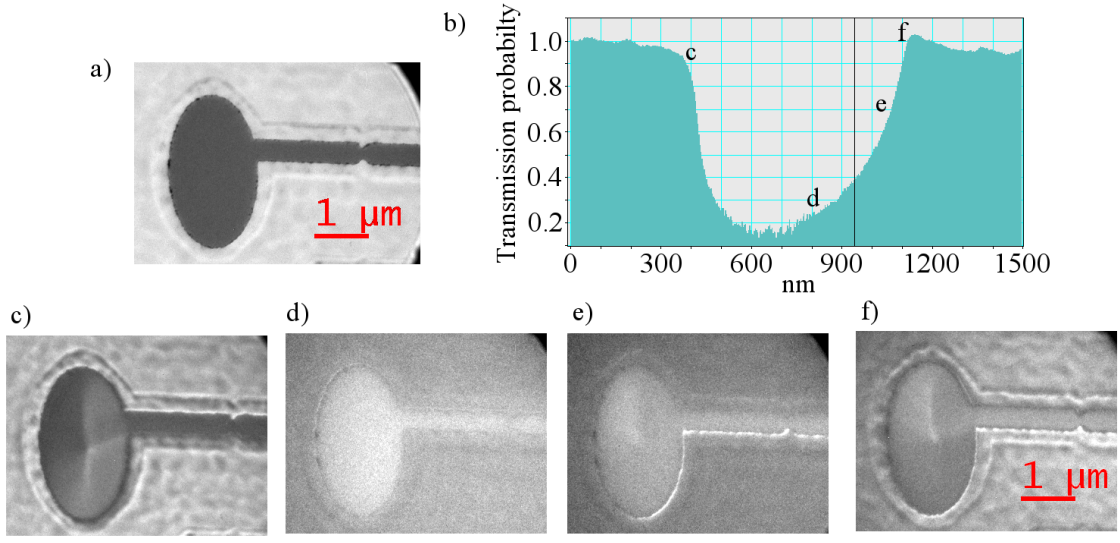

Figure 4.19: (a) In focus image of wire, (b) transmission profile of steeper wedge detailed in 4.18. (c-f) Phase gradient images from four points on the aperture, shown in (b), giving pseudo-Foucault contrast at (c) and (f), no magnetic contrast in (d) and a small amount of visible contrast at (e).

respectively while d and e are taken with the diffraction pattern at different positions within the confines of the aperture. Image e is taken at a higher transmission gradient than at d; it also has a lower value of the central transmission; both of these lead to theoretically higher levels of magnetic contrast and correlates to the images where fig 4.19d shows no magnetic contrast while fig 4.19e has a small visible magnetic contrast within the pad, this is confirmed in figure 4.20 where the intensity profile shows a change in intensity over the top of the pad. This contrast confirms that this imaging technique can produce visible magnetic contrast. However with the current set of wedges this contrast is very small and is only visible for antiparallel domains.

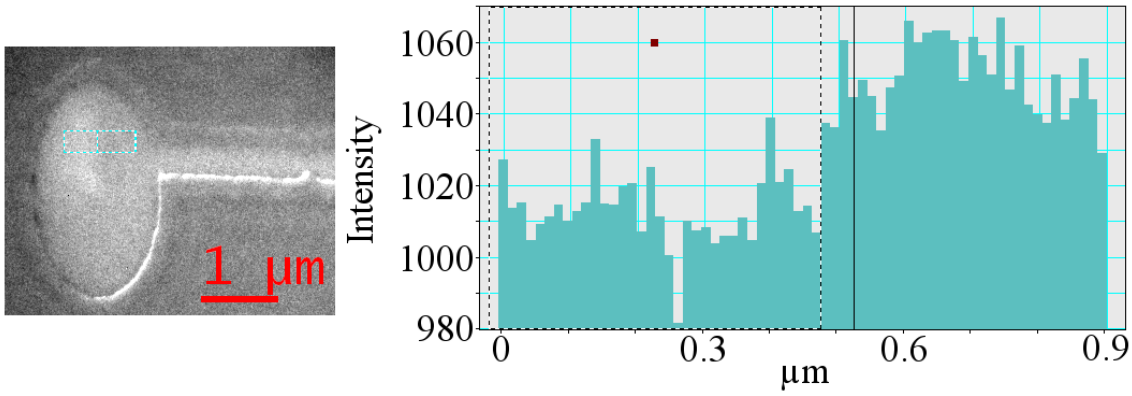

Figure 4.20: Image and line profile of visible magnetic contrast from the steepest point on the steepest wedge: (e) on 4.19.

The transmission gradient (m) and midpoints transmission (c) at point e in figure 4.19 are measured to be $220\%\mu m^{-1}$ and 0.44 respectively. As mentioned in section 4.2, if the image amplitude, transmission gradient and midpoint transmission of the aperture are known, then equation 4.15 can be solved quadratically to give $d\phi/dx$. Equation 4.3 can then in turn be used to calculate the magnetic induction of the sample. The amplitude is calculated by assuming that the in-focus image, shown in 4.19a, is formed of the square of the amplitude with 100% aperture transmission, i.e. $A = \sqrt{(In - focus - image)}$. This along with the values of gradient and midpoint transmission above were used to calculate the magnetic induction from figure 4.20. This is displayed in figure 4.21.

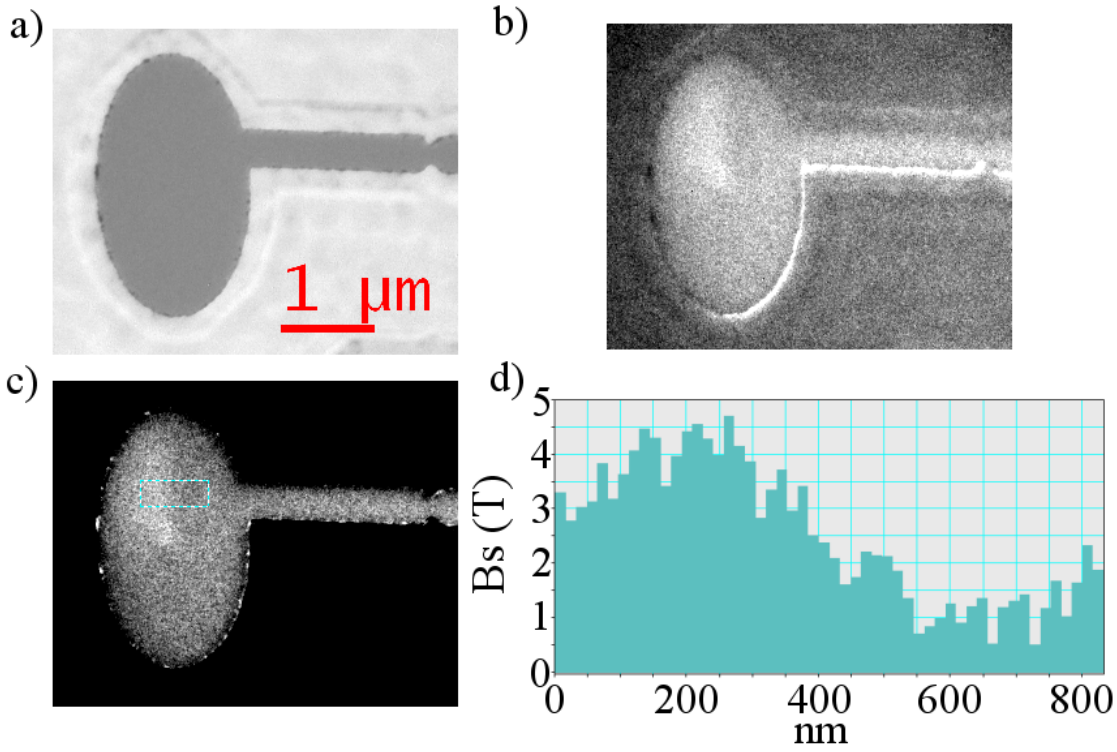

Figure 4.21: (a) In focus, (b) phase gradient image, (c) calculated magnetic induction image and (d) line profile of magnetic induction across top of injection pad.

The quantitative induction difference between opposing domains, displayed in figure 4.21*d*, shows that the induction varies from a spatial average of $3.9T$ to $1.5T$ either side of the domain resulting a difference in induction of $2.4T$. If this were centred about zero, this would correspond to two antiparallel domains of $1.2T$ magnetic induction, this agrees fairly well with the known induction of $1T$ for a sample of $20nm$ thick Permalloy. It is known from simulations that these two domains are 180° to each other and should result in antiparallel inductions of equal magnitude. This offset in the calculated induction, i.e. it not being centred about zero, may be caused by an incorrect measurement of the midpoint transmission, c, resulting in an error in the amplitude value. There are also errors present in the measurement of transmission gradient as this is not consistent across the whole aperture and the exact probe position has been estimated to within $100nm$, in the case discussed above this leads to an estimated error in the gradient measurement of $\pm 50\% \mu m^{-1}$, which in turn leads to an error in the magnetic inducation calculation of $\pm 0.4T$.

This experiment has demonstrated that this technique is capable of producing magnetic contrast with the capacity of extracting quantitative information. However, the levels of contrast are still hampered by the maximum gradient of the wedge aperture. This is limited at this point by the deposition method; gaining higher gradients in the wedges would require thicker, steeper wedges which would be difficult to fabricate using EBD while maintaining the linearity of the transmission profile.

4.4.4 Possible use of selected area aperture

As well as depositing steeper wedge apertures to produce higher magnetic contrast, it may also be possible to place broader apertures in the selected area plane of the microscope rather than the objective aperture plane used above. Figure 4.22 shows an out of scale schematic of how this works. The larger distance between the object and the aperture, changing from 3 to $300mm$ in the CM20, means that the spot splitting will be significantly larger allowing wider apertures to be utilised and preventing the previous problem of producing wedges with sufficient gradient. This

method would require that the back focal plane of the electrons be the same as the selected area plane. This can be accomplished but is complex as it entails both free lens control of all the lenses in the lower column and nonparallel illumination of the sample. The nonparallel illumination means that the electron path changes to focus the diffraction pattern further away from the sample. The free lens control then ensures there is a minimum amount of interference from subsequent lenses before the aperture can perturb the intensity.

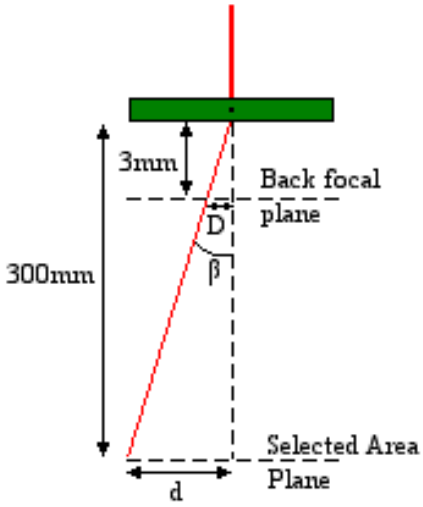

Figure 4.22: Schematic of beam path for use of selected area aperture plane in phase gradient imaging.

The need for free lens control in using the selected area aperture brings new complexities to both the application of this technique and the quantitative calculation of the magnetic induction. The difficulties associated with this potential mode would deter from the main objectives which are to make quantitative magnetic imaging easier in in focus, live imaging modes. As well as this, new microscope technologies such as the JEOL MagTEM microscope recently installed at the University of Glasgow may provide a better solution for the further development of this technique.

4.5 Summary and Conclusion

This imaging technique has been demonstrated to be capable of producing visible quantitative magnetic contrast in in-focus TEM images. This has been severely limited in this study by the transmission gradients of the fabricated apertures. The initial simulations predicted the potential for high levels of magnetic contrast; however due to the overestimation of the spot separation, these levels were not seen experimentally. Despite this, the simulations provided experience in predicting the behaviour of this technique, as well as demonstrating how the images will be affected with varying aperture gradients and transmission levels. The first experiments attempted, with wide wedges, did not produce visible magnetic contrast; however they did show electrostatic contrast in the holey-carbon-film sample, indicating that this technique will work and leading to the discovery of the true real space spot separation. These initial apertures also provided a basis to investigate the deposition technique and how the crystallinity of the deposited platinum varies with the electron current during EBD. This allowed us to optimise the amorphousness of the apertures by minimising the current to $0.098nA$.

After the new spot separation of $72nm$ was calculated, the new set of apertures was deposited at the advised electron current producing wedges with varying gradients up to $250\%\mu m^{-1}$. The phase gradient images from the new set of wedges provided confirmation of pseudo-Foucault contrast gained at the edges of the wedge. Most of the wedge didn't have sufficient gradient to gain visible magnetic contrast, however contrast was seen at the thin end of the wedge where the gradient is close to maximum. This contrast was only just above the visibility limit but was enough to demonstrate a quantitative magnetic induction calculation, assuming equal and opposite magnetic domains, of $1.2 \pm 0.4T$ in a 20nm thick permalloy structure with an expected induction of $1T$. While these induction calculations agreed with the known values in the sample, they had significant errors in both magnitude and offset due to the measurement of the probe position on the aperture. For this technique to be widely viable the wedge apertures must be improved by making them both steeper,

to increase the magnetic contrast, and maintaining the transmission gradient, to minimise errors in the quantitative calculation. While these errors make it unlikely that this technique will be viable without an improved fabrication method, it may have applications in lower contrast systems. Low contrast microscopy techniques, such as environmental TEM, may be improved by using phase gradient apertures to increase relevant contrast.

As well as providing a new method of gaining magnetic contrast, this work compliments the recent work done on generating vortex beams with phase dislocation apertures [14]. These apertures separate the beam with respect to angular momentum, which may be used to extrapolate magnetic information. These new methods could be used in parallel to increase imaging further both of their potentials.

Bibliography

[1] *McVitie S. private communication.*

[2] Egerton R.F. *Electron Energy-Loss Spectroscopy in the Electron Microscope.* Plenum Press.

[3] Kagoshima Y. Shimose K. Koyama T. Wada I. Saikubo A. Hayashi K. Tsusaka Y. and Matsui J. Scanning differential-phase-contrast hard X-ray microscopy with wedge absorber detector. *Jpn. J. Appl. Phys. Part 2 - Lett. Express Lett.*, 43(11A):L1449–L1451, NOV 1 2004.

[4] Mukaide T. Takada K. Watanabe M. Noma T. Iida A. Scanning hard x-ray differential phase contrast imaging with a double wedge absorber. *The Review of scientific instruments*, 80, 2009.

[5] O'Shea K.J. *Putting a leash on the domain wall: A TEM investigation into the controlled behaviour of domain walls in ferromagnetic nanostructures.* PhD thesis, School of Physics and Astronomy, University of Glasgow, 2010.

[6] Johnston A.B. *Investigation of magnetic microstructures using novel transmission electron microscopy techniques.* PhD thesis, School of Physics and Astronomy, University of Glasgow, 1995.

[7] Chapman J.N. Johnston A.B. Heyderman L.J. McVitie S. Nicholson W.A.P. and Bormans B. Coherent Magnetic Imaging by TEM. *IEEE Trans. Magn.*, 30(6, Part 1):4479–4484, NOV 1994.

[8] Chapman J.N. Johnston A.B. Heyderman L.J. Coherent Foucault Imaging - A method for imaging magnetic domain structures in thin films. *J. Appl. Phys.*, 76(9):5349–5355, NOV 1 1994.

[9] FEI. *Nova 200 Nanolab product data sheet.*

[10] Liao Z.M. Xun J. and Yu D.P. Electron transport in an array of platinum quantum dots. *Phys. Lett. A*, 345(4-6):386–390, OCT 3 2005.

[11] Rotkina L. Oh S. Eckstein J.N. and Rotkin S.V. Logarithmic behavior of the conductivity of electron-beam deposited granular Pt/C nanowires. *Phys. Rev. B*, 72(23), DEC 2005.

[12] Shimojo M. Takeguchi M. Mitsuishi K. Tanaka M. and Furuya K. Formation of nanoscale platinum and iron oxide structures using electron beam induced deposition techniques. volume 100 of *Journal of Physics Conference Series.* Swedish Vacuum Soc, 2008. 17th International Vacuum Congress/13th International Conference on Surface Science/Internatinal Conference on Nanoscience and Technology, Stockholm, SWEDEN, JUL 02-06, 2007.

[13] FEI. *Nova 200 Platinum deposition technical note.*

[14] Verbeeck J. Tian H. and Schattschneider P. Production and application of electron vortex beams. *Nature*, 467, May 2010.

Chapter 5

Temporal deflection Imaging

5.1 Introduction

Gaining temporal resolution within fast dynamic processes is difficult within a TEM as magnetic processes at the nanoscale tend to occur on the tens of nanosecond time scale, as determined by the alpha parameter and the exchange stiffness. The most prevalent factor currently limiting this resolution is the minimum detector exposure time. This time defines the shortest time frame that the detector can reliably image without distortion; however images on these time frames are typically limited in electron counts. This means that even if the detector exposures could be shortened to the timescale of magnetic processes, then conventional electron sources are still going to limit the number counts, and therefore the visibility of any potential feature. In the case of the Schottky FEG used in the Philips CM20, the source produces between 0.1 and $1nA$ of electron current. This equates to between 624 and 6240 electrons per microsecond or approximately one per nanosecond. For TEMs with conventional electron gun sources, there is a practical limit of temporal resolution, based on the number of electrons hitting the detector, of $\sim 1ms$. However, magnetic behaviour typically acts at time scales well below this, leading to a need for new imaging techniques that can combine both high spatial and high temporal resolution[1, 2].

Time resolved magnetic imaging within TEMs has been investigated throughout the last four decades. Over this time, two main methodologies for gaining this

resolution have appeared: single shot [2, 3, 4, 5] and multi shot [2, 6, 7, 8] imaging. Which method is chosen is dependent on the process being imaged.

If the process is unique and irreversible then the single shot approach is required [9]. This process, first established by Bostanjoglo et.al. in the 1980s, is where the fast process is imaged once with a single exposure of high intensity electrons [4, 10, 6]. As with most TEM studies, the defining factor of whether this imaging technique is viable is the signal to noise ratio. An example of single shot imaging was performed by LaGrange *et.al.* in which a $15ns$ exposure required an electron pulse containing $10^7 - 10^9$ electrons [2]. Gaining this level of electron current requires modification to the electron gun and is the largest problem currently facing single shot time resolved TEM. One such microscope currently capable of utilising single shot imaging is built at the Lawrence Livermore National Laboratory (LLNL); a modified JEOL 2000FX. In this microscope, a $12ns$, $211nm$ laser pulse is directed towards a $825\mu m$ Ta disk photocathode, producing a $15ns$ pulse of $3 - 4 \times 10^7$ electrons, these high currents make single shot imaging viable [11, 12, 6]. One of the main limiting factors of these high current electron pulses is the electron-electron interaction, known as the Boersch interaction, within the imaging lens system, which limits the spatial resolution of the system [9, 6, 12].

While the single shot imaging is required when imaging irreversible processes, if the process is reversible then multi shot, stroboscopic techniques can be utilised, meaning that lower electron intensities can be used [13, 8]. This technique was first developed in the 1970s by using beam blanking to produce stroboscopic images [7]; more recently high current density electron guns and faster, digital image acquisition have allowed for the development of these techniques to image highly reversible processes [8]. These newer techniques use femtosecond laser pulses to produces electrons in a similar way as in single shot imaging. However the power and duration of the laser pulses are tuned to produce only single electron pulses and time these pulses with respect to the sample process. These single electron images are then summed over millions of iterations to produce a series of images of the process. The ability to

image these processes with iterated single electron exposures means that the problem of electron-electron interaction is no longer present allowing the microscope to run at optimal conditions for both temporal and spatial resolution [2, 6].

Outside the field of electron microscopy, as well as single shot and stroboscopic techniques, temporal resolution can be achieved using streak imaging. This method has been most commonly used in x-ray detectors which use specifically engineered streak cameras to deflect the x-rays across the camera with respect to time [14, 15, 16, 17]. Figure 5.1 shows one such camera used by Chollet et.al. [14]; in this device, the x-rays hit a photocathode, producing photo-electrons, these are then accelerated by an electric field towards the slit. As the photo-electrons pass between the deflection plates, they are swept by a fast voltage ramp, deflecting the beam and converting temporal information into spatial information; the magnetic lens is then used to focus the electrons onto the CCD [14]. These cameras are used extensively in x-ray systems and synchrotrons and have been proven to reach temporal resolutions as high as $280fs$ [18, 19, 20].

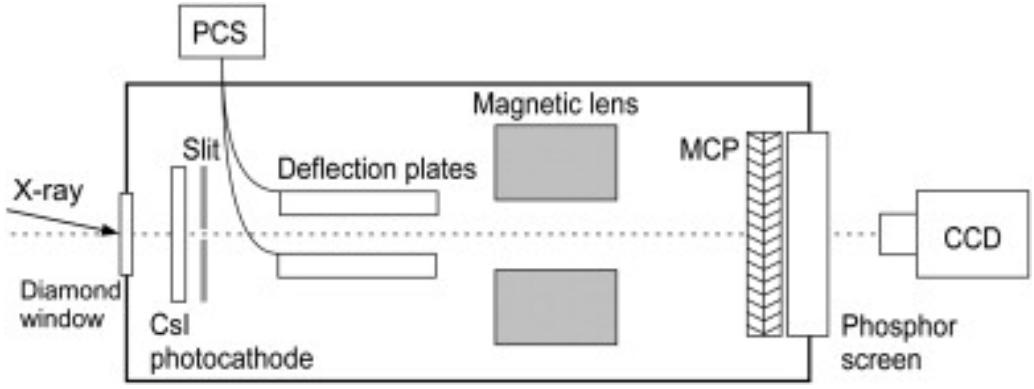

Figure 5.1: Schematic of X-ray streak camera detector [14].

In this chapter I describe the development of a streak imaging technique to extract temporal resolution from magnetic processes within transmission electron microscopes. The strategy taken was to investigate what might be possible by using alternative detector technologies to those commonly used in TEMs. Medipix direct radiation detectors were utilised to reduce the acquisition time of each single ex-

posure [21]. The aim of this technique is to combine the short exposure times of the Medipix detector with the streak imaging technique to increase the temporal resolution beyond the minimum camera acquisition times without significantly modifying the microscope. This will use a bifilar TEM rod, explained in section 5.2.1, to simultaneously induce magnetic behaviour within the sample and deflect the electron beam across the detector. This method will be used to image the domain wall injection into Permalloy nanowires.

This technique will be developed throughout this chapter with the theory and source of deflection discussed first, including the effect this has on the intensity at both the image and diffraction planes. In section 5.2.3, the process that will be studied is discussed; the injection into a domain wall will be simulated and predicted streak images generated. The methods of sample preparation and image synchronisation will then be introduced before the experimental results from Fresnel mode images are first discussed in 5.3.3. The use of Foucault contrast along with a more detailed discussion of the sources of noise and unwanted intensity will then be examined. Finally the use streak imaging in low angle diffraction mode will be discussed.

5.2 Theory of Temporal Deflection Imaging

There are two main parts to streak imaging: deflecting the electron beam, after the sample, in a controlled and predictable way with respect to time, and capturing that deflection on a single exposure image. This steak image will be integrally captured and summed to form a final intensity streak. The latter of these requires both a high speed camera and the ability to synchronise the camera acquisition with both the image deflection and the magnetic process occurring within the sample. The synchronisation method between the magnetic process and the detector exposure will be developed experimentally in 5.3.2. The control of the deflected beam will allow temporal resolution to be extracted from the image. Ideally, the deflection will be linearly proportional with respect to time, creating a linear temporal streak. The source of this deflection along with preliminary experiments guiding the shape and

magnitude of this deflection will be further discussed in section 5.2.3.

One of the main aims of this method is to investigate what limit of temporal resolution may be achieved without modifying the microscope. Similarly to the stroboscopic techniques described above, the Schottky field emission gun utilised in the CM20 produces an insufficient electron current to form an image on the sub-microsecond timescale with a single exposure. Therefore this method will be performed stroboscopically, summing multiple exposures. This constraint requires that the process being imaged be repeatable and reversible. The magnetic contrast for this technique will be gained through both Fresnel and Foucault imaging, described in chapter 3. The relative magnetic image contrast between these two techniques will be compared both theoretically and experimentally to maximise the magnetic signal within the streak.

5.2.1 Bifilar Rod

The bifilar rod is a TEM sample holder, designed and built at the University of Glasgow, which produces pulsed magnetic fields across the sample. The rod consists of two parallel gold wires of $100\mu m$ diameter, positioned slightly below the sample. An identical current is passed through both wires producing a cylindrically symmetric magnetic field around each wire, as shown in figure 5.2. This shows that above the wires there is a net field from left to right, and below from right to left. The sample sits above the wires, in this field.

The main advantage of this rod is its use of currents to create fields. This allows for fast, pulsed fields to be produced using current pulse boxes. Pulses up to $100A$ may be generated, producing fields of up to $1kOe$. This box is limited to pulse times ranging from $100ns - 5\mu s$ depending on the duty cycle of the pulses. These fast field pulses have been used at Glasgow to inject and manipulate domain walls, as well as investigating propagation field, pinning points of samples and domain wall velocities in variety of magnetic structures and materials [22].

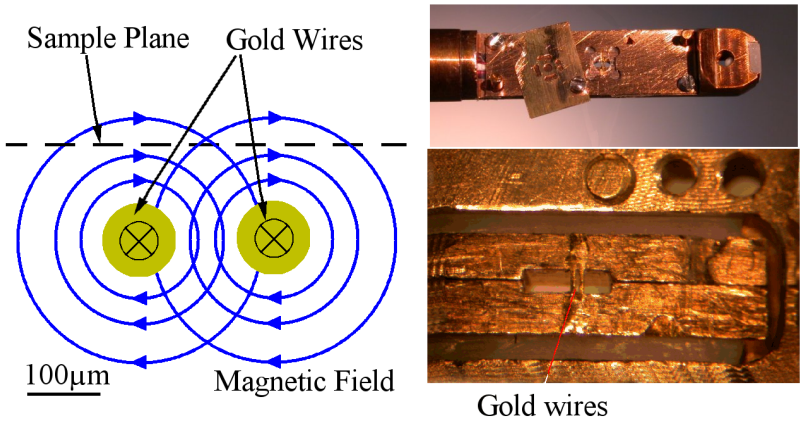

Figure 5.2: Cross sectional schematic of bifilar TEM rod showing surrounding magnetic fields and accompanying photos of the rod.

5.2.2 Image Deflection

The aim of this study is to use the bifilar rod to deflect the electron beam with respect to time. However, any theoretical deflection of the beam by the field at the sample plane will be cancelled by the opposite field below the current carrying wires, producing no net deflection. Figure 5.3 shows one second exposure, in focus images of a straight $300nm$ wide notched wire as a pulsed magnetic field is applied with a 50% duty cycle. In this series of images, the applied pulsed field is $0Oe$ in 5.3a, rising to 200, 400 and $600Oe$ in b, c and d respectively.

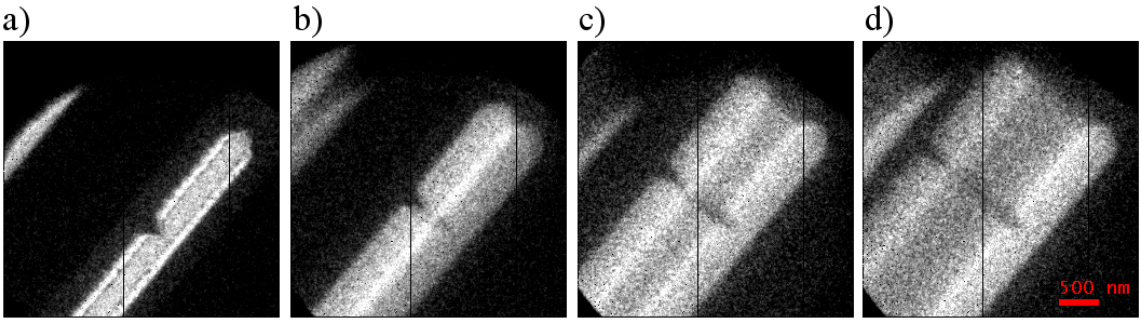

Figure 5.3: Series of Medipix images showing image deflection at (a) $0Oe$, (b) $200Oe$, (c) $400Oe$ and (d) $600Oe$ pulsed magnetic fields, showing a deflection proportional to the applied field of $\sim 2.2nmOe^{-1}$.

These figures demonstrate that, contrary to theory, the image is deflected by the field in the bifilar rod and that this deflection is proportional to the applied field.

Figure 5.4 shows an optical microscope image of the parallel gold wires in the bifilar rod; this shows that the wires are not consistent in either width or direction. These defects in the construction will cause a variation in the field and are most likely the source of the beam deflection. While the image deflection is always proportional to the field, the magnitude of the deflection was dependent on the sample position within the rod. For this reason the deflection magnitude had to be calibrated each time the sample was loaded into the rod.

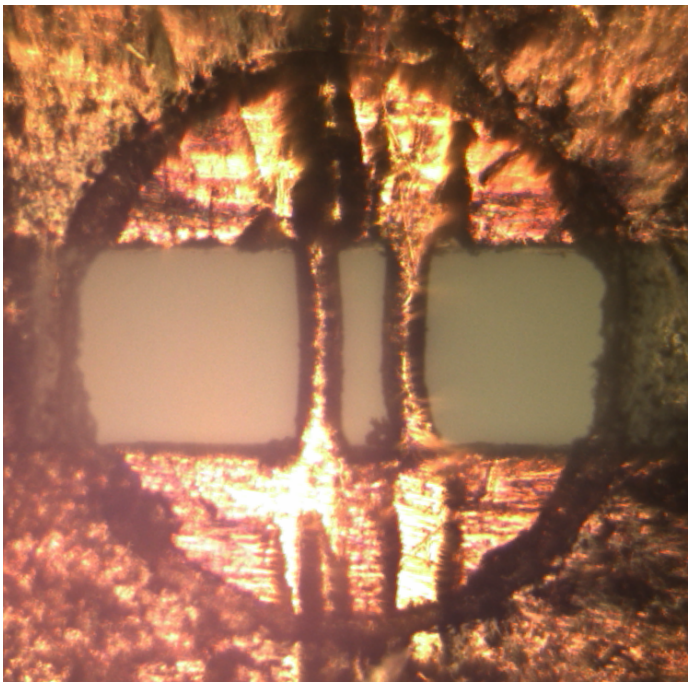

Figure 5.4: Optical microscope image of bifilar rod wires, showing the two parallel $100\mu m$ diameter gold wires with a $100\mu m$ gap.

The proportionality between the applied current and the image deflection means that the deflection of the beam, and subsequently the speed and magnitude of the image streak, will be controlled by increasing the current in the gold wires linearly with respect to time.

To fully understand this technique, the deflection of the beam within the TEM must be understood with respect to both the image and the back focal planes. Figure 5.5 shows a schematic diagram of the electron beam path within a TEM. This

illustrates how the beam passing down the column is affected by the field pulse. The electron path is deflected just below the sample plane; this deflection tilts the existing electron trajectories, displacing both the central diffraction spot and the final image.

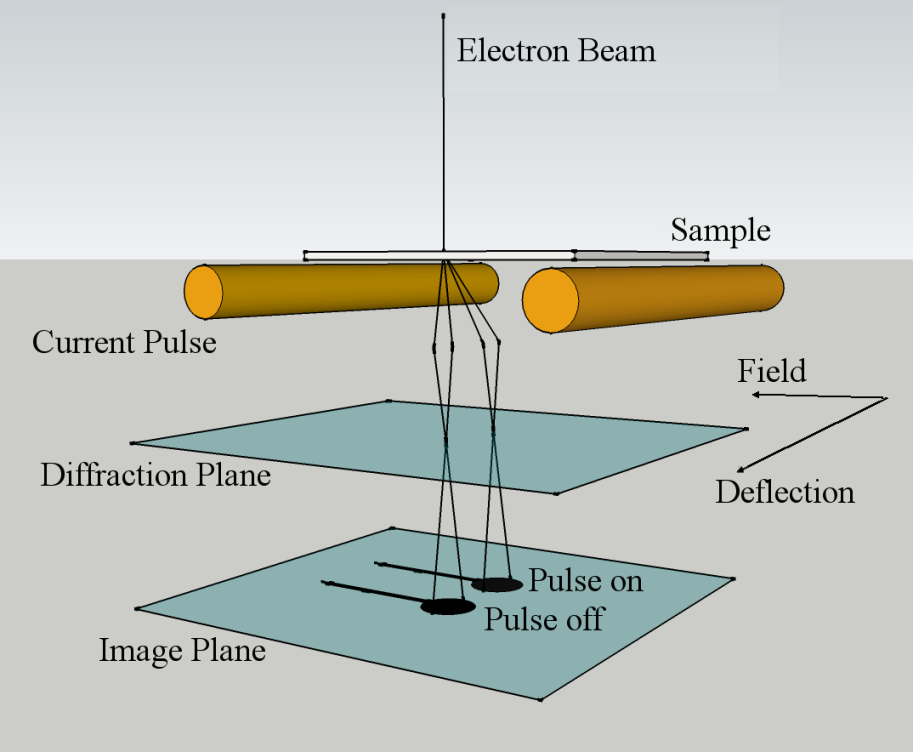

Figure 5.5: Schematic diagram of electron beam path with the pulse on and off, showing the effect of the beam deflection on the image and diffraction planes.

Figure 5.6a shows the deflection of the diffraction pattern at a camera length of 39m and a pulse height of $5Oe$. We know that the deflection is proportional to the applied field and can therefore calculate the deflection gradient on the back focal plane to be $9\mu m^{-1}Oe^{-1}$. Figure 5.6b then shows the deflection induced by a $40Oe$ field relative to the largest objective aperture. This demonstrates that the deflection of the pattern is on the same order of magnitude as the curvature of the $100\mu m$ circular aperture; this magnitude was important for the application of magnetic contrast imaging.

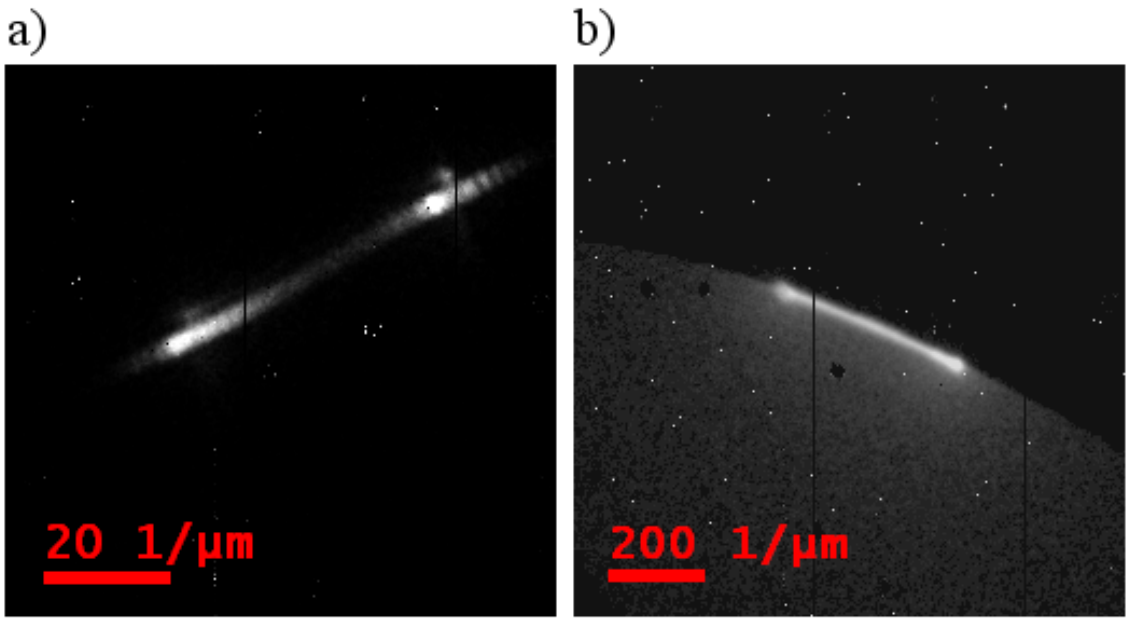

Figure 5.6: (a) Calibration image of beam deflection in the back focal plane for a $5Oe$ pulse at $39m$ camera length and (b) a $40Oe$ pulse shown relative to the curvature of a $100\mu m$ objective aperture.

5.2.3 Domain Wall Injection

To develop this imaging method, the injection of a magnetic domain wall into a 300nm wide permalloy nanowire from an elliptically shaped pad was investigated. This process, shown in figure 5.7, was chosen as it fulfils the criteria, based on quasi-static observations, of being highly repeatable and reversible [23]. The nanowire structures are also near-one-dimensional objects which respond to fields along their major axes. When applied by the bifilar rod, these fields produce image deflection perpendicular to the wires, making them ideal structures for the development of this imaging process.

The wire is first saturated along its axis with the application of a high magnetic field, typically several hundred Oersted, and then reduced to remanence producing the single domain state shown experimentally and in simulation in 5.7a and d respectively. This shows that while the wire is in a single domain state, the pad forms a vortex flux closure state. An injection field is then applied in the opposite direction to the saturation direction; the vortex is displaced within the pad. As the vortex

passes below the axis of the nanowire the magnetisation of the wire reverses injecting a domain wall which is then pinned at the notch. Figures 5.7*b* and *e* show static images and simulations of the injected DW state. The domain wall is pinned at the notch in the wire. If the field is increased further the wall is depinned from this state reversing the rest of the wire, shown in 5.7*c*. With the DW pinned at the notch, then the field can be reversed, forcing the wall back into the pad and reforming the original magnetic state seen in 5.7*a*; this way the injection process is both reversible and repeatable. The offset of the wire to the pad allows the chirality of the injected DW to be predicted to be the same as in the pad vortex for 90% of injected walls [23].

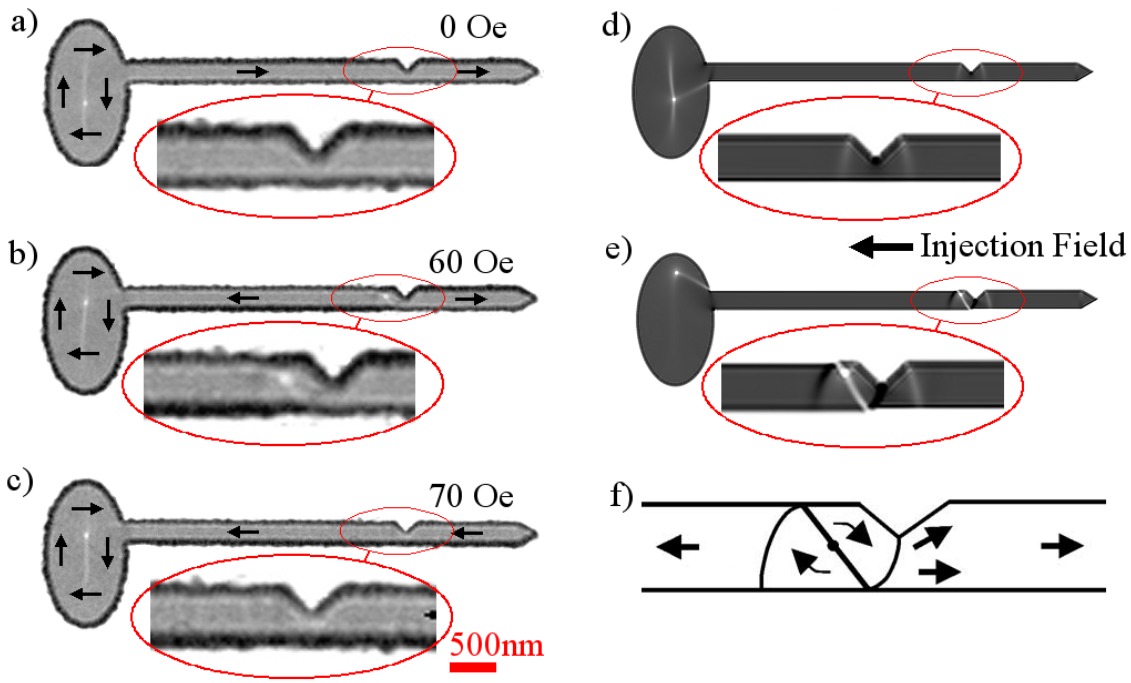

Figure 5.7: Fresnel images and simulations of DW injection and pinning at notch showing both saturation states (a,c,d) and the DW pinned state (b,e) of a 300nm wide nanowire in 20nm thick permalloy.

Simulations

Magnetic modelling is an essential part of the technique development, the injection process and the predicted LTEM images will be computationally simulated to allow for the resultant theoretical intensity streaks to be created. The simulation

of the injection process was performed using OOMMF (object oriented micromagnetic framework) software. The simulations in this study were set up to give output magnetic structures as an applied field is increased incrementally throughout the injection process. These simulations will then be used to create simulated Fresnel and Foucault images of each step, which in turn will generate simulated streak images. This section will outline the process of this simulation and display and discuss the results. The magnetic contrast levels within the streak will be essential for this process to be viable, therefore the difference in contrast between Fresnel and Foucault imaging will be investigated. How the predicted contrast changes with the length and speed of the streak will also be examined along with the effect of increasing the number of iterations. This information will be needed to effectively tune and implement this process experimentally.

To accurately predict the resultant image streaks, first they must be generated from the simulations. The object to be imaged is a $300nm$ wide permalloy nanowire with an elliptical injection pad. OOMMF was used to simulate the injection with the field ramped linearly between 0 and $150Oe$ over $1.5\mu s$, in time resolved steps of $0.01\mu s$. Each step was defined in the simulation by the time restraint of $0.01\mu s$ and not by the value of $\frac{d\mathbf{M}}{dt}$ as used commonly. At each step the field is increased proportionally to the desired ramp, and the magnetisation is relaxed for a simulated time of $0.01\mu s$, the resultant structure is saved before the field is increased for the next step. These simulations used input material properties of saturation induction $B_s = 1.08T$, exchange stiffness $A = 13 \times 10^{-12} J/m$ and zero magnetocrystalline anisotropy, as well as a damping parameter from the Landau-Lifshitz-Gilbert equation $\alpha = 0.5$. This is a default value approximately an order of magnitude higher than the real value for permalloy, this was chosen as it allows for the solver to converge the magnetisation in a reasonable simulation time and showed us an accurate picture of the injection mechanism [24].

Once the simulation is complete the OOMMF files are split into M_x, M_y and M_z components and imported into Digital Micrograph™which is then used to generate

the predicted Fresnel and Foucault contrast images. Figure 5.8 shows OOMMF, Fresnel and Foucault images of the wire in identical states showing how these imaging processes relate to each other.

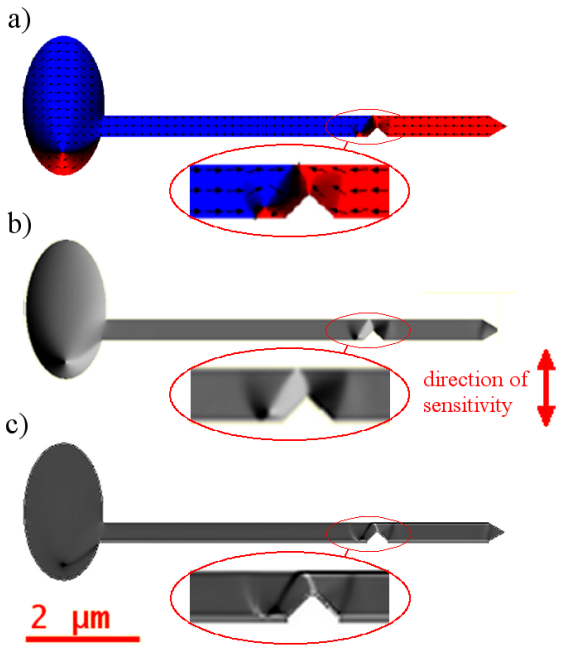

Figure 5.8: (a)OOMMF,(b) Fresnel and (c)Foucault images of the magnetic structure in 300nm wide 20nm thick permalloy nanowire, showing pad vortex and vortex domain wall at the notch.

The injection process was first simulated between 0 and 150Oe. Figure 5.9 shows Fresnel images of these states as well as a series of intermediate states displaying the process of domain wall injection from the pad to the notch. This shows that between 0 and 60Oe the vortex within the pad moves with the field but the magnetisation within the wire changes very little. For this reason subsequent simulations and simulated streaks were only run from 60Oe upwards to save on computational time. Figure 5.10 shows the simulated foucault contrast of the same states with both directions of sensitivity. If Foucault imaging is to be used in this study the sensitivity perpendicular to the wire, shown on the left of figure 5.10, will have to be used due to the deflection of the beam in the diffraction plane, this will be further discussed in section 5.3.

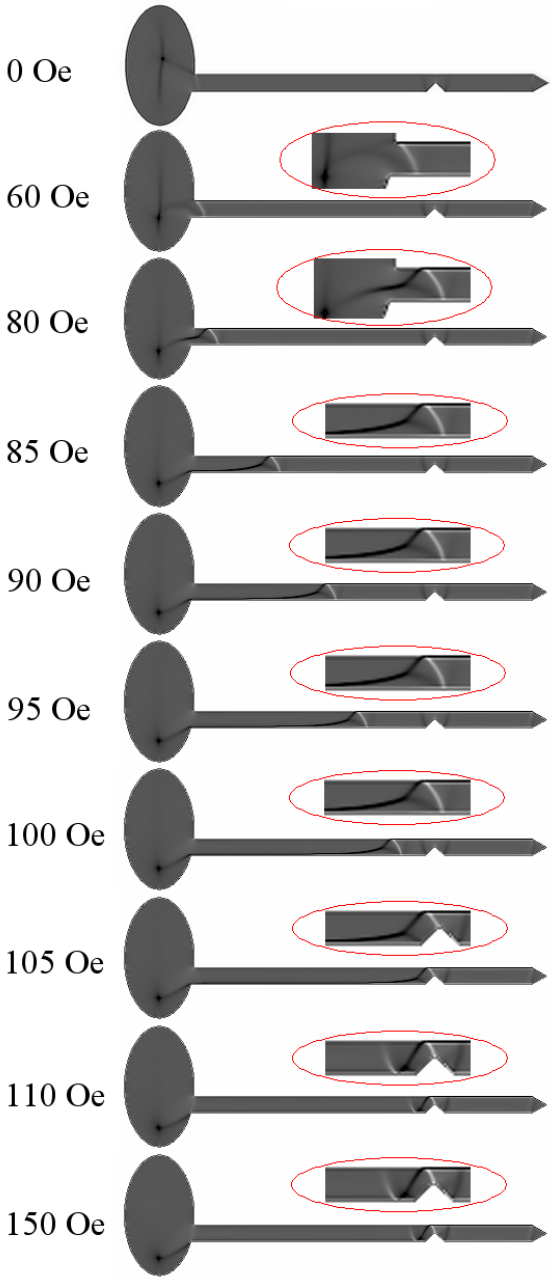

Figure 5.9: Simulated series of Fresnel images showing various stages of domain wall injection in a $300nm$ wide $20nm$ thick permalloy nanowire as the externally applied field is increased form remanence to $150Oe$.

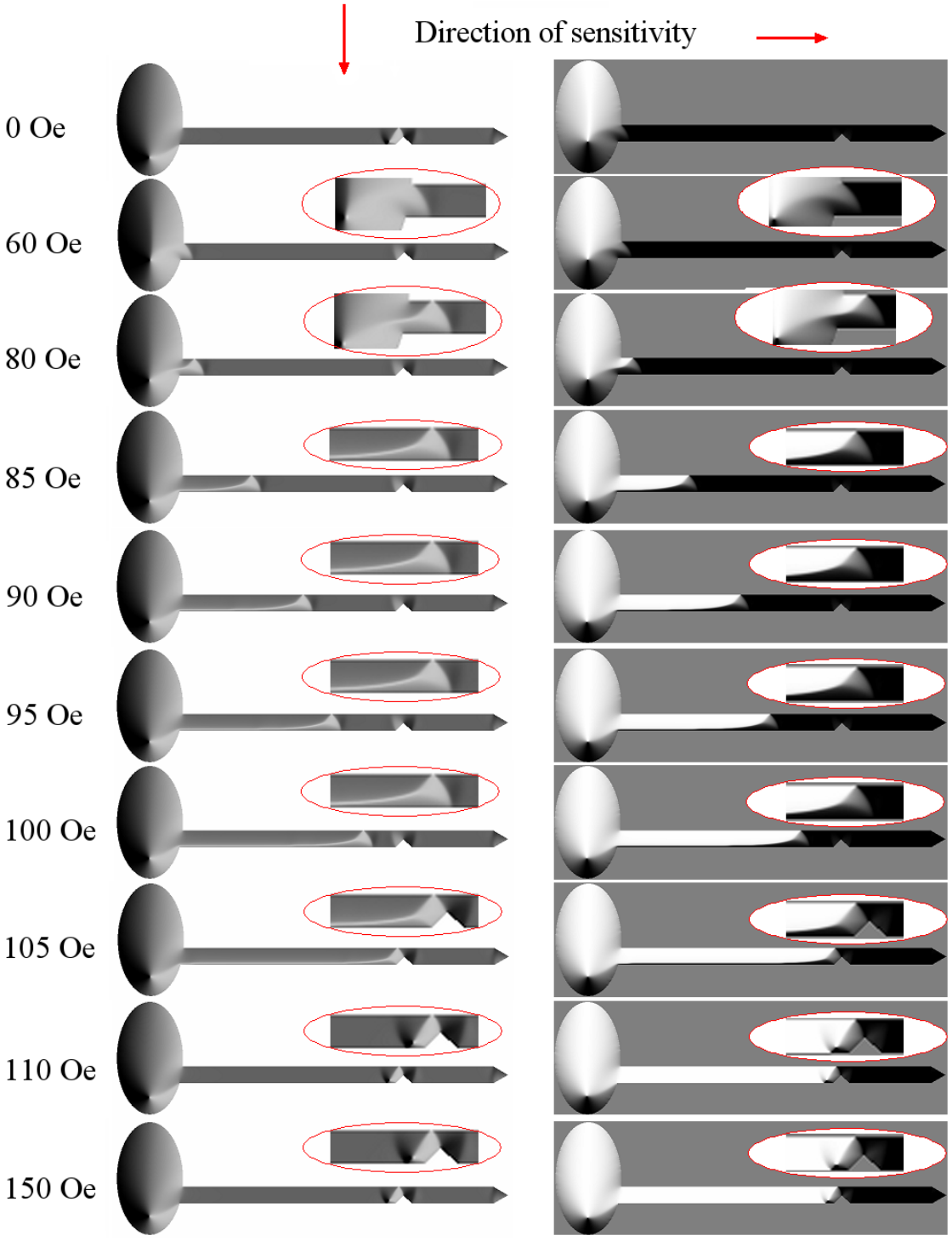

Figure 5.10: Simulated series of Foucault images showing various stages of domain wall injection in a 300nm wide 20nm thick permalloy nanowire as the externally applied field is increased form remanence to 150Oe with directions of sensitivity parallel and perpendicular to the wire axis.

Simulations of streak images were generating by displacing the static images, shown in 5.9 and 5.10, with respect to their relative time within the injection process. The magnitude of this deflection was chosen to be $100nm$ per image, as this agrees with the approximate width of the experimental streak; this also maximises the width of the simulated streak and therefore the simulated visibility of any changes in magnetic contrast whilst maintaining the appearance of a streak.

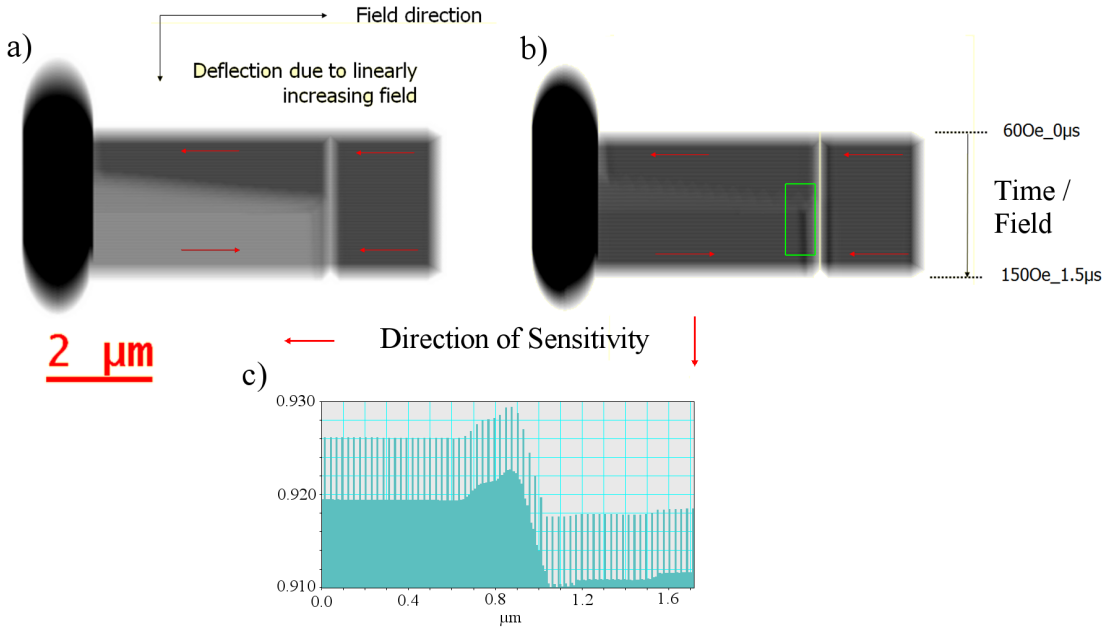

Figure 5.11: Theoretically streaked simulated foucault images between 60 and $150Oe$ with the accompanying intensity line profile of over the green region shown.

Two streaks are shown in figure 5.11, these are the Foucault contrast streak with directions of sensitivity both parallel and perpendicular to the wire along with an intensity line profile of the perpendicularly sensitive streak. Comparing these images to the static ones shown in 5.10 shows that the magnetic contrast is significantly reduced within the streak. The image deflection diminishes the contrast of the domain wall due to the averaging operation inherent in the streak. The large number of counts in the wire and background compared to small variation within the wall means that when the image is streaked, the relative intensity, and therefore the contrast, of the wall is reduced. The systematic spikes in the intensity shown in 5.11c

are an artefact of the discrete image displacements used to simulate the streaks.

These simulations also provide the opportunity to predict the expected levels of magnetic contrast within both static and streaked images. This contrast is defined by equation 5.1, where C is the contrast, and I_{max} and I_{min} are the maximum and minimum intensities of the domain wall contrast feature respectively and I_{mean} is the mean intensity within the DW feature. As discussed in chapter 3, we can expect the noise in the Medipix images to be dominated by statistical shot noise. Shot noise obeys Poisson statistics and is therefore equal to the standard deviation of the signal, σ, which is equal to the square root of the mean intensity, I_{mean}.

$$C = \frac{I_{max} - I_{min}}{I_{mean}} \tag{5.1}$$

A feature was defined as observable to the human eye if $C > 0.02$. This ratio, between the signal of the domain wall feature and the background intensity, effectively describes the observability of any structure in the image. As well as this a structure will only be visible if the signal is significantly larger than the image noise, i.e. $I_{max} - I_{min} >> \sqrt{(I_{mean})}$. Equation 5.1 was applied to the static images shown in figures 5.9 and 5.10 as well as the streak images in 5.11 and their Fresnel equivalents. This led to a contrast, C, of 0.34 in the static Fresnel and 0.60 in the static Foucault images; these get reduced through the averaging process of the simulated streak to 0.006 and 0.010 respectively.

While these calculations show that both the Fresnel and Foucault streaks produce theoretically unobservable magnetic contrast, i.e. $C < 0.02$, the Foucault signal is significantly higher. This leads to the conclusion that Foucault imaging is a better prospect for observing magnetic contrast experimentally, however for these magnetic features to be visible, the counts will need to be increased sufficiently for $I_{max} - I_{min} >> \sqrt{(I_{mean})}$.

5.3 Magnetic streak imaging

5.3.1 Sample Preparation

The nanowire and injection pad structures were milled into 20nm thick continuous Permalloy ($Fe_{20}Ni_{80}$) films. They were fabricated using focussed ion beam lithography (FIB), discussed in chapter 2. Figure 5.12*a* and *b* show SEM and TEM images of these structures respectively. As well as the defined structure, the TEM image shows that the intensity of the image increases significantly in the milled area. This is expected as the Permalloy in this area has been removed. However the line profile of 5.12*b* demonstrates that the intensity in this area is not consistent; the ion etching proceeds along some crystallographic directions faster than others. In the polycrystalline Permalloy film this means that some grains get milled away before others leaving an uneven surface when the milling reaches the membrane. This variation in intensity will produce unwanted contrast within the streak image which will be superimposed on any magnetic contrast changes, reducing the probability of it being observable.

For this reason electron beam deposition, outlined in chapter 2, was used to deposit a $200nm$ thick layer of platinum surrounding the nanostructure. This platinum serves a dual purpose. Firstly it fills the FIB milled area, removing the inconsistencies. It also reduces the surrounding TEM image intensity to near opacity. This decrease in background intensity increases the relative intensity, and therefore the contrast, of the desired magnetic information within the streak. Figures 5.12*c* and *d* show SEM and TEM images of this platinum deposition. Once these first samples were deposited, it quickly became apparent that the deposition area was too small and the image was streaked beyond the area of reduced intensity. Therefore the deposition area was increased to that shown in figures 5.12*e* and f. The intensity profile attached to 5.12f shows how the platinum deposition has reduced the intensity surrounding the wire to less than 20% of the wire itself.

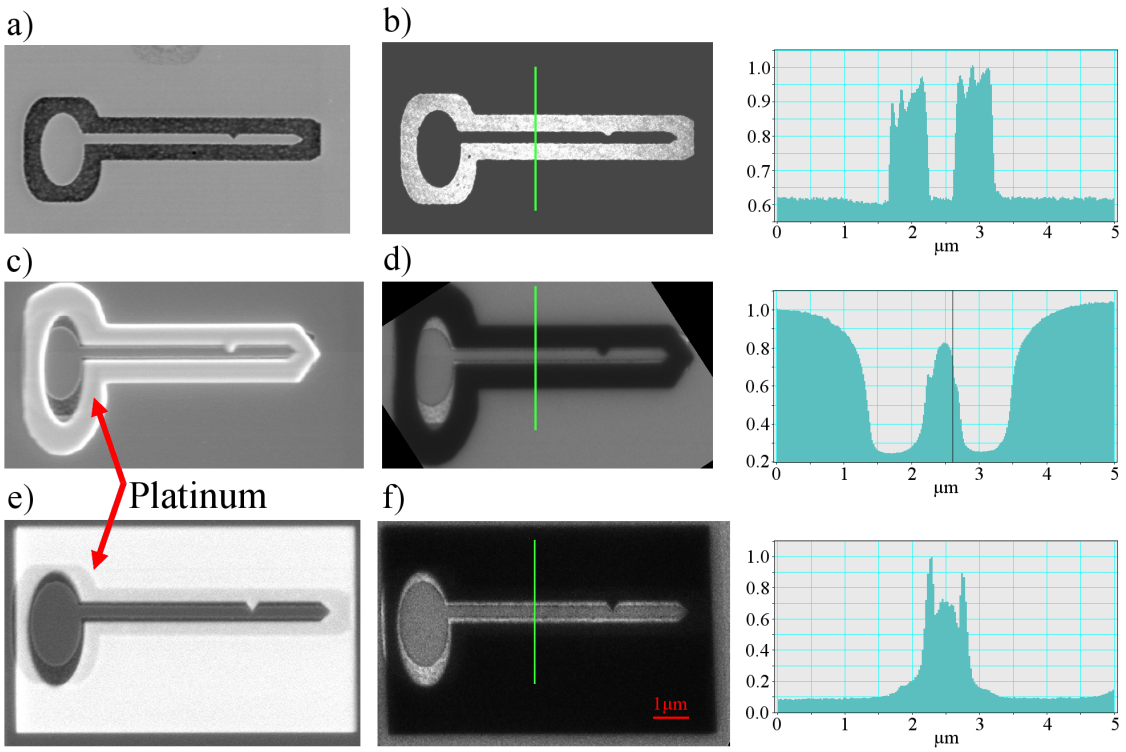

Figure 5.12: SEM (a,c,e) and TEM (b,d,f) images of FIB milled nanowire and surround platinum deposition steps along with normalised intensity profiles from the areas displayed on the TEM images. Succesive images show (a+b) original milled nanowire, (c+d) initial platinum deposition and (e+f) wider deposition to cover whole streak.

5.3.2 Exposure Synchronisation

Synchronisation of the image acquisition and the magnetic field pulse was achieved through voltage pulses supplied by a series of current pulse boxes (figure 5.13). The Hewlett Packard $150MHz$ $8110A$ pulse generator is the master timing box, this starts the imaging process by producing two $0.5\mu s$, $4V$ pulses. The first of these pulses, channel 1, triggers a single square pulse from the Agilent $15MHz$ $33120A$ waveform generator. The rising and falling edges of this pulse triggers the injection and reversal pulses respectively from the $100A$ pulser supply (figure 5.14). The injection and reversal pulses cannot be directly triggered by the HP $150MHz$ pulse generator because the rising and falling edges are not large enough to trigger the $100A$ pulser supply directly; the trigger pulse is also too short to separate the injection and reversal pulses sufficiently to image the injection. The delay between the edges of the trigger and the injection pulses, shown in blue and red in figure 5.14 respectively, are an effect of the capacitors used and are experimentally consistent. The frequency of the square pulse from the Agilent 15MHz waveform generator is set at $27MHz$ as this is well beyond the expected exposure times but fast enough to reverse the wire back to its original state before the next pulse.

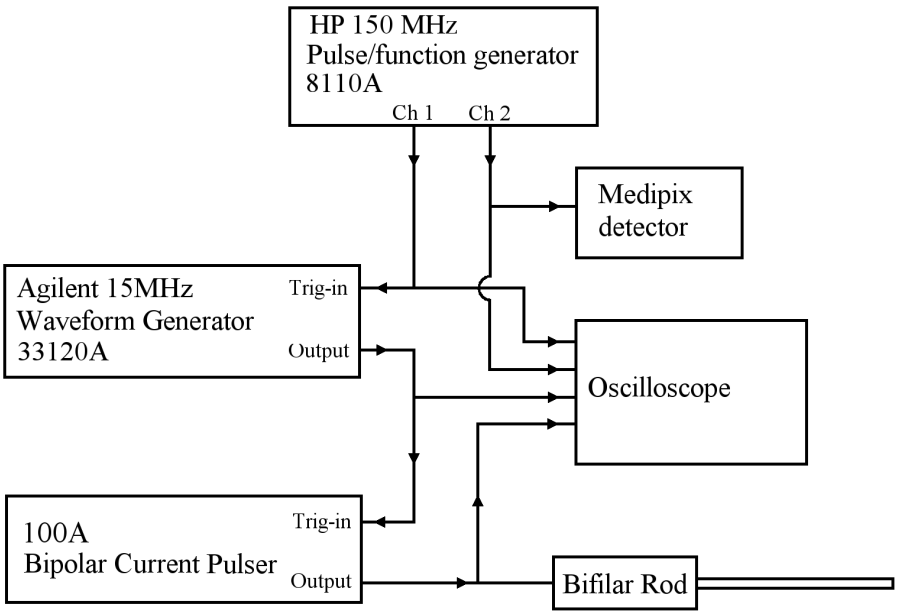

Figure 5.13: Schematic diagram of experimental setup during pulse acquisition.

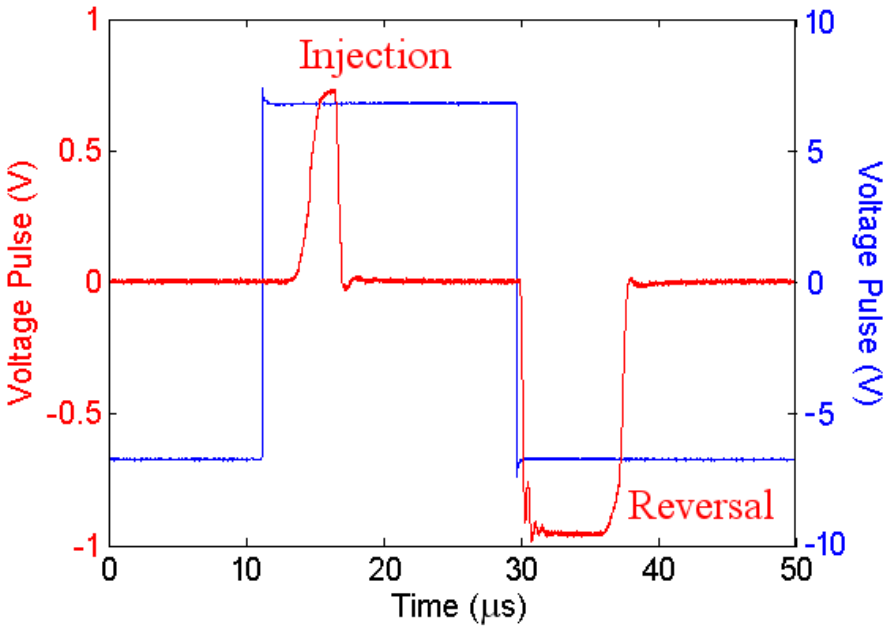

Figure 5.14: Voltage profile of square trigger pulse from the Agilent $15MHz$ $33120A$ waveform generator(blue) and injection and reversal pulses from the $100A$ pulser supply (red).

The second pulse from the HP $150MHz$ pulse generator, channel 2, is connected to the Medipix detector. The rising edge of this pulse triggers the start of the detector exposure. Figure 5.15 shows how this is timed respective to the other trigger pulses. The important factor here is that the delay between the major start pulse and the injection pulse in the bifilar rod (shown in blue and black respectively in fig 5.15) is fixed by the hardware. However the delay between the first and second pulses from the HP $150MHz$ pulse generator can be altered on the nanosecond scale to control the detector exposure start point. This way, the camera exposure can be synchronised to the injection.

The injection pulse applied through the bifilar rod, shown in black in figure 5.15, comes from the $100A$ pulser supply. This box has a maximum pulse length of $5\mu s$ and figure 5.16 shows a series of these pulses of varying maximum voltage. This rod has been previously calibrated and is known to produce a field of $10Oe$ at the sample per $100mV$. Therefore the voltage ramps shown in figure 5.16 produce fields at the

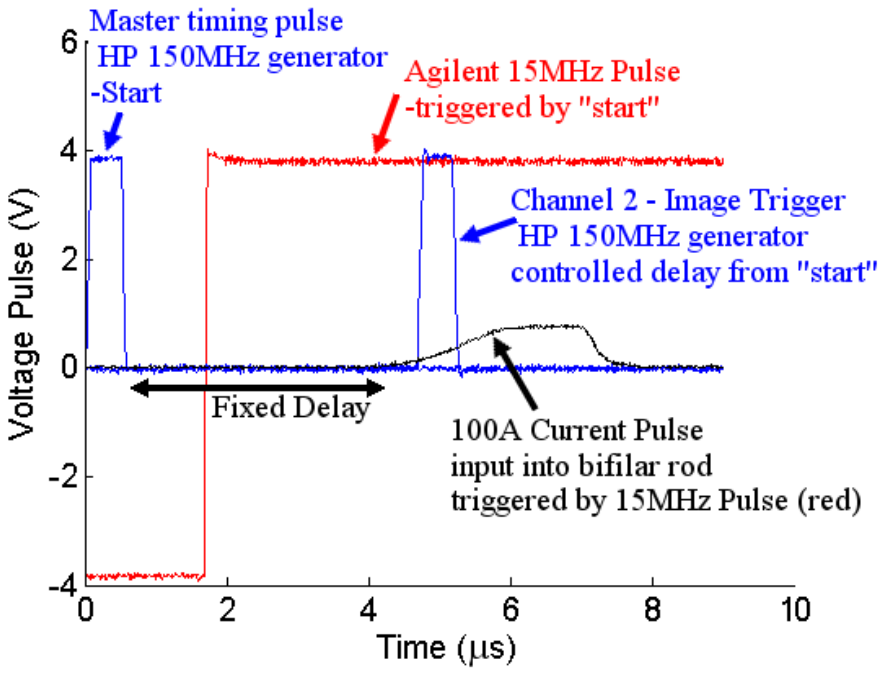

Figure 5.15: Full pulse profile showing initial pulse HP $150MHz$ pulse generator (blue), square trigger pulse from the Agilent $15MHz$ $33120A$ waveform generator (red), Medipix trigger pulse (blue) and injection pulse in bifilar rod (black).

rod with maximum values of 20, 40, 60 and $80Oe$.

The position of the detector acquisition time with respect to the injection pulse also plays a major part in this synchronisation. We know that the minimum practical exposure time for the Medipix detector is approximately $0.5\mu s$. Exposure times of this order of magnitude, along with careful control of the exposure start time allows us to separate specific sections of the image streak. The second $4V$ pulse from the $150MHz$ pulse generator, shown as the second blue peak in 5.15, externally triggers the Medipix detector. Timing the Medipix exposure to highlight the start and end stages of the streak allows us calibrate the total streak width, while removing both ends of the streak and concentrating on the linear section reduces the maximum intensity of the image, increasing the magnetic contrast in the image.

Experimental optimisation of the pulse frequency found that the detector can only be triggered up to a maximum of 42 frames per second. Above this, the acquisition

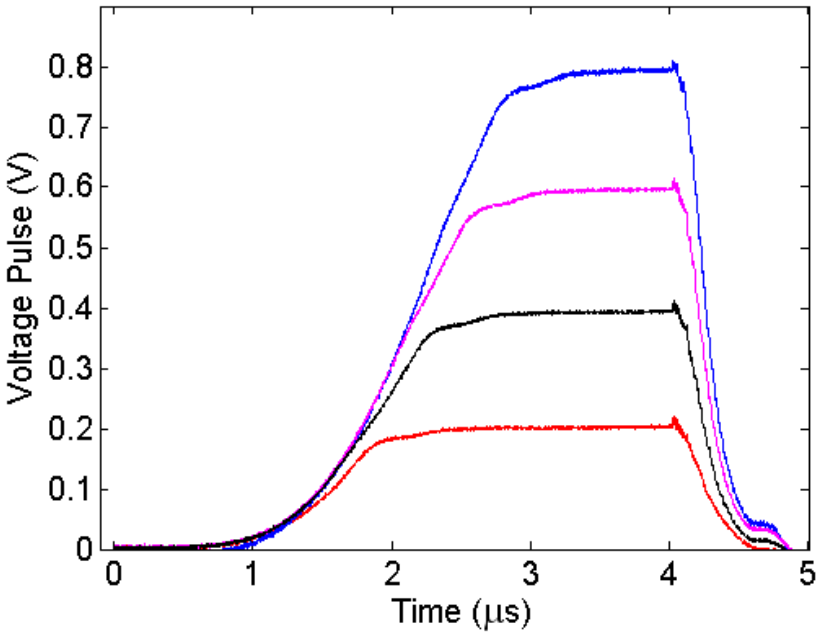

Figure 5.16: Pulse profile of injection voltage in bifilar rod from the $100A$ pulser supply. Showing four different field pulses at differing voltage heights.

frame rate didn't match the input pulse frequency indicating that the maximum rate had been reached. Although the Fitpix chip is capable of bursts of $80fps$ [25], it cannot sustain this synchronously. The limit of $42fps$ is due to the speed of the processor in the PC used.

The electron gun used in the Philips CM20 microscope has an electron current between 0.1 and $1nA$, which corresponds to between 6.241×10^8 and 6.242×10^9 electrons per second or a maximum of 6242 electrons per microsecond. In a 254×254 pixel image this relates to 0.1 electrons per pixel per microsecond. This very low value means that thousands of integrated $1\mu s$ exposures will be required to gain sufficient counts to form an image. However with a frame rate of only $42fps$, gaining thousands of images takes minutes and therefore may be vulnerable to drift or instability within the microscope. This is very important as it limits the practical overall exposure time of the detector.

5.3.3 Fresnel streaks

The simplest magnetic imaging method to implement is Fresnel image streaking, therefore this was done first. It has already been established from figure 5.7 that a $60Oe$ field pulse is sufficient to inject a DW to the notch. This is was repeated and verified with the Medipix images shown in figure 5.17. The region of illumination used in this figure was defined by parallel illumination and a $200\mu m$ C2 aperture; this illumination gives the added effect of maximising the beam area to within the deposited platinum, eliminating the possibility of streaking beyond the blocked area. Figure 5.17 shows the static states that are expected within the streak, from positively saturated to wall injection and subsequent ejection; these images were taken in a series of 4000 integrated exposures of $1\mu s$ each. The most observable change in magnetic structure is the dark edge contrast switching from the upper to the lower edge. This change when imaged as a streak in the direction shown will appear continuous. The added contrast created by the presence of the DW needs to be visible within the streak for this technique to be viable.

Figure 5.18 shows that the contrast, defined in equation 5.1, for the DW within the static image is 0.89 for 4000 exposures of $1\mu s$ duration; this is above the required level of 0.02 however we also know from figures 5.9 to 5.11 that the streak process significantly reduces the magnetic contrast.

Control of the delay time and exposure times allow us to visualise specific parts of the streak and neglect others, this is demonstrated in figure 5.19. Figure 5.19*b* and *c* show $1\mu s$ exposures at the start and end of the steak respectively, associated with the pulse shape and exposure limits shown in figure 5.19*a*. Given that we know the time and field strength at each of these images, they are used to calibrate the total streak width with respect to time and field.

Once the streaks have been calibrated and the expected magnetic structural changes seen, the linear section of the streak can be examined. The area of the streak labelled as linear in figure 5.19*a* was examined using $1\mu s$ exposures. Figure 5.20 shows

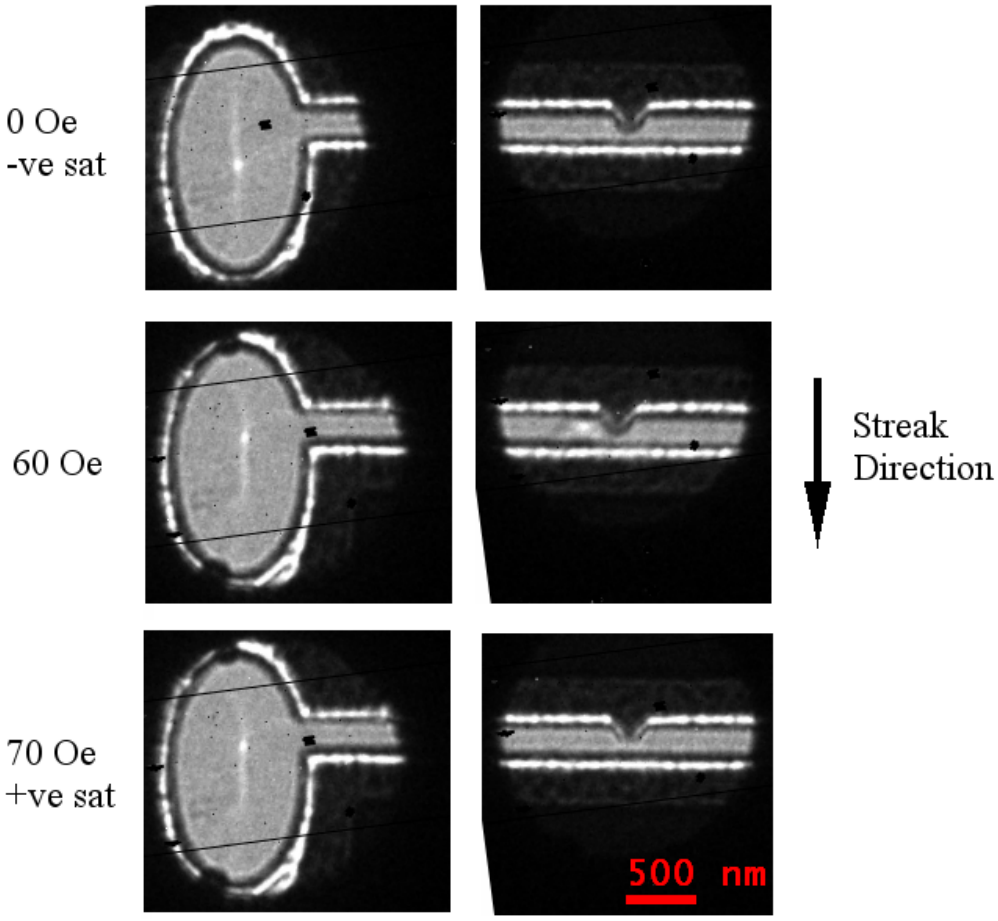

Figure 5.17: Fresnel images showing initial, injected and ejected states in 300nm wide permalloy nanowire; the arrow shows the direction the image will be streaked during the magnetic pulse.

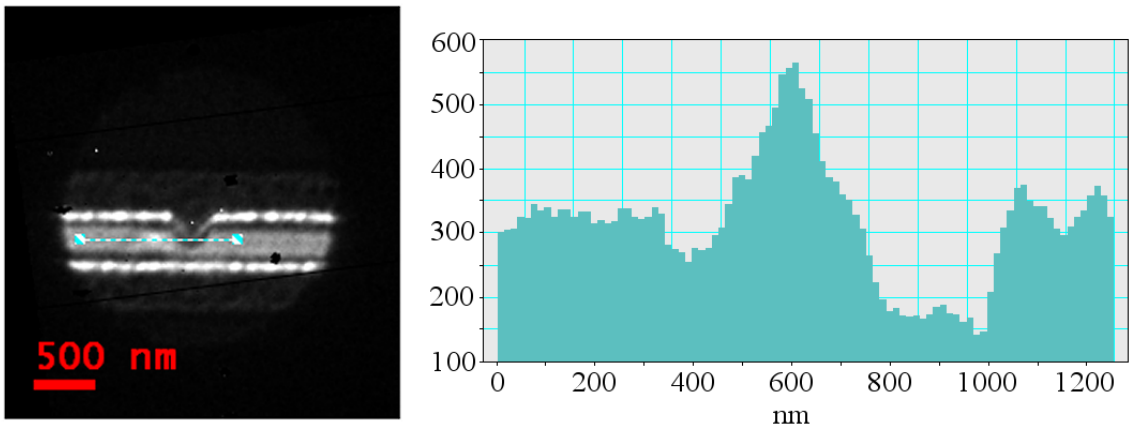

Figure 5.18: Fresnel image and intensity profile across the centre of a vortex DW in notched 300nm wide nanowire.

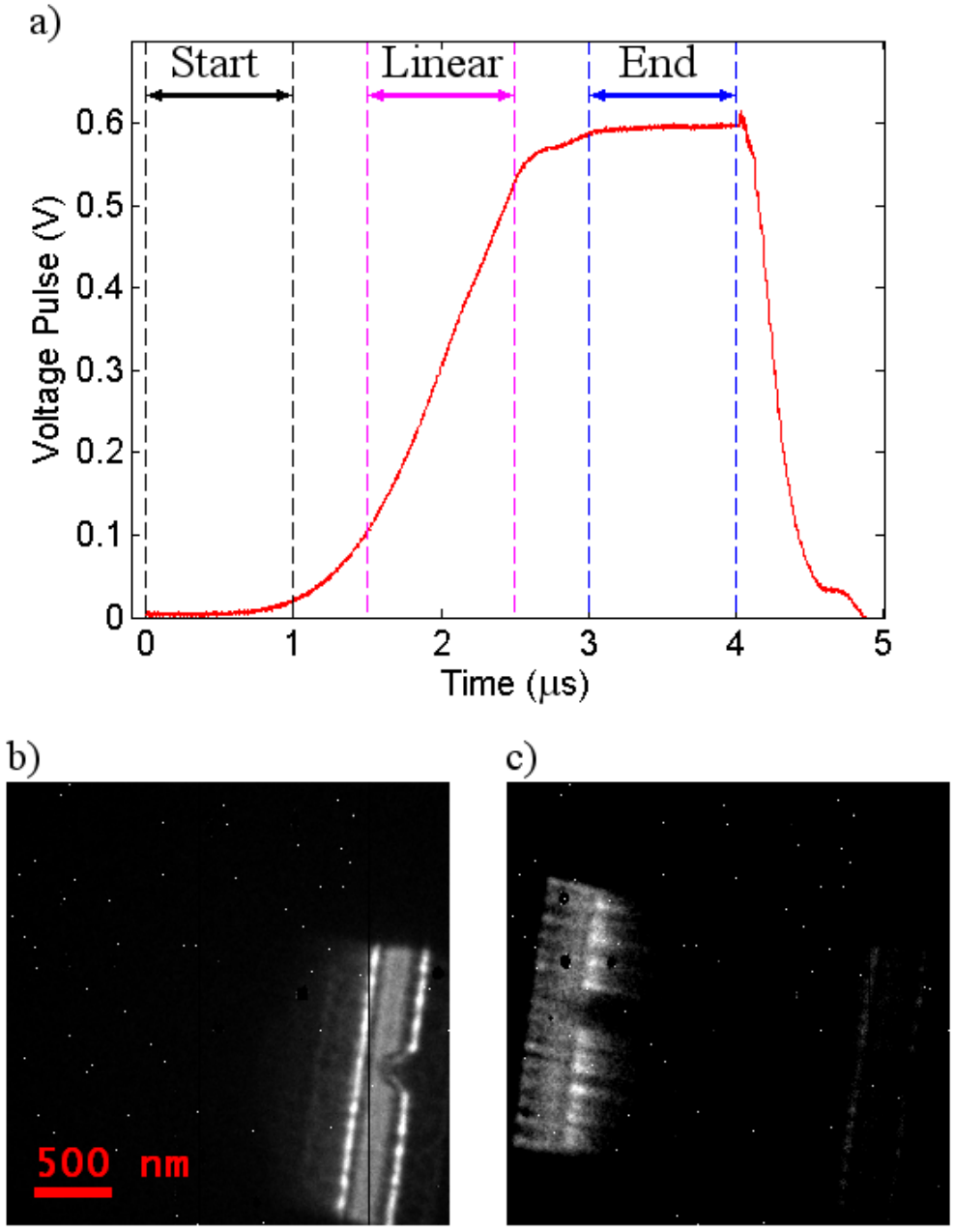

Figure 5.19: (a) Graph of $60Oe$ current pulse, and two integrated Fresnel streak images of 4000, $1\mu s$ exposures, taken at (b) the start and (c) end of the streak.

a Fresnel streak composed from 4000, $1\mu s$ exposures at $40fps$, (identical to the static images shown in 5.17) taken from the linear region of the pulse. It is worth noting that these images take 1.5 minutes to gain just $4ms$ of total exposure, compared to the $1s$ single exposure images shown in 5.17. From figure 5.20, the edge contrast at the extremes of the streak is visible, labelled A, however no magnetic changes are immediately observed within the streak itself, nor is the domain wall immediately apparent at any point.

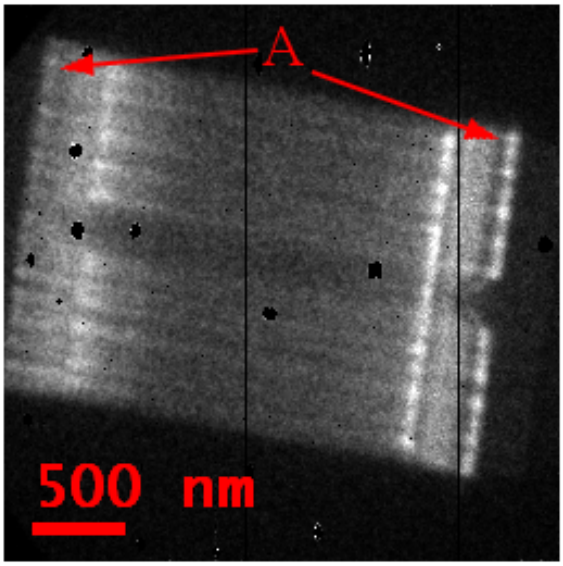

Figure 5.20: Streaked Fresnel image, integrated over 4000 $1\mu s$ exposures centred around the area marked "linear" in figure 5.19.

The Medipix images shown in figure 5.20 are formed of 256×256 pixels, the streak shown has a magnitude of 184 pixels. This was generated by the $600mV$ ($60Oe$) pulse shown in figure 5.16. This pulse ramps from 0 to $60Oe$ in $2\mu s$, the resultant streak can therefore be interpreted to a have a temporal resolution of $350ns$. This initial experiment did not produce visible magnetic contrast within the streak, as the simulations predicted; however the high calculated temporal resolution of the streak is encouraging and the simulations suggest that Foucault imaging will have a higher magnetic contrast in the streak.

5.3.4 Foucault streaks

The final part of the experimental setup is aligning the microscope correctly to maximise the magnetic contrast. Foucault alignment requires exact positioning of the objective aperture, explained in chapter 3. Image 5.6 shows how the diffraction pattern shifts with the magnetic pulse with respect to the curvature of the objective aperture. This shift means that to maintain the Foucault condition throughout the streak, the aperture must be positioned as shown in figure 5.6b. Due to the direction of the streak compared to the magnetisation of the wire, this required position determines that the magnetic contrast will be sensitive to the magnetic induction perpendicular to the wire.

As in the Fresnel case, the static domain wall contrast must first be studied. Figure 5.21 shows Foucault images of the injection pad and DW with sensitivity perpendicular to the wire both before and after injection along with the intensity line profile across the wall. Using equation 5.1, where $I_{max} = 250$, $I_{min} = 115$ and $I_{mean} = 175$, produces a $C = 0.77$.

This contrast is highly dependent on the exact position of the objective aperture. Consequently the aperture drift within the microscope can cause loss of the Foucault condition. Figure 5.22 shows how the Foucault image contrast changes over a 6 minute period due to the objective aperture drift. This illustrates that the mean intensity of the wire changes with time along with the visibility of the DW, beyond the displayed limits the magnetic contrast isn't apparent. This drift means that the total time of acquisition is limited to $\sim$6 minutes. The timing limit of $42fps$ on the Medipix detector combined with this 6 minute time frame results in a practical limit of the maximum total number of exposures of $\sim$16000.

We know that the magnetic contrast from the DW is expected to be reduced significantly within the streak. The level of this reduction in contrast was experimentally investigated by deflecting the image of the wire, with a static DW present, with varying maximum pulse amplitudes. The DW remains present throughout the

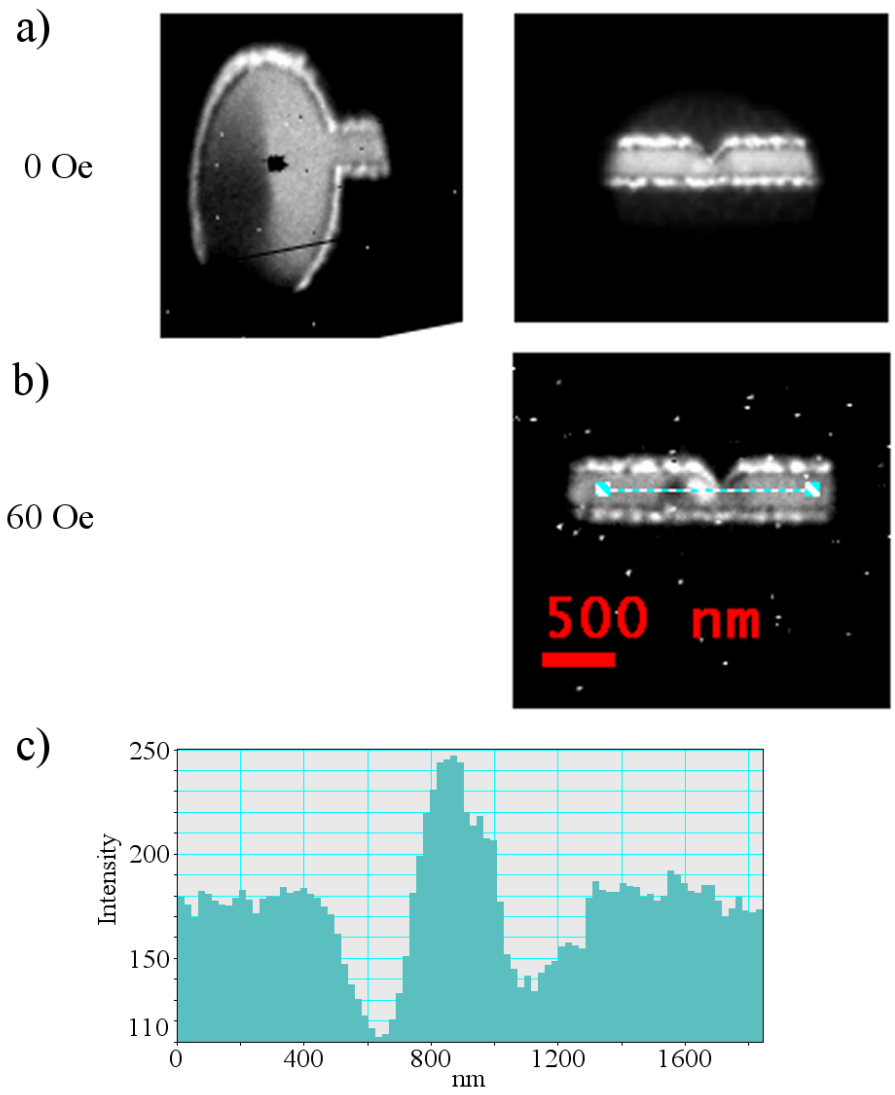

Figure 5.21: Foucault images of injection pad and 300nm wide permalloy wire (a) before and (b) after DW injection with (c) an intensity line profile of the DW.

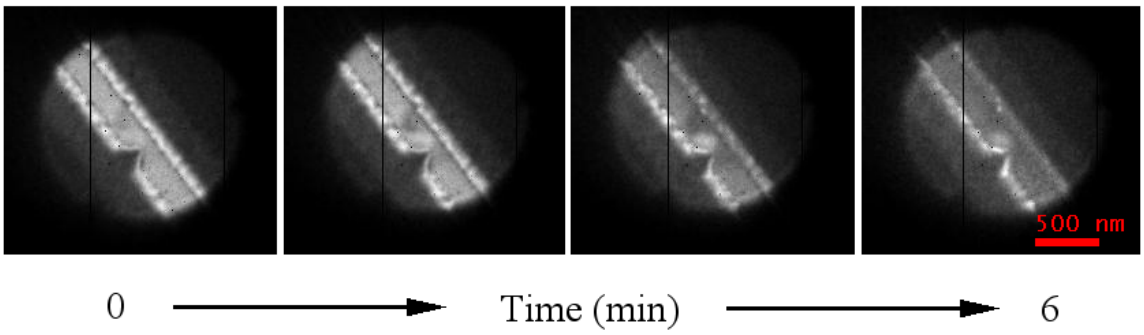

Figure 5.22: Foucault images taken over 6 minute period showing development of Foucault condition due to objective aperture drift.

streak, allowing us to observe quantitatively how the contrast of the domain wall varies with the amplitude of the streak. This was done with pulse amplitudes of $0, 20, 40$ and $50Oe$, shown in figure 5.23a, b, c and d respectively. These images were taken using 2000, $1\mu s$ exposures; this low number of exposures was used to be certain that the Foucault condition was maintained throughout. These results show that the contrast decreases from 0.38 in the static image to within the image noise in the $50Oe$ deflection. These deflections are on the same order of magnitude as the expected deflections during a $60Oe$ injection pulse, therefore this limit will likely be important with gaining observable magnetic changes in injection streaks. Not only must the condition be maintained throughout the time frame, it must also be maintained throughout the streak. We know from figure 5.6b that the shift in the diffraction pattern is of the same order of magnitude as the curvature of the objective aperture, therefore holding the Foucault condition for the full streak will be difficult.

The reduction in contrast within the streak and maintaining the Foucault condition are both going to be significant issues with this technique. Therefore we need to understand and minimise any other sources of contrast that may arise and find a way to increase the relative magnetic contrast within the streak.

The area of illumination of the sample was defined by the C2 aperture. Figure 5.24 shows static and streaked images of just the $200\mu m$ C2 aperture. The static image illustrates that the aperture is not circular but has imperfections. The streaked image shows that these imperfections produce streaked intensity changes indicated by b. This streaked contrast is of the same order of magnitude as any expected magnetic contrast and therefore we must be aware of it when analysing images.

The relative contrast of the magnetic signal can be increased by removing the background, non-magnetic, intensity from the streak. This is achieved by capturing a normal Foucault streak then intentionally removing the Foucault condition and running an identical bright field (BF) streak. The BF streak has the same width

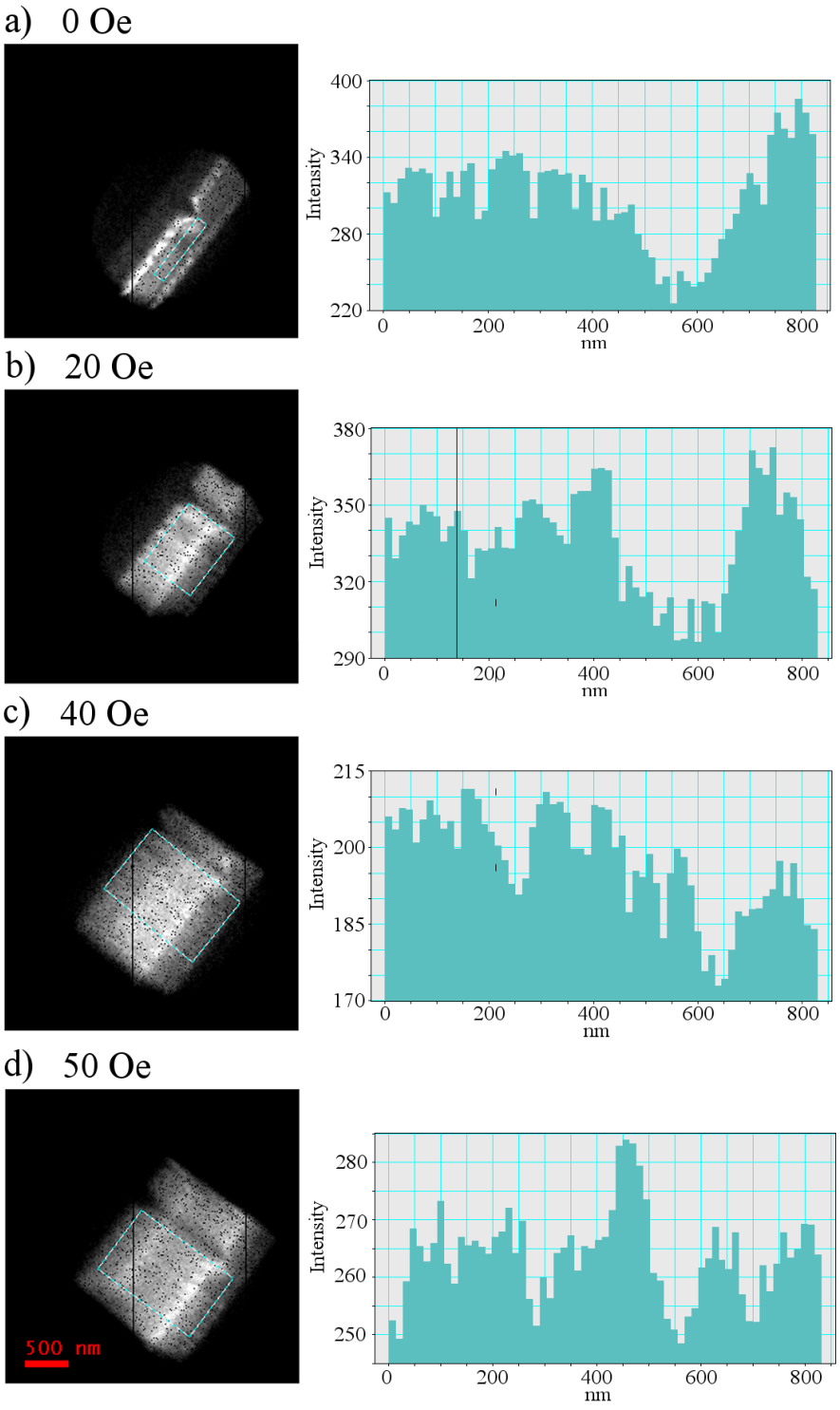

Figure 5.23: Static DW Foucault streaks of $300nm$ wide nanowire with varying field amplitude, with accompanying intensity profiles of areas shown. Displaying reduction in magnetic domain contrast as the streak amplitude is increased.

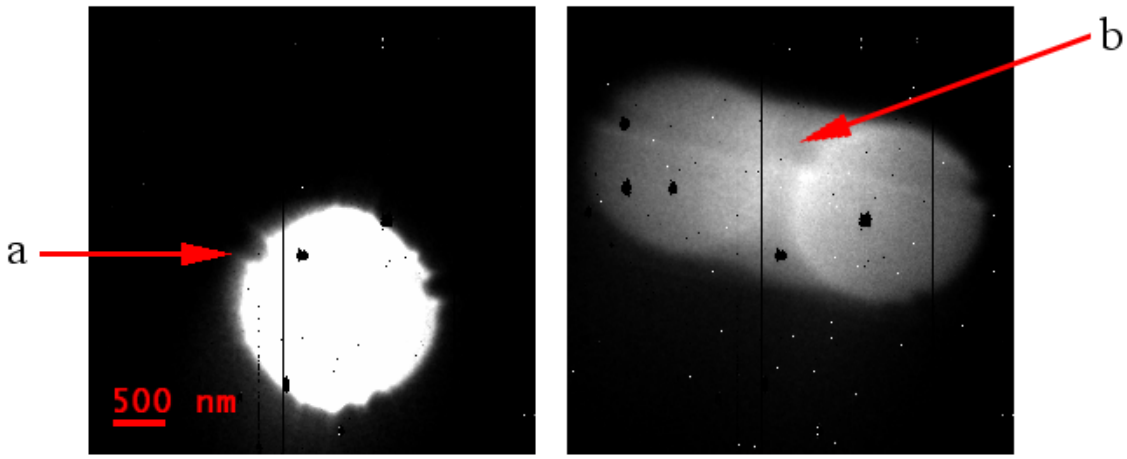

Figure 5.24: Static and streaked images of C2 aperture with a $60Oe$ ramped pulse, showing non-circular shape of the aperture and the resultant contrast within the streak. (a) and (b) point to a notch on the C2 aperture and its resultant streak intensity.

as its Foucault counterpart but will contain no magnetic information; it will also contain any contrast variation from the imperfect C2 aperture. Digital Micrograph is then used to calculate the intensity difference image between the BF and Foucault streaks, removing the background intensity and increasing the relative contribution of the magnetic signal. The magnitude of this background intensity will not match perfectly with the magnetic image as the Foucault condition, by definition, reduces the intensity, however it will still help significantly with increasing the magnetic contrast.

Figure 5.25 shows how this BF removal works in practice. It displays an example of a Foucault and the corresponding bright field streak, the third image then shows the difference image. The streak contrast area marked a on 5.25 is the contrast generated from the notch, this is identical in the bright field streak and therefore all but disappears in the difference image. The contrast marked b is from the deflection of the C2 aperture imperfection, this is known as it only appears after the streak exceeds the original area of illumination. The contrast from the C2 aperture is visible in the difference image because there is a slight difference in sample position between the Foucault and bright field streaks. During the difference calculation, the

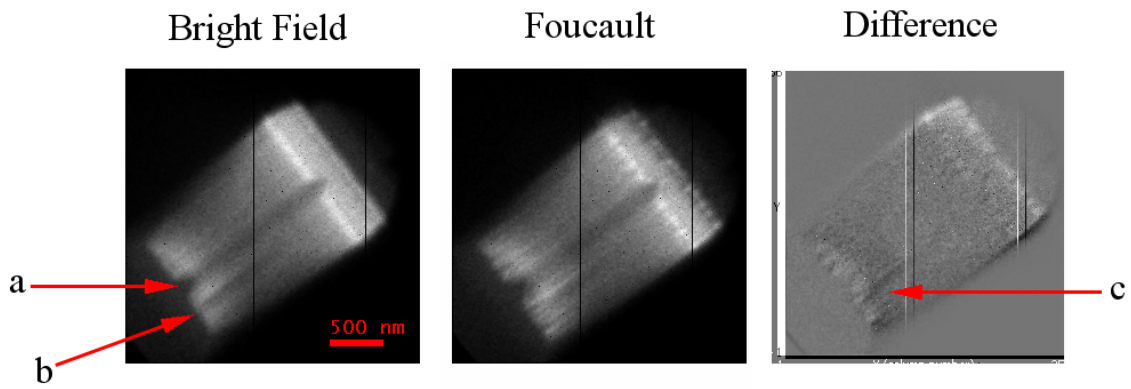

Figure 5.25: Series of images showing the BF, and Foucault streaks and the resultant difference image from a 300nm wide wire deflected with a 60Oe magnetic pulse.

streak images are aligned with respect to the notch on the nanowire, not the C2 aperture; this means that the contrast from this feature does not cancel perfectly in the difference image resulting in the contrast highlighted by *c* in the figure 5.25. The problem of the contrast gained from the streak of the C2 aperture will be avoided by positioning the C2 streak contrast on the far side of the notch to where we expect to see the wall, where it can then be neglected. This image doesn't show any specific magnetic changes but it does demonstrate the technique that will be used.

We already know from figure 5.23 that for images of 2000 exposures, the reduction of magnetic contrast observability due to the streaking will make the domain wall unobservable. Therefore the number of exposures was extended to the the limit of the aperture drift time, i.e. $\sim$16000. At $42fps$ acquisition rate this corresponds to a total acquisition time of just over 6 minutes.

Figure 5.26 shows one streak over a $60Oe$, $2\mu s$ pulse with its accompanying intensity profile over the area shown in green. The red arrow in this figure displays the position of the expected domain wall, recall the DW structure from figure 5.21. The reduced intensity shown between 250 and $350nm$ on the line profile displays this possible domain wall more visibly. However the intensity level indicates this could just as easily be generated from either the C2 or the objective aperture or the

in-focus edge of the wire itself. This streak reaches over 145 pixels, meaning that each pixel represents $14ns$, with a wire width of 35 pixels, this creates a temporal resolution of $\sim 0.5\mu s$. This is slightly lower than the Fresnel streaks as the deflection is larger when the image is defocused.

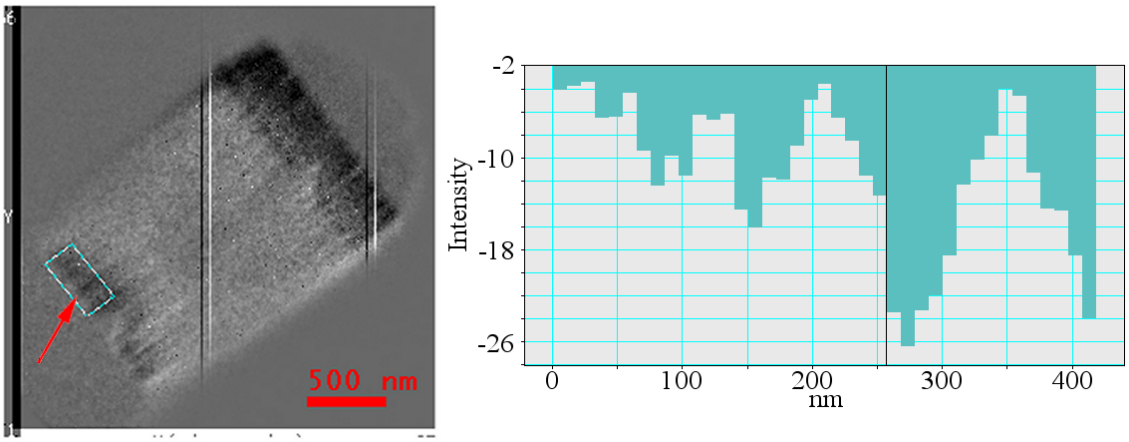

Figure 5.26: Example of one of the best Foucault streak difference images and accompanying intensity profile from the area marked.

The presence of a domain wall in this streak, and several others like it, is far from conclusive. Unlike Fresnel image streaking where the problem was the magnetic contrast levels, the main issue limiting Foucault streaking is the objective aperture stability. If the aperture stability or Medipix frame rate were increased such that the number of exposures could be increased by an order of magnitude or more, then the magnetic contrast changes could become visible over the noise.

5.3.5 Low angle diffraction streaks

Low angle diffraction imaging exploits the distortion of the central diffraction spot in reciprocal space due to the Lorentz interaction of the beam with the magnetic sample. It quantitatively images this deflection directly and allows magnetic information about the sample to be interpreted. In LAD mode the C2 aperture defines the coherence of the beam and the area of parallel illumination, the aperture imperfections will not be discernible. When imaging crystal structure, the electrons are scattered

through angles of $\beta = 10^{-3} - 10^{-4} rad$; this is typically imaged with camera lengths of several tens of centimetres [26]. However we know that the Lorentz deflection angle from magnetic samples is only in the order of $\sim 10 \mu rad$, therefore camera lengths between 50 and 1000m are typically required to visualise the magnetic separation [26, 27]. The intensity in this mode is also predicted to be deflected over a much larger area than its in-focus counterpart, this leads to higher potential resolution within the streak with respect to both field and time.

Figure 5.27 shows a set of initial images taken at the three important magnetic states, namely positive saturation, negative saturation and with a DW at the notch. The corresponding LAD patterns are also shown, these patterns were taken with a $1s$ exposure at a camera length of 100m. The periodic fringes indicated by A on figure 5.27 are the $3.35 \mu m^{-1}$ fringes related to the multiple edges of the nanowire, platinum deposition and surrounding Permalloy film. On the central and right hand LAD images, referring to the wire section of the sample, the bright spot indicates the magnetic structure. This is clear due to its shift of position as the DW passes through the wire between 5.27b and d. The right hand LAD pattern of the notched wire with the DW present in 5.27c shows two bright spots clearly separated, this separation, due to the two magnetic domains now in the wire confirms this detail as purely dependent on the magnetic behaviour. The LAD patterns of the injection pad include what appears as a ring surrounding the central magnetic spot (still formed from the wire), this ring is a consequence of the vortex present in the pad.

The applied field, parallel to the wire produces a Lorentz deflection in the direction shown in figure 5.27. When streaked this deflection axis will essentially become a continuous bright line, therefore to observe any magnetic contrast changes, these changes will need to be off axis. The intensity changes described in the previous paragraph are on this deflection axis and therefore will be within the main streak; this will make them unobservable. Figure 5.28a and c show LAD images at the negative and positive single domain states, respectively, and injected domain wall state in Figure 5.28b taken at a camera length of $39m$, with their intensity profiles. The

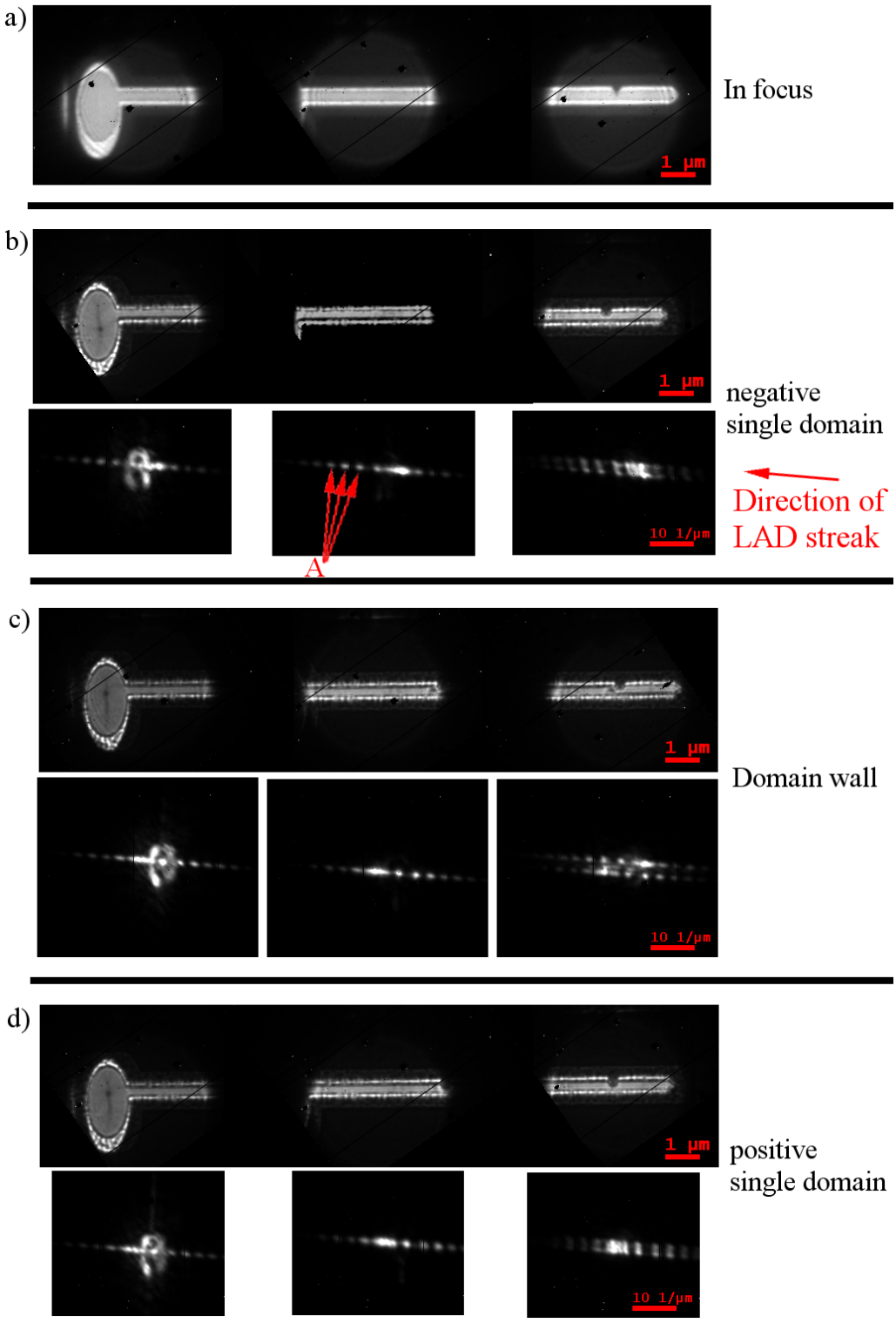

Figure 5.27: LAD images of pad, wire and notch in 300nm wide permalloy nanowire in three magnetic states with their accompanying Fresnel images; showing clear differences in the LAD pattern in both the pad and notched regions as the DW is pinned at and passes the notch.

contrast limits have been set to highlight the difference in the intensity surrounding the LAD spots. This shows that when the wall is present, there is a small increase in intensity in the area either side of the main spots. This increase in intensity is due to the presence of the wall; the magnetisation within the wall is perpendicular to the wire and the intensity is therefore off the deflection axis, meaning that it could be visible within the streak. The increase is however small so will require a very high number of exposures to become observable.

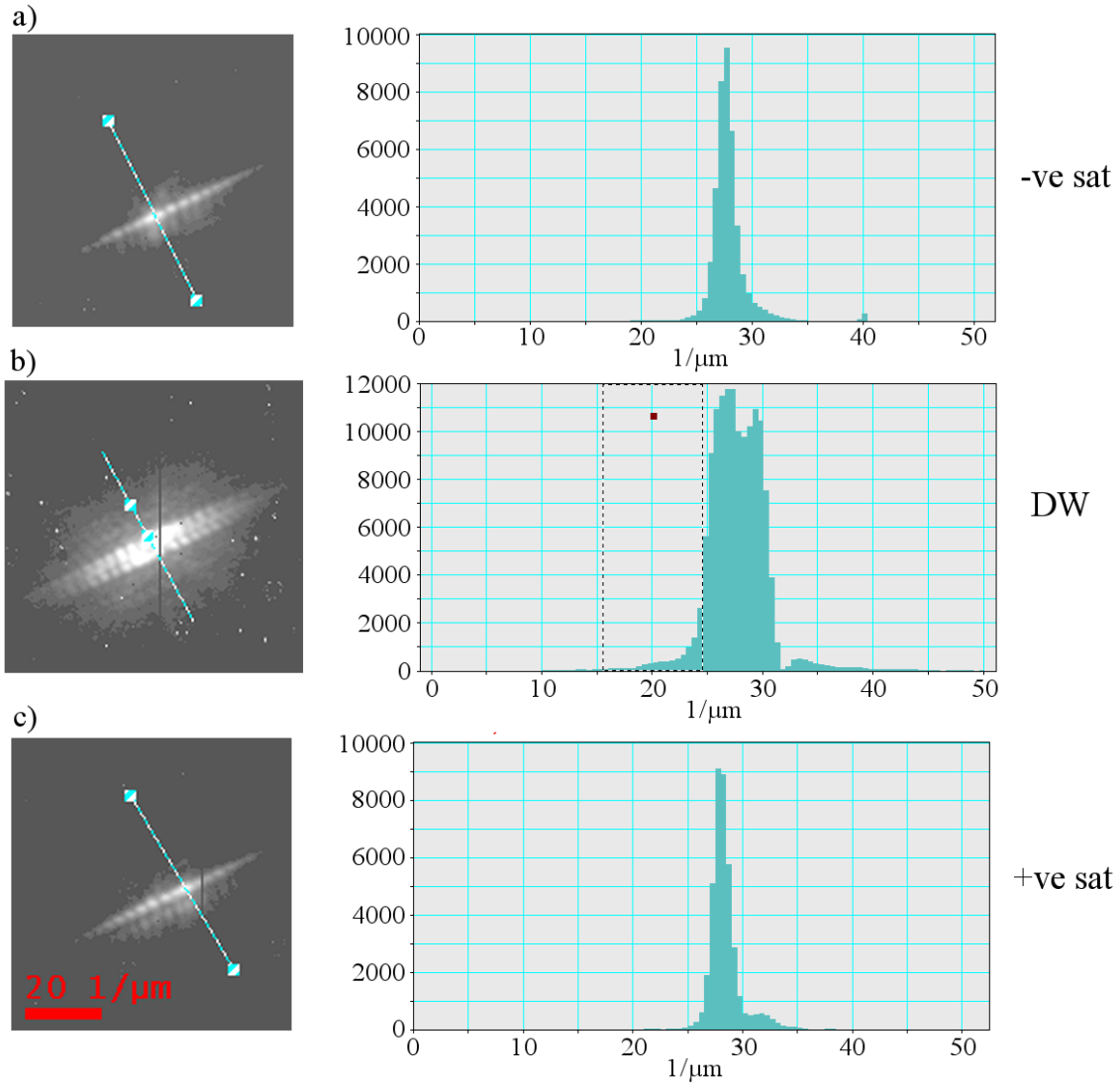

Figure 5.28: Surrounding intensity changes in LAD images in (a) negatively single domain, (b) pinned domain wall and (c) positive single domain states along with accompanying intensity profiles. Displaying change in off-axis intensity due to the presence of the DW.

With the desired intensity changes now understood, the LAD streaks must be calibrated. Figure 5.29*a* shows a static LAD image of the nanowire at a camera length of $39m$, figure 5.29*b* then shows a streaked image with a $50mV$ ($5Oe$) pulse at the same camera length. We know that the deflection is directly proportional to the field. Therefore we can calibrate the deflection as $9\mu m^{-1}Oe^{-1}$. Extrapolating this to the $60Oe$ needed to inject a domain wall indicates that the streak will extend well beyond the view of the camera. This could be fixed by running at a higher camera length but this would mean that the streak covers fewer total pixels, reducing the potential temporal resolution. For this reason the streak was shifted to the point where the end was on the camera. It is then possible, taking the maximum point of the streak as $60Oe$ and knowing the pulse shape, to measure the point of injection in both field and time.

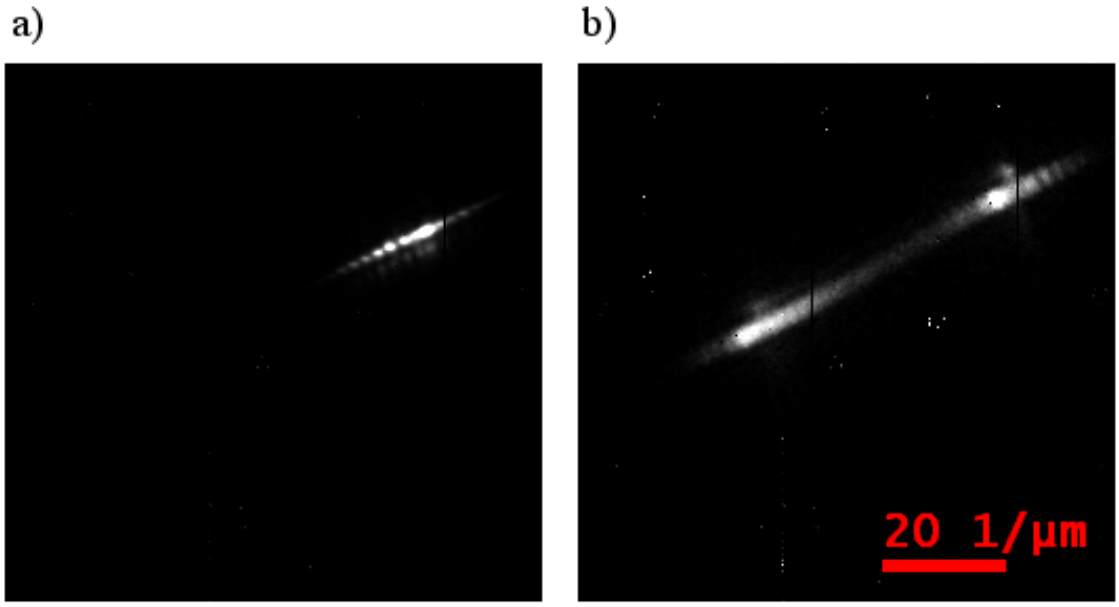

Figure 5.29: LAD images taken at 39m camera length showing static pattern (a) and a $50mV$ streak (b), these were used to calibrate the streak magnitude in reciprocal space.

The main advantage of using LAD mode is independence of both aperture and object drift, this stability was capitalised upon by running the LAD streaks for $200,000$ to $300,000$ exposures. The images shown in figure 5.30 show a streak from a $60Oe$

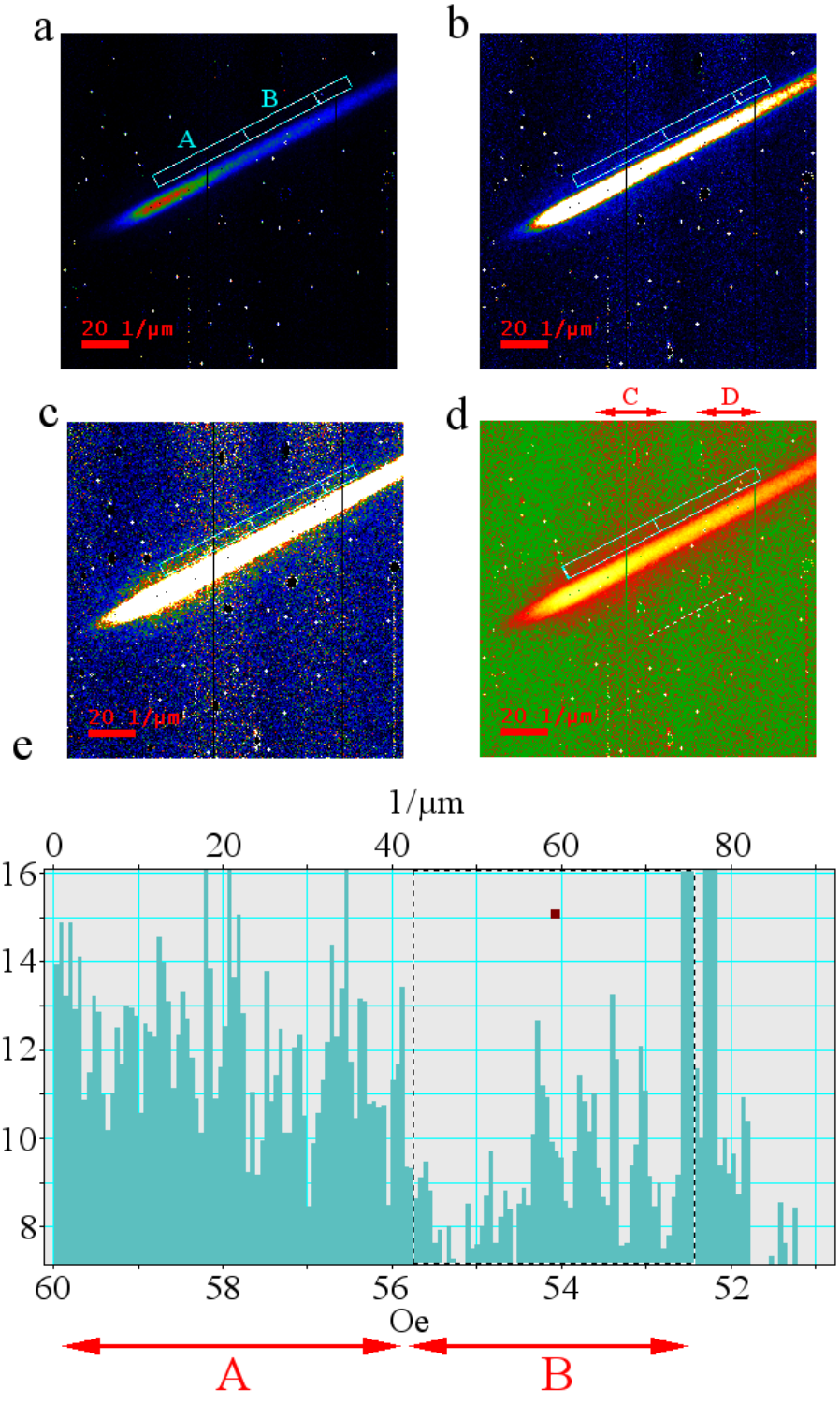

Figure 5.30: Final LAD streak at four different contrast limits, taken with 300,000 exposures, and intensity profile of area marked in images.

pulse, comprised of $300,000$, $1\mu s$ exposures seen with varying contrast limits. The false colour used in these images in an attempt to highlight the intensity variations more easily. Although this method did allow for these large numbers of exposures, this work was performed at the end of the electron gun's life with extremely low beam current, hence the low number of counts shown in figure 5.30*e*. These images display the gradual brightening of the beam at the end of the streak caused by the non-linear section of the pulse, shown in figure 5.16. The intensity profile of the area marked, shown in figure 5.30*e*, displays a slight increase in the intensity between the areas marked A and B; this increase in intensity is only slightly above the noise level of the image and could be due to the domain wall, or what appears to be columns of increased signal marked as C and D in 5.30*d*. We know that the deflection of the LAD is $9\mu m^{-1}Oe^{-1}$ and we know the scale of the image, using this combined with taking the point of maximum intensity as at $60Oe$ allows us to calibrate the deflection with respect to field and time, as shown on the second x-axis of figure 5.30*e*.

5.4 Summary and Conclusion

This imaging process has potential, however all three methods used in this study had limitations that lead to unconfirmed results. The Fresnel imaging mode produced no visible magnetic changes within the experimental streak. The edge contrast in the initial and final states is observable but the DW is not. We know from the Fresnel simulations that the expected magnetic contrast within the streak is extremely low and it is unlikely, even with an increase in exposures, that the DW would become visible.

The initial Foucault results confirmed the higher contrast to the Fresnel mode predicted by simulations. Figure 5.23 showed that the expected decrease in the magnetic simulation due to the streak is significant. Contrast calculations from this figure showed that at the required field magnitude the DW will be unobservable within the streak, leading to an increase in the number of exposures taken to 16000.

The removal of the bright field streak lead to streak images with potential DWs visible within the streak, however these DWs could not be verified. These images will need substantially higher contrast before these walls can be verified as injection rather than streaked intensity from other sources.

Using LAD mode in the microscope should have generated higher intensity counts as the beam is condensed to a point. The problem arose from the low number of intensity counts, seen in figure 5.30, due to the low beam current produced at the end of the electron gun's lifetime; increasing this current may allow the counts in the streak to be increased above the noise level and therefore clarify the signal. Another option of improving this technique by transferring it into another microscope with a brighter source and more stable objective aperture; however due to the specialist equipment used, i.e. the Medipix detector and the bifilar rod, this could not be done at the time of this experiment.

Bibliography

[1] Browning N.D. Bonds M.A. Campbell G.H. Evans J.E. LaGrange T. Jungjohann K.L. Masiel D.J., McKeown J. Mehraeen S. Reed B.W., and Santala M. Recent developments in dynamic transmission electron microscopy. *Curr. Opin. Solid State Mat. Sci.*, 16(1, SI):23–30, FEB 2012.

[2] LaGrange T. Reed B.W. Santala M.K. McKeown J.T. Kulovits A. Wiezorek J.M.K. Nikolova L. Rosei F. Siwick B.J. Campbell G.H. Approaches for ultrafast imaging of transient materials processes in the transmission electron microscope. *Micron*, 43(11, SI):1108–1120, NOV 2012.

[3] Bostanjoglo O. and Rosin T. Stroboscopic study on ultrasonic activity in electron-microscope. *Microscopy*, 32(5-6):190, 1976.

[4] Bostanjoglo O. Tornow R.P. and Tornow W. Nanosecond transmission electron microscopy and diffraction. *Journal of Physics E: Scientific Instruments*, 20(5):556–557, MAY 1987.

[5] Dmer H. and Bostanjoglo O. High-speed transmission electron microscope. *Rev. Sci. Instrum.*, 74:4369, 2003.

[6] Armstrong M.R. Boyden K. and Browning N.D. et.al. Practical considerations for high spatial and temporal resolution dynamic transmission electron microscopy. *Ultramicroscopy*, 107(4-5):356–367, APR-MAY 2007.

[7] Bostanjoglo O. and Rosin T. Ultrasonically induced magnetic reversals observed by stoboscopuc electron microscopy. *Optica Acta*, 24(6):657–664, 1977.

[8] Zewail A.H. Four-Dimensional Electron Microscopy. *Science*, 328(5975):187–193, APR 9 2010.

[9] LaGrange T. Campbell G.H. Reed B. Taheri M. Pesavento J.B. Kim J.S. and Browning N.D. Nanosecond time-resolved investigations using the in situ of dynamic transmission electron microscope (DTEM). *Ultramicroscopy*, 108(11):1441–1449, OCT 2008.

[10] Bostanjoglo O. High-speed electron microscopy. In *Advances in imaging and electron physics, Vol 121*, volume 121 of *Advances in imaging and electron physics*, pages 1–51. Academic press inc., 2002.

[11] Browning N.D. Bonds M.A. Campbell G.H. Evans J.E. LaGrange T. Jungjohann K.L. Masiel D.J. McKeown J. Mehraeen S. Reed B.W. and Santala M. Recent developments in dynamic transmission electron microscopy. *Curr. Opin. Solid State Mat. Sci.*, 16(1, SI):23–30, FEB 2012.

[12] Reed B.W. Armstrong M.R. Browning N.D. Campbell G.H. Evans J.E. LaGrange T. and Masiel D.J. The Evolution of Ultrafast Electron Microscope Instrumentation. *Microscopy and Microanalysis*, 15(4):272–281, AUG 2009.

Annual Meeting on Microscopy and Microanalysis, Albuquerque, NM, AUG, 2008.

[13] Lobastov V.A. Srinivasan R. and Zewail A.H. Four-dimensional ultrafast electron microscopy. *Proc. Natl. Acad. Sci. U. S. A.*, 102(20):7069–7073, MAY 17 2005.

[14] Chollet M. Ahr B. Walko D.A. Rose-Petruck C. and Adams B. Hard X-ray streak camera at the Advanced Photon Source. *Nucl. Instrum. Methods Phys. Res. Sect. A-Accel. Spectrom. Dect. Assoc. Equip.*, 649(1):70–72, SEP 1 2011.

[15] Chollet M. Ahr B. Walko D.A. Rose-Petruck C. and Adams B. 2-ps Hard X-Ray Streak Camera Measurements at Sector 7 Beamline of the Advanced Photon Source. *IEEE J. Sel. Top. Quantum Electron.*, 18(1):66–73, JAN-FEB 2012.

[16] Feng J. Shin H.J. Nasiatka J.R. Wan W. Young A.T. Huang G. Comin A. Byrd J. Padmore H.A. An x-ray streak camera with high spatio-temporal resolution. *Appl. Phys. Lett.*, 91(13), SEP 24 2007.

[17] Murnane M.M. Kapteyn H.C. and Falcone R.W. Xray streak camera with 2 ps response. *Appl. Phys. Lett.*, 56(20):1948–1950, 1990.

[18] Lindenberg A.M. Kang I. Johnson S.L. Missalla T. Heimann P.A. Chang Z. Larsson J. Bucksbaum P.H. Kapteyn H.C. Padmore H.A. Lee R.W. Wark J.S. Falcone R.W. Time-resolved x-ray diffraction from coherent phonons during a laser-induced phase transition. *Phys. Rev. Lett.*, 84:111–114, Jan 2000.

[19] Lindenberg A.M. Kang I. Johnson S.L. Falcone R.W. Heimann P.A Chang Z. Lee R.W. and Wark J.S. Coherent control of phonons probed by time-resolved x-ray diffraction. *Optics Letters*, 27(10):869–871, May 2002.

[20] Shakya M.M. and Chang Z.H. Achieving 280 fs resolution with a streak camera by reducing the deflection dispersion. *Appl. Phys. Lett.*, 87(4), Jul 2005.

[21] McMullan G. et al. Electron imaging with medipix2 hybrid pixel detector. *Ultramicroscopy*, 107(401), 2007.

[22] Yi G. Nicholson W.A.P. Lim C.K. Chapman J.N. McVitie S. Wilkinson C.D.W. A new design of specimen stage for in situ magnetising experiments in the transmission electron microscope. *Ultramicroscopy*, 99:65–72, 2004.

[23] McGrouther D. McVitie S. Chapman J.N. and Gentils A. Controlled domain wall injection into ferromagnetic nanowires from an optimized pad geometry. *Appl. Phys. Lett.*, 91(2), JUL 2007.

[24] Donahue M.J. and Porter D.G. Oommf user's guide, 1999.

[25] *http://aladdin.utef.cvut.cz/ofat/others/Fitpix/FITPix.html.*

[26] Togawa Y. Small-angle electron scattering of magnetic fine structures. *Microscopy*, 62(1):S75–86, May 2013.

[27] Chapman J.N. and Scheinfein M.R. Transmission electron microscopies of magnetic microstructures. *J. Magn. Magn. Mater.*, 200(1-3):729–740, OCT 1999.

Chapter 6

Domain Wall structure in Synthetic Antiferromagnetic Nanowires

6.1 Introduction

The nucleation and propagation of domain walls in magnetic nanowires has attracted recent attention over the last decade in both academia and industry due to its potential application in magnetic storage media [1, 2, 3, 4, 5]. These devices, including race track memory, are envisaged to utilise spin polarised currents to move domains in a nanowires in an attempt to produce non-volatile memory devices with high performance and reliability [6, 7, 8]. Much of the work in this field has concentrated on single layer Permalloy nanowires due to their simple, soft magnetic properties with minimal magnetostriction and anisotropy effects [9, 10, 11, 12]. However domain walls in these wires have widths comparable to the wire width. This limits the potential bit-density of the storage media as these relatively wide walls contain no stored information. These devices are also limited by the Joule heating associated with current induced domain wall movement; this has the potential to damage and degrade the devices by heating the wire beyond its Curie point, limiting their application.

The aim of this study is to use antiferromagnetically coupled multilayer nanowires to generate domain walls with simpler structure and narrower width to both transverse and vortex domain walls. These structures will solve both of the above limitations by reducing the distance between domains in bit media, increasing their potential aerial density and having the ability to be moved with current densities of up to order of magnitude lower than traditional walls.

6.2 Synthetic Antiferromagnets

Synthetic antiferromagnets (SAFs) are multilayer structures formed of two ferromagnetic layers separated by a nonmagnetic metallic layer. This spacer layer is the electrical conductor through which the Ruderman-Kittel-Kasuya-Yosida (RKKY) interaction occurs. This interaction, also known as indirect exchange, is a coupling between two magnetic materials through a nonmagnetic metallic spacer layer. The conduction electrons in this spacer act as a mediary between the two magnetic layers with the electrons getting spin polarised by one of the magnetic layers and coupling it to the other. The spin polarisation of the conduction electrons, and therefore the interlayer coupling, oscillates between ferromagnetic and antiferromagnetic with increasing distance from the initial polarisation point. The period of oscillation for this interaction, i.e. the distance by which the coupling decays from ferromagnetic to antiferromagnetic and back to ferromagnetic again, is material dependent and has been proven to range between 10 and 20Å for transition metals such as copper [13, 14], chromium [15, 16] and ruthenium [17, 18]. An example of this for a chromium spacer of varying thickness between two layers of iron is shown in figure 6.1 [17]. This graph shows that the coupling oscillation changes on the angstrom scale and fluctuates sharply with the peaks at 7 and 25Å denoting antiferromagnetic alignment. The sensitivity of the period of oscillation means that to ensure the coupling is both continuous and maximised the mean thickness of this spacer layer and any variation in that thickness needs to be accurate to within an Angstrom.

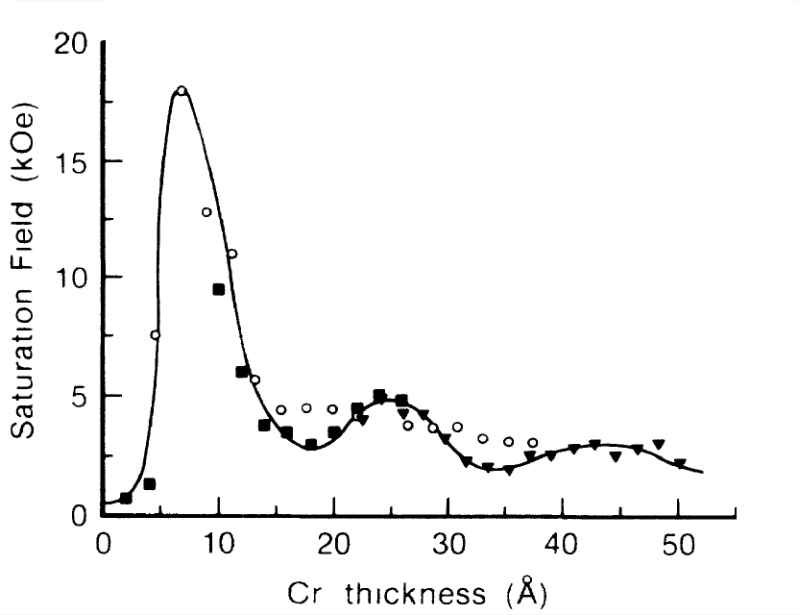

Figure 6.1: RKKY oscillation for a chromium spacer of varying thickness between two layers of iron [17].

In this study the structures were be formed of $Co_{80}Fe_{20}$ ferromagnetic layers separated by a Ruthenium spacer layer. $Co_{80}Fe_{20}$ was chosen because cobalt iron alloys they are soft, isotropic magnetic materials with high magnetic moments and the magnetocrystalline anisotropy is minimised at this specific composition. It also has a high Curie temperature making it ideal for this type of magnetic study [19, 20]. In addition to this, Co, Fe and Ru are all suitable for plasma deposition at the University of Leeds in which films can be deposited with thickness accuracy of $\sim$1Å[21].

When the two magnetic layers are antiferromagnetically coupled, the net structure is known as a synthetic antiferromagnet (SAF). When a domain wall forms in a SAF, the two antiparallel magnetic layers mean that two coupled wall structures form, one in each layer. Figure 6.2 illustrates a schematic of such a wall; this figure shows how the coupling between the layers forms a flux closure path (shown by red arrows). This flux closure means that the stray fields are dramatically reduced when compared to a domain wall in a single layer wire, decreasing the magnetostatic energy even when the individual layers are single domain.

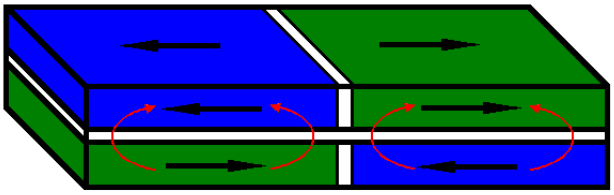

Figure 6.2: Schematic diagram of a domain wall in a SAF structure, red arrows illustrate the path of the magnetic flux within the material.

These changes in the magnetostatic energy and ground state magnetic structure led to a change in the predicted domain wall structure compared to their single layer equivalents. Figure 6.3 shows a micro-magnetic simulation of a domain wall in a SAF nanowire, with the magnetic orientation of the upper layer shown in a, compared to a transverse wall in a single layer wire of equivalent total thickness; the lower layer of the SAF structure in 6.3a has equal and opposite magnetisation to the upper layer. This simulation was done on a SAF with two $5nm$ magnetic layers separated by $1.5nm$ ruthenium layer and a single $10nm$ thick single layer wire in a and b respectively. The SAF structure had an assumed interlayer coupling of $-0.5mJm^{-2}$ [22]. It can be seen from figure 6.3 that the DW in the SAF is considerably narrower than in the single layer case, this is due to the reduction in the magnetostatic energy between the two systems. These narrow walls have the potential of increasing the areal density of magnetic storage devices by reducing the required distance between bits. These walls would also be expected to have a high magnetisation gradient, increasing the spin torque induced by an applied current; this increase in torque means that the walls will be capable of moving under significantly lower current densities, again potentially improving spintronic technologies.

So far the SAF structures discussed have had two magnetic layers of equal thickness; however these samples have several issues associated with them. The equal magnetic layers mean that when viewed in transmission balanced SAF structures have zero net magnetic moment as all moments are cancelled by the opposing layer. For the purposes of transmission electron microscopy, this means that the Lorentz deflection of the electron beam is equal and opposite as the electrons pass through

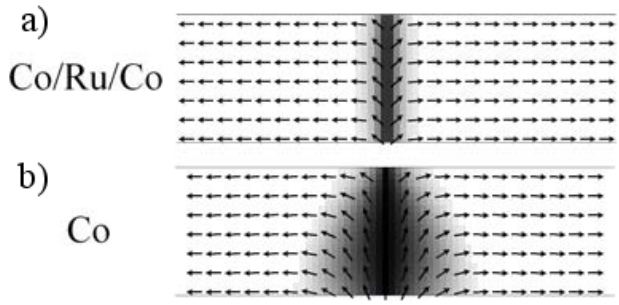

Figure 6.3: OOMMF simulations of DWs in (a) the upper layer of a 100nm wide Co(5nm)/Ru(1.5nm)/Co(5nm) SAF nanowire and (b) a single 10nm thick Co nanowire [22].

each of the layers; this means that any domain walls within these structures will be invisible to Lorentz microscopy. The second problem with these so called balanced SAFs is that there is no dominant magnetic layer. The equal layer thickness means that any behaviour induced by the application of magnetic fields or currents will apply to both layers simultaneously and allowing neither layer to dictate the total magnetic structure.

Both of these problems can be solved by introducing an imbalance to the relative magnetic layer thicknesses. This entails depositing one of the ferromagnetic layers thicker than the other, generating a net magnetic moment proportional to the imbalanced between the layers. This structure could be considered to be a synthetic ferrimagnet, however for the purposes of this study it will be referred to as an unbalanced SAF.

The presence of net moment and stray fields in unbalanced samples has several advantages; firstly the thicker layer will control the net magnetic behaviour. For example under the influence of an external magnetic field the thicker layer will be most strongly influenced by the field while the behaviour of the thinner layer will be dictated by the RKKY coupling to the thicker layer. This is only possible in unbalanced samples because the Zeeman energy is proportional to the net magnetisation. This dominance of the thicker layer will allow us to control the magnetic behaviour with an external field in the same way as in a single layer film and will be used in

this study to inject and manipulate DWs to investigate magnetic behaviour in SAF nanowires. The second main advantage of this imbalance is that these walls should be more easily visible in Fresnel imaging mode. The net moment means that when viewed in transmission, the Lorentz deflection of the electrons from the thicker layer is greater that from the thinner, generating a net deflection and resulting in a visible domain wall.

The issue with unbalanced SAFs is that the flux closure and the reduction in the magnetostatic field within these samples are compromised when compared to their balanced equivalent. This difference in magnetostatic fields between the balanced and unbalanced samples may alter the narrow domain wall structure seen in the balanced sample in 6.3. In this study both balanced and unbalanced samples were investigated and their domain wall structures compared with respect to the ratio of their layer thicknesses.

6.2.1 SAF Hysteresis

Hysteresis loops, explained in chapter 1, are typically used to gain an overall picture of the magnetic behaviour as the applied field is varied. In the case of SAF materials, these loops illustrate how the two magnetic layers interact. Figure 6.4 shows schematics of the expected hysteresis loops from balanced and unbalanced SAFs. Both loops reach saturation at high applied fields with both magnetic layers aligned parallel with the field. As the field is reduced, the Zeeman energy associated with the field reduces and the interlayer coupling becomes more prevalent. To minimise the coupling energy the parallel magnetic layers begin to diverge and move towards antiparallel alignment whist still being held by the eternal field, this is displayed by the black arrows in figure 6.4*b*. As the field is reduced below the coupling strength the thicker layer moves back to parallel with the applied field and the RKKY interaction forces the thinner layer into an AFM state. One of the most important impacts of this reversal process is that, when viewed in the TEM there is a large amount of magnetic ripple produced by the relative magnetic layers. The stable states both be-

fore and after the reversal produce very little ripple, allowing the operator to clearly see this reversal occurring. The antiferromagnetic alignment between the layers is reached as the coupling field overcomes the applied field. Reducing the field further to remanence results is a remnant magnetisation M_r equal to the difference between the upper and lower layer magnetisations. In the balanced SAF this is zero, hence the loop shape of 6.4*a*.

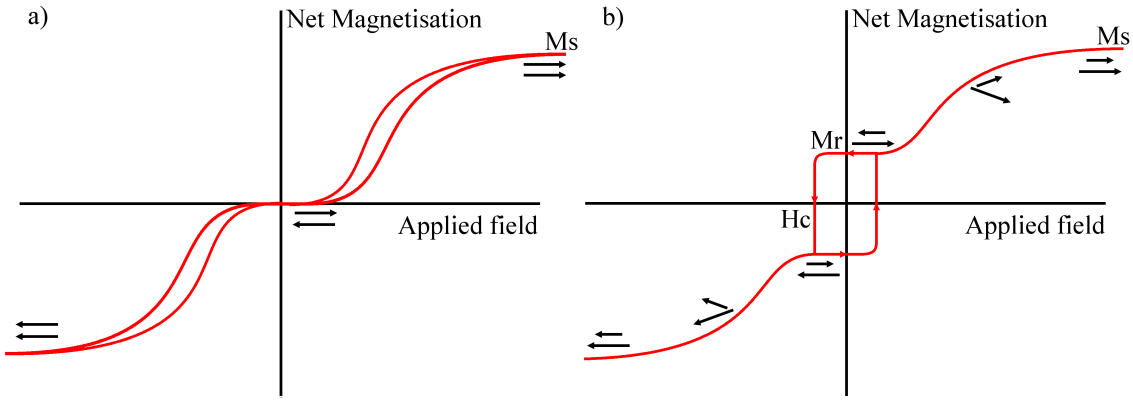

Figure 6.4: Diagrams of typical hysteresis loops in both (a) balanced and (b) 2:1 unbalanced SAF films.

As the field is increased in the opposite direction, but kept below the coupling field, the thicker layer determines the total magnetic structure. As the field is increased the field causes the thicker layer to reverse in the same way it would a single layer film, with the RKKY interaction holding the thinner layer antiparallel to it. The result of this reversal is the thicker layer ending parallel to the new field direction and the thinner layer antiparallel to it. In this study this reversal between the two different AFM states is the most important as it was during this reversal that the desired domain walls formed.

The applied field is then increased beyond the exchange field producing the opposite effect as the first reversal. Both layers move as the Zeeman energy, forcing both layers parallel, is balanced with the interlayer coupling, forcing both layers antiparallel. Until the field is sufficiently high to force the structure into a ferromagnetic state with both layers parallel to the field. All three of the these reversals will produce

significant ripple within an TEM image and will therefore be readily identifiable by a user [23, 24, 25, 26].

The first experimental step of this study was to find how the RKKY coupling varied with our specific choice of ferromagnetic and spacer materials. As explained previously, we would expect the coupling to oscillate between ferromagnetic and antiferromagnetic with changing spacer thickness [17]. The positions of these coupling peaks for our materials was found by taking hysteresis loops of a set of balanced SAF samples with varying Ruthenium thickness. Figures 6.5*a* and *b* shows two sets of loops surrounding the first and second antiferromagnetic coupling peaks respectively. The AFM peak is defined as the point where both the coercivity and the remnant magnetisation are minimised. These peaks are also characterised by a flattening of the magnetisation around remanence as the two layers reverse into an AFM state from an initial saturated position. From figure 6.5 it can be seen that the first and second peaks occur at 7Å and 20Å respectively.

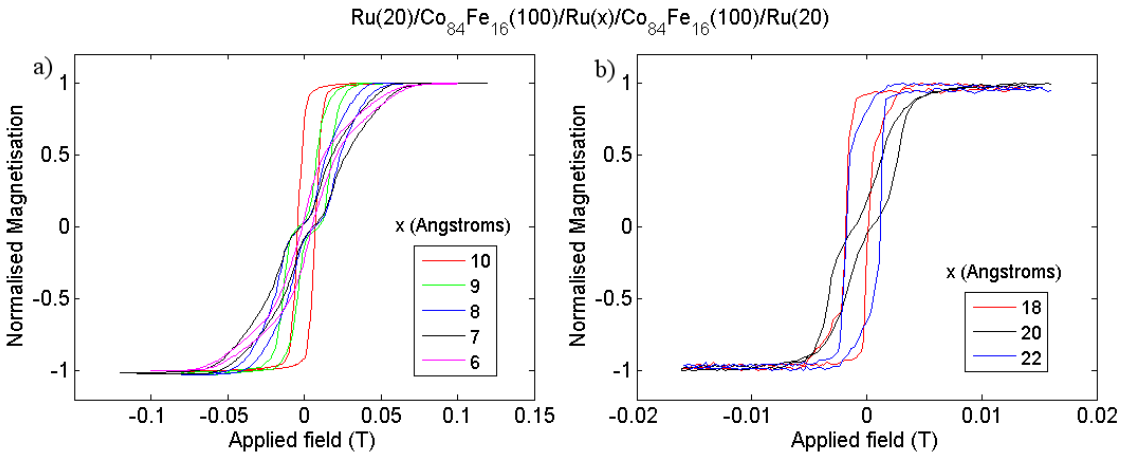

Figure 6.5: Hysteresis loops of balanced SAF structures with varying ruthenium thickness, these loops surrounds (a) the first AFM peak at 7Å and (b) the second AFM peak at 20Å.

6.3 Mathematical Simulations

In this study, the structure of the domain wall will be investigated with respect to the thickness ratio between the two magnetic layers. Figure 6.6 shows OOMMF simulations and the respective x-axis magnetic induction of the top (thicker) layer of a series of $100nm$ wide SAF nanowires with thickness ratios varying from a balanced sample in 6.6a to a 2:1 ratio in 6.6f. The thinner layer in each case is controlled by the interlayer coupling and forms the exact opposite of that shown in this figure.

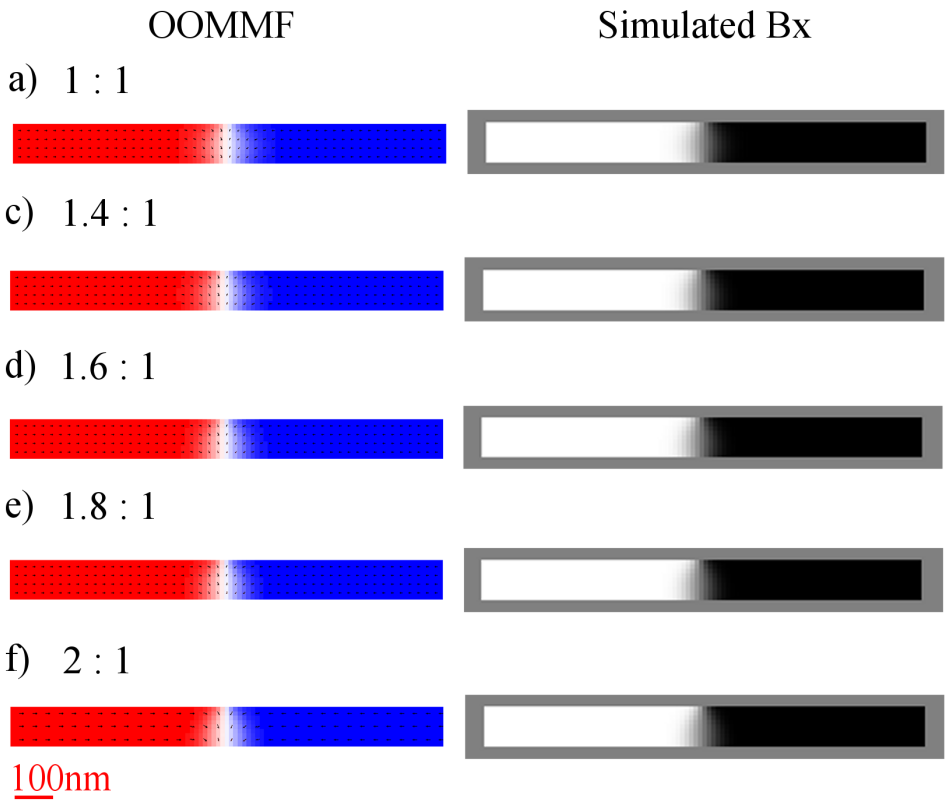

Figure 6.6: OOMMF simulations of DW structures in 100nm wide SAF multilayer nanowires magnetic layer thickness ratios varying between 1:1 to 2:1. Displaying change in DW structure with thickness ratio.

Figure 6.6 demonstrates how the structure varies with thickness. The balanced sample wall shown in figure 6.6a is symmetrical across the wire with equal wall width at both the upper and lower edges. This series of images shows that as the upper layer increases in thickness the wall structure changes. This is most clearly demonstrated

by comparing the two extremes shown in 6.6a and f. The 2:1 sample wall shown in 6.6f is wider on the lower edge than on the upper, similar to that of a transverse wall in a single layer nanowire. Domain walls in single layer nanowires of comparable widths and thicknesses would be expected to be transverse. The narrow walls are a result of the minimisation of magnetostatic fields in these multilayer samples and the residual fields generated by the unbalance in thickness is the source of the change of wall structure. This variation in structure will be investigated experimentally in this study with the expectation that as the thickness ratio increases the wall will change from a narrow to a transverse type structure.

6.4 Sample Fabrication

The first set of SAF samples were plasma sputtered at the University of Leeds, these utilised the second AFM peak with a Ruthenium spacer thickness of 20Å. The thickness of the upper $Co_{80}Fe_{20}$ layer was varied to produce both balanced and unbalanced samples with layer structures of $Co_{80}Fe_{20}(100)/Ru(20)/Co_{80}Fe_{20}(100)$ and $Co_{80}Fe_{20}(100)/Ru(20)/Co_{80}Fe_{20}(50)$ respectively, with the thickness measurements in angstroms. This was accompanied by one sample of equal 100Å $Co_{80}Fe_{20}$ layers and 12Å ruthenium, to produce ferromagnetic interlayer coupling and was used as a control sample. Each of these samples was deposited on both solid and membrane substrates so all relevant measurements could be taken.

Focussed ion beam milling was then used to fabricate nanowire structures with widths of $800nm$ and elliptical injection pads. Investigation of the magnetic behaviour in these wires found that the domain wall injection into the wire occurred above the interlayer coupling field. This meant that the type of domain wall that was injected at this point could not be predictably identified.

The desired domain walls between the two opposing AFM states need to be able to be injected repeatedly and predictably. For this reason a new set of samples were deposited with the 20Å spacer layer being replaced by a 7Å layer utilising

the first AFM coupling peak. The thicknesses of the magnetic layers were altered compared to the first set so that while the unbalance ratio varied, the total thickness of the magnetic material was kept constant at $200nm$. 20Å of Ruthenium was also deposited below and on top of the SAF to minimise contamination and damage during fabrication and imaging. Figure 6.7a and b show cross section images of the 1:1 balanced sample and the 2:1 unbalanced sample respectively. These images show the $Co_{90}Fe_{10}$ and the spacer layers clearly, the EBD platinum layer is deposited to protect the sample when cutting the cross section.

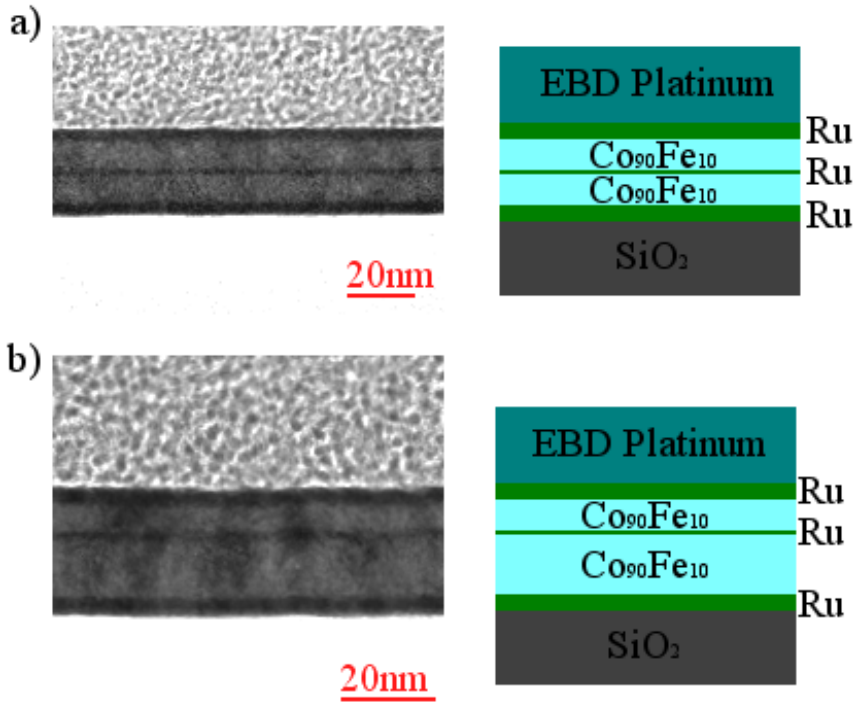

Figure 6.7: Cross sectional images and associated schematics of (a) 1:1 balanced and (b) 2:1 unbalanced SAFs.

Figure 6.8 then shows a minor hysteresis loop of the 2:1 unbalanced continuous film. This loop shows that a magnetic reversal occurs between ∼40 and $60Oe$. This is a reversal between the two opposing AFM states and the domain walls generated during the reversal will be of the desired type. The limits of the loop at $\pm 100Oe$ are the limits of the applied field in the B-H looper.

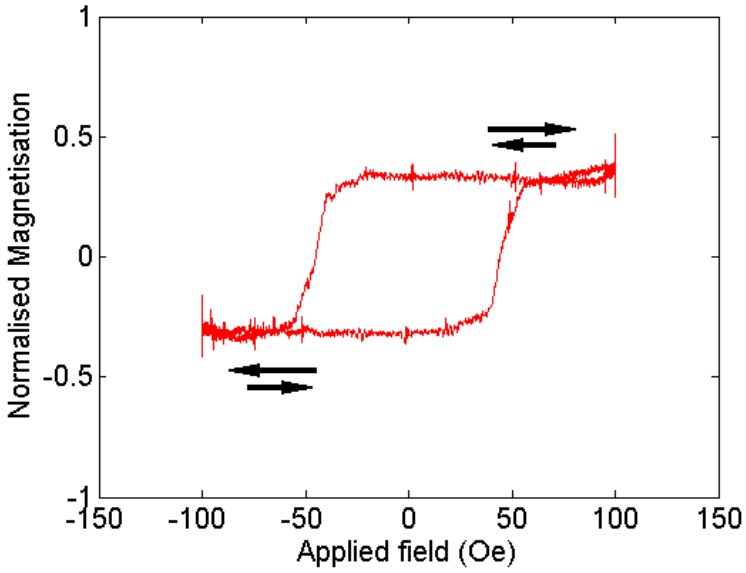

Figure 6.8: Minor hysteresis loop, measured in the B-H looper, of 2:1 unbalanced sample with 7Å ruthenium spacer layer.

6.4.1 Samples fabricated by focussed ion beam milling

The FEI Nova 200 dualbeam instrument was used to fabricate nanostructures in the balanced and unbalanced films. Two types of nanostructure were used, a curved nanowire with 90° corner and a straight, notched nanowire with a diamond shaped injection pad. Both of these structures were deposited with widths of $200nm$, $600nm$ and $1\mu m$, as shown in figure 6.9. These structures were chosen as they provide two different methods of nucleating a DW. A domain wall is formed in the curved wire with the application of a magnetic field perpendicular to the 90° corner. This creates opposite domains in the two arms of the wire which form a stable domain wall when the field is reduced to remanence. The straight wire forms a DW with the standard technique of a DW being injected from the pad and pinning at the notch.

Figure 6.10a shows a Fresnel image of the $1\mu m$ wide wire with a $-180Oe$ applied hard axis nucleation field in the direction shown. Figure 6.10b to f then show the wall behaviour as this field is reduced to remanence and increased in the opposite direction until the wall is ejected from the wire. This series of images show that the multilayer system is acting like a single layer FM wire. As well as this unanticipated behaviour,

the nucleated DW shown most clearly in the remanent image, and marked in red, is a transverse DW and not the narrow wall predicted previously. This led us to believe that the milling technique altered the interlayer coupling in the SAF surrounding the milled area. The domain walls marked by the in red in figure 6.10 show that the magnetic behaviour directly surrounding the milled area acts identically to the wire itself and seemingly independently from the rest of the continuous film. The size of this magnetically independent area within the continuous film is in the same order of magnitude as the width of the wire.

This change in magnetic behaviour is believed to be most likely caused by sample damage from tail of the gallium beam or ion implantation and was unobserved in the 20Å sample [5]. It was therefore concluded that that this damage is only significant enough to alter the coupling at the first AFM peak, as this peak is more highly dependent on the spacer thickness. While this damage may be reduced by tuning this technique with regards to ion current and the number of milling passes used, it is unlikely to be removed entirely; therefore FIB milling was replaced as the fabrication technique and EBL attempted.

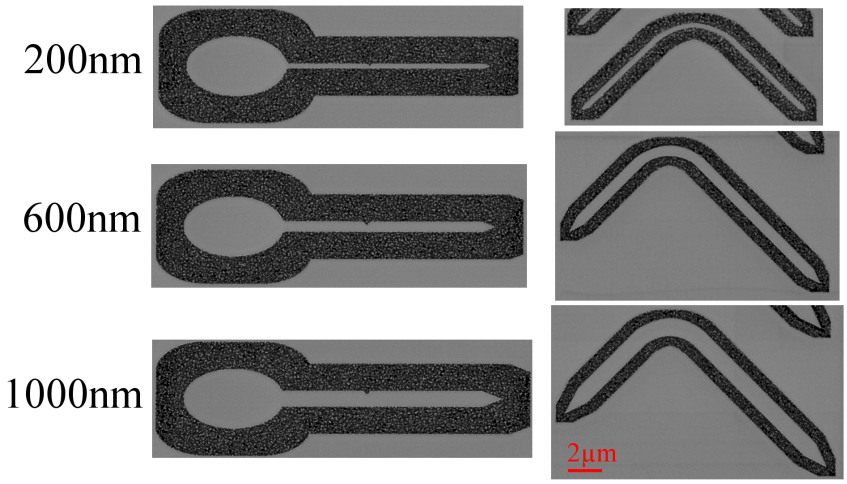

Figure 6.9: SEM images of curved and straight wires at $200nm$, $600nm$ and $1\mu m$ widths milled in the 2:1 unbalanced, 7Å spacer sample.

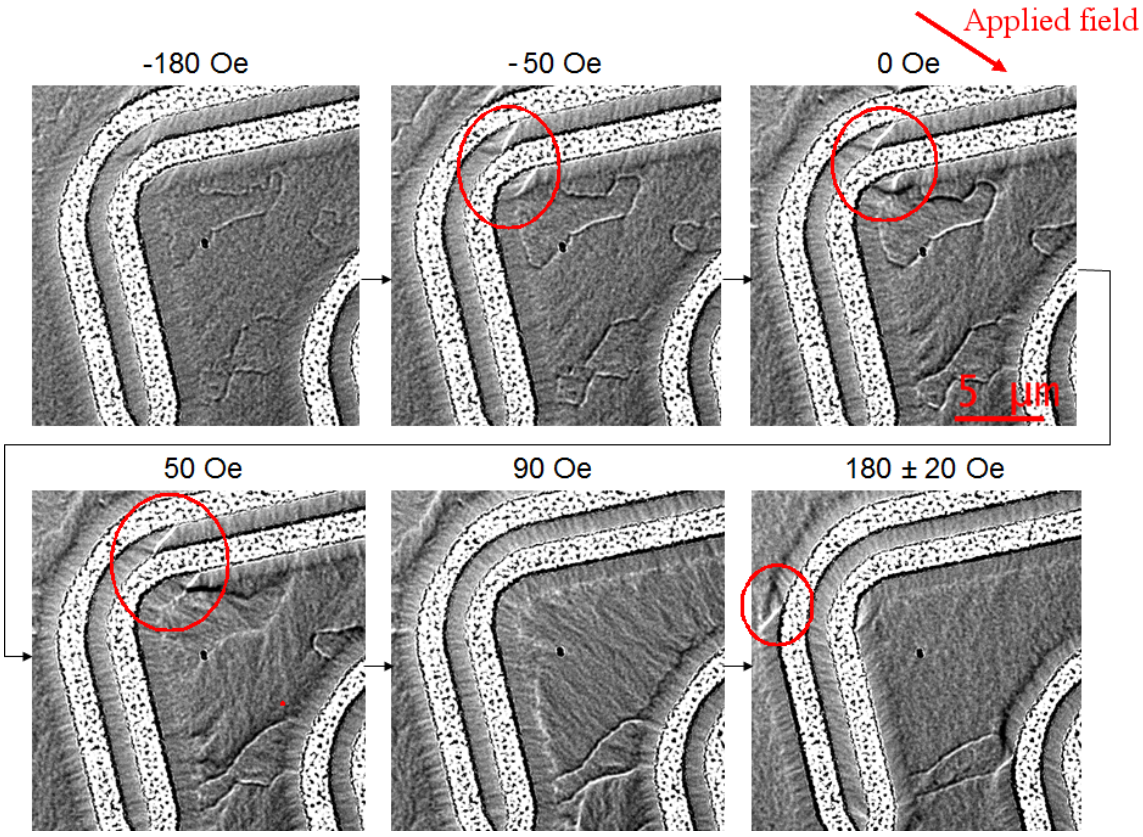

Figure 6.10: Fresnel series of the $1\mu m$ as a hard axis field is varied, showing nucleation and remnant domain wall states as well as the ejection between 50 and $90Oe$.

6.4.2 Samples fabricated by electron beam lithography

Electron beam lithography, was used to fabricate wires of $600nm$, $800nm$, $1\mu m$ and $1.2\mu m$ in both balanced and 2:1 unbalanced SAFs. Figure 6.11 shows in TEM focus images of these wires and intensity profiles across them. The lower edges of these wires, indicated by A in figure 6.11, are darker than the rest of the wire. This reduction in intensity, confirmed by the intensity profiles shown, indicates a sudden increase in the sample thickness indicative of flagging. This flagging has been formed from an imperfect lift-off during EBL, outlined in section 2.5, and results in both magnetic and spacer layers being distorted. This means that the orientation of the three layers in the SAF is unknown and may produce unpredictable magnetic behaviour.

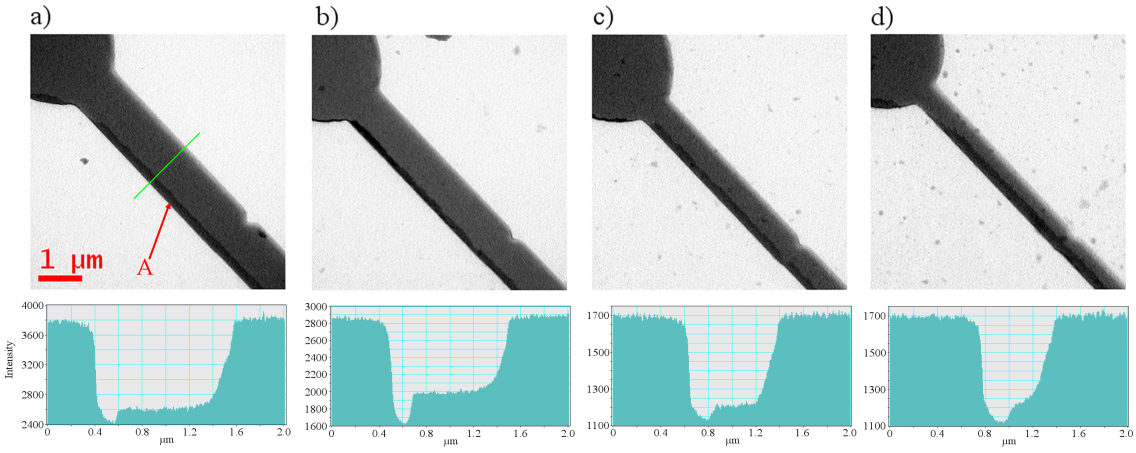

Figure 6.11: In focus TEM images of 2:1 thickness ratio SAF, EBL milled nanowires with (a)$1.2\mu m$, (B) $1\mu m$, (c) $800nm$, (d) $600nm$ widths. Intensity profiles across the wires clearly display a drop in intensity at the lower edge due to the thickness increase of the flag.

Figure 6.12 shows Fresnel images of the $1\mu m$ wire in a 2:1 thickness ratio as the applied field is varied. Figure 6.12a displays a structure under a positive $650Oe$ applied field, this structure is uniformly magnetised in a ferromagnetic state as indicated by the strong dark edge running the full length of the structure, highlighted by the blue arrow. The large and small red arrows in this figure represent the direction of magnetisation of the thicker and thinner magnetic layers respectively. In figure

6.12*b* the field has been reduced to remanence and domain structures are observed to have formed. There is a long domain wall across the width of the pad and another at the junction between the pad and the wire. Both of these walls have dark and bright fringes indicating that they are 360° walls formed as the narrow layer collapses into an AFM state with respect to the thicker layer. The strength of the dark edge along the bottom of the structure in figure 6.12*b* has reduced compared to *a*, indicating that this structure is now in an AFM state and confirming that the DWs seen in this figure are 360° walls. In figure 6.12*c*, an AFM domain wall has been injected into the wire near to one of the notches. This occurs at $-40Oe$ which is approximately the same as the AFM reversal in the continuous film, shown in figure 6.8. By figure 6.12*d*, at -80Oe applied field, the domain wall has passed through the wire and the dark contrast that was dominant in the lower edge of figure 6.12*b* has now shifted leaving the wire in the opposite AFM state to that shown in 6.12*b*. The apparent change in wire length between 6.12*a* and *b* is due to the tilt angle used for the magnetic field application, imaging the wire in transmission whist at these angles produces this seeming shortening of the wire.

This series of images shows that that the DW is injected at the same approximate field as the AFM reversal in the continuous film. This is encouraging as it indicates that the DW shown in figure 6.12c is most likely an AFM wall. However these structures are not ideal as the flagged edge alters the edge contrast and makes the magnetic states, and therefore the DW type, harder to identify conclusively. The behaviour observed in the non-flagged region shows that the interlayer coupling is stable and AFM walls are forming. However the contrast change induced by the flag along with its tendency to form undesired pinning points makes these wires and this fabrication technique unsuitable for further investigation. For this reason the argon milling was used as a fabrication technique in an attempt to remove the possibility of flagging.

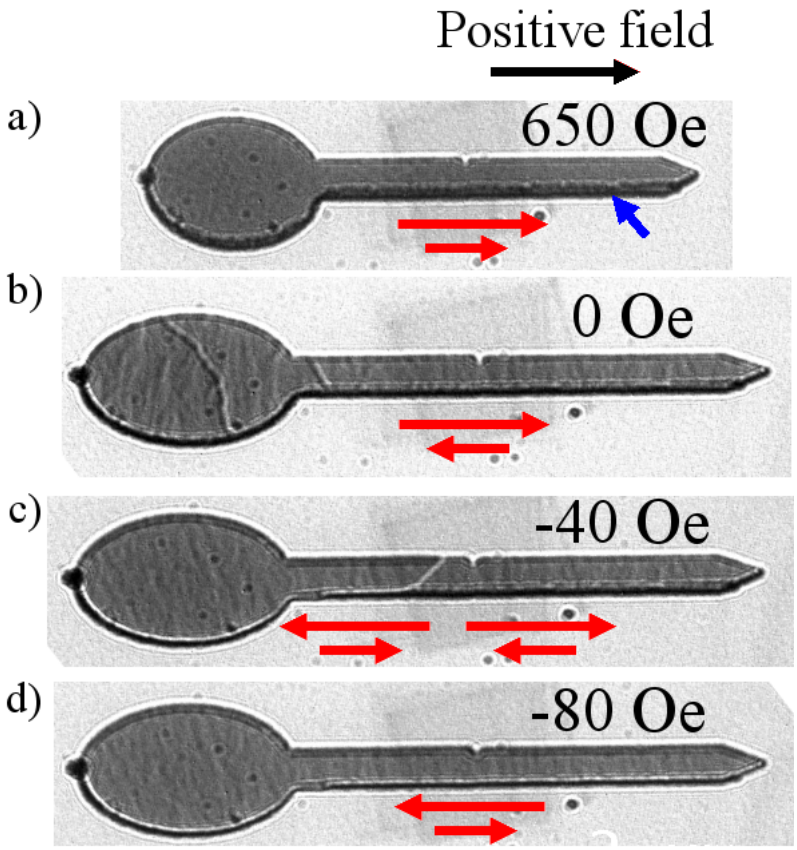

Figure 6.12: Fresnel series from 1μm EBL wire in 2:1 thickness ratio with varying applied field, displaying (a) FM, (b) positive AFM, (c) DW and (d) negative AFM states. Large and small red arrows indicate net direction of the thick and thin magnetic layers respectively.

6.4.3 Samples fabricated by argon ion milling

As discussed in chapter 2, this fabrication process uses EBL to generate a hard mask negative of the desired pattern on top of the magnetic multilayer before irradiating the whole sample with argon ions. The hard mask protects the desired nanostructure allowing the surrounding area to be milled. This method of fabrication avoids the possible flagging complications of EBL while maintaining milling spatial resolution. Figure 6.13 shows in focus images of argon milled wires in a 2:1 thickness sample of $1\mu m$, $800nm$ and $600nm$ widths. These images show that these wires have no flagging as well as well-defined edges and notches.

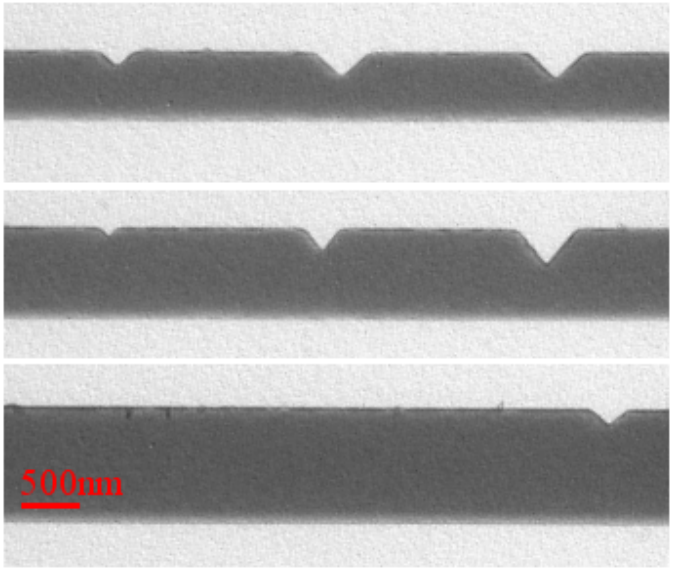

Figure 6.13: In focus TEM images of (a)$1\mu m$, (B) $800nm$ and (c) $600nm$ argon milled nanowires in a 2:1 thickness ratio SAF.

We know from previous experiments that a ferromagnetic state is only reached with applied fields between 400 and $700Oe$. Figure 6.14 shows a series of Fresnel images with an applied field varying over a minor loop well below these known values. This loop shows how the magnetic structure changes from a positive AFM state, shown in figure 6.14a, to a negative AFM state. Between $140Oe$ in figure 6.14a and $0Oe$ in b we see an increase in the magnetic dispersion characterised by an increase in the ripple contrast. Figure 6.14c then shows that a field of $-80Oe$ is sufficient to reverse

the AFM structure in the pad causing a DW to be injected into the wire. This wall in characterised by both the bright fringe of the wall itself and the change in edge contrast either side of the wall. In figure 6.14*d*, the DW from 6.14c has moved through the whole wire and a 360° wall has formed, characterised by the bright and dark fringes of the visible wall. This wall then annihilates at $-240Oe$ in figure 6.14*e*, the edge contrast in this image in unchanged from *d* and the area left of the wall in *c* (marked with the red arrow), indicating that the wire is still in an AFM state.

This behaviour demonstrates that the magnetic coupling is sufficient to hold the SAFs in an AFM state throughout the injection and that this injection occurs well below the interlayer coupling fields. Having established that argon milling produces clean edge wires with the desired interlayer coupling. This method was used to fabricate nanowires to investigate the structure of AFM DWs in wires of varying widths and layer thicknesses.

6.5 Domain Wall structures

Five different SAF samples were deposited, characterised by the ratio of their ferromagnetic layer thicknesses, the table below shows the structures of these five samples. It can be seen from this table that while the thickness ratio was varied, the total thickness of magnetic material was maintained at 200Å. This was done to ensure that any magnetic contrast seen when viewed in transmission (as in a TEM) was as comparable as possible between samples. Both the ruthenium capping layers and the 7Å spacer layer were consistent between samples.

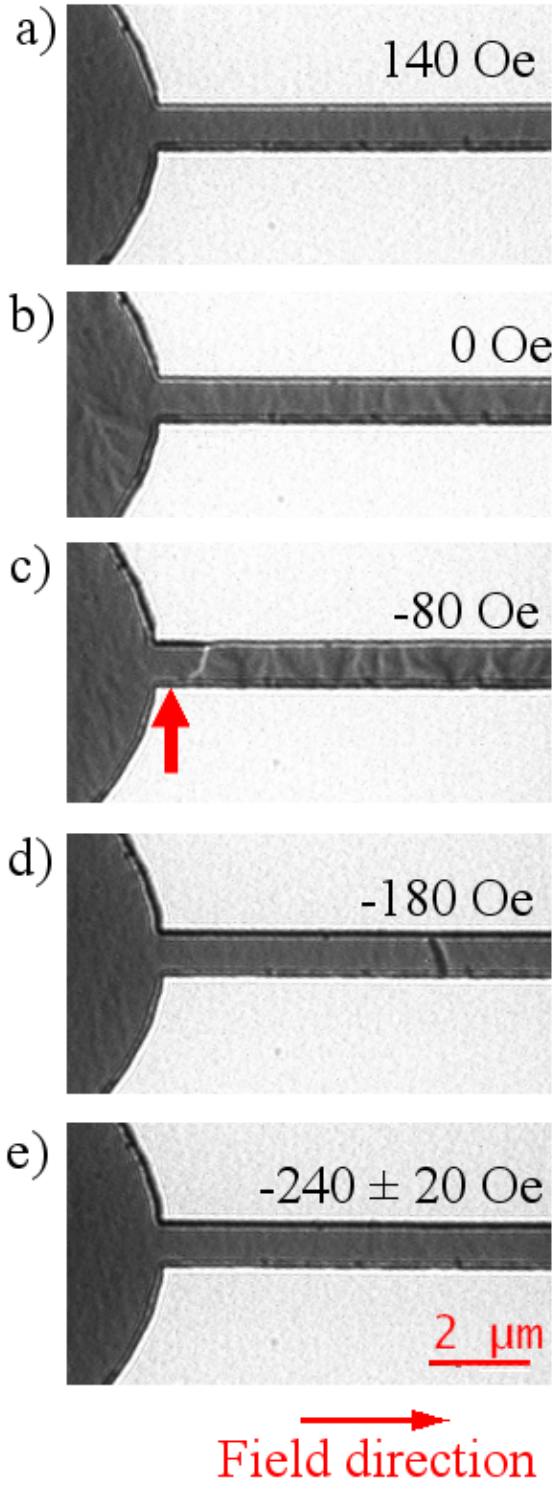

Figure 6.14: Fresnel series from $800nm$ in 2:1 unbalanced sample, argon milled wire with varying applied field around a minor injection loop, showing AFM wall injection at $\sim -80Oe$. All images shown are in AFM states.

SAF samples		
Thickness Ratio	Lower layer (Å)	Upper layer (Å)
1 : 1	100	100
1 : 1.25	111	89
1 : 1.5	120	80
1 : 1.75	127	73
1 : 2	133	67

The continuous films were argon milled into nanowires of 700nm, 800nm and 900nm widths. Figure 6.15 shows a TEM image and line profile of the 900nm wide wire in the 1.25:1 sample. This figure shows that the edges of the wires are not perfect; the upper edge (right hand side of profiles) is more gradual than the lower. The range of this gradual edge is shown by the red markers on the line profile in 6.15 and is measured to be ∼250nm. This is an effect of the argon beam not being perfectly optimised. The variation of the edge should have no effect on the interlayer coupling and therefore the behaviour of the nanowire, however it will affect the Fresnel contrast observed during Lorentz microscopy; the edge contrast in this technique is dependent on the gradient of magnetisation at the edge of the wire, therefore this gradual edge will produce less contrast than its steeper counterpart.

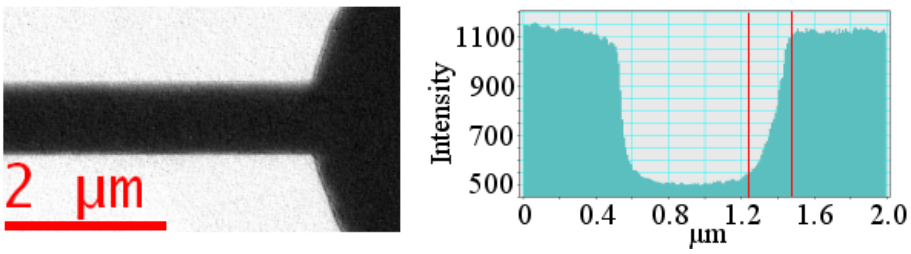

Figure 6.15: In focus and intensity line profiles of SAF nanowires of width (a) 700nm, (b) 800nm and (c) 900nm.

Figure 6.16 shows a series of Fresnel images throughout a full sweep from negative to positive saturation of the 800nm wire on the 1.25:1 sample. 6.16a is a negatively saturated state taken at −900Oe displaying a clear dark fringe on the upper edge of

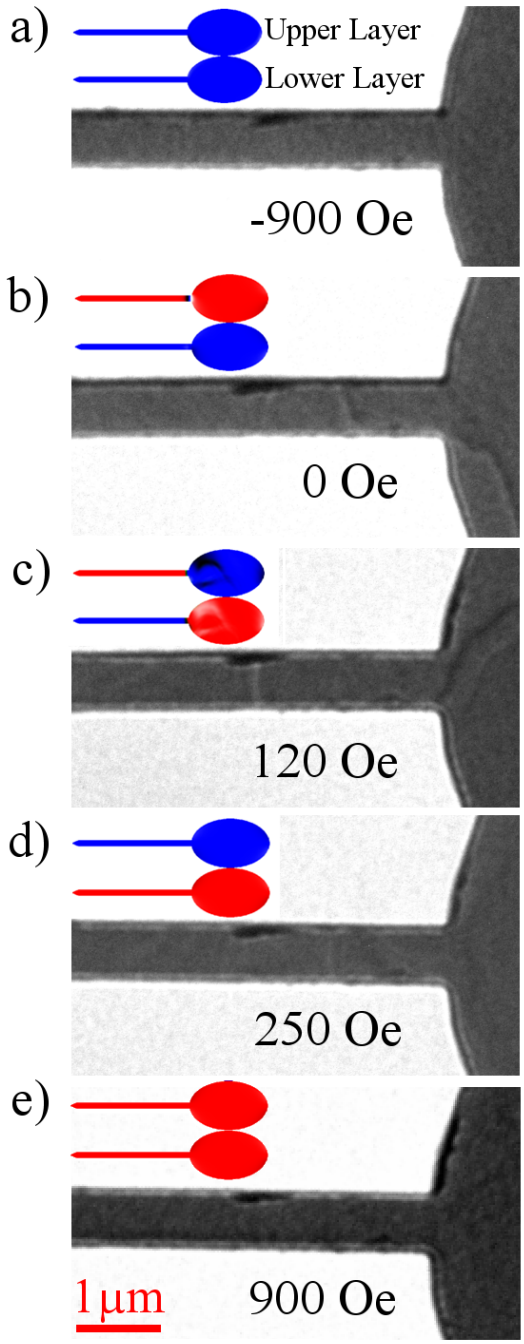

Figure 6.16: Fresnel images of a full sweep from positive to negative saturation of the 800nm wire on the 1.25:1 sample. Showing (a) positive FM, (b) positive AFM, (c) AFM DW, (d) negative AFM and (e) negative FM states.

the wire, 6.16*b* then shows the remanence state at $0Oe$, as expected as the field is reduced the interlayer coupling overcomes the Zeeman energy and the thinner layer reverses creating a net AFM structure. This reversal of the thinner layer generates a single layer 360° wall shown in figure 6.16*b*, characterised by the neighbouring bright and dark fringes. As the field is increased in the opposite direction, with the thicker layer controlling the net state, an AFM wall is injected. Figure 6.16*c* shows this wall pinned at an edge defect. Again the new magnetic state can be identified by the change in the edge contrast, this is most clearly seen either side of the wall on the upper edge of 6.16*c*. Figures 6.16*d* and 6.16*e* then show the positive AFM and FM states respectively as the field is increased further.

This series of images, and similar versions for each unbalance ratio, allowed us to identify the magnetic state of any part of the wire using the edge contrast. They also show us the fields required to saturate the coupled layers into a ferromagnetic state, this occurred between $\sim$400 and $700Oe$ and appears to be independent of the unbalance ratio; this is because this required field is mainly dependent on the interlayer coupling strength and not the layer thickness. For this reason, when investigating AFM walls, the applied fields were kept below this value to ensure all areas of the wire remain in an AFM state.

6.5.1 Magnetic behaviour of balanced sample

The first wires studied in this set of samples were in the 1:1 balanced sample. Figure 6.17 shows a series of Fresnel images of the $1\mu m$ wire as an applied field is varied from positive to negative $750Oe$. Figure 6.17*a* and *b* show a negative ferromagnetic state at $-750Oe$ and an AFM state at remanence respectively. These structures are identifiable by their edge contrast and as a significant ripple contrast was observed during the reversal between these two states, the 360° walls seen in figure 6.17*b* are formed in one of the layers during this first reversal. Figure 6.17*c* then shows a domain wall being injected from the pad at $300Oe$, highlighted by the red circle, with the two 360° domain walls from 6.17*b* still being present. Increasing the field

to $750Oe$ results in the final ferromagnetic state shown in 6.17d.

The edge contrast does not change between the left hand side of figure 6.17c, highlighted by the blue arrow, and that shown in figure 6.17d. We know that the structure shown in d is in a ferromagnetic state. Therefore the wall in c must be a single layer wall separating an AFM and FM states and not the desired wall separating two AFM states. This is confirmed as the field required to form this wall is within the range of the interlayer coupling and by the fact that the 360° walls from 6.17b are unperturbed. If this wall had been in both layers then it would need to cross the 360° walls and force them to annihilate.

The important result of figure 6.17 is that the desired domain walls between two AFM states do not form. This is because there is no thicker layer to control the net magnetisation and both layers are equally susceptible to the applied field. This means that as the applied field is varied over the range shown there are only two reversals, from FM to AFM and from AFM to FM. The reversal between the two opposing AFM states which would form the desired walls, does not occur in this sample.

The lack of injection process for AFM walls in the balanced sample does not preclude their existence in these samples. The initial reversal from a ferromagnetic state to an AFM state shown between figures 6.17a and b occurs in both layers simultaneously, this process can create AFM walls. If for example, the top layer reverses in the pad, forming an AFM state, but the bottom layer reverses in the wire (possibly nucleated from a defect or pinning point) then as these two domains converge an AFM wall will form. Figure 6.18 shows such a wall as the applied field is varied.

Figure 6.18a most clearly shows that this wall has a narrow straight structure perpendicular to the wire. Figure 6.18b to f then show how the Fresnel image of this wall varies as the field is reduced to remanence. This series shows that while

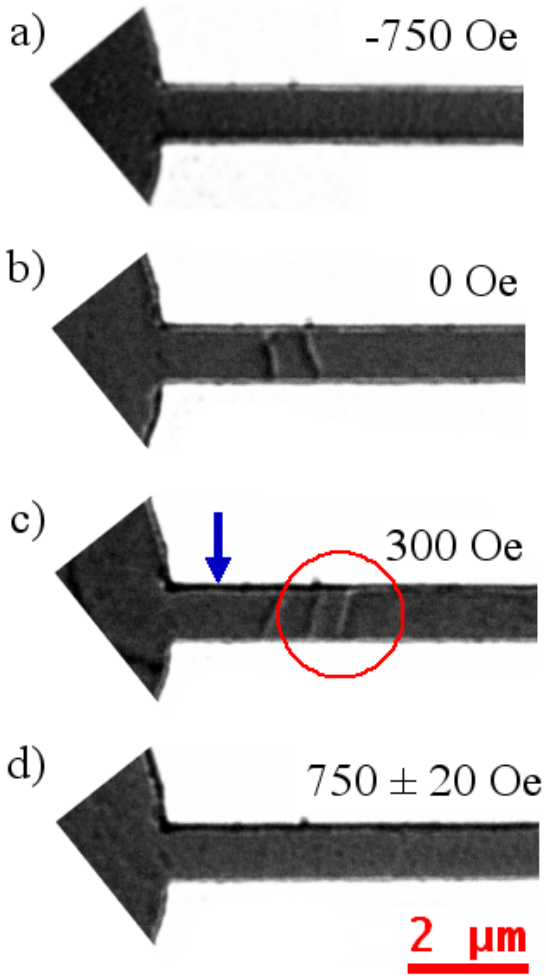

Figure 6.17: Fresnel images of the 800nm wide wire on the balanced sample as applied field is varied from negative to positive saturation.

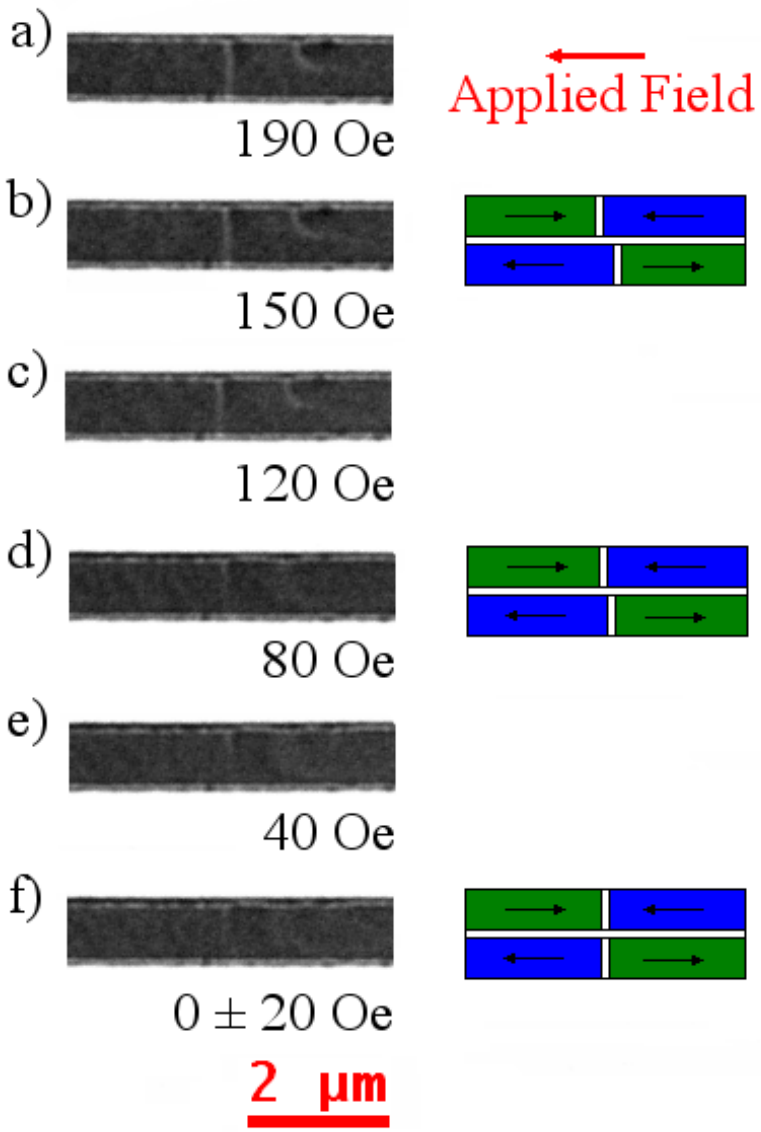

Figure 6.18: Fresnel images of 2:1 thickness ratio 800nm wide wire containing AFM domain wall at varying applied fields.

the wall remains static, the Fresnel fringe gradually reduces in intensity to almost invisibility at zero applied field. This happens because the Lorentz deflection, the source of the Fresnel intensity, is equal and opposite in each of the layers, cancelling the net deflection when seen in transmission. As the field is increased, it reinforces the domains parallel with it, and the DWs in each of the layers are displaced with respect to one another. This allows the walls to become visible, and is shown in the cross sectional schematics in 6.18.

6.5.2 Wire Thickness Variation

As shown in the table above, the SAF structures were fabricated with varying relative magnetic layer thicknesses. The thickness ratios varied from 1:1 balanced to 2:1 unbalanced samples. These samples were used to investigate the dependence of the sample thickness ratio on the domain wall structure. For the purposes of this study, the central wire width of 800nm was used to ensure wire consistency. Figure 6.19 shows two AFM walls from each thickness ratio. To ensure these walls were AFM walls rather than single layer or FM walls, the applied field was kept within the minor loop shown in figure 6.8. The edge contrast either side of the wall was also compared to the known AFM states within the wires, as shown in figure 6.16.

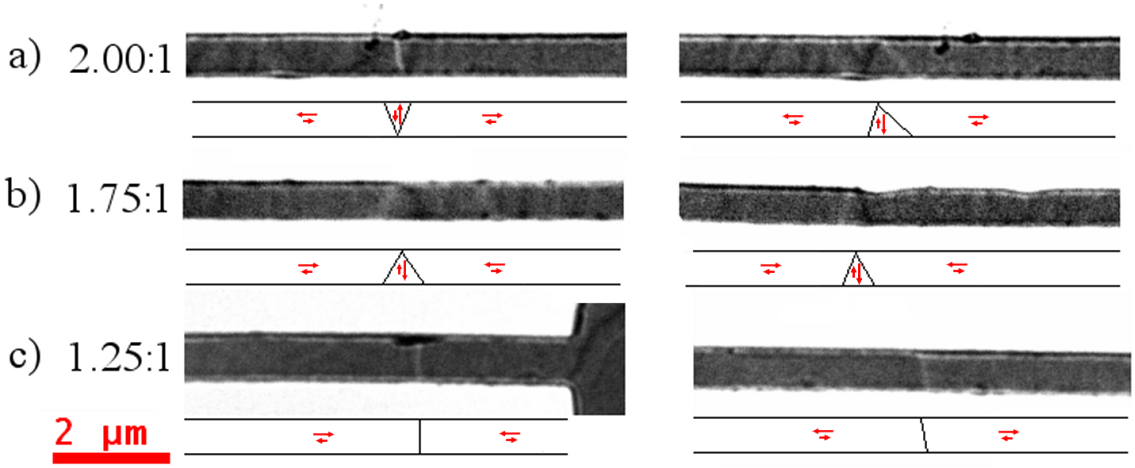

Figure 6.19: Two domain walls from each of (a) 2:1, (b) 1.75:1 and (c) 1.25:1 thickness ratios and schematic diagrams of each wall in an $800nm$ wide wire, large and small red arrows represent thicker and thinner layer magnetisation direction respectively.

Figure 6.19*a* and *b* shows that for the 2:1 and 1.75:1 samples, the domain walls have a transverse structure, falling to the expected narrow walls structure in 6.19*c* for the 1.25:1 sample. The difference in the DW contrast between the 2:1 and 1.75:1 samples, i.e. why the 2:1 wall is more visible that the 1.75:1, is because the 2:1 sample has a larger net magnetisation and therefore a higher magnetisation gradient. This higher magnetisation gradient causes a larger Lorentz deflection angle of the electron beam, and therefore a brighter Fresnel fringe.

The change from transverse to narrow DW structures as the thickness ratio reduces is because of the difference in the magnetostatic energy. The flux closure of the SAF structure reduces the magnetostatic energy by decreasing the net stray and demagnetising fields. This reduction in magnetostatic energy is minimised when the magnetic layers are of equal thickness in the balanced SAF; in unbalanced structures the energy reduction is compromised and net magnetisation means that the stray fields are still present. As with transverse and vortex domain walls in conventional nanowires, the structure of the wall is determined by the balance between the magnetostatic and exchange energies assuming consistent anisotropy and applied field. As the layer thicknesses get closer to a balanced state, the magnetostatic energy is reduced and the narrow DW state becomes energetically favourable over the transverse orientation. Figure 6.19 shows that the threshold for this change in structure lies between 1.75:1 and 1.25:1 thickness ratio.

Figure 6.20 shows images and line profiles of a narrow DW from the 1.25:1 sample and a transverse wall from the 2:1 sample in *a* and *b* respectively. The structure of these walls is not directly comparable as the transverse wall is formed of two separate 90° walls and the narrow wall is a single 180° rotation. However the full width of the wall, i.e. the size of the gap between the two magnetic domains, can be compared. The intensity profiles show that while the fringe of the narrow wall has an approximate width of $200nm$, the transverse wall has a full width of over a micrometre. One of the central aims of this study was to investigate the potential of these walls to reduce the distance between bits in magnetic recording media and

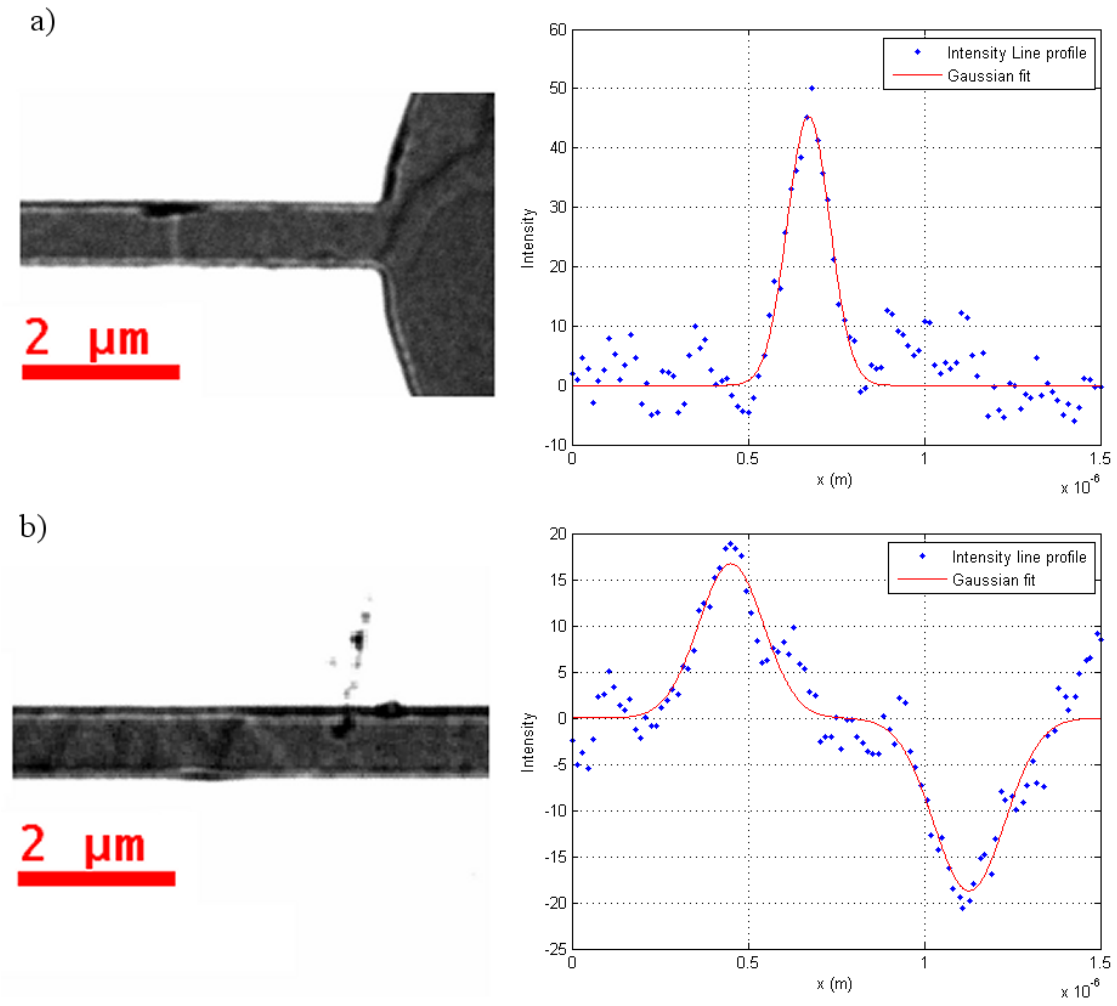

Figure 6.20: Fresnel images and intensity profiles for narrow and transverse domain walls in (a) 1.25:1 and (b) 2:1 samples respectively. Profiles are taken across the wall in the centre of the wire.

therefore increase their bit-density. Figure 6.20 confirms the existence of these walls and their significantly narrower structure compared to their transverse equivalents.

6.5.3 Wire Width Variation

Once it was established that the narrow domain walls form in the 1.25:1 sample, the structure of these walls was investigated with respect to the wire width. Figure 6.21 shows images and intensity profiles of narrow DWs in 700, 800 and 900nm wide wires. The intensity profiles of these walls have been fitted with Gaussian fits to measure their widths. Full width half maximums (FWHM) and full width tenth maximum (FWTM) of these Gaussians were used to measure this width. Note these are not measures of the domain walls widths but the width of the Fresnel fringes. While these are not measurements of the domain wall widths, they do allow for comparison between walls as long as the defocus of the microscope is consistent. The intensity profiles in figure 6.21 have had the background intensity removed to allow for the fitting of the Gaussian. This is the source of the negative intensity shown.

The table below shows two examples of each of these measurements from each of the wire widths. These demonstrate that while the FWHM and FWTM of these fringes vary in width from 120nm to 175nm and from 220nm to 320nm respectively, they are independent of wire width. This is as expected as once the magnetostatic energy is low enough for narrow walls to form. Their structure is determined by the exchange energy which is independent of wire width. As the wire width is reduced further in the 1.25:1 sample, the stray field and therefore the magnetostatic energy will increase; because of this it is postulated that as well as the thickness ratio, there will also be a threshold in the wire width below which transverse walls will form.

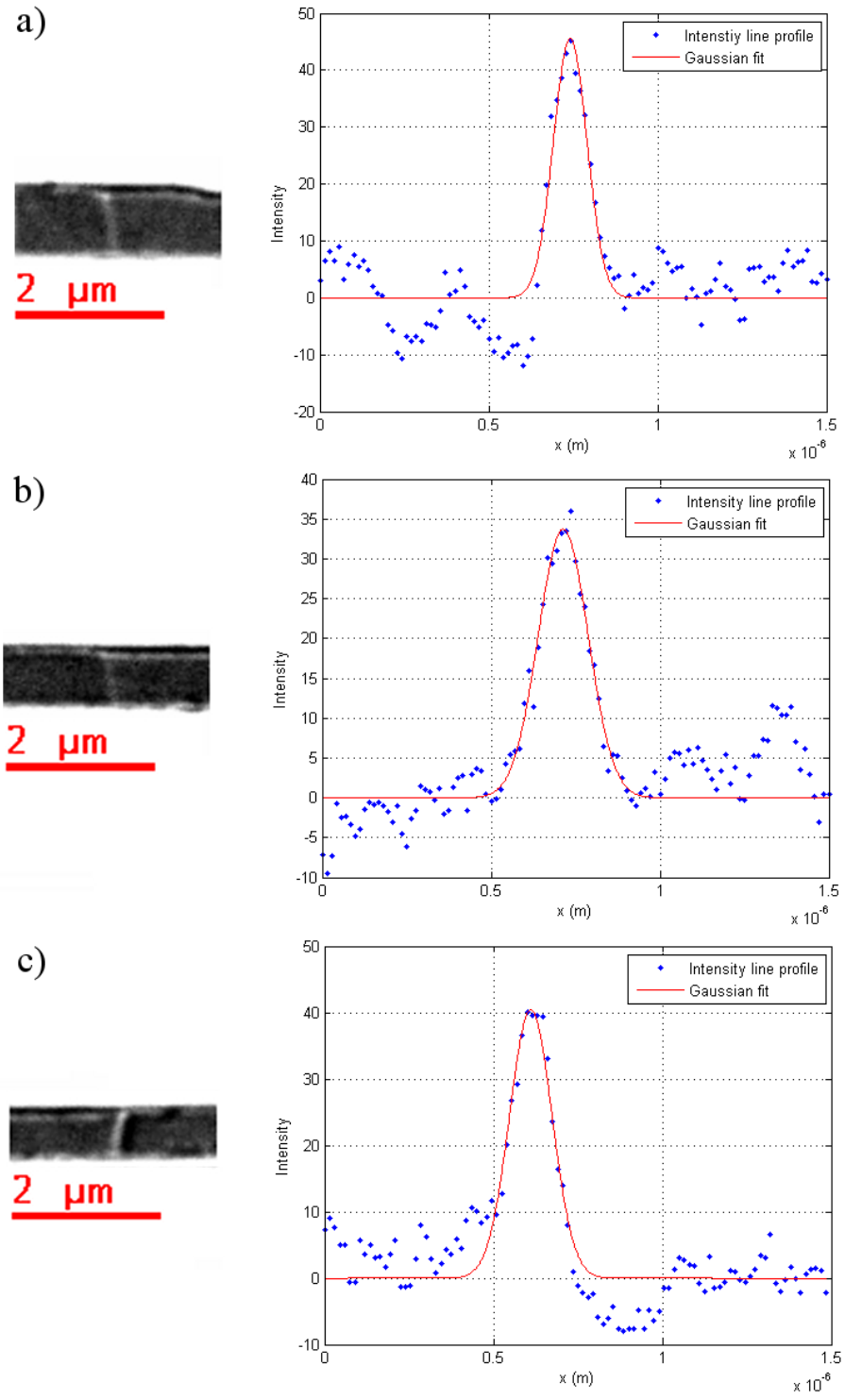

Figure 6.21: Images and intensity profiles after background removal of narrow domain walls in the 1.25:1 sample in (a) 900nm, (b) 800nm and (c)700nm wire widths. All images are taken with a consistent defocus of $42\mu m$.

Fringe width wrt. wire width		
Wire Width	FWHM (nm)	FWTM (nm)
700nm	165 ± 10	295 ± 10
	150 ± 10	270 ± 10
800nm	150 ± 10	275 ± 10
	175 ± 10	320 ± 10
900nm	120 ± 10	220 ± 10
	145 ± 10	260 ± 10

6.6 Summary and Conclusion

The narrow domain wall structures predicted in the synthetic antiferromagnets have been proven to form experimentally. These narrow, uniform walls were only found in samples with 1.25:1 thickness ratio, with DWs in nanowires above this ration forming transverse states.

The initial investigation utilised the second AFM coupling peak with a 20Åruthenium spacer layer. It was found that with this level of coupling, the DW injection field for the fabricated nanowires was above the interlayer coupling field leading to FM and single layer walls rather than the desired AFM walls. The second set of samples fixes this by reducing the spacer layer to 7Å, increasing the coupling strength beyond the required injection fields.

Having explored various milling techniques and their influence on the SAF structure and coupling; argon milling was used to fabricate nanowires of three different widths in samples with varying thickness ratios. These samples were then used to investigate the shape and structure of AFM walls as the wire dimensions vary.

The desired domain walls between two opposing AFM states were not able to be injected in a repeatable fashion in the balanced sample; therefore the main focus of this study was on the domain wall structure in the unbalanced SAF structures.

The domain wall structure in unbalanced samples was observed to change with the unbalanced ratio from transverse type walls in the 1.75:1 and 2:1 samples to narrower straight walls in the 1.25:1 samples. This was due to the influence of the magnetostatic energy. As with single layer samples, the domain wall structure is mainly determined by the balance between the exchange and magnetostatic energies. The narrow walls form because of the reduction in stray fields and therefore the magnetostatic energy within SAF structures. The closer a sample is to having equal magnetic layer thickness, the lower the net stray field and therefore the lower the magnetostatic energy. The change in the balance between exchange and magnetostatic energies as the thickness ratio varies is the source of the change in DW structure. The only samples in this study that produced repeatable and predictable narrow domain walls was the 1.25:1 sample. This was because while the magnetostatic energy is sufficient for the narrow domain walls to form, the unbalance ratio is high enough for the thicker layer to determine the net magnetic structure and therefore allow external fields to be used to inject domain walls into the nanowire.

The structure of the narrow DWs in the 1.25:1 sample were then investigated with respect to wire width. It was found that narrow DWs formed in wires of widths 900, 800 and 700nm. The wall widths were compared by fitting Gaussian plots to the Fresnel fringes and comparing their FWHM and FWTMs. It was found that the domain wall width did not vary with wire width within error. This corresponds to the wall structure being mainly determined by the exchange energy as the magnetostatic energy has been reduced sufficiently for these walls to form. As the wire widths are decreased below those used in this study, the shape anisotropy, which can be thought of as a magnetostatic energy term, will increase. The investigation into the wall variation with thickness ratio taught us that as the magnetostatic energy increases, transverse walls will form. This lead to the postulation that as there will also be a threshold of wire width, below which narrow DWs are not energetically favourable and transverse walls will form.

Bibliography

[1] Marrows C.H. Spin-polarised currents and magnetic domain walls. *Adv. Phys.*, 54(8):585–713, 2005.

[2] Beach G.S.D. Tsoi M. and Erskine J.L. Current-induced domain wall motion. *J. Magn. Magn. Mater.*, 320(7):1272–1281, APR 2008.

[3] McGrouther D. McVitie S. Chapman J.N. and Gentils A. Controlled domain wall injection into ferromagnetic nanowires from an optimized pad geometry. *Appl. Phys. Lett.*, 91(2), JUL 9 2007.

[4] O'Shea K.J. Tracey J. Bramsiepe S. Stamps R.L. Probing nanowire edge roughness using an extended magnetic domain wall. *Appl. Phys. Lett.*, 102(6), 2013.

[5] Basith M.A. McVitie S. McGrouther D. Chapman J. N. Reproducible domain wall pinning by linear non-topographic features in a ferromagnetic nanowire. *Appl. Phys. Lett.*, 100(23), 2012.

[6] Parkin S.S.P. Hayashi M. and Thomas L. Magnetic domain-wall racetrack memory. *Science*, 320(5873):190–194, 2008.

[7] Zhang Y. Zhao W.S. Ravelosona D. Klein J.O. Kim J.V. and Chappert C. Perpendicular-magnetic-anisotropy CoFeB racetrack memory. *J. Appl. Phys.*, 111(9), 2012.

[8] Thomas L. Yang S-H. Ryu K-S. Hughes B. Rettner C. Wang D-S. Tsai C-H. Shen K-H. Parkin S.S.P. Racetrack Memory: a high-performance, low-cost, non-volatile memory based on magnetic domain walls. In *2011 IEEE International electron devices meeting*, 2011.

[9] Klaeui M. Head-to-head domain walls in magnetic nanostructures. *J. Phys.-Condes. Matter*, 20(31), 2008.

[10] Basith M.A. McVitie S. McGrouther D. Chapman J.N. and Weaver J.M.R. Direct comparison of domain wall behavior in permalloy nanowires patterned by electron beam lithography and focused ion beam milling. *J. Appl. Phys.*, 110(8), 2011.

[11] Vogel A. Wintz S. Gerhardt T. Bocklage L. Strache T. Im M-Y. Fischer P. Fassbender J. McCord J. and Meier G. Field- and current-induced domain-wall motion in permalloy nanowires with magnetic soft spots. *Appl. Phys. Lett.*, 98(20), 2011.

[12] Togawa Y. Kimura T. Harada K. Tonomura A. and Otani Y. Control of magnetic domain wall displacement using spin current in small in-plane magnetic field in Permalloy nanowires. *J. Phys. D-Appl. Phys.*, 44(6, SI), FEB 16 2011.

[13] Bennett W.R. Schwarzacher W. and Egelhoff W.F. Concurrent enhancement of kerr rotation and antiferromagnetic coupling in epitaxial fe/cu/fe structures. *Phys. Rev. Lett.*, 65:3169–3172, Dec 1990.

[14] Parkin S.S.P. Bhadra R. and Roche K.P. Oscillatory magnetic exchange coupling through thin copper layers. *Phys. Rev. Lett.*, 66:2152–2155, Apr 1991.

[15] Ungeris J. Celotta R.J. and Pierce D.T. Observation of 2 Different Oscillation Periods in the Exchange Coupling of Fe/Cr/Fe(100). *Phys. Rev. Lett.*, 67(1):140–143, JUL 1 1991.

[16] Wang Y. Levy P.M. and Fry J.L. Interlayer magnetic coupling in fe/cr multilayered structures. *Phys. Rev. Lett.*, 65:2732–2735, Nov 1990.

[17] Parkin S.S.P. More N. and Roche K.P. Oscillations in Exchange Coupling and Magnetoresistance in Metallic Superlattice Structures - Co/Ru, Co/Cr and Fe/Cr. *Phys. Rev. Lett.*, 64(19):2304–2307, MAY 7 1990.

[18] Parkin S.S.P. Systematic Variation of the Strength and Oscillation Period of Indirect Magnetic Exchange Coupling Through the 3D, 4D, and 5D Transition-Metals. *Phys. Rev. Lett.*, 67(25):3598–3601, DEC 16 1991.

[19] Bardos D.I. Mean magnetic moments in bcc feco alloys. *J. Appl. Phys.*, 40(1371), 1969.

[20] Sahoo S. *Interacting magnetic nanoparticles in discontinuous Co80Fe20/Al2O3 multilayers and in granular FeCl2-Fe heterostructures.* PhD thesis, Universitt Duisburg-Essen, 2003.

[21] *Lepadatu S. private communication.*

[22] *Courtesy of S. Lepadatu, University of Leeds*, April 2010.

[23] Inomata K. Nozaki T. Tezuka N. and Sugimoto S. Magnetic switching field and giant magnetoresistance effect of multilayers with synthetic antiferromagnet free layers. *Appl. Phys. Lett.*, 81(2):310–312, JUL 8 2002.

[24] An N. Jander A. and Dhagat P. Electrically Tunable Thin Film Magnetic Core Using Synthetic Antiferromagnet Structure. *IEEE Trans. Magn.*, 44(11):4100–4103, NOV 2008.

[25] Fullerton E.E. et. al. Antiferromagnetically coupled magnetic media layers for thermally stable high-density recording. *Appl. Phys. Lett.*, 77(23):3806–3808, DEC 4 2000.

[26] Byeon S.C. Misra A. and Doyle W.D. Synthetic antiferromagnetic soft underlayers for perpendicular recording media. *IEEE Trans. Magn.*, 40(4, Part 2):2386–2388, 2004.

Chapter 7

Conclusions and Future Work

The work carried out in this study aimed to develop imaging techniques in transmission electron microscopy to make quantitative and temporally resolved magnetic imaging easier to implement and analyse than current imaging processes. The motivation behind this work was to investigate magnetic structures and behaviours in nanostructures as this knowledge is essential for the further development of magnetic memory and data storage devices. With the same motivation, the third project undertaken investigated the existence and properties of narrow domain wall structures in synthetic antiferromagnetic (SAF) samples. These narrow walls, a product of the interlayer coupling between the layers in the SAF, reduce the distance between bits in magnetic nanowires and therefore have the potential to increase the bit density in magnetic recording media beyond the current level.

Linear Phase Gradient Imaging

The first imaging technique developed used specifically engineered graded transmission apertures to linearly perturb the diffraction pattern with the aim of producing quantitative magnetic domain contrast proportional to magnetic induction. The objective apertures were deposited using EBID with a varying transmission gradient of up to $250\%\mu m^{-1}$. Most images gained using these wedges showed no visible magnetic contrast, however those that did, displayed contrast only just above the visibility limit. Figure 4.21 shows such a phase gradient image and the calculated

magnetic induction of a 20nm thick permalloy sample. The errors in this calculation are mainly as a result of the measurement of the phase gradient and midpoint transmission. This showed an induction difference of $\sim 2.4T$ indicating two opposing magnetic domains of $1.2 \pm 0.4T$ with an expected induction of $1T$.

While these calculations agree within error with the expected values, this method is still severely limited by the low levels of magnetic contrast. This could potentially be increased by depositing steeper wedges and thereby increasing the transmission gradient, however generating these wedges predictably with a continuous gradient was not possible using EBID. The use of the selected area aperture suggested at the end of chapter 4 would involve using free lens control on the microscope which would deter form the main objectives on the technique to produce simply calculable quantitative magnetic contrast. Any potential future work on this technique will require an improved deposition method to controllably increase the transmission gradient. The JEOL MagTEM microscope recently installed at the University of Glasgow may also be capable of improving this technique as its imaging resolution is higher than that of the CM20 at < 1Å. This work is complimentary to the wider field with respect to the recent attraction of phase vorteces in TEMs. These techniques also utilise specifically engineered apertures to gain electron vortex beams separated by angular momentum. This technique may also have applications in soft matter and biomedical microscopy as it may increase the visibility in these otherwise low contrast systems.

If this technique were to become viable, then it will produce quantitative magnetic information. Considering the already substantial capability if DPC imaging, this new technique will be of most consequence when used in parallel with standard Lorentz microscopy in direct imaging modes.

Temporal deflection Imaging

This technique used a magnetic pulse TEM rod to produce an image streak across the detector with respect to time. This was used with the aim of increasing temporal resolution in magnetic imaging. The results of this technique in Fresnel mode verified the prediction from simulation that the magnetic contrast within the streak would not be visible over the background intensity. Foucault and LAD modes were then utilised and both were also found to have limitations; Foucault mode was restricted in its total exposure time by the objective aperture drift, maximising the integrated exposure counts and therefore the total intensity. The limit was too low for the Foucault intensity to become visible over the noise. Finally LAD mode was attempted at the end of the electron gun's lifetime; this led again to an inadequate number of counts to observe the magnetic intensity over the noise.

To improve this technique in either imaging or LAD mode, the total intensity counts in the image must be increased. This is limited by the total acquisition time of the integral process. There are two main ways this can be improved; either increase the stability of the system or the frame rate of the acquisition. The Foucault imaging was limited by the stability of the objective aperture position, stabilising this further will allow the Foucault condition to be held for longer, increasing the maximum total number of acquisitions.

The JEOL ARM200 MagTEM at the University of Glasgow may be capable of solving all these problems. The objective aperture positions in this instrument are electronically controlled, rather than manually; this mechanism means that the aperture is less susceptible to drift and the Foucault condition will be able to be held for longer. The ARM200 also uses a cold FEG electron source rather than the Schottky FEG used in the Philips CM20, this leads to a more consistent, and more intense electron beam. Along with the improved and more stable sample positioning this microscope is significantly more suitable for this imaging technique and may provide the conditions needed to establish it.

Domain Wall structure in Synthetic Antiferromagnetic Nanowires

The narrow domain walls predicted in simulations have been proven to form in SAF nanowires of varying widths. These walls only formed in samples with magnetic layer thickness ratio below 1.25:1, with samples of ratios above this, forming walls with transverse structure. This change in structure with relative magnetic layer thickness is due to the increase in magnetostatic fields with increase imbalance. Once the apparent threshold of 1.25:1 thickness ratio was found, the Fresnel fringe width was investigated with respect to the wire width. While these fringe widths are not equal to the wall width itself they still allow for the comparison between walls. This study found that these fringes didn't vary within error as the wire width was varied from 900 to 700nm.

These narrow domain walls have been proven to exist, and the method of how to produce them identified; however the exact width and specific structure of these walls has yet to be investigated. This can be and is being done using DPC imaging in the JEOL MagTEM microscope. DPC has the advantage over the Fresnel methods used in this study as it is capable of quantitative induction measurements. These measurements will allow the structure of these walls to be mapped with respect to the magnetisation direction of both layers individually at sub-angstrom resolution. This will be done for both 180° and 360° walls in single and multilayers. Fresnel images will accompany these DPC images to confirm the structures and compare them with previously imaged walls. The continued development of Lorentz microscopy in both imaging and scanning modes will allow this work to be done with increased precision. Once the structure of these walls is more fully understood, full comparisons of how these walls vary can be done and their industrial application considered.